SANDIA REPORT
SAND2011-6643
Unlimited Release
Printed September 2011

Computational Thermal, Chemical, Fluid, and Solid Mechanics for Geosystems Management

Mario J. Martinez, C. Michael Stone, Patrick K. Notz, Daniel Z. Turner, Polly L. Hopkins, Sam Subia, Carlos Jove-Colon, Harry K. Moffat, James E. Bean, Thomas Dewers, Katherine Klise, John Red-Horse, Richard Field, Mikhail Mesh, Scott Davison, Hongkyu Yoon, Brian Carnes, Nicholas Alger, Joseph Bishop, Pania Newell

Prepared by
Sandia National Laboratories
Albuquerque, New Mexico 87185 and Livermore, California 94550

Sandia National Laboratories is a multi-program laboratory managed and operated by Sandia Corporation, a wholly owned subsidiary of Lockheed Martin Corporation, for the U.S. Department of Energy's National Nuclear Security Administration under contract DE-AC04-94AL85000.

Issued by Sandia National Laboratories, operated for the United States Department of Energy by Sandia Corporation.

Available to DOE and DOE contractors from
U.S. Department of Energy
Office of Scientific and Technical Information
P.O. Box 62
Oak Ridge, TN 37831

Telephone: (865) 576-8401
Facsimile: (865) 576-5728
E-Mail: reports@adonis.osti.gov
Online ordering: http://www.osti.gov/bridge

Available to the public from
U.S. Department of Commerce
National Technical Information Service
5285 Port Royal Rd.
Springfield, VA 22161

Telephone: (800) 553-6847
Facsimile: (703) 605-6900
E-Mail: orders@ntis.fedworld.gov
Online order: http://www.ntis.gov/help/ordermethods.asp?loc=7-4-0#online

SAND2011-6643
Unlimited Release
Printed September 2011

Computational Thermal, Chemical, Fluid, and Solid Mechanics for Geosystems Management

Mario J. Martinez
Thermal and Fluid Processes

Polly L. Hopkins, Harry K. Moffat
Nanoscale and Reactive Processes

Mikhail Mesh
Analytical Structural Dynamics

James E. Bean, Joseph Bishop, Pania Newell, Nicholas Alger
Computational Structural Mechanics and Applications

Richard Field
Component Science and Mechanics

Patrick K. Notz, Daniel Z. Turner, Sam Subia
Computational Thermal and Fluid Mechanics

John Red-Horse, Brian Carnes
Validation and Uncertainty Quantification

Carlos Jove-Colon
Radiological Consequence Management and Response Technologies

Scott Davison
Chemical and Biological Systems

Katherine Klise
National Security Applications

Thomas Dewers, Hongkyu Yoon
Geomechanics

C. Michael Stone
(Retired)

Sandia National Laboratories
P.O. Box 5800
Albuquerque, New Mexico 87185

Abstract

This document summarizes research performed under the SNL LDRD entitled "Computational Mechanics for Geosystems Management to Support the Energy and Natural Resources Mission." The main accomplishment was development of a foundational SNL capability for computational thermal, chemical, fluid, and solid mechanics analysis of geosystems. The code was developed within the SNL Sierra software system. This report summarizes the capabilities of the simulation code and the supporting research and development conducted under this LDRD.

Acknowledgments

This work was supported by the Sandia National Laboratories Laboratory Directed Research and Development program, Project No. 130739. We appreciate productive discussions with Profs. M. Delshad and M.F. Wheeler from the Center for Subsurface Modeling at the University of Texas at Austin concerning computational multiphase flow. We also thank Arthur Ratzel (4800) for his support during the inception of this project, Larry Costin (retired) and Tom Pfeifle (6914) for their support with project management. The report was improved by the technical reviews provided by S. R. Sobolik and A. B. Dodd.

Contents

Figures

Tables

Acronyms and Abbreviations

ASC	Advanced Simulation and Computing
BES	Basic Energy Sciences
BLUP	Best Linear Unbiased Predictor
CCS	carbon capture and storage
CDF	cumulative distribution function
CCDF	Conditional Cumulative Distribution Function
CFSES	Center for Subsurface Energy Security
CRADA	Cooperative Research and Development Agreement
DOE	Department of Energy
DOF	degrees-of-freedom
ECIS	Energy, Climate and Infrastructure Security
EDZ	excavation disturbed zone
EFRC	Energy Frontiers Research Center
ELWS	estimated limiting waste stream
EoS	equation(s) of state
ERN	Energy, Resources, and Nonproliferation
GSLIB	Geostatistical Software LIBrary
GEM	Gibbs energy minimization
GFEM	Galerkin finite element method
HKFT	Helgeson-Kirkham-Flowers-Tanger
HLW	high-level waste
HLWG	high-level waste glass
iid	independent identically distributed
ICES	Institute for Computational Engineering and Sciences
KL	Karhunen-Loève
LBFVM	Lattice Boltzmann and Finite Volume Method
LDRD	Laboratory Directed Research and Development
MCMC	Markov-chain Monte Carlo
MD	Multimechanism Deformation
MLE	maximum likelihood estimation
NAPL	non-aqueous phase liquids
NCL	normal consolidation line
NEAMS	Nuclear Energy Advanced Modeling and Simulation
NOX	nitrous oxide
NW	nuclear weapons
PCE	Polynomial Chaos Expansion
PDE	partial differential equation
Pdf	probability density function
PLC	power law creep
P-T	pressure-temperature
P-T-X	pressure-temperature-composition
P-V-T	pressure-volume-temperature
PWR	pressurized water reactor
RF	random field
R-K	Redlich-Kwong
RV	random variable
SCM	surface complexation model
sCO_2	supercritical CO_2
SGSIM	Sequential Gaussian Simulation
SMAX	maximum principal stress
SNL	Sandia National Laboratories
SOFC	solid oxide fuel cell
SP	stochastic process
TCE	trichloroethylene
THMC	thermal, hydrological, mechanical, chemical
TST	transition state theory
UNF	used nuclear fuel
UQ	uncertainty quantification
VCS	Villars-Cruise-Smith
VRV	random variable vector
WP	waste package
YMP	Yucca Mountain Project

Executive Summary

The main objective of the LDRD project entitled "Computational Mechanics for Geosystems Management to Support the Energy and Natural Resources Mission" was to enable a foundational capability for advanced modeling of coupled multiphysics subsurface processes to support current and future Sandia National Laboratories (SNL) projects in geosystems. Multiphase, multicomponent, reactive flow systems arise in many crucial SNL projects: geologic sequestration of CO_2 (a National Academy of Engineering challenge problem), geologic disposal of nuclear waste material, thermochemistry/decomposition of porous high explosive, nuclear weapons (NW) encapsulant foams and ablative materials, advanced designs of thermal/flow batteries, and many other projects in the energy security and conventional/nuclear weapons programs. Not all of these programs involve geosystems, but they all involve porous materials, and the research and development from this project can be directly applied.

Prior to this project, SNL did not have an institutional computational geosciences capability for modeling coupled thermal, chemical, geomechanical and flow problems, instead relying on commercial or freely available software. The final implementation of the simulation capability resides in the Sierra software system. The development of the Sierra Mechanics software platform has been primarily funded by the Department of Energy (DOE) Advanced Simulation and Computing (ASC) program for more than ten years. For this project, Sierra provides a massively parallel, objected oriented platform actively supported by SNL to fulfill the engineering sciences mission.

There are many pieces necessary to enable a parallel processing multiphysics simulator for nonisothermal reactive multicomponent multiphase fluid and solid mechanics in heterogeneous geologic media. While the Sierra system provides foundational support for solving discrete systems of equations, most of the needed physics modules did not exist.

The flow module, implemented in Sierra/Aria, is discussed in Chapter 2, and includes single phase and several two-phase flow models: two-phase immiscible, two-phase water and air, and two-phase, three-component CO_2-H_2O-NaCl, with thermodynamically generated phase behavior. This latter model in particular was developed to support SNL activities in geologic CO_2 sequestration, the target problem studied by the Center for Subsurface Energy Security (CFSES), a BES-funded program joint with University of Texas at Austin (UT/Austin). These flow models can be coupled to energy transport and reactive species transport, enabling multiphysics applications with phase change and chemical reaction. The transport of reactive species in porous materials under multiphase conditions, a capability also developed in this project, is discussed in chapter 3.

Sierra/Adagio is a large deformation and strain quasi-static solid mechanics module which utilizes the concept of effective stress for modeling mechanics of geomaterials. Several new constitutive models developed and implemented in this project are summarized in chapter 4. These models are able to treat multiphase nonlinear behavior (such as creep or consolidation) of clays and salt beds as a function of the volume fraction and capillary pressure for two-phase fluid systems. This project also enabled the application of the SNL-developed Geomodel for general treatment of geologic materials.

Strategies for multiphysics coupling in general are presented in chapter 5. The techniques enabling the general coupling of reactive flow and energy transport with geomechanics developed and utilized in this project are discussed here. The resulting algorithms allow the use of different grids for each of the physics modules using the concept of "REGIONS," and utilize the "TRANSFER" functionality in Sierra to provide transfer of information between grids. The coupling capability enables the so-called Thermal-Hydrological-Mechanical-Chemical multiphysics modeling capability for geosciences.

The treatment of phase behavior, based in the principle of Gibbs free energy minimization, is necessary to model complex fluid mixtures, in particular the CO_2-H_2O-NaCl system involved in CO_2 sequestration, a target problem for this project. Chapter 6 summarizes our work in developing the multiphase thermodynamics capability of performing phase equilibrium for fluid mixtures. Much of this work was implemented in Cantera (Moffat and Goodwin 2011), a general open-source thermodynamics package which is linked in the Sierra software system as a third-party library. Also discussed is an adaptive table lookup capability that makes the phase behavior thermodynamics available to the flow solver, or any other Sierra module, in an efficient manner. This obviates the need to perform so-called thermodynamic "flash" calculations dynamically, a highly CPU-intensive procedure.

A key feature of geologic materials is that they exhibit highly heterogeneous properties, e.g., porosity, permeability, geomechanics moduli, etc. Chapter 7 summarizes research into the statistical representation of heterogeneous properties exploring the use of Karhunen-Loeve expansions, and includes research in conditional simulation. The capability of dealing with heterogeneous properties is a newly developed feature in Adagio and Aria developed under this project.

The last chapter presents several application problems chosen to demonstrate the capabilities fulfilling goals and milestones for this project. Several applications were performed jointly with other SNL and work-for-others funded projects, as a vehicle to quickly demonstrate the potential impact of this research.

The accomplishments from this project support SNL in addressing many of the issues associated with protecting our economic and national security by assisting in the development of a diverse energy portfolio. In particular, the simulation software developed here enables SNL to address the wide range of multiphysics and multiscale issues associated with the entire energy cycle from in situ fuel extraction to waste disposal. The progress to date provides the proof of concept that our techniques for coupling multiphysics modules are viable and generally applicable.

We have made significant progress toward integrating the coupled, multiphysics simulation software with SNL and DOE strategic goals of energy security and environmental management. Since its inception, this project was key to supporting the joint SNL/UT/Austin Center for Subsurface Energy Security. The software developed in this project forms the basis for advanced multiphysics models supporting the multiscale research performed by CFSES in establishing the science foundation for viable CO_2 sequestration processes. The simulation software has been used in several key SNL energy projects, in particular, Clay/Shale and Salt Repository studies. This capability supports SNL initiatives directed at establishing SNL as a center for repository

management and analysis (nuclear waste and compressed air energy storage), and energy security (CO_2 sequestration). In addition to CFSES, this work has led to several new projects at SNL, including a new LDRD project on experiments and models for investigating clay/shale high level waste repositories. Munitions/Weapons Safety will fund further development and validation of reactive transport to study hot gas channeling in foam decomposition. This work led to two new projects funded in the current fiscal year from the DOE Office of Electricity for compressed air energy storage and flow batteries (electrochemical porous electrodes and membranes), and to negotiations with the Southwest Partnership for Carbon Storage to apply the simulation capability to study coupled geomechanics effects associated with supercritical CO_2 injection in deep saline aquifers. The Nuclear Energy Advanced Modeling and Simulation (NEAMS) project is tasked to evaluate and develop multiphysics modeling capability for nuclear waste forms and disposal systems. Chapter 8 includes model problems aimed at demonstrating that the multiphysics capabilities key to the success of NEAMS exist in Sierra.

1. Introduction

1.1. Purpose and Goals

This report summarizes the accomplishments resulting from the LDRD project entitled "Computational Mechanics for Geosystems Management to Support the Energy and Natural Resources Mission." The main objective of this project was to enable an advanced modeling capability for Sandia National Laboratories (SNL) to support current and future projects in geosystems. U.S. energy needs include more economical extraction of fossil fuels, protection of water resources, reduction of the impact of fossil fuels on climate change, mining nuclear fuel sources with minimal environmental impact, and technologies for safe disposal of energy wastes. SNL has active and potential programs in each of these areas. Long-term solutions to these needs require the ability to model and predict behavior of subsurface systems including complex, heterogeneous mineral and porous rock thermal-chemical-mechanical behavior as well as the interactions with multiphase pore fluids.

The main goal of this project was the development of a foundational capability for coupled thermal, hydrological, mechanical, chemical (THMC) simulation of heterogeneous geosystems utilizing massively parallel processing. To solve these complex issues, this project integrated research in numerical mathematics and algorithms for chemically reactive multiphase systems with computer science research in adaptive coupled solution control and framework architecture. This report summarizes and demonstrates the capabilities that were developed together with the supporting research underlying the models.

Key accomplishments:

- General capability for modeling nonisothermal, multiphase, multicomponent flow in heterogeneous porous geologic materials.
- General capability to model multiphase reactive transport of species in heterogeneous porous media.
- Constitutive models for describing real, general geomaterials under multiphase conditions utilizing laboratory data.
- General capability to couple nonisothermal reactive flow with geomechanics (THMC).
- Phase behavior thermodynamics for the CO_2-H_2O-NaCl system. General implementation enables modeling of other fluid mixtures. Adaptive look-up tables enable thermodynamic capability to other simulators.
- Capability for statistical modeling of heterogeneity in geologic materials.
- Simulator utilizes unstructured grids on parallel processing computers.

1.2 Collaborations

From its inception, this project has been closely allied with securing and supporting the joint SNL/University of Texas at Austin (UT/Austin) Center for Subsurface Energy Security (CFSES), a BES-funded Energy Frontiers Research Center (EFRC). Several of the applications discussed in the following represent work jointly supported by this LDRD and CFSES. We have ongoing collaboration with UT/Austin faculty and staff in the Institute for Computational Engineering and Sciences (ICES) and Petroleum Engineering department regarding modeling of

multiscale (pore scale to field scale) multiphase multicomponent subsurface systems. We have used this opportunity to guide our LDRD developments to position us to address both SNL-centric subsurface energy initiatives as well as position us to address broader national issues, such as CO_2 sequestration.

We also have established collaboration with the University of Utah via the Southwest Partnership for CO_2 sequestration. The capability to model coupled flow and geomechanics of representative geomaterials is the focus of this effort.

This project has also spawned and impacted a number of internal SNL collaborations, including the weapons program, energy storage (compressed air energy storage; flow batteries), the Nuclear Energy Advanced Modeling and Simulation (NEAMS) project, and waste disposal in clay, shales, and salt beds.

1.3 Software Developed in this Project

The Sierra software system was used as a platform for the development of the computational mechanics code developed in this project. The development of the Sierra Mechanics software platform has been primarily funded by the Department of Energy (DOE) Advanced Simulation and Computing (ASC) program for over ten years. The goal is the development of massively parallel multiphysics capabilities to support the SNL engineering sciences mission. Sierra Mechanics was designed and developed to run seamlessly on massively parallel computing hardware, spanning the hardware compute space from a single workstation to compute systems with thousands of processors. The foundation of Sierra Mechanics is the Sierra toolkit, which provides finite element application code services such as: (1) mesh and field data management, both parallel and distributed; (2) transfer operators for mapping field variables from one mechanics application to another; (3) a solution controller for code coupling; and (4) included third party libraries (e.g., solver libraries, MPI communications package, etc.).

The Sierra Mechanics code suite is comprised of application codes that address specific physics regimes. The two Sierra Mechanics codes which were utilized in this project include Aria (Notz et al. 2007) and Adagio (Sierra Solid Mechanics Team, 2009). The suite of physics supported by Aria includes low Reynolds number incompressible flow all the way to high Reynolds number, turbulent, reactive fluid flow (for modeling fires). Under the current LDRD project, a nonisothermal, multiphase, multicomponent porous flow capability has been added. Adagio supports large deformation quasi-static mechanics, including SNL-developed matrix-free iterative solution algorithms that allow extremely large and highly nonlinear problems to be solved efficiently. Adagio supports several constitutive models applicable to geomaterials, and under this LDRD, several new models specific to multiphase flow systems were added. Support for dynamic, flexible solution control enabling fluid flow and geomechanics (THMC) resides within the Sierra Mechanics called Arpeggio.

The following summarizes the physical/mathematical models developed in this project, the chapter describing the details of the models, and the code in which they were implemented.

Sierra/Aria

- Nonisothermal, single and multiphase, multicomponent flow in heterogeneous porous media (chapter 2)
- Multiphase, reactive species transport (chapter 3)

Sierra/Adagio

- Geomaterial-specific, two-phase, elasto-plastic constitutive geomechanics models (chapter 4)

Sierra/Arpeggio

- Solution control for general THMC coupling between Aria and Adagio (chapter 5), or for general coupling of physics modules within a Sierra code

Cantera

- Real fluid equations of state (EoS) thermodynamic models with capability to perform multicomponent compositional (e.g., CO_2-H_2O-NaCl) equilibrium (chapter 6); Cantera can be included in Sierra codes as a third party library
- Multidimensional adaptive tables of EoS and phase diagrams (chapter 6)

Dakota

- Numerical implementation of Karhunen-Loève (KL) expansion method for random field represention of spatially heterogeneous material properties (chapter 7)

2. Flow Physics Models

2.1 Introduction

In this chapter we present the physics models for multiphase flow in heterogeneous porous media developed and implemented in Sierra/Aria under this project. Prior to this effort, computational flow in porous media was not available in Sierra. This capability to model the flow and transport of fluids in the subsurface is a crucial piece needed to complete the development of a general subsurface simulation tool. In the following we will present the flow physics models starting from the simplest, for single phase flow, to the most complex, which include nonisothermal, multicomponent multiphase systems with complex phase behavior.

The numerical method used to solve the equations is summarized briefly in Appendix A. Martinez and Stone (2008) discussed the general formulation of multiphase, multicomponent flow in deformable porous media. The following sections use specific cases of this general description.

2.2 Single Phase Flow and Energy

2.2.1 Model Formulation

The general mass balance equation for single phase flow implemented in Aria is,

$$\frac{\partial(\phi\rho)}{\partial t} = \nabla \bullet (\rho \mathbf{v}) + Q \tag{2.1}$$

where the Darcy velocity (really a flux) vector is,

$$\mathbf{v} = -\frac{\mathbf{k}}{\mu} \bullet (\nabla p - \rho \mathbf{g}) \tag{2.2}$$

and ϕ is porosity, ρ is fluid density, Q is a mass source, $\mathbf{k}$ is the permeability tensor, p is fluid pressure, and μ is the fluid viscosity. The energy equation is implemented in the enthalpy form for single phase flow:

$$\frac{\partial}{\partial t}\left[(1-\phi)\rho_s e_s + \phi\rho e\right] + \nabla \bullet \left[\rho \mathbf{v} h - \lambda_e \nabla T\right] + Q_e = 0 \tag{2.3}$$

where e denotes fluid internal energy, e_s is the internal energy of the porous structure (sometimes referred to as the porous matrix or skeleton), h is fluid enthalpy, and λ_e is the effective thermal conductivity. Notice that this model assumes thermal equilibrium between the porous skeleton and the flowing fluid.

For a slightly compressible medium, we need to account for the porous medium and fluid compressibilities. In Aria, a general temperature and pressure dependent density model is the `Compressible_Boussinesq` model,

$$\rho = \rho_{ref}\left[1+\alpha\left(p-p_{ref}\right)+\beta(T-T_{ref})\right] \tag{2.4}$$

in which α is the isothermal fluid compressibility defined by,

$$\alpha = \frac{1}{\rho_{ref}}\frac{\partial\rho}{\partial p}, \tag{2.5}$$

and β is a thermal expansion coefficient (negative for volumetric expansion with increasing temperature). If the problem is isothermal, this term may be omitted. One may also define the density as a constant (`CONSTANT`) or a polynomial (`POLYNOMIAL`) as a function of pressure or temperature.

For ideal gas flow the density can be specified as `Single_Component_Ideal_Gas`,

$$\rho = \frac{R}{M}\frac{p}{T} \tag{2.6}$$

in which R is the universal gas constant and M is the molecular weight. The density is both pressure and temperature dependent.

Following Aziz and Settari (1979), the following model specifies a dependence of porosity on pressure (`Porosity=Rock_Compressible`) for a slightly compressible medium,

$$\phi = \phi_{ref}\left[1+C_r\left(p-p_{ref}\right)\right], \tag{2.7}$$

with C_r is defined as the rock compressibility, and implies,

$$\frac{1}{\phi_{ref}}\frac{\partial\phi}{\partial p}\bigg|_{p_{ref}} = C_r, \tag{2.8}$$

Again, the porosity can also be defined as constant (`CONSTANT`) or a polynomial (`POLYNOMIAL`) in terms of pressure. In single phase flow either the density or porosity has to be defined functionally in terms of the pressure; both cannot be constant.

Specifying the foregoing models, the single phase mass balance equation can then be written in terms of pressure as (for isothermal problems),

$$\rho_{ref}S_0\frac{\partial p}{\partial t} = \nabla\bullet\left(\rho\mathbf{v}\right)+Q \tag{2.9}$$

where the product $\rho_{ref} S_0$ is typically called the aquifer storativity by hydrologists, and we have defined,

$$S_0 = \phi_{ref} \left[C_r + \alpha \right], \tag{2.10}$$

in which we have ignored the second-order product of αC_r .

The viscosity can be specified as a constant or a polynomial in terms of temperature or pressure.

2.2.2 Verification Examples

Single Phase Water Injection

Fluid injection from a well into a confined aquifer of uniform porosity and permeability is described by the so-called well function solution, see e.g., chapter 8 of Bear (1979). The line source solution for pressure in a confined aquifer is: $p - p_0 = \frac{\mu Q_w}{4\pi kH} W(u)$, where $u = \frac{\mu r^2 S}{4kt}$ and in which the storage coefficient, assuming incompressible fluid density, is $S = \phi C_r$. H is the thickness of the confined aquifer and Q_w is the volume flow rate. $W(u)$ is the well function (an exponential integral) for a confined aquifer. The values for the line source solution in Figure 2.2-1 below were computed using a 4th order asymptotic representation of the well function valid for $u < 1$.

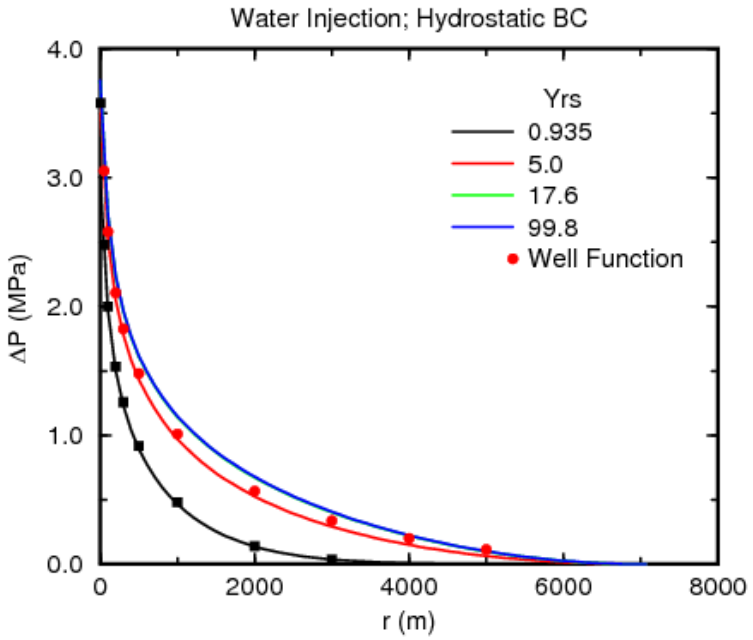

Figure 2.2-1. Numerical and analytical solutions for injection of water from a well into a confined aquifer. Solid lines are the numerical solution in a rectangular (1/4 symmetry) region on a coarse grid (~50 m grid blocks), while the symbols (both solid squares and circles) represent the analytical solution.

Parameters used in this problem are similar to values using by Ebigbo et al. (2007) on benchmark problems for modeling the CO_2 leakage through an abandoned well:

$C_r = 10^{-8}$ Pa^{-1}
$\phi = 0.15$
$H = 100$ m
$k = 2\text{x}10^{-14}$ m^2
$\mu = 2.54\text{x}10^{-4}$ Pa-s
$\rho = 1045$ kg/m^3

The values are representative of brine at high pressure. The mass flow rate into the quarter region is 8.87 kg/s for brine, so the equivalent well mass flow rate for the analytical solution is 4x8.87 kg/s.

The profiles of overpressure are along the diagonal of a rectangular 5 km x 5 km domain, 100 meters thick. Grid blocks are about 50 m x 50 m by 12.5 m in the vertical direction. The brine injection flux is specified on the two corner sides of the stack of corner elements comprising the injection "well." Even though no attempt is made to resolve the well, the numerical solution is accurate at 50 meters and beyond. The Sierra/Aria solutions at 17.6 and 100 years are the same, i.e., it has reached steady state by 17.6 years. The analytical solution is self-similar, and strictly speaking has no steady solution. The numerical problem has a steady solution because the head is held constant at the outer boundaries of the rectangle. The solution at 5 years shows some deviation at large radius, owing to this boundary condition, both the fact that a fixed head is specified and the fact that it is specified on the edges of a rectangle as opposed to a radial boundary (the analytical solution is obviously axisymmetric).

This solution was obtained with the immiscible physics model, to be discussed in the following, but with the non-wetting saturation set to zero as initial condition and on the boundaries, so the non-wetting mass balance equation is only along for the ride, and the wetting balance reverts to the single phase mass balance equation described above.

Elder Problem

As an example of a coupled thermal-hydrological problem, we consider buoyantly driven convection in a fluid-saturated porous layer. This problem was discussed by Elder (1967), under the Boussinesq approximation, providing both experimental and numerical results. In Sierra/Aria, the problem is described by the single phase heat and mass flow equations described in Eqns. (2.1) through (2.3).

Figure 2.2-2(c) shows the steady solution and summarizes the boundary conditions for buoyant convection in a bottom-heated 10-to-1 aspect ratio (W/H = width/height = 10) porous (30% porosity) layer. All boundaries are closed to flow, the sides are insulated to heat loss. The bottom is heated over a centrally located region of length $4H$ by holding the temperature at 40^o C while the remainder of the boundary is held at 20^o C. The fluid thermophysical properties are constant except for the density which is modeled with the `Compressible_Boussinesq` Sierra/Aria density option,

$$\rho = \rho_{ref}\left[1+\alpha\left(p-p_{ref}\right)+\beta(T-T_{ref})\right]$$

with β = -3.3x10^{-3} K^{-1} and negligible α.

We find a steady solution on a 100x20 uniform grid (only half the domain is modeled, because the problem is symmetric) of 4-node quadrilateral bilinear elements by solving a false transient until the solution is independent of time.

The solutions to this problem are a function of the Rayleigh number, defined by Elder as:

$$Ra = \frac{k\, g\, \beta \Delta T\, H}{\kappa_m \nu}$$

in which k is the permeability, g is gravity, ΔT is the temperature difference, κ_m is the diffusivity based on the effective thermal conductivity and the fluid heat capacity, and ν is the kinematic viscosity. Figure 2.2-2 shows the solution for various values of Rayleigh number. The number of convection cells and hot fingers increases with increasing Rayleigh number. This behavior is the same as what Elder shows in terms of the relationship between the number of cells and the Rayleigh number, though the values of Rayleigh number differ slightly, possibly because the present formulation is non-Boussinesq; the density is allowed to vary with temperature for all terms of the flow and energy equations.

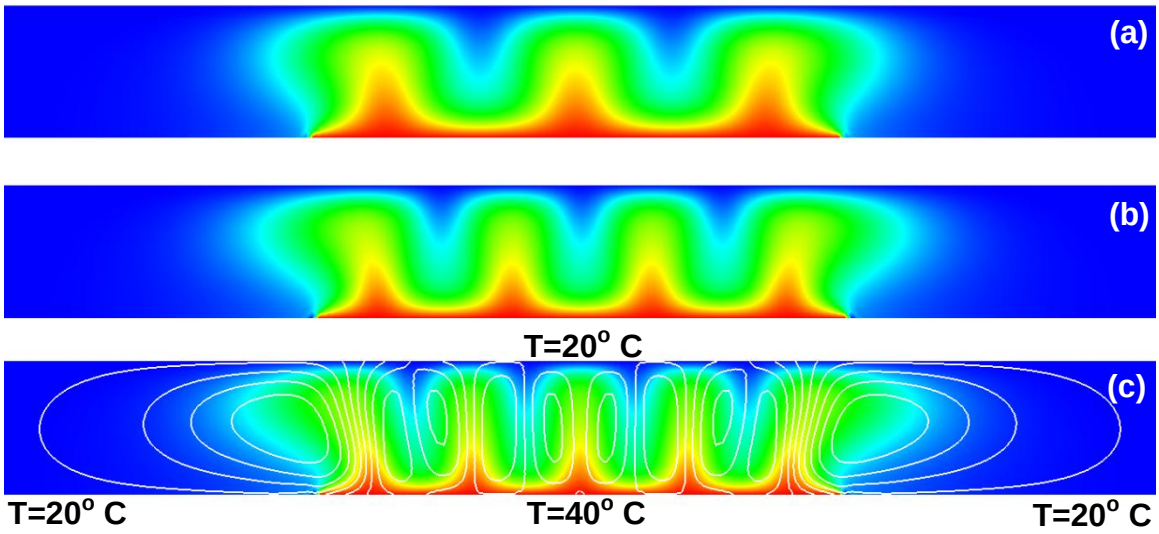

Figure 2.2-2. Buoyant Convection in a Porous Layer heated from below for a) Ra=72.5, b) Ra=106, and c) Ra=154.

2.3 Two-Phase Immiscible Flow

2.3.1 Model Formulation

In this section, we define a formulation for two-phase flow of immiscible fluids, that is, without mass transfer between the phases. Common examples include oil/water, under pressure and temperature conditions where phase transitions are negligible, and systems involving non-aqueous phase liquids (NAPL) occurring in subsurface contamination by organic liquids, e.g., solvents, fuels, oils. The present model formulation follows from the general two-phase formulation described in Martinez and Stone (2008).

If we disallow partitioning of components across phases, then we get the following system of mass balance equations for a wetting and non-wetting phase,

$$\begin{aligned} \frac{\partial\left(\rho_w\phi\left(1-S_n\right)\right)}{\partial t} &= \nabla\bullet\left(\rho_w\frac{k_{rw}}{\mu_w}\mathbf{k}\bullet\left(\nabla p-\rho_w\mathbf{g}\right)\right)+Q_w \\ \frac{\partial\left(\rho_n\phi S_n\right)}{\partial t} &= \nabla\bullet\left(\rho_n\frac{k_{rn}}{\mu_n}\mathbf{k}\bullet\left(\nabla p+\nabla p_c-\rho_n\mathbf{g}\right)\right)+Q_n \end{aligned} \tag{2.11}$$

In these equations, the subscript *w* represents wetting phase properties and the subscript *n* non-wetting phase properties. We have also incorporated the Darcy flux terms, including pressure and gravitational forces, as well as capillary pressure:

$$p_c = p_n - p_w \tag{2.12}$$

The symbol p in the equations is used in place of wetting phase pressure, p_w. Also, the pore space is assumed saturated with fluids,

$$S_w + S_n = 1 \tag{2.13}$$

This constraint has been incorporated in the wetting phase mass balance.

In addition to the density models described in the previous section, models for density and viscosity can be specified as constant, polynomial with respect to other primary or secondary variables, or by tabular functions, or a user-defined plug-in.

Capillary Pressure and Relative Permeability

Both the capillary pressure and relative permeability are functions of phase saturations. Either of these can be specified by the user in a tabular form, as a function of either phase saturation. A plug-in can also be written by the user for either of these functions. Several commonly used functions are built-in to the code.

The models described by Udell and Fitch (1985) have been implemented. The capillary pressure (`Udell_Cubic_Immiscible`) is defined as,

$$p_c = \sigma\sqrt{\frac{\phi}{k}}\left(c_1(1-s)+c_2(1-s)^2+c_3(1-s)^3\right) \tag{2.14}$$

where σ is the surface tension, *k* is permeability, and the scaled saturation is given by,

$$s = \left(S_w - S_{w,r}\right)\Big/\left(\left(1-S_{nw,r}\right)-S_{w,r}\right) \tag{2.15}$$

with residual wetting saturation, $S_{w,r}$ and residual non-wetting saturation $S_{nw,r}$. The coefficients are input parameters; Udell and Fitch give coefficients corresponding to data from a particular type of sand. The relative permeability functions specified by Udell and Fitch are cubic (`Udell_Cubic`) functions of the scaled saturation,

$$\begin{aligned} k_{rw} &= s^3 \\ k_{rn} &= (1-s)^3 \end{aligned} \tag{2.16}$$

Also available are the so-called van Genuchten (1978) functions. The capillary pressure is defined as,

$$p_c = p_{c0}\left(s^{-1/\lambda}-1\right)^{1/\beta} \qquad \lambda = 1-1/\beta, \qquad \beta > 1 \tag{2.17}$$

in terms of the scaled saturation defined above and in which p_{c0} plays the role of the "entry" pressure. The corresponding relative permeabilities are given by,

$$\begin{aligned} k_{rl} &= \sqrt{s}\left[1-\left(1-s^{1/\lambda}\right)^{\lambda}\right]^2 \\ k_{rg} &= \sqrt{1-s}\left[1-s^{1/\lambda}\right]^{2\lambda} \end{aligned} \tag{2.18}$$

2.3.2 Verification Example

Five-Spot Problem

To verify the two-phase immiscible flow implementation, the 5-spot waterflood problem, as described by Helmig (1997), is selected. This two-dimensional problem involves the injection of water (wetting phase) into an oil (non-wetting phase) saturated domain (300m x 300m). Capillary pressure and gravitational effects are not included. Two variations to the problem geometry and boundary conditions are considered (Figure 2.3-1). Case 1 involves water injection at the lower left corner and oil extraction at the upper right corner. In Case 2 water injection occurs at both the lower left and upper right corners; oil extraction occurs at both the upper left and lower right corners as indicated in Figure 2.3-1. Table 2.3-1 presents boundary and initial conditions as well as pertinent properties used in the calculations.

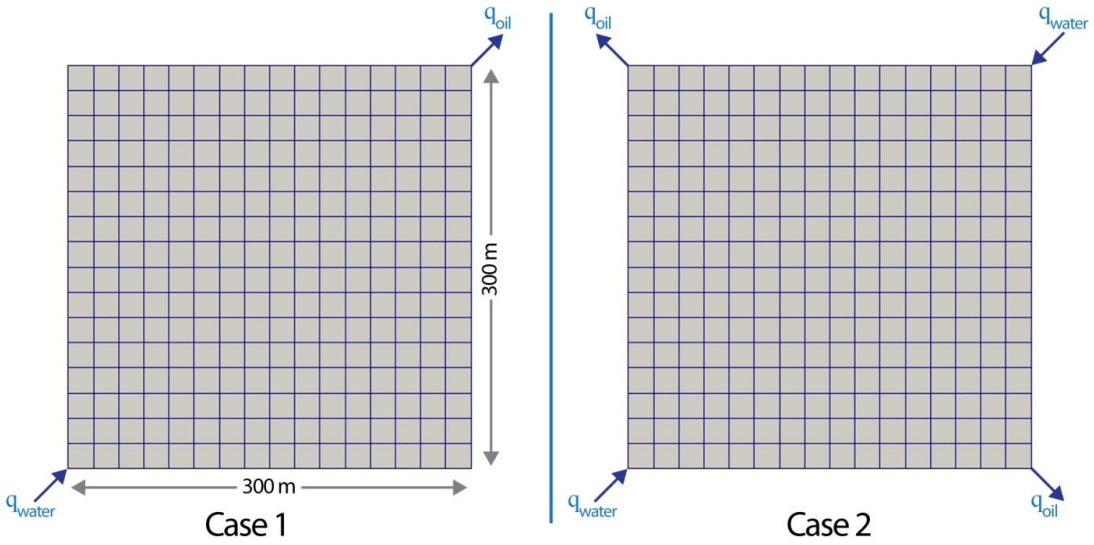

Figure 2.3-1. Schematic and mesh used for Case 1 (left) and Case 2 (right).

Table 2.3-1. Material properties, boundary and initial conditions.

Fluid Properties	**Value**	**Units**
Water density	1000	kg/m^3
Oil density	1000	kg/m^3
Water dynamic viscosity	0.001	kg/ms
Oil dynamic viscosity	0.001	kg/ms
Solid Matrix Properties		
Porosity	0.2	-
Intrinsic permeability	10^{-7}	m^2
Relative permeability	Udell cubic model	
Initial Conditions		
Oil saturation	1.0	-
Pressure	$2x10^5$	Pa
Case 1 Boundary Conditions		
At lower left corner (x=0, y=0):		
Oil pressure	$2x10^5$	Pa
Water injection rate	0.12	kg/s
At upper right corner (x=300,y=300):		
Water saturation	0.0	-
Oil extraction rate	0.12	kg/s
Case 2 Boundary Conditions		
At lower left and upper right corners (x=0, y=0) and (x=300, y=300):		
Oil pressure	$2x10^5$	Pa
Water injection rate	0.12	kg/s
At upper left and lower right corners (x=0,y=300) and (x=300, y=0):		
Water saturation	0.0	-
Oil extraction rate	0.12	kg/s

A difference to be noted is the applied form of the relative permeability function. Helmig uses relative permeability with a quadratic dependence on saturation. The Udell cubic was selected as the most representative among the available functions currently available. This is expected to contribute to some difference in solutions.

The mesh (Figure 2.3-1) is made up of 16x16 quadrilateral elements of equal size (18.75m x 18.75m), the same mesh used by Helmig. The simulations using this mesh were carried out with a fixed time step of 1 day for a total of 200 days. Water saturation contours at 200 days are shown in Figure 2.3-2 for both cases. The progress of the front, measured as the distance of the 0.1 contour line along the x-axis, is within a few percent (less than 4%) of the distance presented by Helmig (1997) in Figure 5.45c (pg. 296).

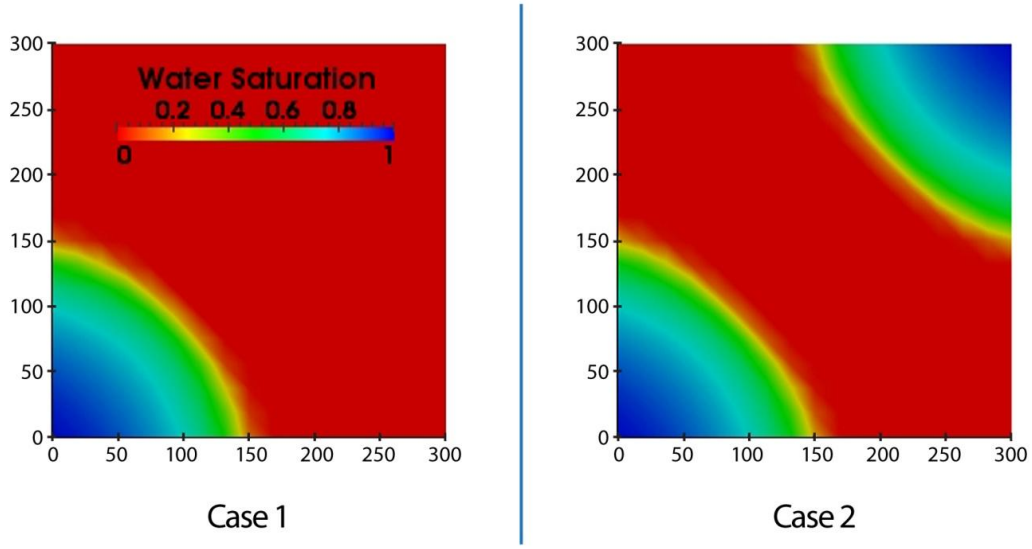

Figure 2.3-2. Water saturation contours at 200 days for Case 1 (left) and Case 2 (right).

The original injection/extraction boundary conditions were applied uniformly to the outside edges of the corner elements. A linear variation and a point source/sink were both considered with no significant change in results. Another variation described in the paper and performed with Aria was to rotate the mesh of Case 2 by 45 degrees in the counter-clockwise direction. Water saturation results were indistinguishable from the original orientation.

Finally, the mesh was refined by dividing each element side into 4 equal intervals to produce 16 elements per original element. The water saturation contours from Case 1 at 200 days are compared with those from the original mesh in Figure 2.3-3. Clearly the degree of spreading, in particular at the front, is due to the mesh resolution.

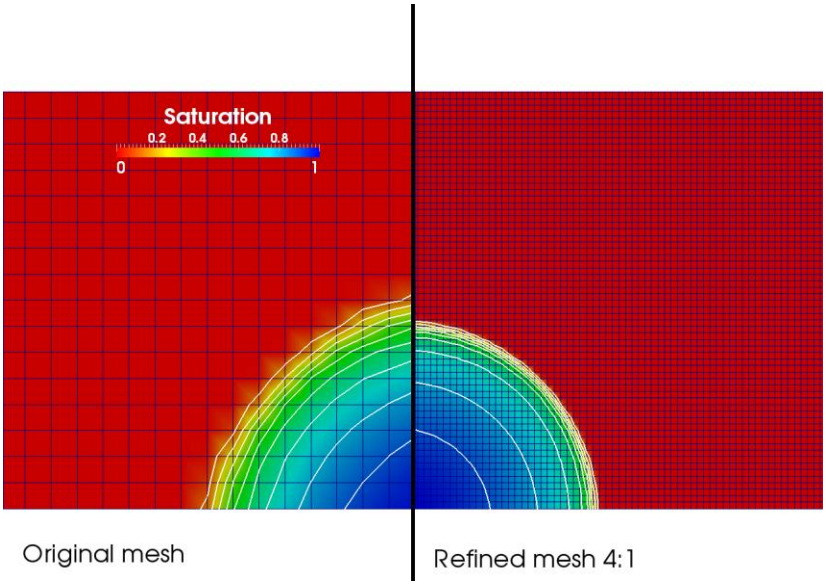

Figure 2.3-3. Comparison of water saturation contours with original (left) and refined (right) mesh.

This sample problem contributes to confidence that the two-phase immiscible flow formulation has been implemented correctly and that the solution method is capable of handling problems of this type. Additionally, the directional independence of this problem has been verified.

In addition to this verification problem, section 2.6 presents another verification problem involving capillary exclusion of dense non-aqueous phase liquid by an embedded lens of finer textured material, with a high entry pressure. Another verification problem is included in chapter 8, involving the leakage from an abandoned well during sequestration of CO_2 into a deep subsurface brine reservoir.

2.4 Two-Phase Air, Water, and Energy

2.4.1 Model Formulation

This model describes the nonisothermal two-component, two-phase transport of water and air in a porous medium. The air is treated as a non-condensible gas, but it can dissolve in the liquid phase. The water can exist as water vapor or liquid. The model allows the fluids to partition between the two phases, depending on pressure and temperature conditions. Two single phase states (all liquid or all gas) and one two-phase state are allowed.

The component mass balance equations describing two-phase transport of water, air and energy are:

Water: $$\frac{\partial}{\partial t}\left(\phi\left(S_l Y_{wl}\rho_l + S_g Y_{wg}\rho_g\right)\right) + \nabla \bullet \left(Y_{wl}\rho_l \mathbf{v}_l + Y_{wg}\rho_g \mathbf{v}_g + \mathbf{J}_{wg}\right) + Q_w = 0 \qquad (2.19)$$

Air: $$\frac{\partial}{\partial t}\left(\phi\left(S_l Y_{al}\rho_l + S_g Y_{ag}\rho_g\right)\right) + \nabla \bullet \left(Y_{al}\rho_l \mathbf{v}_l + Y_{ag}\rho_g \mathbf{v}_g + \mathbf{J}_{ag}\right) + Q_a = 0 \qquad (2.20)$$

Energy:
$$\frac{\partial}{\partial t}\left[(1-\phi)\rho_s e_s + \phi\left(\rho_l S_l e_l + \rho_g S_g e_g\right)\right] + \nabla \bullet \left(-\lambda_T \nabla T + \rho_l \mathbf{v}_l h_l + \rho_g \mathbf{v}_g h_g + h_{wg}\mathbf{J}_{wg} + h_{ag}\mathbf{J}_{ag}\right) + Q_e = 0 \tag{2.21}$$

where
$$\mathbf{J}_{\alpha g} = -\rho_g D_{wa} \nabla Y_{\alpha g} \tag{2.22}$$

is the gas-phase binary diffusion flux for water vapor through air. In these equations, subscript *l* refers to the liquid phase and *g* to the gas phase. In addition to previously defined variables,

$Y_{\alpha\beta}$ = mass fraction of component α (*w* for water or *a* for air) in phase β

S_β = saturation of phase β (*l* for liquid, *g* for gas)

ρ_β = phase density

e_β = internal energy of phase β (e_s is solid phase internal energy)

λ_T = effective thermal heat conduction

h_β = enthalpy of phase β

$h_{\alpha g}$ = component enthalpy in gas phase

The liquid and gas phase Darcy velocities are:

$$\mathbf{v}_l = -\frac{k_{rl}}{\mu_l}\mathbf{k} \bullet \left(\nabla P_l + \rho_l \mathbf{g}\right)$$
$$\mathbf{v}_g = -\frac{k_{rg}}{\mu_g}\mathbf{k} \bullet \left(\nabla P_g + \rho_g \mathbf{g}\right) \tag{2.23}$$

In addition, the following constraints must hold:

$$S_l + S_g = 1 \tag{2.24}$$

$$Y_{w\beta} + Y_{a\beta} = 1, \text{ for } \beta = l \text{ or } g \tag{2.25}$$

Thermodynamics

A challenging numerical issue with solving multicomponent, multiphase systems is the treatment of phase behavior, i.e., phase transitions can result in the appearance and disappearance of phases. The model must have the flexibility of dealing with dynamically evolving two-phase and single phase (all gas or all liquid) regions in the same grid. The difficulty arises from the fact that logical primary variables, defined as a set of variables such that all other secondary variables appearing in the mathematical model can be determined, are not persistent across the possible phase states. In the two-phase state, the liquid or gaseous saturation is a logical solution variable; it allows determination of the volume fraction occupied by each phase. However, saturation is not a variable in either of the two single phase states, but rather a constant. Martinez and Stone

(2008) review methods that have been applied to this problem; in the following we discuss a persistent variables formulation for the air-water-heat physics.

A persistent variables formulation can be developed by choosing the following primary variable vector:

$$U = \begin{bmatrix} \rho_w \\ P_a \\ T \end{bmatrix} \tag{2.26}$$

where

$$\rho_w = \rho_l Y_{wl} S_l + \rho_g Y_{wg} \left(1 - S_l\right) \tag{2.27}$$

is the bulk density of water in the pore space of the two-phase system. The system pressure is

$$P = P_a \left(\rho_a, T\right) + P_w(\rho_w, T) \tag{2.28}$$

where P_a and P_w denote partial pressures of air and water, respectively, and ρ_a is the partial density of air. The liquid and gas phase pressures are given in terms of the system pressure and capillary pressure,

$$\begin{aligned} P_l &= P - P_c(S_l) \\ P_g &= P \end{aligned} \tag{2.29}$$

Currently, thermodynamic properties for water in the liquid and two-phase states are represented by rational polynomials, as determined by Zyvoloski et al. (1995). Water in the gas-saturated state is currently treated as an ideal gas. Air is modeled as a non-condensible ideal gas. Dissolution of air in liquid water is approximated by a Henry's Law model,

$$Y_{al} = P_a / P_H^a(T) \tag{2.30}$$

In this persistent variables formulation, the liquid saturation can be determined as follows,

$$S_l = \begin{cases} 1 & \rho_w > \rho_{l,sat} \\ 0 & \rho_w < \rho_{g,sat}^w \\ \dfrac{\rho_w - \rho_{g,sat}^w}{\rho_{l,sat} - \rho_{g,sat}^w} & \text{otherwise} \end{cases} \tag{2.31}$$

where $\rho_{g,sat}^w$ is the saturated water vapor density, and $\rho_{l,sat} \equiv \rho_{l,sat}^w / \left(1 - P_a / P_H^a(T)\right)$, with $\rho_{l,sat}^w$ the saturated liquid water density.

2.4.2 Verification Example

Heat Induced Dryout in a Heatpipe

The steady heat pipe problem discussed by Udell and Fitch (1985) is the basis for this steady, thermal two-phase flow example problem. The problem involves the injection of heat into a one-dimensional horizontal column of porous material in which the void volume is filled with air and water (liquid and vapor). This problem has been used as a benchmark for the TOUGH2 code (Pruess 1987) and for the PorSalsa code (Martinez et al. 2001). This problem exercises features of evaporation/condensation and vapor and liquid flows in the code. Binary diffusion in the gas phase is included, and a saturation-dependent effective thermal conductivity is specified.

The material properties specified for this problem are the same as in the steady heat pipe problems posed by Udell and Fitch (1985). The grid used was the same as in the TOUGH2 calculation; a 2.25 m column is discretized into 90, 2.5 cm finite elements. The material has 40% porosity and 1 Darcy permeability (=10^{-12} m^2). The capillary pressure-saturation relation is a polynomial function fit to data by Udell and Fitch (`Udell_Cubic_Air_Water`) and the relative permeabilities are given by cubic functions of saturations, (`Udell_Cubic`) as described in section 2.3. In addition, the effective, saturation-dependent thermal conductivity was specified as (`Thermal Conductivity=Saturation_Power_Law`),

$$\lambda_T = \lambda_0 + \sqrt{S_l}\left(\lambda_1 - \lambda_0\right),$$

with $\lambda_0 = 0.582$ W/m-K and $\lambda_1 = 1.13$ W/m-K.

The steady solution is determined by computing a transient solution, starting from an arbitrary initial condition, until a steady-state solution is obtained. The initial conditions are $T = 70^o$ C, P_g = 1 atm, and $S_l = 0.5$. To initiate the transport, the left end ($x = 0$) is abruptly saturated with liquid, while the temperature and pressure are maintained at 70^o C and 0.10133 MPa, respectively. At the same time, a 100 W/m^2 heat flux is applied at $x = L$, which is also closed to the flow of air and water.

Figure 2.4-1 compares the steady profiles of liquid saturation (S), air mole fraction (X) and temperature (T) as given by TOUGH2, PorSalsa, and our implementation in Sierra/Aria. The mole fractions are determined from the mass fractions ($Y_{\alpha\beta}$) according to

$$X_{ag} = \frac{Y_{ag} W_w}{Y_{ag} W_w + Y_{wg} W_a}$$

where W_a and W_w are the molecular weights of air and water, respectively. The steady solution features a counter flow of water vapor toward the "condenser" under a vapor pressure gradient from the "evaporator" region, where heat is applied, balanced by an opposed flow of liquid wicked back toward the evaporator by capillary forces. It is noted that complete dry-out of the porous material occurs at about 2.1 m; the region closer to the evaporator is superheated single phase gas. This problem demonstrates the ability of our persistent variables formulation to deal

with phase appearance and disappearance. The solutions agree very well, including the location of the dry-out point.

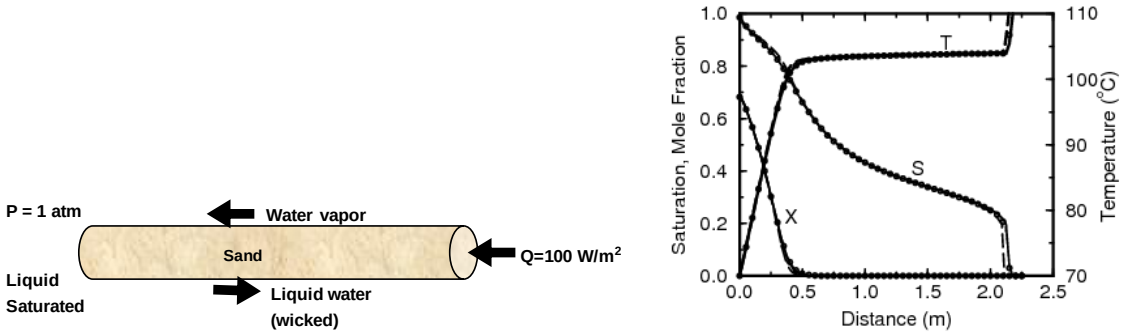

Figure 2.4-1. Comparison of steady heat pipe solutions given by Sierra/Aria (symbols), TOUGH2 (solid lines) and PorSalsa (dashed lines) for temperature (T), air mole fraction (X), and liquid saturation (S).

In addition to this verification example, section 2.6 includes another verification problem involving isothermal vertical infiltration across a capillary interface.

2.5 Two-Phase CO_2-H_2O-NaCl System

2.5.1 Model Formulation

The following presents a formulation for describing three-component two-phase flow for the CO_2-H_2O-NaCl system. This system is important to the subsurface sequestration of CO_2 for reducing greenhouse gas emissions. The two phases are brine, denoted by subscript *w*, a liquid phase of water with salt and CO_2 dissolved in it, and "gas," denoted by subscript *g*, a (generally supercritical) CO_2-rich phase, with some water dissolved in it, but no salt. The formulation also deals with precipitation of salt from the liquid phase. The notation differs slightly from the models discussed above; this formulation uses typical symbols from the reservoir simulation literature for composition in two-phase gas-liquid systems: *x* for mass fractions (or mole fractions) in liquid (brine) phase and *y* for mass fractions in the gas (CO_2) phase.

To deal with the precipitation of NaCl from the liquid to form solid salt, the fluid system is treated as a three-phase system, with two flowing phases composed of the brine and CO_2 phases, and one non-flowing solid phase, which is the solid salt precipitate. Obviously, the formulation holds for other chloride salts, e.g., CaCl, KCl.

Water: $$\frac{\partial}{\partial t}\phi\left(S_w\rho_w x_w + S_g\rho_g y_w\right) + \nabla\bullet\left(\rho_w x_w \mathbf{v}_w + \rho_g y_w \mathbf{v}_g + \mathbf{J}_w^{H_2O} + \mathbf{J}_g^{H_2O}\right) = Q^{H_2O} \qquad (2.32)$$

CO_2: $$\frac{\partial}{\partial t}\phi\left(S_w\rho_w x_{CO_2} + S_g\rho_g y_{CO_2}\right) + \nabla\bullet\left(\rho_w x_{CO_2} \mathbf{v}_w + \rho_g y_{CO_2} \mathbf{v}_g + \mathbf{J}_w^{CO_2} + \mathbf{J}_g^{CO_2}\right) = Q^{CO_2} \qquad (2.33)$$

Salt: $$\frac{\partial}{\partial t}\phi\left(S_w\rho_w x_{NACL} + S_s\rho_s\right) + \nabla\bullet\left(\rho_w x_{NACL}\mathbf{v}_w + \mathbf{J}_w^{NACL}\right) = Q^{NACL} \quad (2.34)$$

Nomenclature

S_s	=	saturation of solid salt precipitate
S_w	=	brine phase saturation
S_g	=	CO_2-rich phase ("gas") saturation
x_w	=	mass fraction of water in the brine phase
x_{CO_2}	=	mass fraction of CO_2 in the brine phase
x_{NACL}	=	mass fraction of salt dissolved in brine phase
y_{CO_2}	=	mass fraction of CO_2 in the "gas" (CO_2-rich) phase
y_w	=	mass fraction of water in the gas phase
ρ_w	=	density of brine phase
ρ_g	=	density of CO_2-rich phase ("gas")
$\rho_s(T, p)$	=	density of solid precipitate
$\mathbf{J}_\beta^\alpha$	=	diffusion flux of component α in phase β; can also include dispersion

Subscripts

w	=	refers to brine phase
g	=	refers to CO_2 phase
s	=	refers to solid salt phase

This model treats all the separate-phase CO_2 as a single CO_2-rich phase. The phase diagram for the CO_2-H_2O system displays a saturation line where liquid water, liquid CO_2 and a vapor phase can co-exist. The saturated water vapor pressure on this line is small, so the vapor phase is mostly CO_2.

Constraints:

$$S_w + S_g + S_s = 1 \quad (2.35)$$

$$x_w + x_{CO_2} + x_{NACL} = 1 \quad (2.36)$$

$$y_w + y_{CO_2} + y_{NACL} = 1 \quad (2.37)$$

We also have the constraint on the overall composition, which can replace either of the last two constraints above,

$$z_w + z_{CO_2} + z_{NACL} = 1 \quad (2.38)$$

The diffusion is approximated here by the formula for ordinary binary diffusion (c.f. Bird Stewart and Lightfoot, 1960, sec. 16.2), specialized for diffusion in a multiphase porous medium. For example, diffusion of CO_2 dissolved in the brine phase is approximated by,

$$\mathbf{J}_w^{CO_2} = -\phi S_w \tau \rho_w D_w^{CO_2} \nabla x_{CO_2} . \tag{2.39}$$

In general, the diffusion of component α in the β phase would look like,

$$\mathbf{J}_\beta^\alpha = -\phi S_\beta \tau \rho_\beta D_\beta^\alpha \nabla \xi_\alpha \tag{2.40}$$

where ξ_α is the mass fraction of the diffusing component in the β phase (x or y), and τ is the tortuosity factor, a property of the porous medium. The diffusion fluxes in a given phase satisfy,

$$\sum_\alpha \mathbf{J}_\beta^\alpha = 0 \tag{2.41}$$

which, taking account of Eqns. (2.36) and (2.37), requires that all the diffusion coefficients in a phase are equal,

$$D_\beta^\alpha = D_\beta \quad \forall \alpha \tag{2.42}$$

With this restriction, summing the three mass balance equations will result in the mass balance equation for the mixture, the so-called pressure equation (see Eqn. (2.43) below).

In the numerical implementation, in order to maintain the condition in Eqn. (2.41), one would compute two of the three diffusion fluxes in the brine phase from the definition in Eqn. (2.40) and the remaining one from the constraint Eqn. (2.41), for example,

$$\mathbf{J}_w^{H_2O} = -\mathbf{J}_w^{NaCl} - \mathbf{J}_w^{CO_2} .$$

To solve for the pressure, in all compositional situations, we can solve a pressure equation, obtained by summing all component balances. Since the resulting equation is not independent, it replaces one of the three mass balance equations presented earlier.

Pressure Equation:

$$\frac{\partial}{\partial t}\phi\left(S_w\rho_w + S_g\rho_g + S_s\rho_s\right) + \nabla \bullet \left(\rho_w \mathbf{v}_w + \rho_g \mathbf{v}_g\right) + Q^{H_2O} + Q^{CO_2} + Q^{NACL} = 0 \tag{2.43}$$

In the numerical implementation, this equation could be obtained after all boundary conditions have been applied to the discrete equations, by summing the three residual equations together.

2.5.2 Thermodynamic Equilibrium and Solution Algorithm

Recall, the primary variables for this system are defined as a set of variables that allow one to compute all the remaining (secondary) variables appearing in the mass and energy balance equations. For this problem, the primary solution vector (assuming we will also solve an energy balance for *T*) is $\lfloor P, z_{CO_2}, \rho_{NACL}, T \rfloor$, where

$$z_{CO_2} = \frac{S_w \rho_w x_{CO_2} + S_g \rho_g y_{CO_2}}{S_w \rho_w + S_g \rho_g} = (1-\nu) x_{CO_2} + \nu y_{CO_2}, \tag{2.44}$$

is the over-all mass fraction of CO_2 in the flowing phases. We have introduced the fraction of gas, defined as,

$$\nu = \frac{\rho_g S_g}{\rho_w S_w + \rho_g S_g}. \tag{2.45}$$

Similarly, the overall density of salt is defined by,

$$\begin{aligned} \rho_{NACL} &= \rho_w S_w x_{NACL} + \rho_s S_s \\ &= (1-\nu) x_{NACL} F + \rho_s S_s \end{aligned} \tag{2.46}$$

where we have introduced, for later convenience, the flowing mass density,

$$F = \rho_w S_w + \rho_g S_g \tag{2.47}$$

Note that the accumulation term in the CO_2 balance can be written as $\phi F z_{CO_2}$.

In this formulation, solve for *P* from the pressure equation, z_{CO_2} from the CO_2 mass balance, ρ_{NACL} from the NaCl balance and *T* from an energy balance.

Since we are dealing with a definite chemical system, the phase equilibrium can be done ahead of time. This is the subject of chapter 6 on thermodynamics. Here we will assume the equilibrium phase behavior is made available in the following form:

$$\begin{aligned} x_{CO_2}^{sat} &= f(T, P, x_{NACL}) \\ y_{CO_2}^{sat} &= f(T, P) \\ x_{NACL}^{sat} &= f(T, P, x_{CO_2}) \end{aligned} \tag{2.48}$$

The "sat" superscript in these equations indicates these values as the equilibrium composition under thermodynamically saturated two-phase conditions. These relations, together with the

mass fraction constraints, are sufficient to solve for the composition. The phase densities are defined by temperature, pressure, and composition,

$$\rho_w = \rho_w\left(T, p, x_w, x_{NACL}, x_{CO_2}\right) \tag{2.49}$$

$$\rho_g = \rho_g\left(T, p, y_w, y_{CO_2}\right) \tag{2.50}$$

This model has been implemented in Sierra/Aria and is undergoing verification. Dissolution of components as described in Eqn. (2.48) is implemented with the adaptive grid tabular scheme discussed in chapter 6. This greatly simplifies the computation of phase behavior, which is implemented in a simplified "flash" calculation module. The explicit forms for composition obviate the need to compute thermodynamics using complex equation of state models at each iteration and at each grid point, as is normally done in oil industry compositional simulators.

2.6 Novel Treatment of Capillary Interfaces

The subsurface is structured into layered or otherwise heterogeneous geologic formations which differ in their texture, resulting in variations in pore size distributions and intrinsic permeability. The treatment of capillary pressure across a material interface is important to proper modeling the interplay of capillary imbibition, gravity forces and pressure gradients, the driving forces for multiphase flows. Capillary pressure is continuous across a material interface but phase saturations are discontinuous. Saturation is usually a primary variable in multiphase systems, allowing one to determine the volume fraction occupied by each phase. Owing to this discontinuity, many numerical schemes use cell-centered discretizations. Even vertex-centered discretizations, such as PorSalsa (Martinez et al. 2001), utilize a material-centered geologic property model, wherein a unique material is assigned node-wise. In this project we implemented a method which assigns materials to elements and allows the saturation to jump across a material interface. Some pros and cons of these two treatments include:

Cell-centered and/or material-centered grid model (assign material type node-wise)

- Fuzzy material interface; interface lies somewhere inside each finite element
- Difficult to mesh while respecting complex geometries, e.g., pinchouts, multi-material junctions

Finite element centric material with multiple degrees-of-freedom (DOF) on interfaces

- Captures discontinuous saturation values on interfaces
- Requires constraint equation(s) on interfaces; increases DOF count
- Requires code logic for automated assembly of capillary interfaces and constraints

Two examples verifying the implementation of the multiple DOF scheme follow.

2.6.1 Flow Through a Two-Layer Medium

Figure 2.6-1 summarizes a model problem in which isothermal liquid water is injected at the top of a layered region. The bottom of the domain is saturated with liquid water. The two materials are identical except for the capillary pressure function. Material 1 has a higher capillary pressure than Material 2, as shown in Figure 2.6-1. One grid used for numerical simulation is shown in the figure and will be referred to as mesh 2; mesh 1 is a uniform mesh with 10 elements in each material. The correct steady solution should have a continuous capillary pressure but discontinuous liquid saturation across the material interface.

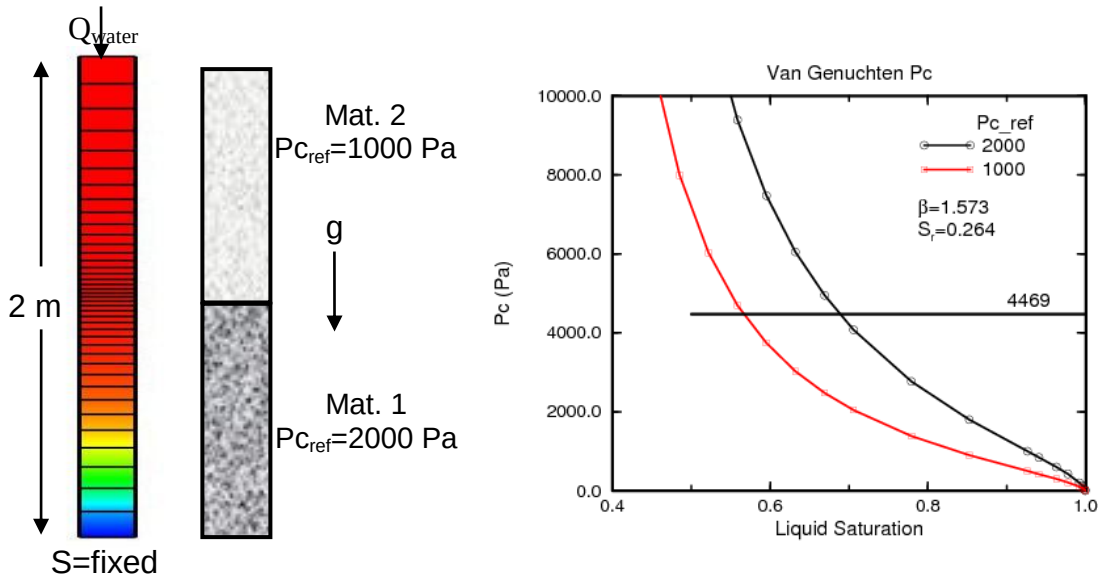

Figure 2.6-1. Problem definition and material capillary pressure. The black curve represents the capillary pressure for material 2 and the red curve for material 1.

The material-centered discretization in the code PorSalsa (Martinez et al. 2001) yields a solution which approaches a discontinuous saturation at the interface as the mesh is refined (see Figure 2.6-2). However, the interface location is shifted by a half grid spacing. The element discretization in Aria allows for a discontinuous saturation across the material interface by enforcing the continuity of capillary pressure and allowing for the jump in saturation. The solutions indicate that the limiting value of (continuous) capillary pressure is somewhere near 4469. Checking with the capillary pressure curves for the two materials in Figure 2.6-1, this value of capillary pressure yields saturations of about 0.69 and 0.58 in materials 1 and 2, respectively. These values agree with the saturations given by the Aria solution in Figure 2.6-2, which can be obtained on a coarser grid than needed in the material-centered discretization.

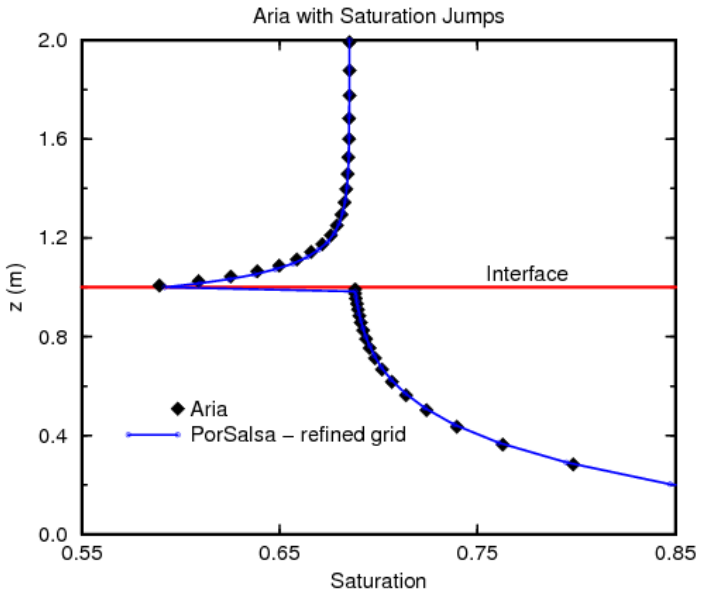

Figure 2.6-2. Saturation jump across a material interface.

2.6.2 Capillary Exclusion

This problem was described by Huber and Helmig (2000) in a paper discussing various numerical discretizations for heterogeneous porous materials. The problem is motivated by an experiment (see Huber and Helmig 2000) involving the infiltration under gravity and capillary forces of trichloroethylene (TCE) into a water-wet rectangular container (height 65 cm, width 90 cm) filled with coarse sand. In the center of this box is a fine sand lens region measuring 13.7 cm in height and 52.5 cm in width, see figure 2.6-3, which shows only the symmetric portion of this domain. The fine material has a higher capillary wicking potential than the coarse sand, but the fine sand also has a higher entry pressure. This means the saturation level of TCE in the coarse sand has to increase significantly before it will enter the fine sand material. Another view is that the fine material prefers to retain the (wetting) water, and requires a high entry pressure before TCE can displace the wetting phase. The van Genuchten models for capillary pressure and relative permeability are used in the simulation, with parameters as defined in Huber and Helmig. Figure 2.6-3 shows the computed distribution of TCE on three discretizations after 100 minutes of infiltration. The solutions on the two coarser grids compare very well with those given in Figure 6 of Huber and Helmig, using similar mesh densities. In the figure, each finer mesh is obtained by splitting each quadrilateral element in the coarser grid into four smaller elements, resulting in 580, 2223, and 8701 nodes, respectively, for the coarsest to finest grids shown. Note however, that Huber and Helmig use the material-centric discretization, wherein the interface between fine and coarse sand lies between two grid points, whereas here the actual jump in saturation is computed at the interface.

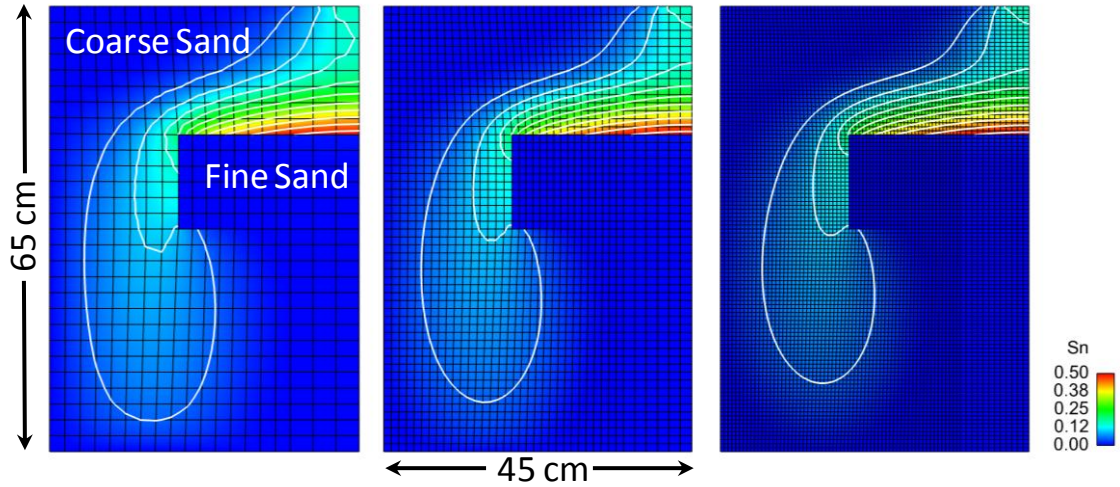

Figure 2.6-3. Distribution of TCE after 100 minutes of infiltration using the van Genuchten models. Contours are for S_n = 0.05, 0.1, 0.15, etc.

3. Reactive Flow

3.1 Introduction

This chapter describes our implementation for modeling transport of species and chemicals in porous media. The intent is that it be general enough to also meet current and future SNL requirements for treating reactive explosives, foam decomposition, and composite ablation. The model allows transport of species in multiple phases. The description of transfer between phases and of chemical reactions can be specified by source terms. The current implementation allows extension of the model to more general geochemical systems.

3.2 Multiphase Species Transport in Porous Media

3.2.1 Model Formulations

The multiphase transport of reactive species is described as follows:

$$\frac{\partial}{\partial t}\left(\phi S_\beta R_{d,k}^\beta C_k^\beta\right) + \nabla\cdot\left(\mathbf{v}_\beta C_k^\beta - \phi S_\beta \mathbf{D}_\beta \cdot\nabla C_k^\beta\right) = Q_k^\beta \tag{3.1}$$

where

C_k^β is the concentration of species *k* in phase β,

ϕ is porosity

S_β is the saturation of phase β

$R_{d,k}^\beta = 1 + \rho_{solid} K_{d,k}^\beta / \phi S_\beta$ is a so-called retardation factor

$K_{d,k}$ is the material-dependent distribution coefficient for species *k*

The dispersion-diffusion tensor (see chapter 10 of Bear 1972) is given by,

$$\begin{aligned} \phi S_\beta \mathbf{D}_\beta &= \phi S_\beta \mathbf{D}_{hyd,\beta} + \tau \phi S_\beta D_{k,\beta} \mathbf{I} \\ \phi S_\beta \mathbf{D}_{hyd,\beta} &= \alpha_T \left|\mathbf{v}_\beta\right| \mathbf{I} + (\alpha_L - \alpha_T) \frac{\mathbf{v}_\beta \mathbf{v}_\beta}{\left|\mathbf{v}_\beta\right|} \end{aligned} \tag{3.2}$$

where α_L and α_T are material-dependent dispersivities, τ is tortuosity, and $D_{k,\beta}$ is a diffusion coefficient for species *k* in phase β. Notice that the hydrodynamic dispersion tensor is phase-dependent (through the phase velocity) and *material* dependent, but not species dependent, whereas the molecular diffusion coefficient is phase and species dependent. The tortuosity is material dependent.

The distribution coefficient is often modeled as a constant, but it really depends on temperature. In the numerical implementation, the user has the option of specifying a functional form dependent any other species concentration ("plug-in"). This facilitates the capability to describe other forms of adsorption (e.g., nonlinear dependence on concentration, like Langmuir, Freunlich or others, see Bear 1979).

If the species in a particular phase are non-dilute, then an additional constraint applies,

$$\sum_{k=1}^{N} Y_k = 1 \tag{3.3}$$

where we have introduced the mass fractions $Y_k = C_k / \rho$ and dropped the phase superscript for simplicity; ρ is the phase density. In view of this constraint, in practice only *N*-1 species are solved from the system (Eqn. (3.1)) and the remaining mass fraction is obtained from the constraint. In addition the overall mass balance is solved, for example Eqn. (2.11) discussed earlier for single phase flow.

Chemical Reaction and Sources

The general capability in Sierra/Aria to have user-specified source functions allows general descriptions of reactive transport problems. Several built-in sources for common geo-problems are available, including a plug-in for radioactive decay chains:

$$Q_k^{\beta} = -\lambda_k R_k C_k^{\beta} + \lambda_{k-1} R_{k-1} C_{k-1}^{\beta} \tag{3.4}$$

In general the source terms can be functions of all species concentrations, space, and time. This generality allows for the modeling of a wide variety of reactive flow problems. In the following sections several examples of chemically reactive flow problems are presented.

3.2.2 Biodegradation Example

In this section we present numerical results for a biodegradation problem studied by Kindred and Celia (1989) which involves the growth of subsurface bacteria populations. The growth rate is determined by the availability of oxygen and various inorganic nutrients. This relationship is represented by corresponding source terms in the transport equations, as detailed by Kindred and Celia, and which were incorporated into Aria using "plug-ins." One transport equation (Eqn. (3.1)) is solved for each of the substrate, oxygen, and biomass concentrations. The 1D problem domain consists of a 50.0 m length section of a porous medium with an initial oxygen concentration of 3.0 mg/L and a constant advection velocity of 1.0 m/day. The concentration of substrate at the left boundary is fixed at 10.0 mg/L and the concentration of oxygen is fixed at 3.0 mg/L. A constant time step of 0.2 days and a diffusion constant of 0.2 m^2/day were used. The constant I_b is related to the amount of biomass inhibition. Since no inhibition is used in this example (I_b = 1.0), the solution for biomass at the inflow boundary is extremely high. As illustrated in Figure 3.2-1, strong correlation is achieved between the published solution and the Sierra/Aria solution for the oxygen and biomass concentrations. The differences in the substrate concentration at the front location are due to the advection stabilization scheme used, which for this problem is slightly over-diffusive.

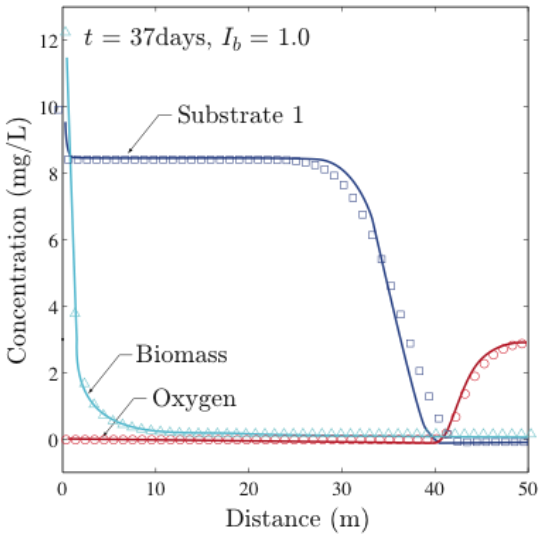

Figure 3.2-1. Comparison of biodegradation example solutions at time = 37 days given by Sierra/Aria (symbols) and published results in Kindred and Celia (1989) (solid lines).

3.3 Calcite Formation

3.3.1 Introduction

This section describes the geochemical formulation of calcite formation, which is considered a key mechanism for mineralization of CO_2 in deep saline aquifers. Modeling approaches for determining multiphase chemical equilibrium solutions to this chemical system are discussed in section 3.4.

Carbonate-bearing phases such as calcium carbonate ($CaCO_3$) or calcite are ubiquitous in natural geologic environments and play an important role in the carbon global cycle and other geochemical processes where CO_2 is controlled by heterogeneous chemical reactions between co-existing minerals and fluids. The carbonate phase formation is important to many geochemical and industrial processes over a wide range of temperatures and pressures. For example, some of these processes are related to scale formation by precipitation of carbonate and silica phases in geothermal wells during CO_2 breakout (Moller, Greenberg et al. 1998), interactions between calcium-bearing phases such as cementitous materials and CO_2 injected at elevated pressures (Carey, Wigand et al. 2007; Carey, Svec et al. 2009; Carey, Svec et al. 2010), and mineral and/or solution trapping of CO_2 injected into porous subsurface geologic environments (Bachu, Gunter et al. 1994; Bachu and Adams 2003). The latter is related to geological storage/disposal of CO_2 and it is also the focus of the current study in terms of CO_2 solubility in the aqueous phase and its relation to carbonate solubility.

The issue of mineral trapping of CO_2 and the geochemical basis for its consideration as a long-term carbon sink has been studied at length from model conceptualization to experimental investigations (Gunter and Perkins 1993; Bachu, Gunter et al. 1994; Perkins and Gunter 1995; Gunter, Perkins et al. 2000; Kaszuba, Janecky et al. 2003; Kaszuba, Janecky et al. 2005;

Kharaka, Cole et al. 2006; Benezeth, Palmer et al. 2007; Newell, Kaszuba et al. 2008; Hangx and Spiers 2009). In general, these studies suggest that carbonate-bearing phases such as calcite, magnesite ($MgCO_3$), siderite ($FeCO_3$), and ankerite ($Ca(Fe, Mg, Mn)(CO_3)_2$) are the likely candidates for CO_2 mineral trapping if their mineral components are present in the pore solutions or the host mineral phases (Gunter and Perkins 1993; Kharaka, Cole et al. 2006). Other candidates such as dawsonite ($NaAl(CO_3)(OH)_2$) have been suggested but its absence in experiments (Kaszuba, Janecky et al. 2005; Newell, Kaszuba et al. 2008) and limited natural occurrence relative to carbonate minerals diminishes its consideration even when it has been reported at various localities (Benezeth, Palmer et al. 2007). Mineral trapping has been regarded as a long-term and near-permanent form of disposing CO_2 in subsurface environments (Lemieux 2011). However, the process is sluggish given the slow rates for silicate mineral dissolution in providing Ca (e.g., calcite formation) plus other needed components for carbonate precipitation (Lemieux 2011). The latter process may also be slow depending on local physico-chemical conditions for mineral growth to occur. Solution or solubility trapping in the pore solutions is also considered to be an efficient mechanism for both short- and long-term disposition of CO_2 in an aquifer environment (Gunter and Perkins 1993; Gunter, Perkins et al. 2000; Kharaka, Cole et al. 2006; Lemieux 2011).

3.3.2 Geochemical Modeling of Fluid-Mineral Equilibria

It is necessary to represent the complex chemical interactions and feedbacks between the CO_2–rich phase (whether at subcritical or supercritical conditions) and the aqueous pore solution and mineral phases in the aquifer to accurately represent the carbon mass partitioning in each phase during CO_2 injection. This knowledge would then provide information to assess the capacity for sequestering of CO_2 in subsurface porous geologic formations. For this purpose, reactive-transport models need to consider heterogeneous chemical reactions that capture solution-mineral equilibria and dissolution/precipitation kinetics given the importance of precipitation of carbonate-bearing solids in mineral (and solution trapping of CO_2 as well) as envisioned in carbon sequestration in subsurface environments. Such approaches involving the assessment of solution-mineral equilibria have been adopted in various forms to evaluate water-rock interactions in cases in which CO_2 has been injected in the brine-bearing geologic formation (Kharaka, Cole et al. 2006) or in the study of potential non-sedimentary disposal environments such as porous basaltic rock (McGrail, Schaef et al. 2006). In all these cases, geochemical modeling of equilibria (and dissolution/precipitation kinetic phenomena, if necessary) between solids and fluids is crucial in the representation of these interactions in the porous aquifer formation. These models also need to capture the compositional complexities of pore waters where their chemistry, in most cases, is not limited to a few components, particularly those having saline or briny compositions.

The system $Ca\text{-}CO_3\text{-}H_2O\text{-}CO_2$ is adequate for this purpose since it involves equilibria between gas and aqueous solution, and heterogeneous kinetics between the calcite ($CaCO_3$) solid and aqueous solution. It should be noted that most pore waters in geologic formations can contain various amounts of aqueous species such Na, Cl, Ca, Mg, and SO_4; particularly for brines. However, for the sake of simplicity, we will restrict the following representation of carbonate equilibria to the system $Ca\text{-}CO_3\text{-}H_2O\text{-}CO_2$. The pertinent reactions for the system can be summarized as follows:

$$CaCO_3 + H^+ \rightleftarrows Ca^{++} + HCO_3^- \tag{3.5}$$

$$HCO_3^- \rightleftarrows H^+ + CO_3^- \tag{3.6}$$

$$CO_{2(aq)} + H_2O \rightleftarrows H^+ + HCO_3^- \tag{3.7}$$

$$CO_{2(g)} + H_2O \rightleftarrows H^+ + HCO_3^- \tag{3.8}$$

$$H_2O \rightleftarrows H^+ + OH^- \tag{3.9}$$

$$CaHCO_3^+ \rightleftarrows Ca^{++} + HCO_3^- \tag{3.10}$$

$$CaCO_{3(aq)}^\circ + H^+ \rightleftarrows Ca^{++} + HCO_3^- \tag{3.11}$$

The above set of chemical reactions should be sufficient to describe the Ca-CO_3-H_2O-CO_2 system accurately and under some conditions it could be simplified further by ignoring the aqueous species $CaHCO_3^+$ and $CaCO_{3(aq)}$ or reactions (3.10) and (3.11). Each of this species has a Gibbs energy of formation ($\Delta G_{f,i}^\circ$) for a given species i that can be used to compute Gibbs energy for the n^{th} reaction ($\Delta G_{rxn,n}^\circ$) by the simple relation:

$$\Delta G_{rxn,n}^\circ = \sum_n \upsilon_i \Delta G_{f,i}^\circ \tag{3.12}$$

where υ_i is the corresponding number of moles of the ith species in the reaction. By convention, the υ_i coefficients in the above reactions are taken as positive for products and negative for reactants. $\Delta G_{rxn,n}^\circ$ of the nth reaction can be related to the solubility constant K_n° by:

$$\ln K_n^\circ = \frac{-\Delta G_{rxn,n}^\circ}{RT} \quad , \tag{3.13}$$

where *R* and *T* are the gas constant and absolute temperature, respectively. K_n° is the equilibrium constant which is also expressed according to the mass action law as:

$$K_n^\circ = \prod_n a_i^{\upsilon_i} \tag{3.14}$$

where a_i corresponds to the activity of the ith aqueous species. In case of a gas it would instead be denoted as the fugacity of the ith species. Note that K_n° is a standard state thermodynamic

constant at infinite dilution and it is therefore related to the standard state properties of the phases taking part in the reaction.

Other constraints that must be satisfied in the above equilibria are mass and charge balance equations, for example, the total mass of Ca in solution is given by:

$$m_{T,Ca} = m_{Ca^{++}} + m_{CaHCO_3^+} + m_{CaCO^\circ_{3,aq}} + \ldots \tag{3.15}$$

The charge balance constraint is expressed as:

$$\sum z_i m_i = 0 \tag{3.16}$$

where z_i is the charge and m_i is the molal concentration of the aqueous species in solution. All these mass and charge relations need to be obeyed in the equilibrium speciation calculation. It should also be noted that

$$a_i = \gamma_i m_i \tag{3.17}$$

where γ_i is the activity coefficient and m_i is the molal concentration of the ith species. γ_i is obtained from the Pitzer or b-dot formulations available in either EQ3/6 (Wolery and Jarek 2003) and Cantera codes (Moffat and Jove Colon 2009).

Thermodynamic data for each of the aqueous and solid species in reactions (3.5) through (3.11) can be obtained from the thermodynamic databases developed for the Yucca Mountain Project (YMP) for the code EQ3/6, which are also available in Cantera.

3.3.3 Rate Laws

Various types of rate laws have been applied to mineral phases; see Lasaga (1998) for a comprehensive review of kinetic rate laws applied to mineral phases. This reference discusses several types of rate law expressions applied to mineral dissolution/precipitation processes ranging from simple linear expressions to more complex ones. Among the most commonly adopted formulation of mineral dissolution is that based on transition state theory (TST):

$$r_f = \mathrm{f}_m \mathrm{k}_f \mathrm{s}_m \prod a_{ac}^N \left(1 - \exp\left(\frac{A_+}{\sigma_+ RT}\right)^m\right)^n \tag{3.18}$$

$$r_b = \mathrm{f}_m \mathrm{k}_b \mathrm{s}_m \prod a_{ac}^N \left(1 - \exp\left(\frac{-A_-}{\sigma_- RT}\right)^m\right)^n \tag{3.19}$$

In Eqns. (3.18) and (3.19), k_f and k_b are the forward and backward rate constants, respectively. s_m is the total surface area of the solid, f_m is a 'fudge' factor denoting the fraction of mineral surface area active in the dissolution/precipitation process (it is usually taken as unity), a_{ac}^{N} stands for the activity of the catalyzing/inhibiting activated complex of the rate-limiting reaction, m and n are positive values that are constrained experimentally; in most cases these exponents are simplified by having unity values. R and T are the gas constant and absolute temperature, respectively. σ corresponds to a stoichiometric factor related to the average molar stoichiometry of the activated complex. A_+ and A_- designate the chemical affinities for the forward and backward reactions. Chemical affinity is defined as:

$$A = -RT\ Ln\left(\frac{Q_n}{K_n^\circ}\right) \tag{3.20}$$

where Q_n is the ion activity product for reaction n given by:

$$Q_n = \prod_n a_i^{\upsilon_i} \tag{3.21}$$

Note that the above expression (Eqn. (3.21)) is very similar to that for K_n° (Eqn. (3.14)) and the difference is that Q_n is strictly an actual measure of the activities at given reaction coordinates. That is, A_+ and A_- represent how far or close the system is to equilibrium. For example, if K_n° equals Q_n then $A = 0$ and the system is at equilibrium. Another important definition in the above expressions is the thermodynamic relation between k_f and k_b, and the equilibrium constant K_n°:

$$K_n^\circ = \frac{k_f}{k_b}. \tag{3.22}$$

It should be noted that Eqns. (3.18) and (3.19) have been applied in more simplified forms based on assumptions about the identity of the activated complex. Still, the main application of this rate law has been to represent the dissolution of silicates with a reasonable degree of success.

TST expressions (e.g., Eqns. (3.18) and (3.19)) have not been commonly used to describe calcite dissolution but are still widely adopted for silicate dissolution (Schott, Pokrovsky et al., 2009). One notable exception is the TST-based rate laws advanced by Pokrovsky and Schott (1999), Gautelier et al. (2007), and Schott et al. (2009) for carbonate phases. These authors advanced TST rate laws combined with a surface complexation model (SCM) for Mg-bearing carbonates where the SCM accounts for the inhibitory effects of carbonate ions on dissolution. This TST-SCM model seems to explain both carbonate dissolution and precipitation phenomena for a wide range of pH and solution compositions. However, one potential drawback would be the retrieval of SCM constants at temperatures other than 25°C since there is a strong reliance on experimental data for the retrieval of surface complexation constants. Still, this model is based

on relatively numerous experimental observations and seems to accurately capture the dissolution dependencies on solution composition.

The more commonly adopted rate laws for calcite and other carbonate phases are essentially empirical and one of the widely used forms is that developed by Plummer et al. (1978) defined as:

$$r_{overall} = k_1 a_{H^+} + k_2 a_{H_2CO_3} + k_3 a_{H_2O} - k_1 a_{HCO_3^-} \tag{3.23}$$

Note that this rate expression is consistent with linear rate law formulations (i.e., rate constant multiplied by either the activity or species concentrations). This reaction includes both forward and backward rates and depends on the activities of aqueous carbonate species in solution. The reaction can be separated into forward and backward rates as follows:

$$r_f = k_1 a_{H^+} + k_2 a_{H_2CO_3} + k_3 a_{H_2O} \tag{3.24}$$

$$r_b = k_4 a_{HCO_3^-} \tag{3.25}$$

The rate constants k_1, k_2, k_3, and k_4 have been studied by Plummer et al. (1978), and Shiraki and Brantley (1995); the latter is a study at elevated temperatures. Shiraki et al. (2000) provides a similar model and rate expressions for calcite dissolution:

$$r_{overall} = k_1 \left[H^+ \right] + k_2 \left[HCO_3^- \right] + k_3 \left[OH^- \right] \tag{3.26}$$

where the values in brackets denote concentrations of the designated aqueous species in solution. Again, these rate expressions for calcite dissolution/precipitation are entirely empirical. It should be noted that Chou et al. (1989) reported results on carbonate phase dissolution that are consistent with others such as Plummer et al. Moreover, their rate expressions have the forms similar to those developed by Plummer et al. (1978).

3.4 Chemical Equilibrium and Kinetics: Computational Implementations

3.4.1 Mass Action Law Reactions: EQ3/6

This section outlines a common method for calculating the equilibrium composition of the calcite formation system outlined in Eqns. (3.5) through (3.11). In reactive transport problems, reaction (3.5) is usually treated in terms of a reaction rate law, whereas reactions (3.6) through (3.11) are not considered rate-limiting in the dissolution/precipitation process. These are, therefore, defined in terms of chemical equilibrium. That is, it would suffice to assign equilibrium constants to reactions (3.6) through (3.11) to determine the equilibrium concentration of all carbonate species. The computer codes EQ3/6 (and similarly PHREEQC) are able to treat reactions in this way with a specified rate law. There is also the importance of units utilized in the rate expressions and their consistency with those adopted for the reactive transport formulations. Since experimental dissolution/precipitation rates are usually expressed in units of moles/(surface area * time), sometimes it is necessary to make unit conversions to bridge consistency with the concentration units utilized in the reactive transport calculations. Overall, the empirical rate expressions for calcite seem simple enough in their implementation. In the next section, reactive transport modeling coupled with a mixed kinetic-equilibrium approach will be discussed briefly.

A potential scheme to implement a simplified form of the calcite equilibrium problem (given as an example in the EQ3/6 Manual (Wolery and Jarek 2003)) in reactive transport is to express the problem using the most relevant reactions at the near-neutral pH region. That is, calcite equilibria is defined with no kinetics and all relevant reactions are delineated by mass action law equilibrium constants with a reduced set of aqueous species. Let us assume for the moment that for this case, calcite equilibria can be defined by the following solid and aqueous species: $CaCO_{3(solid)}$, Ca^{++}, HCO_3^-, H^+, H_2O, and $CO_{2(g)}$. This essentially will result in a mass action law expression (i.e., reaction (3.5)) that can be recast as:

$$\log K_{calcite} = \log m_{Ca^{++}} + \log \gamma_{Ca^{++}} + \log m_{HCO_3^-} + \log \gamma_{HCO_3^-} - \log m_{H^+} - \log \gamma_{H^+} \qquad (3.27)$$

The activity of the relevant species is defined as $m_i \gamma_i$ where m_i is the molality or moles of component i per kg of H_2O solvent and γ_i is the activity coefficient of component i that can be computed from formulations such as that of Pitzer or Helgeson's b-dot. Note that the activity of calcite solid is conventionally taken as unity so it also vanishes from the equation.

Similarly, the mass law expression for $CO_{2(g)}$ (or reaction (3.8)) is given as:

$$\log K_{CO_{2(g)}} = \log m_{HCO_3^-} + \log \gamma_{HCO_3^-} + \log m_{H^+} + \log \gamma_{H^+} - \log f_{CO_{2(g)}} - \log X_W - \log \gamma_W \qquad (3.28)$$

where $\log X_W$ is the mole fraction of H_2O solvent and depends on the concentration of carbonate species in solution. $\log f_{CO_{2(g)}}$ and pH are considered known inputs in this example. The above equations can be rearranged to have the unknowns on the left hand side:

$$\log m_{Ca^{++}} + \log m_{HCO_3^-} = \log K_{calcite} - \log \gamma_{Ca^{++}} - \log \gamma_{HCO_3^-} + \log m_{H^+} + \log \gamma_{H^+} \tag{3.29}$$

$$\log m_{HCO_3^-} - \log X_W = \log K_{CO_{2(g)}} - \log \gamma_{HCO_3^-} - \log m_{H^+} - \log \gamma_{H^+} + \log f_{CO_{2(g)}} + \log \gamma_W \tag{3.30}$$

We could assume for simplicity that this is a dilute solution so all γ_i can be assumed to be unity and thus end up dealing only with species molalities.

Since this is an iterative Newton-Raphson approach, X_W will change with solute concentration and can be modified as done in EQ3/6 for any k + 1th step in the iteration as:

$$\log X_{W,k+1} = \log X_{W,k} + \sum_{s' \in S} \frac{\partial \log X_W}{\partial \log m_{s'}} (\log m_{s',k+1} - \log m_{s',k}) \tag{3.31}$$

where S refers to the relevant set of solute species (s') in solution. In this case the right hand side term for the solute concentration can be expressed as:

$$W_{s'} = \frac{\partial \log X_W}{\partial \log m_{s'}} \tag{3.32}$$

where s' is not equal to W.

Then, Eqn. (3.30) in this calcite example would take the form:

$$\log X_{W,k+1} - W_{Ca^{++}} \log m_{Ca^{++},k+1} - W_{HCO_3^-} \log m_{HCO_3^-,k+1} = \log X_{W,k} - W_{Ca^{++}} \log m_{Ca^{++},k} - W_{HCO_3^-} \log m_{HCO_3^-,k} \tag{3.33}$$

Evaluation of Eqn.(3.32) for H_2O is not considered important for dilute solutions since X_W is not expected to change significantly with changes is solute concentration. Of course, this could become important in concentrated solutions.

In the Eqns. (3.29), (3.30), and (3.33) we have three equations with three unknowns and these are linear in accord with four log concentration variables. These equations can be solved simultaneously in matrix form as:

$$\begin{bmatrix} 1 & 1 & 0 \\ 0 & 1 & -1 \\ -W_{Ca^{++}} & -W_{HCO_3^-} & 1 \end{bmatrix} \begin{bmatrix} \log m_{Ca^{++}} \\ \log m_{HCO_3^-} \\ \log X_W \end{bmatrix} = \begin{bmatrix} R_{Ca^{++}} \\ R_{HCO_3^-} \\ R_W \end{bmatrix} \tag{3.34}$$

For simplicity, the known elements of the RHS vector (R_i) corresponds to those in the RHS of the mass action Eqns. (3.29), (3.30), and (3.33).

Charge and mass balance constraints are maintained at each iteration in the code run. These constraints are represented in EQ3/6 as:

$$\alpha_s = \sum_c z_c m_c + \sum_a z_a m_a \tag{3.35}$$

where c denotes cation and a corresponds to anion. z_c and z_a stands for the charge of the cation and anion, respectively. Similarly, m_c and m_a are cation and anion molalities in the aqueous solution, respectively. The parameter α_s is related to a residual function β_s by:

$$\beta_s = \frac{\alpha_s}{\sum_c z_c m_c + \sum_a |z_a| m_a} \tag{3.36}$$

In EQ3/6, s is an aqueous species whose concentration is adjusted to make the residuals zero and it is related to the charge-mass balance constraint by:

$$m_{s,k+1} = m_{s,k} - \frac{\alpha_{s,k}}{|z_s|} \tag{3.37}$$

There are, of course, more details on how this is implemented in EQ3/6. This is just an example applicable to the calcite problem with a reduced set of relevant species, and thus reactions, to describe its equilibrium. Note that this example assumes a dilute solution where changes in X_W with solute concentration are small enough as to be ignored.

3.4.2 Solubility of Calcite in Brine via Gibbs Energy Minimization: Cantera

This section demonstrates the use of Cantera for calculating the equilibrium composition of the calcite formation system outlined in Eqns. (3.5) through (3.11), utilizing a Gibbs energy minimization approach.

Cantera is a general purpose open-source object-oriented constitutive modeling tool set for problems involving chemical thermodynamics, kinetics, and/or transport processes (Moffat and Goodwin 2011). Its origins trace back to applications in the modeling of combustion systems and chemical vapor deposition processes. Cantera also has the capability for treating kinetics this has not been developed yet for fluid-solid interactions. This is a topic of future research. Cantera can perform calculations similar to those based on mass action law equations such as EQ3/6 to obtain the same result; however, the method to compute multiphase chemical equilibria is different. There are no prescribed mass action law reactions as inputs and chemical equilibrium is computed using the Gibbs energy minimization (GEM) approach (Smith and Missen 1982; Karpov, Chudnenko et al. 1997). Chemical equilibrium is obtained by minimizing the total Gibbs free energy of the system through optimization of component abundances. The method implemented in Cantera for this GEM approach is referred to as Villars-Cruise-Smith (VCS) and it is described in detail by Smith and Missen (1982). This method as implemented in Cantera has been was extended to deal with non-ideal systems which makes it suitable for many geochemical problems of interest.

An example of the application of chemical equilibrium computation is the solubility of calcite at various conditions of ionic strength and $CO_{2(g)}$ pressure. Figure 3.4-1 depicts the solubility of calcite as a function of NaCl concentration for a mole fraction of $XCO_{2(g)}$ of 0.0091 at 298.15 K (Moffat and Jove Colon 2009). The calculation of activity coefficients for neutral $CO_{2(aq)}$ aqueous species was computed using the Pitzer model implemented in Cantera from parameter data retrieved from Corti et al. (1990) and described in Mariner (2007). Notice the strong correspondence between the Cantera prediction and the solubility data from Wolf et al. (1989).

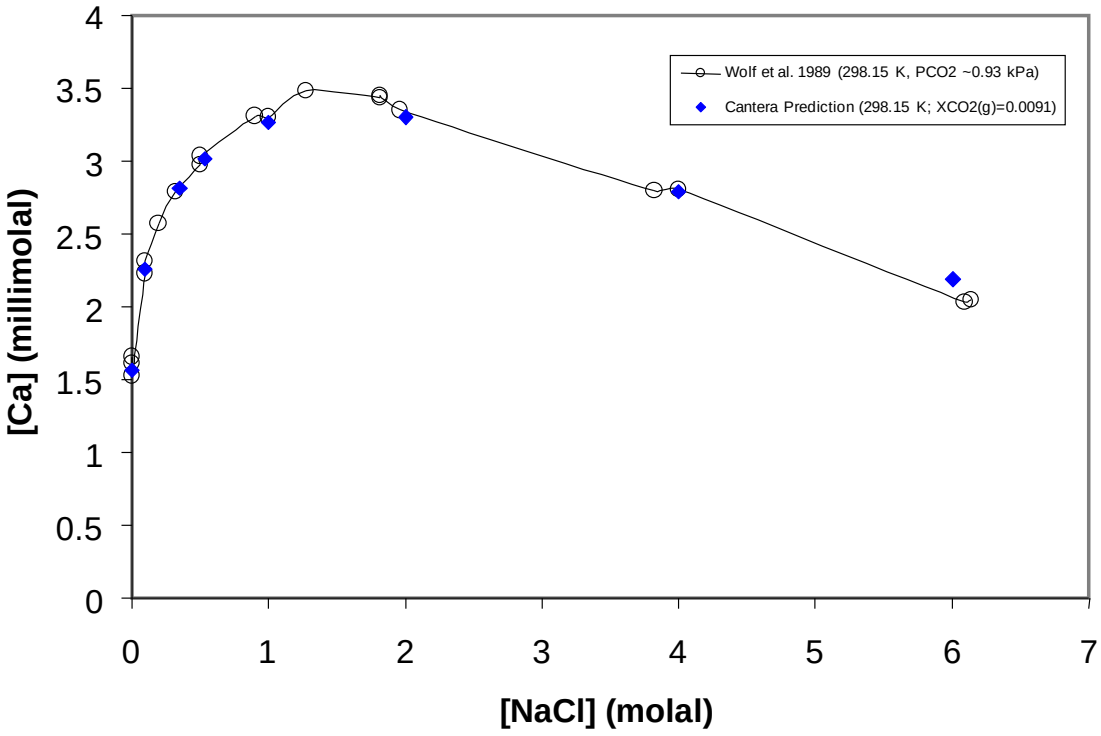

Figure 3.4-1. Plot of calcite solubility as a function of NaCl concentration at 298 K and PCO_2 fixed at 0.92 kPa (experimental) or at the equivalent XCO_2 of 0.0091 after Moffat and Jove Colon (2009). The solid line connecting the data points of Wolf, Breitkopf et al. (1989) is just a guide for the eye.

Of more relevance to the current study are calcite solubility calculations but in reaction path form where changes in the aqueous phase chemistry are tracked as CO_2 mass is added to the system. The calculations were conducted under isothermal-isobaric conditions of 318.15 K and 125 bars. Figures 3.4-2a and 2b show the trends in pH and Ca^{++} molal concentration consistent with a decrease in pH with added CO_2 and augmentation in aqueous Ca due to the increase in calcite solubility. The Cantera code run is in the form of a titration or reaction path mode where moles of CO_2 are added in small increments and each step generates an equilibrium aqueous speciation computation where charge and mass balance are maintained.

The capability for reaction path modeling is extremely useful for characterizing chemical feedbacks and mapping phase solubilities in multicomponent systems. Moreover, Cantera can do this type of calculation for a wide range of pressures and temperatures without the input restrictions of pressure-temperature grids conditioned for mass action law equilibrium constants. This flexibility makes this approach more desirable for the efficient computation of thermodynamic properties of mixed fluid systems as a function of pressure, temperature, and composition. The use of these properties in Aria is facilitated by the use of multi-dimensional adaptive tables, which are discussed in section 6.6.

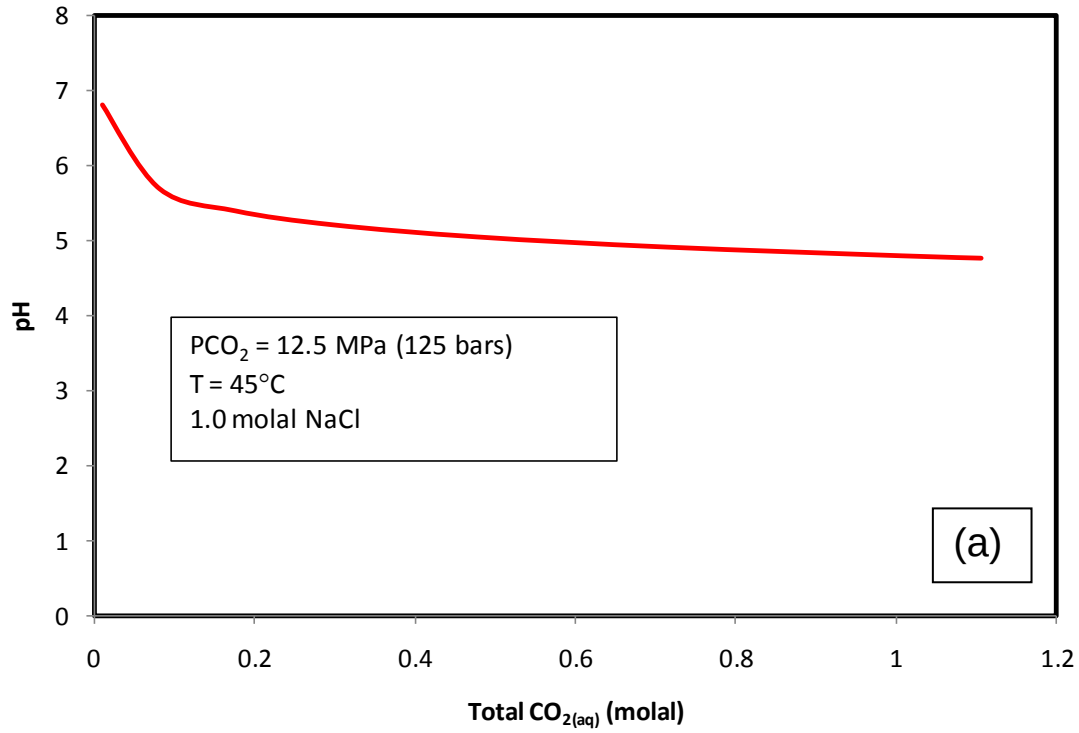

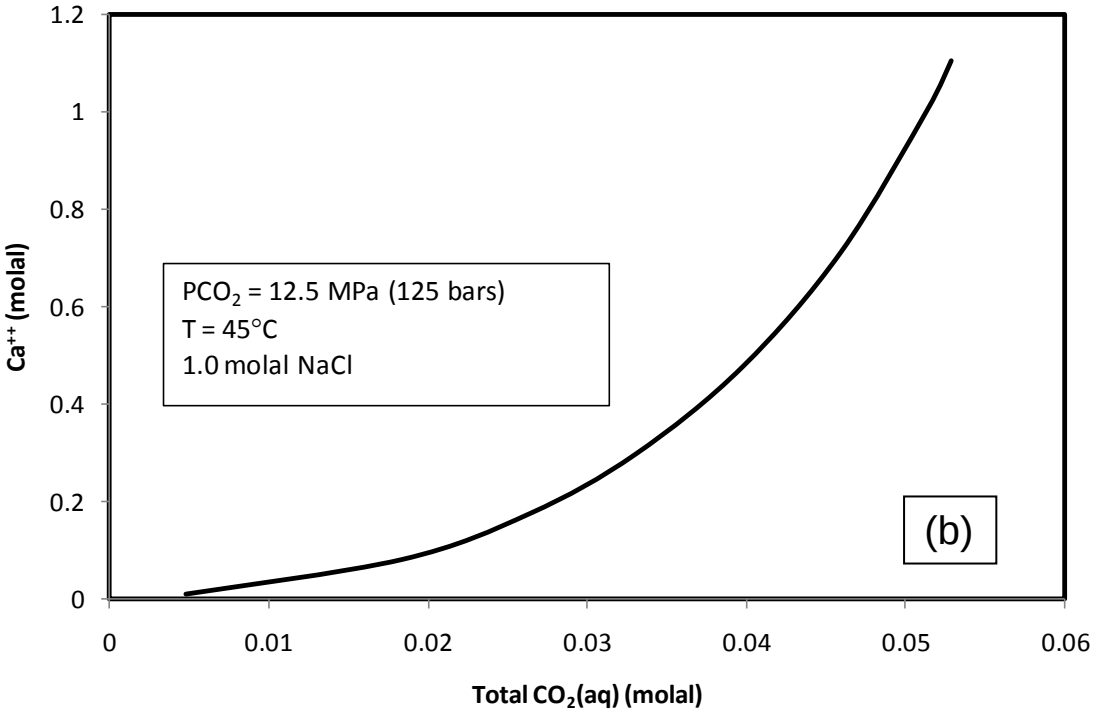

Figure 3.4-2. Plot of pH (a) and aqueous Ca^{++} (b) concentration in 1 m NaCl solution as a function of total added CO_2 at temperature of 45°C (318 K) and 125 bars—supercritical CO_2 conditions.

4. Mechanics Models

4.1 Introduction

This chapter documents the governing equations and implementation of two constitutive models for describing the response of two different types of geologic materials in the Sierra Solid Mechanics code Adagio (Spencer et al. 2011). Adagio supports large deformation quasi-static mechanics, including SNL-developed matrix-free iterative solution algorithms that allow extremely large and highly nonlinear problems to be solved efficiently. Adagio supports several constitutive models applicable to geomaterials, including elasto-plastic, visoplastic, crushable soil, and power law creep models. Under this LDRD, two new models specific to multiphase flow systems were added. These models have been implemented within the framework of the LAME constitutive model library (Scherzinger and Hammerand 2007) for use by Adagio.

The first constitutive model, described in section 4.2, incorporates the influence of liquid saturation and suction on the isothermal elasto-plastic response of porous materials. The mathematical formulation and numerical implementation for this model is based on the work of Borja (2004). This rate independent constitutive model, in contrast to all the other models in LAME, generally requires information (phase saturation and suction) from a code capable of simulating two-phase flow (liquid and gas) in a porous media. The solution controller Arpeggio will be used to provide the connection between the porous flow code Aria and the solid mechanics code Adagio.

The second model, the Multimechanism Deformation (MD) model, is used to model the creep behavior of salt, specifically the primary and secondary creep response of intact or undamaged salt. The MD model is based on the work of Munson and Dawson (1979,1982,1984) and was later extended by Munson et al. (1989). Historically the MD model has been implemented in a number of SNL solid mechanics codes including SANTOS (Stone 1997) and JAS3D (Blanford et al. 2001). A version of the MD model is currently in the Sierra Solid Mechanics code Adagio (2011). The implementations of the MD model in SANTOS, JAS3D, and Adagio are all essentially the same and use the forward Euler method to integrate the constitutive equations. The MD model has been used (Stone 1997) in two-dimensional simulations to model the creep closure of waste disposal rooms for the Waste Isolation Pilot Plant in New Mexico. Unfortunately, many attempts to use the MD model in three-dimension simulations have not been successful. Generally, it was found that the simulations were too time consuming and it was frequently difficult to obtain convergence of the equilibrium equations especially when contact surfaces were used. In section 4.3 we describe an implicit integration algorithm for the MD model which has allowed the solution of some relatively large three-dimensional coupled thermal-mechanical problems for a generic salt repository (Stone et al. 2010).

4.2 Borja's Cam-Clay Model for Partially Saturated Porous Materials

The mathematical description of this constitutive model follows very closely the work presented in Borja (2004). The usual continuum mechanics sign convention will be used; positive strains correspond to elongation and positive stresses to tension. Fluid pressures are taken to be positive in compression.

The discussion begins with some standard definitions used to describe porous media in section 4.2.1 and briefly introduces the concept of generalized effective stress for partially saturated porous media in section 4.2.2. The equations describing the nonlinear elasticity and plasticity components are described in sections 4.2.3 and 4.2.4, respectively. The numerical scheme used to integrate the constitutive equations is described in section 4.2.5. An initial verification of the implementation of this model is discussed in section 4.2.6 where the solutions for three test problems described in Borja (2004) are presented.

4.2.1. Porous Media Definitions

In this section we will briefly summarize some of the basic terminology and definitions used to describe a porous material. A representative volume V of the porous material is assumed to be a multiphase continuum consisting of a solid phase and one or two fluid phases (typically gas and/or liquid). The solid phase is comprised of the solid particles or grains occupying volume V_s while the gas and liquid phases occupy volumes V_g and V_l respectively. The solid portion is sometimes called the matrix or skeleton. We assume that the pore volume V_v is filled with gas, liquid, or a combination of the two phases (Eqn. (4.1)),

$$V = V_s + V_v = V_s + V_g + V_l \tag{4.1}$$

The liquid and gas phase saturations are defined, using Eqns. (4.2) and (4.3), as the ratios of the phase volumes to the pore volume and are subject to the constraint (Eqn. (4.4)),

$$S_l = \frac{V_l}{V_v} \tag{4.2}$$

$$S_g = \frac{V_g}{V_v} \tag{4.3}$$

$$S_l + S_g = 1 \tag{4.4}$$

Typically a soil is said to be saturated when $S_l = 1$ and partially saturated when $S_l < 1$.

It is useful to introduce three measures representing the amount of pore space in a given volume of soil. If we assume that the solid phase is incompressible then the deformation of the porous soils is due solely to the reduction of pore volume.

The void ratio e is defined as the ratio of the pore volume to the solid volume,

$$e = \frac{V_v}{V_s} \tag{4.5}$$

The specific volume ν is defined as the ratio of the total volume to the solid volume,

$$\nu = \frac{V}{V_s} = 1 + e \tag{4.6}$$

The porosity ϕ is defined as the ratio of the void volume to the total volume,

$$\phi = \frac{V_v}{V} = \frac{e}{1+e} \tag{4.7}$$

Using these equations we can derive the following relationships between the different quantities,

$$e = 1 - \nu = \frac{\phi}{1-\phi} \tag{4.8}$$

$$\nu = 1 + e = \frac{1}{1-\phi} \tag{4.9}$$

$$\phi = \frac{e}{1+e} = \frac{\nu - 1}{\nu} \tag{4.10}$$

As an example, a material having a porosity $\phi = 0.2$ has a void ratio $e = 0.25$ and a specific volume $\nu = 1.25$.

4.2.2 The Generalized Effective Stress Concept for Partially Saturated Porous Materials

It is generally accepted that the mechanical response of saturated soils can be described using the effective stress concept (Terzaghi 1943). Recalling that we have assumed that tensile stresses are positive the effective stress tensor $\boldsymbol{\sigma}$ may be defined as the *sum* of the total stress $\boldsymbol{\sigma}^T$ and the pore pressure $p_l \mathbf{I}$ (Eqn. (4.11)). The pore pressure is the pressure exerted by the pore fluid on the soil skeleton. The symbol $\mathbf{I}$ appearing in Eqn. (4.11) is the second order identity tensor; therefore, the pore water pressure only affects the normal components of the effective stress tensor.

$$\boldsymbol{\sigma} = \boldsymbol{\sigma}^T + p_l \mathbf{I} \tag{4.11}$$

For reference the total stress tensor is the stress tensor that appears in the Cauchy's equation of motion or the equilibrium equations (Malvern 1969). It should be noted that in the soil mechanics literature compressive stresses are often assumed to be positive and thus Eqn. (4.11) would be written $\boldsymbol{\sigma} = \boldsymbol{\sigma}^T - p_l \mathbf{I}$.

A generalization of the effective stress concept extended to partially saturated materials was proposed by Bishop (1959). The variables χ, p_l, p_g appearing in Eqn.(4.12) are a weighting factor, and the liquid and gas phase pressures, repectively.

$$\boldsymbol{\sigma} = \boldsymbol{\sigma}^T + \left[\chi p_l + (1-\chi) p_g \right] \mathbf{I} \tag{4.12}$$

The weighting factor χ will be assumed to be equal to the liquid saturation.

$$\boldsymbol{\sigma} = \boldsymbol{\sigma}^T + p_p \mathbf{I} \tag{4.13}$$

The "effective pore pressure" p_p is

$$p_p = S_l p_l + S_g p_g \tag{4.14}$$

A possible advantage of using S_l for the weighting factor is that when $S_l = 1$, Eqn. (4.12) reduces to the effective stress definition for liquid saturated soils (Eqn. (4.11)).

Another stress variable that is frequently encountered in discussions of unsaturated constitutive models is the net stress $\boldsymbol{\sigma}^{net}$. It is defined as

$$\boldsymbol{\sigma}^{net} = \boldsymbol{\sigma}^T + p_g \mathbf{I} \tag{4.15}$$

The matric suction s (or capillary pressure) is defined as the difference between the gas phase and liquid phase pressures. The matric suction increases as the liquid saturation decreases and generally exhibits hydraulic hysteresis.

$$s(S_l) = p_g - p_l \tag{4.16}$$

We can rewrite Eqn. (4.12) using Eqns. (4.15) and (4.16) to relate the effective stress to the net stress and suction

$$\boldsymbol{\sigma} = \boldsymbol{\sigma}^{net} - \chi s \mathbf{I} \tag{4.17}$$

The Barcelona Basic Model (Alonso et al. 1990) is probably the most well-known model for partially saturated soils. It uses the net stress and suction as two independent stress variables. The Borja model used here is described in terms of the generalized effective stress. Another model formulated in terms of generalized effective stress is the model proposed by Loret and Khalili (2002).

4.2.3 Nonlinear Elasticity Model

The elastic formulation is based on a two invariant hyperelastic model developed from a stored energy function (Borja et al., 1997; Borja and Tamagnini, 1998). The model produces a bulk modulus that is a linear function of the mean effective stress. The shear modulus may be chosen to be a constant or a function of the mean effective stress. When the latter is used the hyperelastic model leads to coupled volumetric and deviatoric elastic responses.

The model is restricted to isotropic materials and thus can be developed in terms of stress and strain invariants. For example the elastic strain tensor $\boldsymbol{\varepsilon}^e$ can always be decomposed into deviatoric $\mathbf{e}^e$ and volumetric ε_v^e parts.

$$\boldsymbol{\varepsilon}^{\mathbf{e}} = \frac{1}{3}\varepsilon_v^e \mathbf{I} + \mathbf{e}^{\mathbf{e}} \tag{4.18}$$

The volumetric ε_v^e and deviatoric ε_s^e elastic strain invariants are defined using the following equations.

$$\varepsilon_v^e = tr\left(\boldsymbol{\varepsilon}^{\mathbf{e}}\right) = \varepsilon_{ii}^e \tag{4.19}$$

$$\varepsilon_s^e = \sqrt{\frac{2}{3}}\left\|\mathbf{e}^{\mathbf{e}}\right\| = \sqrt{\frac{2}{3}\mathbf{e}^{\mathbf{e}} : \mathbf{e}^{\mathbf{e}}} = \sqrt{\frac{2}{3}\mathrm{e}_{ij}^e \mathrm{e}_{ij}^e} \tag{4.20}$$

The hyperelastic formulation assumes a stored energy function with these two elastic strain invariants as the independent variables

$$\psi\left(\varepsilon_v^e, \varepsilon_s^e\right) = \bar{\psi}\left(\varepsilon_v^e\right) + \frac{3}{2}\mu^e \cdot \left(\varepsilon_s^e\right)^2 \tag{4.21}$$

$$\bar{\psi}\left(\varepsilon_v^e\right) = -p_0\tilde{\kappa}\exp(\omega) = -p_0\tilde{\kappa}\exp\left\{-\left(\frac{\varepsilon_v^e - \varepsilon_{v0}^e}{\tilde{\kappa}}\right)\right\} \tag{4.22}$$

$$\mu^e = \mu_0 + \frac{\alpha}{\tilde{\kappa}}\bar{\psi}\left(\varepsilon_v^e\right) \tag{4.23}$$

Eqn. (4.22) is the stored energy function for isotropic conditions $\left(\varepsilon_s^e = 0\right)$ and Eqn. (4.23) represents the functional form of the elastic shear modulus. The hyperelastic formulation used in this model requires five material constants (p_0, $\tilde{\kappa}$, ε_{v0}^e, μ_0, α) compared to the two usually needed in isotropic linear elasticity. The parameter p_o is the mean effective stress corresponding to ε_{vo}^e. $\tilde{\kappa}$ is the elastic compressibility index. μ_o is a constant term used in the shear modulus

function (Eqn.(4.23)). α is a constant term that controls the elastic volumetric-deviatoric coupling. When $\alpha = 0$ then the shear modulus is simply μ_o.

The effective stress tensor is defined as the partial derivative of the stored energy function (Eqn. (4.21)) with respect to the elastic strain tensor. Using the chain rule gives

$$\boldsymbol{\sigma} = \frac{\partial \psi\left(\varepsilon_v^e, \varepsilon_s^e\right)}{\partial \boldsymbol{\varepsilon}^{\mathbf{e}}} = \frac{\partial \psi\left(\varepsilon_v^e, \varepsilon_s^e\right)}{\partial \varepsilon_v^e}\frac{\partial \varepsilon_v^e}{\partial \boldsymbol{\varepsilon}^{\mathbf{e}}} + \frac{\partial \psi\left(\varepsilon_v^e, \varepsilon_s^e\right)}{\partial \varepsilon_s^e}\frac{\partial \varepsilon_s^e}{\partial \boldsymbol{\varepsilon}^{\mathbf{e}}} \tag{4.24}$$

Defining the effective stress invariants

$$p = \frac{\partial \psi\left(\varepsilon_v^e, \varepsilon_s^e\right)}{\partial \varepsilon_v^e} = \frac{1}{3} tr(\boldsymbol{\sigma}) = \frac{1}{3}\sigma_{ii} \tag{4.25}$$

$$q = \frac{\partial \psi\left(\varepsilon_v^e, \varepsilon_s^e\right)}{\partial \varepsilon_s^e} = \sqrt{\frac{3}{2}}\|\mathbf{s}\| = \sqrt{\frac{3}{2}\mathbf{s}:\mathbf{s}} = \sqrt{\frac{3}{2}s_{ij}s_{ij}} \tag{4.26}$$

where $\mathbf{s} = \boldsymbol{\sigma} - p\mathbf{I}$.

The functional relationships between the elastic strain invariants and the effective stress invariants are

$$p = p_0 \exp\left[-\left(\frac{\varepsilon_v^e - \varepsilon_{v0}^e}{\tilde{\kappa}}\right)\right]\left[1 + \frac{3\alpha}{2\tilde{\kappa}}\left(\varepsilon_s^e\right)^2\right] \tag{4.27}$$

$$q = 3\left[\mu_o - \alpha p_o \exp\left(-\frac{\varepsilon_v^e - \varepsilon_{v0}^e}{\tilde{\kappa}}\right)\right]\varepsilon_s^e \tag{4.28}$$

4.2.4 Plasticity Model

Yield and Plastic Potential Functions

Many of the constitutive models developed for partially saturated soils (e.g., Alonso et al. 1990) are extensions of the principles of Critical State Soil Mechanics (Schofield and Wroth 1968) for saturated soils. Wood (1990) provides background information on the Cam-Clay models and Critical State Soil Mechanics concepts and Simo and Hughes (1998) consider the mathematical and computational aspects related to inelastic constitutive modeling.

The Borja model (Borja 2004) is based on the modified Cam-Clay plasticity theory extended to partially saturated soils. It can be classified as a strain-hardening/softening model where the concept of a yield surface is used to indicate when plastic deformations occur. The equation for the yield function is given by Eqn. (4.29) and the relevant parameters are shown in Figure 4.2-1 (Borja 2004).

$$F = \frac{q^2}{M^2} + \left(p - p_s\right)\left(p - \bar{p}_c\right) = 0 \tag{4.29}$$

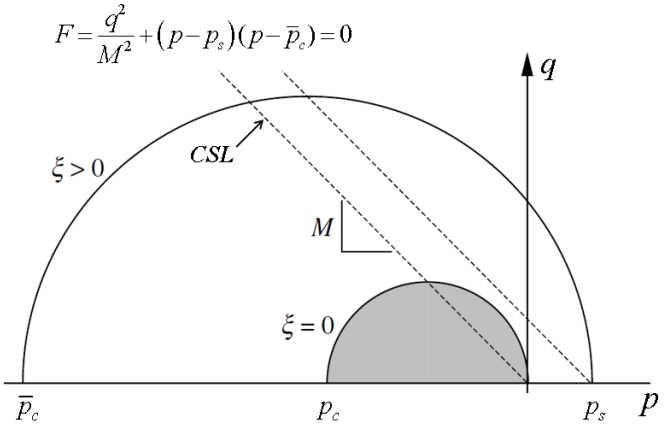

Figure 4.2-1. Yield Surface: *p*-*q* plane (Borja 2004).

This particular form for the yield function uses two stress invariants $\left(p, q\right)$ and is independent of the Lode angle. The yield surface is an ellipsoid which intersects the mean effective stress axis $\left(q = 0\right)$ at $p = p_s$ and $p = \bar{p}_c$. In Eqn. (4.29) $\bar{p}_c$ is the effective preconsolidation stress which is assumed to depend on the plastic volumetric strain ε_v^p, the matric suction s, and the liquid saturation S_l. p_s represents the apparent adhesion resulting from matric suction. In an effective stress formulation $p_s = 0$; however, in a net stress formulation p_s is assumed to be a linear function of the matric suction, $p_s = k \cdot s$ (Alonso et al. 1990). The parameter M is the slope of the critical state line.

The flow rule used in this model is

$$\dot{\boldsymbol{\varepsilon}}^p = \dot{\gamma} \frac{\partial G}{\partial \boldsymbol{\sigma}} \tag{4.30}$$

where the plastic potential function *G* is

$$G = \frac{\beta q^2}{M^2} + \left(p - p_s\right)\left(p - \bar{p}_c\right) \tag{4.31}$$

When $\beta = 1$ the yield function (Eqn. (4.29)) and the plastic potential function (Eqn. (4.31)) are identical and the flow rule is associative; otherwise, when $\beta \neq 1$ the flow rule is non-associative.

The non-negative parameter $\dot{\gamma}$ is the consistency parameter that satisfies the Kuhn-Tucker complementary conditions (loading/un-loading conditions) (Simo and Hughes 1998)

$$\begin{aligned} &\dot{\gamma} \geq 0 \qquad F \leq 0 \\ &\text{and} \quad \dot{\gamma} F = 0 \end{aligned} \tag{4.32}$$

and the consistency condition

$$\dot{\gamma} \dot{F} = 0 \tag{4.33}$$

Compressibility Laws for Saturated Conditions

Two compressibility laws are commonly used to define the relationship between specific volume v_{sat} and preconsolidation stress p_c in the Cam-Clay model for saturated clayey soils. The compressibility law is used to define the hardening function used in the plasticity formulation.

The first compressibility law (Eqn. (4.34)) is a linear relation between specific volume and the natural logarithm of the preconsolidation stress (see Figure 4.2-2). λ is the compressibility index and v_o is the value of specific volume v_{sat} at the reference preconsolidation stress p_{co}.

$$v_{sat} = v_o - \lambda \ln \frac{p_c}{p_{co}} \tag{4.34}$$

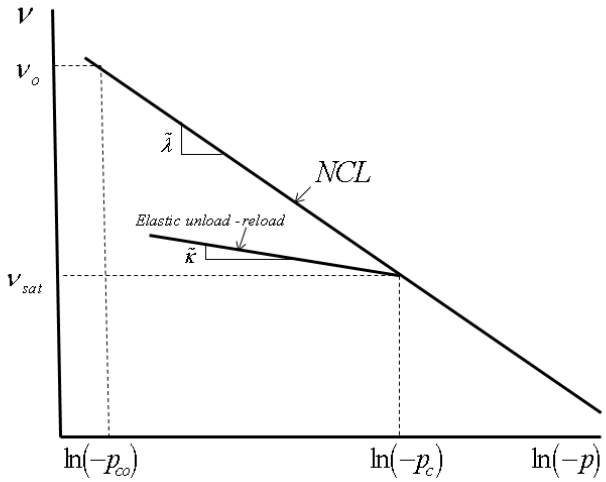

Figure 4.2-2. Semi-logarithmic compressibility law.

In some cases this compressibility law can produce unphysical values of $v_{sat} < 1$ (negative void ratio or porosity) even at reasonable values of stress, therefore, Borja et al. (1997) advocate using the following bilogarithmic relationship (see Figure 4.2-3)

$$\ln v_{sat} = \ln v_o - \tilde{\lambda} \ln \frac{p_c}{p_{co}} \tag{4.35}$$

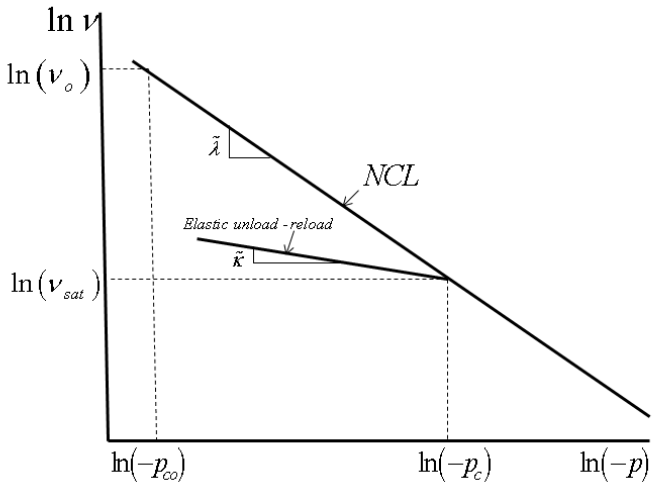

Figure 4.2-3. Bi-logarithmic compressibility law.

These equations are used to describe the *normal consolidation line* (NCL) for saturated clays. For convenience we will set $p_{co} = -1$ so these equations become

$$v_{sat} = v_o - \lambda \ln(-p_c) \tag{4.36}$$

Note Eqn. (4.15) in Borja (2004) is missing the negative sign. In that paper he also uses N instead of v_o and $\tilde{\lambda}$ instead of λ.

$$\ln v_{sat} = \ln v_o - \tilde{\lambda} \ln(-p_c) \tag{4.37}$$

For a volume strain measure ε_v we use the natural strain definition (Eqn. (4.38)) where V and V_o are the current and initial volumes respectively. For the second expression we have used Eqn. (4.6).

$$\varepsilon_v = \ln\left(\frac{V}{V_o}\right) = \ln\left(\frac{v}{v_o}\right) \tag{4.38}$$

The volumetric strain rate can be obtained by taking the time derivative of Eqn. (4.38)

$$\dot{\varepsilon}_v = \frac{\dot{v}}{v} \tag{4.39}$$

Taking the time derivative of Eqn. (4.36) and dividing by v_{sat} gives for the semi-logarithmic case

$$\dot{\varepsilon}_v = \frac{\dot{v}_{sat}}{v_{sat}} = -\frac{\lambda}{v_{sat}}\frac{\dot{p}_c}{p_c} \tag{4.40}$$

and for the bi-logarithmic case Eqn. (4.37)

$$\dot{\varepsilon}_v = \frac{\dot{v}_{sat}}{v_{sat}} = -\tilde{\lambda}\frac{\dot{p}_c}{p_c} \tag{4.41}$$

The elastic component of the volumetric strain rate can be obtained from Eqn. (4.27) if we assume isotropic loading, $\dot{\varepsilon}_s^e = 0$, and identify p with p_c then

$$\dot{\varepsilon}_v^e = -\tilde{\kappa}\frac{\dot{p}_c}{p_c} \tag{4.42}$$

Defining the total volumetric strain rate to be the sum of the elastic and plastic volumetric strain rates

$$\dot{\boldsymbol{\varepsilon}} = \dot{\boldsymbol{\varepsilon}}^e + \dot{\boldsymbol{\varepsilon}}^p \tag{4.43}$$

and combining Eqns. (4.41) and (4.42) gives the equation for plastic volumetric strain rate when the bilogarithmic compressibility function is used.

$$\dot{\varepsilon}_v^p = \left(\tilde{\kappa} - \tilde{\lambda}\right)\frac{\dot{p}_c}{p_c} \tag{4.44}$$

Eqn. (4.44) is the plastic strain rate that Borja uses throughout his development. However he uses Eqn. (4.36) to evaluate the specific volume in his example problems. This would appear to be inconsistent but by restricting his analysis to infinitesimal deformation the differences between the engineering strain and natural strain are small (Borja and Tamagnini, 1998). In our implementation we have two options. The first uses the combination of Eqns. (4.36) and (4.44); the second uses Eqns. (4.37) and (4.44).

Using the semi-logarithmic compressibility function the plastic volumetric strain rate is

$$\dot{\varepsilon}_v^p = \left(\frac{\kappa - \lambda}{v_{sat}}\right)\frac{\dot{p}_c}{p_c} \tag{4.45}$$

Under the assumption of infinitesimal deformations the value of v_{sat} would be the initial value of specific volume.

Compressibility Law Modification for Partially Saturated Conditions

Gallipoli et al. (2003) showed that the ratio of the void ratio in a partially saturated state to the corresponding void ratio in a saturated state, when both were measured at the same effective mean stress, could be reasonably approximated by

$$\tilde{c}(\xi) = \frac{e}{e_{sat}} = 1 - \tilde{c}_1 \left[1 - \exp(c_2 \xi) \right] \tag{4.46}$$

where $\tilde{c}_1$ and c_2 are fitting constants. Based on their examination of data from Sivakumar (1993) and Sharma (1998) these fitting constants values were found to 0.369 and 1.419 respectively.

The independent variable ξ in Eqn. (4.46) is called the bonding parameter (Gallipoli et al. 2003) and represents the inter-particle bonding due to water menisci. They reason that the magnitude of the inter-particle bonding should be the result of two effects: (1) the number of water menisci per unit volume of solid fraction and (2) the intensity of the stabilizing force exerted at the inter-particle contacts by a single meniscus. The bonding variable is assumed to be a function of the matric suction and liquid saturation

$$\xi = f(s)(1 - S_l) \tag{4.47}$$

The factor $(1 - S_l)$ is introduced to grossly represent the effect of the number of menisci per unit volume of solid fraction. The function $f(s)$ obtained from an analytic solution by Fisher (1926) for the ratio of the inter-particle forces at a given suction and the forces at zero suction for a single meniscus and equal size spherical particles. The function varies from 1.0 to 1.5 for values of suction between zero and infinity.

Borja (2004) approximated the function from Gallipoli et al. (2003), which assumed the particles were 1 μ (approximately the texture of compacted kaolin) with the following equation

$$f(s) = 1 + \frac{s / p_{atm}}{10.7 + 2.4(s / p_{atm})} \tag{4.48}$$

where p_{atm} is the normalizing pressure (atmospheric).

Since we are using specific volume rather than void ratio we need to derive an expression for $c(\xi) = v / v_{sat}$.

$$c(\xi) = v / v_{sat} = \frac{1 + e}{1 + e_{sat}} = \frac{1/e_{sat} + e/e_{sat}}{1/e_{sat} + 1} \tag{4.49}$$

Substituting Eqn. (4.46) into Eqn. (4.49) we get

$$c(\xi) = \frac{\nu}{\nu_{sat}} = 1 - c_1\left[1 - \exp\left(c_2 \xi\right)\right] \tag{4.50}$$

where $c_1 = \tilde{c}_1\left(1 - 1/\nu_{sat}\right) = \tilde{c}_1\left(1 + 1/e_{sat}\right)$.

We need to obtain a functional relationship between the effective preconsolidation stress $\bar{p}_c$ and the preconsolidation stress p_c. It is convenient to choose ν_o as the specific volume at $p_{co} = -1$.

For the semi-log case the desired relationship is given by

$$\bar{p}_c = -\exp\left[a(\xi)\right]\left(-p_c\right)^{b(\xi)} \tag{4.51}$$

where

$$a(\xi) = \frac{\nu_o \left\{c(\xi) - 1\right\}}{\lambda c(\xi) - \kappa} \tag{4.52}$$

$$b(\xi) = \frac{\left(\lambda - \kappa\right)}{\lambda c(\xi) - \kappa} \tag{4.53}$$

For the bilogarithmic compressibility law Eqn. (4.35) the relationship is

$$\bar{p}_c = p_c\left[c(\xi)\right]^{\frac{1}{\tilde{\lambda} - \tilde{\kappa}}} \tag{4.54}$$

In order to numerically integrate the constitutive equations the implicit first order accurate backward-Euler scheme was used. Complete details of the numerical integration procedure are presented in Borja (2004).

The model requires initialization of state variables before the simulation can proceed. The true state variables are the elastic strain tensor $\boldsymbol{\varepsilon}^e$ and the preconsolidation stress p_c. There are two ways the elastic strain tensor can be specified. The first is by specifying the initial elastic strains as initial conditions. From the initial elastic strains the initial stresses can be computed,

$$p = p_0 \exp\left[-\left(\frac{\varepsilon_v^e - \varepsilon_{v0}^e}{\tilde{\kappa}}\right)\right]\left[1+\frac{3\alpha}{2\tilde{\kappa}}\left(\varepsilon_s^e\right)^2\right]$$

$$q = 3\left[\mu_o - \alpha p_o \exp\left(-\frac{\varepsilon_v^e - \varepsilon_{v0}^e}{\tilde{\kappa}}\right)\right]\varepsilon_s^e$$

From these the stress invariants can be calculated and used to calculate the effective stress tensor.

$$\boldsymbol{\sigma} = p\mathbf{I} + \sqrt{\frac{2}{3}}q\mathbf{n}$$

where $\mathbf{n} = \dfrac{\mathbf{e}^e}{\|\mathbf{e}^e\|}$ and $\mathbf{e}^e = \boldsymbol{\varepsilon}^e - \dfrac{1}{3}\varepsilon_v^e\mathbf{I}$

Specifying the initial elastic strain tensor may be useful for some problems but is not practical for problems where the initial effective stresses vary with position in the finite element model. Thus the second way is to specify the initial effective stresses as initial conditions and then we use the nonlinear elasticity model to determine the initial elastic strain tensor. This is done by iteratively solving the two equations given above for the elastic strain invariants using Newton Raphson iteration. The elastic strain tensor $\boldsymbol{\varepsilon}^e$ can then be computed from

$$\boldsymbol{\varepsilon}^{\mathbf{e}} = \frac{1}{3}\varepsilon_v^e\mathbf{I} + \mathbf{e}^{\mathbf{e}} = \frac{1}{3}\varepsilon_v^e\mathbf{I} + \sqrt{\frac{3}{2}}\varepsilon_s^e\mathbf{n} \tag{4.55}$$

since $\mathbf{n} = \dfrac{\mathbf{s}}{\|\mathbf{s}\|}$ can be computed from the specified initial stress tensor.

Most porous flow models require the user to specify the porosity of each material. Therefore, in order to maintain some consistency between Aria and Adagio we have chosen to require the initial porosity to be specified in this model rather than specific volume or void ratio. The specific volume can be calculated from the porosity using $v = \dfrac{1}{1-\phi}$. The final state variable that we need is the preconsolidation stress p_c corresponding to the specified initial porosity and mean effective stress p . For the semi-logarithmic compressibility model we use

$$p_c = -\exp\left\{\frac{\nu - \nu_o + \kappa\log_e(-p)}{\kappa - \lambda}\right\} \tag{4.56}$$

and for the bi-logarithmic model we use

$$p_c = -\exp\left[\frac{\log_e(\nu) - \log_e(\nu_o) + \tilde{\kappa}\log_e(-p)}{\tilde{\kappa} - \tilde{\lambda}}\right] \tag{4.57}$$

Table 4.2-1 summarizes the input variables required by the model.

Table 4.2-1. Input variables required by model.

Model Variable	Input Variable Name	Model Variable Description
p_o	P0	reference mean effective stress in nonlinear elastic model (4.22)
κ or $\tilde{\kappa}$	KAPPA	unload-reload elastic slope in nonlinear elastic model (4.22)
ε_{vo}	EV0	reference elastic volume strain in nonlinear elastic model (4.22)
μ_o	MU0	shear modulus term in nonlinear elastic model (4.23)
α	ALPHA	coupling coefficient in nonlinear elastic model (4.23)
k	K	coefficient used in net stress formulation $p_s = k \cdot s$
p_{atm}	PATM	reference pressure used in Borja's $f(s)$ function (4.48)
c_1	C1	fitting parameter used in $c(\xi)$ (4.50)
c_2	C2	fitting parameter used in $c(\xi)$ (4.50)
ν_o	N	specific volume at $p = -1$ (4.34) and (4.35)
m	M	slope of critical state line (4.29)
λ or $\tilde{\lambda}$	COMPRESSION INDEX	slope of NCL line (4.34) and (4.35)
β	BETA	associative/non-associative flow rule parameter (4.31)
ϕ	POROSITY	porosity= $\phi = \frac{\nu - 1}{\nu}$ (4.10)
-	VERSION	Option Flag for compressibility function =0 for bi-log NCL >0 for semi-log NCL

4.2.5 Verification Examples

Borja (2004) presented three problems that we have used to verify the model implementation in the Adagio only mode. For these problems we specify the effective pore pressure, the suction (= capillary pressure) and the non-wetting phase saturation using Adagio's function definition capabilities. In a coupled hydro-mechanical problem, Aria would compute these quantities and Arpeggio would control the flow of these data to Adagio. At this time we have not tested the complete coupling of Aria and Adagio for this model. There is one task remaining and that is to compute the effective pore pressure in the Aria calculation and to verify that the data transfer from Aria to Adagio is operating as required.

These verification problems were all run using a single three dimensional hexagonal finite element aligned with the coordinate axes. The semi-log compressibility model was used in order to compare with the results presented by Borja (2004). The following model parameters are used in these verification problems. The hyperelastic model parameters are: $\kappa = \tilde{\kappa} = 0.03$, $\alpha = 103$, $\varepsilon_{vo} = 0$ and $\mu_o = 0$. The plasticity model parameters are: $M = 1.0$, $\lambda = \tilde{\lambda} = 0.11$, $\nu_o = N = 2.76$, $k = 0.6$, and $\beta = 1$. A relationship between liquid saturation S_l and suction s (van Genuchten, 1980) with $S_1 = 0.25$, $S_2 = 1$, $s_a = 20$ kPa, $n = 2.5$, and $m = 0.6$ was specified.

$$S_g = 1 - S_l = 1 - \left\{ S_1 + (S_2 - S_1)\left[1 + \left(\frac{s}{s_a} \right)^n \right]^{-m} \right\} \tag{4.58}$$

The non-wetting phase saturation S_g was evaluated using (4.58) for s starting at 20 kPa and linearly decreasing to 0 kPa. The initial value of S_g was 0.25518. The fitting parameters c_1 and c_2 were 0.185 and 1.42, respectively.

Isotropic stress relaxation due to loss of suction

The first problem involves isotropic stress relaxation due to loss of suction. A reduction in suction corresponds to an increase in liquid phase saturation or equivalently a wetting of the material. From an effective stress state initially inside the effective yield surface the suction is linearly decreased from 20 kPa to 0 in 40 steps. In Borja's problem definition the hyperelastic parameter p_o = -20 kPa, the initial elastic strain tensor $\boldsymbol{\varepsilon}^e$ =0 and the initial preconsolidation stress p_c = -10 kPa were specified. Using Eqns. and we have p = -20 kPa and q = 0 kPa .

In our setup of the problem, rather than specifying the initial elastic strain tensor $\boldsymbol{\varepsilon}^e$ we specified the initial effective normal stresses. From the given initial preconsolidation stress p_c and the mean stress $p = (\sigma_1 + \sigma_2 + \sigma_3)/3$ = -20 kPa the values of specific volume (ν =2.4895) and the porosity (ϕ =0.5977) were computed using Eqns. (4.56) and (4.10), respectively. This value of porosity was used as input to the model.

From the initial values of suction (s = 20 kPa) and non-wetting phase saturation (S_g =0.25518) and using p_{atm} =101.3 kPa we can determine the initial bonding variable using Eqns. (4.47) and (4.48).

$$\xi = f(s)(1 - S_l) = \left[1 + \frac{s/p_{atm}}{10.7 + 2.4(s/p_{atm})} \right](1 - S_l)$$

$$\xi = \left[1 + \frac{20/101.3}{10.7 + 2.4(20/101.3)} \right](0.2552) = (1.0177)(0.2552) = 0.26$$

The suction was decreased from 20 kPa to zero in 40 steps while holding the boundaries of the element fixed. Under these conditions the element does not undergo any deformation and thus the components of the total strain tensor are zero during the suction reduction. As the suction is reduced the yield surface collapses. Figure 4.2-4 illustrates the evolution of the bonding parameter ξ. Plastic yielding occurs when the effective yield surface (indicated by $\bar{p}_c$) reaches the effective stress state p = -20 kPa. This occurs when the bonding variable is approximately ξ =0.078. From that point the stress state is forced to remain on the collapsing effective yield surface and plastic deformation occurs. The zero suction yield surface expands (indicated by p_c becoming more negative) (see Figure 4.2-5). When the suction is zero the effective yield surface and the zero suction yield surface are the same. Since the total strain is constant the elastic and plastic strain are equal but opposite in sign (see Figure 4.2-6). The plastic strain is negative indicating compressive strains. Since the loading conditions are isotropic the stress state moves along the mean effective stress axis $(q = 0)$ and all components of normal stress and strain are identical. This problem illustrates the idea of wetting collapse which can occur when a soil undergoes plastic compaction when the suction is decreased.

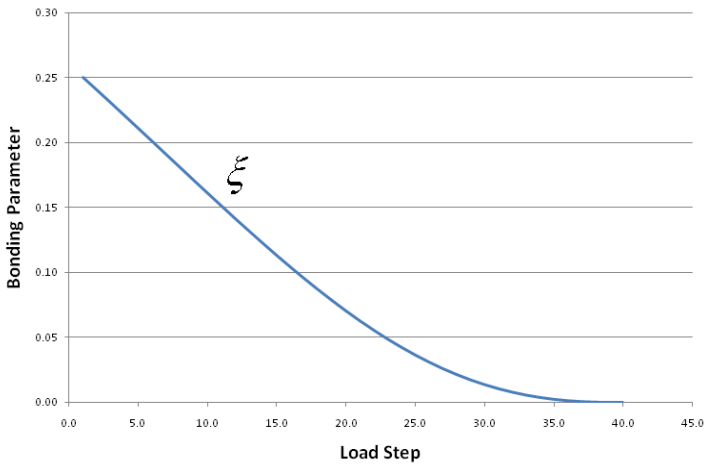

Figure 4.2-4. Test Problem 1: Evolution of bonding parameter.

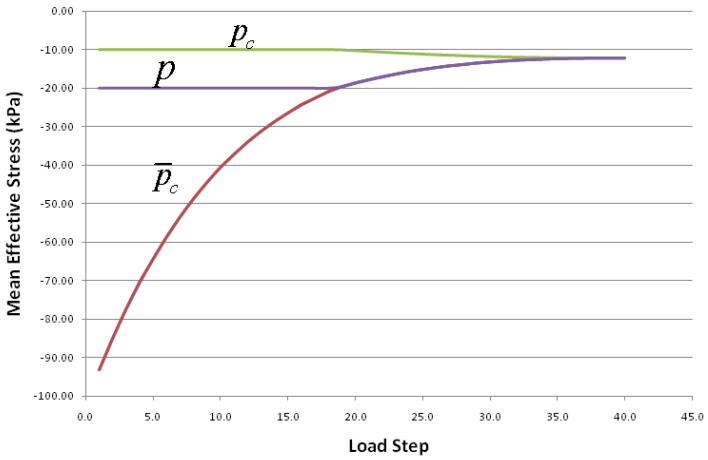

Figure 4.2-5. Test Problem 1: Evolution of mean stress variables.

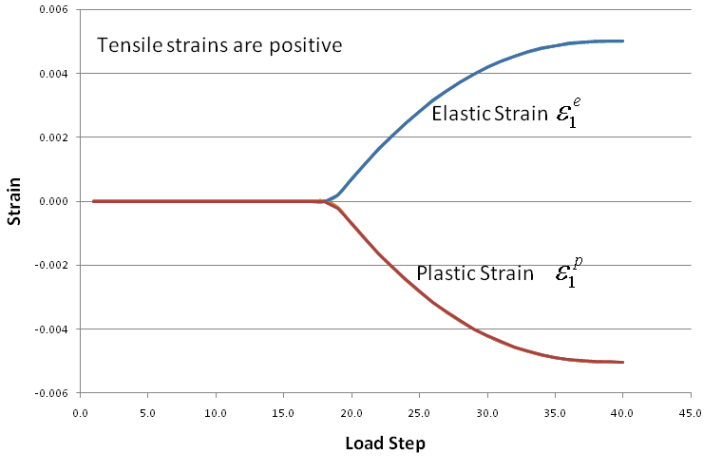

Figure 4.2-6. Test Problem 1: Evolution of strain.

Deviatoric stress relaxation due to loss of suction

In this problem the element is subjected to an initial elastic strain state $\varepsilon_1^e = -\varepsilon_2^e = 0.00351,\ \varepsilon_3^e = 0$, with an initial preconsolidation stress $p_c = -100\,\text{kPa}$ and $p_o = -100\,\text{kPa}$. The suction history and boundary conditions (fixed displacement) are the same as in the first problem.

In contrast to the first problem the elastic strain tensor was set as an initial condition in the Adagio input file and the initial stresses were computed during the initialization phase. Using Eqns. (4.27) and (4.28) the initial stress invariants $(p,q) = (-108.5\,\text{kPa}, 125.2\,\text{kPa})$ are calculated. The elastic strain tensor has deviatoric components therefore the initial stress state is

not isotropic $(q \neq 0)$. In order to compute the initial specific volume we use Eqn. (4.56) with the initial mean stress *p* and the initial preconsolidation stress p_c. This gives an initial specific volume of 2.251 which corresponds to a porosity of 0.5557.

The stress state starts out inside the effective yield surface. As the suction decreases the stress state (p,q) remains constant until the effective yield surface collapses to the stress state point (See Figures 4.2-7, 4.2-8, and 4.2-9). This occurs at step 15 at a value of bonding parameter $\xi = 0.113$. As the suction continues to be reduced the stress state remains on the effective yield surface and plastic strains are computed. During the suction decrease the stress state (p,q) relaxes. This is indicated by the reduction in effective shear stress q in Figure 4.2-9 and the reduction in effective mean stress *p* in Figure 4.2-8. At the same time the zero suction yield surface increase slightly in size as indicated by the decrease in p_c in Figure 4.2-8. Figure 4.2-10 shows the elastic and plastic strain components computed by the model for these loading conditions.

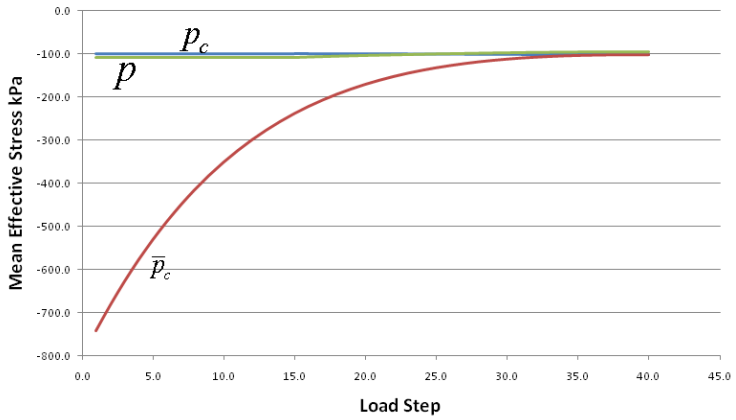

Figure 4.2-7. Test Problem 2: Evolution of mean stress variables.

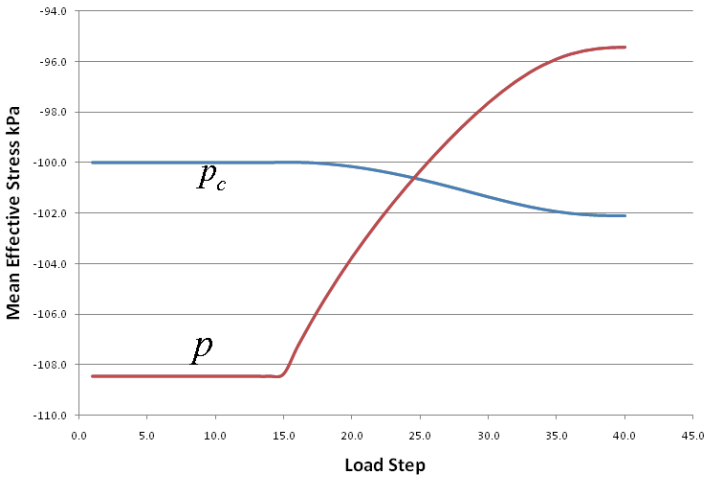

Figure 4.2-8. Test Problem 2: Evolution of mean stress variables *p* and p_c .

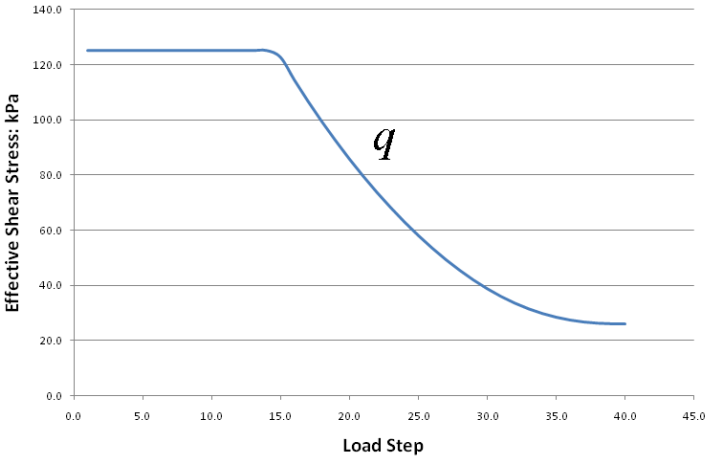

Figure 4.2-9. Test Problem 2: Evolution of effective shear stress *q*.

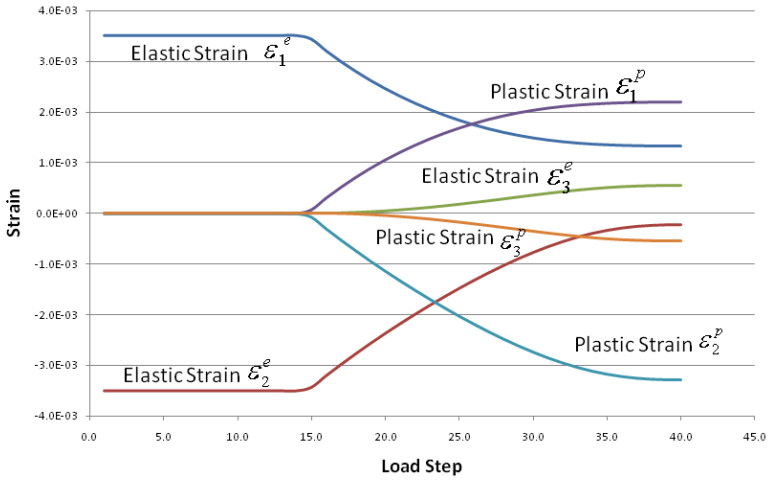

Figure 4.2-10. Test Problem 2: Evolution of strain variables.

Constrained compression combined with loss of suction

This problem uses the same material parameters and initial conditions as the previous problem. However, in this case an incremental compressive strain is applied, $\Delta\varepsilon_2 = -0.001$ at each load step while holding the other element boundaries fixed. A specified uniaxial displacement history was applied to the nodes on one surface of the finite element to provide the equivalent strain conditions. As in the first two cases the suction was reduced from 20 kPa to zero in the first 40 steps (Figure 4.2-11); however, the strain increments were applied for another 122 steps. The initial stress state $(p,q) = (-108.5 \text{ kPa}, 125.2 \text{ kPa})$ lies inside the effective yield surface.

Figure 4.2-12 shows the evolution of the mean stress variables computed by the model. Figure 4.2-13 shows the stress path resulting from the combined suction reduction and applied load. Figure 4.2-14 shows the specific volume computed by the model.

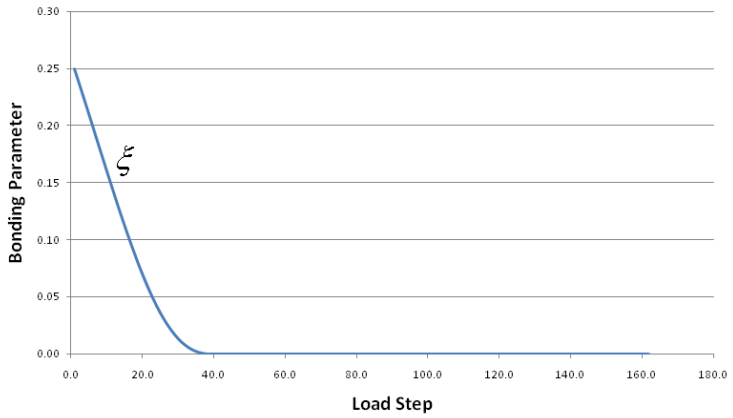

Figure 4.2-11. Test Problem 3: Evolution of bonding parameter.

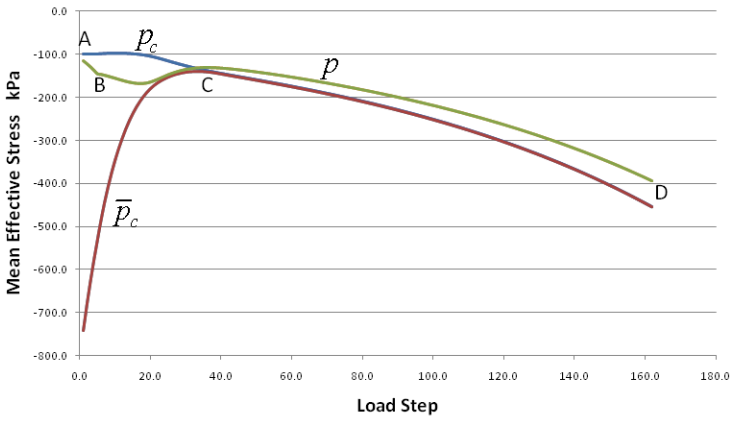

Figure 4.2-12. Test Problem 3: Evolution of mean stress variables.

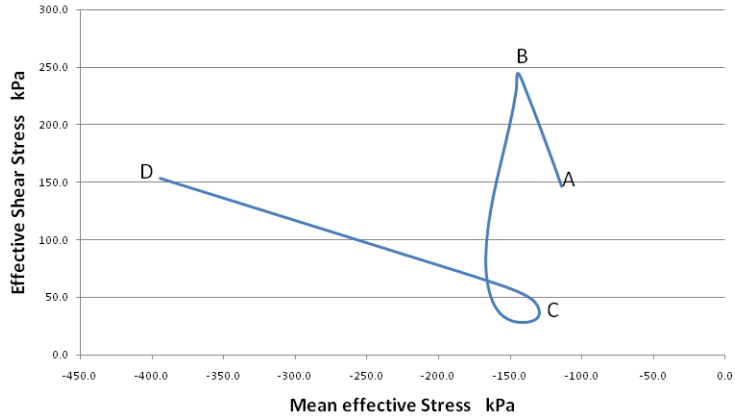

Figure 4.2-13. Test Problem 3: Stress path in *p*-*q* space.

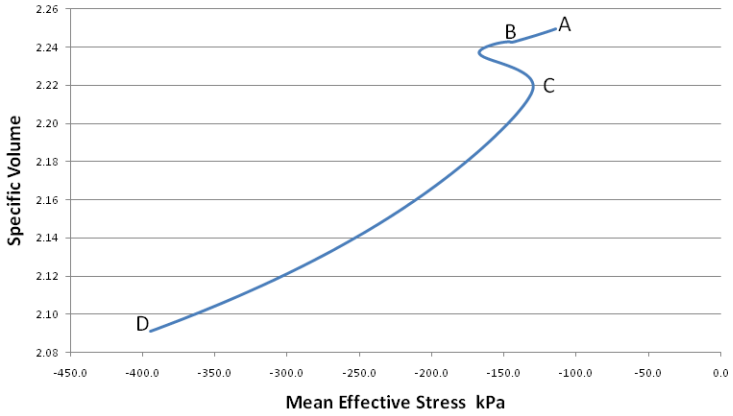

Figure 4.2-14. Test Problem 3: Evolution of specific volume.

During the first five load steps (path A to B) the model shows elastic response. The bonding parameter has a value of 0.211 at point B when plastic deformation begins. In Figure 4.2-13 the path from B to C shows the combined effect of suction reduction and applied loading contributes to the reduction in effective shear stress q. At point C the suction has been reduced to zero and the effective yield surface and the zero suction yield surface are the same ($\bar{p}_c = p_c$).

4.3 Multimechanism Deformation Creep Model

The Multimechanism Deformation Creep Model (MD model), developed by Munson and Dawson (1979,1982,1984) and later extended by Munson et al. (1989), is based on the concept of a deformation mechanism map (Munson 1979); the active temperature and stress regime determines which micromechanical mechanisms are active. The MD model mathematically represents the primary and secondary creep behavior of salt due to dislocations under relatively low temperatures (compared to the melting temperature) and low to moderate stresses which are typical of mining and storage cavern operations. In this section the model and its implementation are discussed with particular emphasis on the implicit formulation used to integrate the creep equations.

4.3.1 MD Model Equations

The MD model defines the creep strain rate tensor as follows.

$$\dot{\boldsymbol{\varepsilon}}^c = \dot{\varepsilon}^c_{eq}\mathbf{g} \tag{4.59}$$

In Eqn.(4.59), $\dot{\varepsilon}^c_{eq}$ is the equivalent creep strain rate and $\mathbf{g}$ is the gradient of the flow potential defined by the equivalent stress σ_{eq}

$$\mathbf{g} = \frac{\partial \sigma_{eq}}{\partial \boldsymbol{\sigma}} \tag{4.60}$$

In the MD model the equivalent stress is taken to be the Tresca stress σ_{eq}^{T} which is twice the maximum shear stress. The Tresca stress can be expressed in terms of the principal stresses. If the principal stresses are ordered such that $\sigma_1 \geq \sigma_2 \geq \sigma_3$

$$\sigma_{eq} = \sigma_{eq}^{T} = \sigma_1 - \sigma_3 \tag{4.61}$$

The Tresca stress can also be written in terms of stress invariants

$$\sigma_{eq}^{T} = 2\cos\psi\sqrt{J_2} \tag{4.62}$$

where ψ is the Lode angle, J_2 and J_3 are the second and third invariants of the deviatoric stress tensor $\mathbf{s}$, and s_1, s_2, and s_3 are the principal deviatoric stresses (Hill 1950).

$$\mathbf{s} = \boldsymbol{\sigma} - \frac{1}{3} tr\left(\boldsymbol{\sigma}\right)\mathbf{I} = \boldsymbol{\sigma} - \sigma_m \mathbf{I} \tag{4.63}$$

$$\psi = \frac{1}{3}\sin^{-1}\left[\frac{-3\sqrt{3}J_3}{2J_2^{3/2}}\right] \qquad -\frac{\pi}{6} \leq \psi \leq \frac{\pi}{6} \tag{4.64}$$

$$J_2 = \frac{1}{2}\mathbf{s}:\mathbf{s} = \frac{1}{2}s_{ij}s_{ij} = \frac{1}{2}\left(s_1^2 + s_2^2 + s_3^2\right) \tag{4.65}$$

$$J_3 = \det\mathbf{s} = \frac{1}{3}s_{ij}s_{jk}s_{ki} = s_1 s_2 s_3 \tag{4.66}$$

Three thermally activated dislocation creep mechanisms are included in the MD model.

1. Dislocation climb ($\dot{\varepsilon}_{s_1}$) which is active high temperatures and low stresses
2. An unnamed, but experimentally observed mechanism ($\dot{\varepsilon}_{s_2}$) at low temperatures and low stresses
3. Dislocation slip ($\dot{\varepsilon}_{s_3}$) which is active at high stresses

The equivalent steady state creep strain rate $\dot{\varepsilon}_s$ is defined as the sum of the steady state creep rates for each mechanism.

$$\dot{\varepsilon}_s = \sum_{i=1}^{i=3} \dot{\varepsilon}_{s_i} \tag{4.67}$$

$$\dot{\varepsilon}_{s_1} = A_1 e^{-Q_1/RT} \left(\frac{\sigma_{eq}}{G} \right)^{n_1} \tag{4.68}$$

$$\dot{\varepsilon}_{s_2} = A_2 e^{-Q_2/RT} \left(\frac{\sigma_{eq}}{G} \right)^{n_2} \tag{4.69}$$

$$\dot{\varepsilon}_{s_3} = H\left(\sigma_{eq} - \sigma_0\right)\left(B_1 e^{-Q_1/RT} + B_2 e^{-Q_2/RT} \right) \sinh\left(\frac{q\left(\sigma_{eq} - \sigma_0\right)}{G} \right) \tag{4.70}$$

The parameters $A_1, A_2, B_1, B_2, n_1, n_2, q, \sigma_0$ are material constants, Q_1 and Q_2 are activation energies, G is the shear modulus, R is the universal gas constant, and T is the absolute temperature. The function H with argument $\sigma_{eq} - \sigma_0$ is the Heaviside step function

$$H\left(\sigma_{eq} - \sigma_0\right) = \begin{cases} 0, \text{ when } \sigma_{eq} - \sigma_0 < 0 \\ 1, \text{ when } \sigma_{eq} - \sigma_0 \geq 0 \end{cases} \tag{4.71}$$

In the MD Creep model, primary creep effects are included by introducing a transient function F as a multiplying factor on the equivalent steady state strain rate.

$$\dot{\varepsilon}_{eq}^{c} = F \cdot \dot{\varepsilon}_s \tag{4.72}$$

The function F appearing in Eqn. (4.72)has three branches: a work hardening branch ($F > 1$), an equilibrium branch ($F = 1$), and a recovery branch ($F < 1$).

$$F = \begin{cases} \exp\left[\Delta \left(1 - \dfrac{\zeta}{\varepsilon_t^f} \right)^2 \right] & \zeta < \varepsilon_t^f \quad \text{Hardening Branch} \\ 1 & \zeta = \varepsilon_t^f \quad \text{Equilibrium Branch} \\ \exp\left[-\delta \left(1 - \dfrac{\zeta}{\varepsilon_t^f} \right)^2 \right] & \zeta > \varepsilon_t^f \quad \text{Recovery Branch} \end{cases} \tag{4.73}$$

The choice of the particular branch depends on the transient strain limit ε_t^f and the internal variable ζ . The transient strain limit is defined by Eqn. (4.74)where K_0, *c*, and *m* are material parameters, and *T* is the absolute temperature.

$$\varepsilon_t^f = K_0 e^{cT} \left(\frac{\sigma_{eq}}{G} \right)^m \tag{4.74}$$

The internal variable ζ used in the calculation of the transient function *F* is obtained by integration of an evolution equation

$$\dot{\zeta} = \left(F - 1 \right) \dot{\varepsilon}_s \tag{4.75}$$

Δ and δ , appearing in Eqn.(4.73), are the work hardening and recovery parameters and are given by Eqns. (4.76)and (4.77) respectively. In these equations α , β , α_r , and β_r are material parameters. The recovery parameter δ is assumed to be constant (i.e., $\delta = \alpha_r$) in this implementation.

$$\Delta = \alpha + \beta \log_{10} \left(\frac{\sigma_{eq}}{G} \right) \tag{4.76}$$

$$\delta = \alpha_r + \beta_r \log_{10} \left(\frac{\sigma_{eq}}{G} \right) \tag{4.77}$$

The gradient of the flow potential is calculated using the chain rule

$$\mathbf{g}^T = \frac{\partial \sigma_{eq}^T}{\partial \boldsymbol{\sigma}} = \frac{\partial \sigma_{eq}^T}{\partial J_2} \frac{\partial J_2}{\partial \boldsymbol{\sigma}} + \frac{\partial \sigma_{eq}^T}{\partial J_3} \frac{\partial J_3}{\partial \boldsymbol{\sigma}} \tag{4.78}$$

$$\frac{\partial J_2}{\partial \boldsymbol{\sigma}} = \mathbf{s} \tag{4.79}$$

$$\frac{\partial J_3}{\partial \boldsymbol{\sigma}} = \mathbf{t} = \mathbf{s}^2 - \frac{2}{3} J_2 \mathbf{I} \tag{4.80}$$

$$\frac{\partial \sigma_{eq}^T}{\partial J_2} = \frac{2}{\sigma_{eq}^T} \frac{\cos\psi \cos 2\psi}{\cos 3\psi} \tag{4.81}$$

$$\frac{\partial \sigma_{eq}^{T}}{\partial J_3} = \frac{\partial \sigma_{eq}^{T}}{\partial \psi}\frac{\partial \psi}{\partial J_3} \tag{4.82}$$

where

$$\frac{\partial \sigma_{eq}^{T}}{\partial \psi} = -\frac{4}{\sigma_{eq}^{T}}\cos\psi \sin\psi J_2 \tag{4.83}$$

$$\frac{\partial \psi}{\partial J_3} = -\frac{\sqrt{3}}{2J_2^{3/2}\cos 3\psi} \tag{4.84}$$

Substituting these results into Eqn.(4.78) gives the gradient when the Tresca flow potential is used.

$$\mathbf{g}^{T} = \left(\left[\frac{\cos 2\psi}{\cos 3\psi}\right]\frac{\mathbf{s}}{\sqrt{J_2}} + \left[\frac{\sqrt{3}\sin\psi}{J_2\cos 3\psi}\right]\mathbf{t}\right) \tag{4.85}$$

The Tresca stress is continuous for all values of Lode angle; however, the gradient $\mathbf{g}^{T}$ is discontinuous when $\psi = \pm\frac{\pi}{6}$ or $\cos(3\psi) = 0$. This is due to the presence of corners in the flow potential. Special consideration must be given to the gradient computation at these locations. To eliminate the indeterminacy at these values of Lode angle, the gradients at these values of Lode angle are computed on each side of $\psi = \frac{\pi}{6}$ or $-\frac{\pi}{6}$ and then averaged. This is equivalent to using a flow potential based on the von Mises stress when $\psi = \pm\frac{\pi}{6}$. Ultimately, it must be decided when to use the Tresca flow potential or the von Mises flow potential for calculating the gradient. This will be addressed in section 4.3.3.

4.3.2 Numerical Integration Algorithms for the MD Creep Model

We assume that the deviatoric stress tensor $\mathbf{s}$ and internal variable ζ at time *t* are known. For an increment of time we use

$$\Delta t = t_{n+1} - t_n \tag{4.86}$$

and for the deviatoric stress tensor and internal variable ζ at times t_n and t_{n+1} we use

$$\begin{aligned} \mathbf{s}_n &= \mathbf{s}(t_n) \qquad & \mathbf{s}_{n+1} &= \mathbf{s}(t_{n+1}) = \mathbf{s}(t_n + \Delta t) \\ \zeta_n &= \zeta(t_n) \qquad & \zeta_{n+1} &= \zeta(t_{n+1}) = \zeta(t_n + \Delta t) \end{aligned} \tag{4.87}$$

The generalized trapezoidal rule provides an algorithm for obtaining $s_{ij\ n+1}$ and ζ_{n+1}.

$$\begin{aligned}\mathbf{s}_{n+1} &= \mathbf{s}_n + \Delta t\dot{\mathbf{s}}_{\ n+\alpha} = \mathbf{s}_n + \Delta t\left[\alpha\dot{\mathbf{s}}_{n+1} + (1-\alpha)\dot{\mathbf{s}}_n\right] \\ \zeta_{n+1} &= \zeta_n + \Delta t\dot{\zeta}_{n+\alpha} = \zeta_n + \Delta t\left[\alpha\dot{\zeta}_{n+1} + (1-\alpha)\dot{\zeta}_n\right]\end{aligned} \tag{4.88}$$

The forward Euler method is obtained with the choice $\alpha = 0$. The forward Euler method is an explicit integration method because it only uses information at the beginning of the step to compute the values at the end of the step. While extremely simple there is a time step size restriction that must be satisfied for the integration to be stable.

$$\begin{aligned}\mathbf{s}_{n+1} &= \mathbf{s}_n + \Delta t\dot{\mathbf{s}}_n \\ \zeta_{n+1} &= \zeta_n + \Delta t\dot{\zeta}_n\end{aligned} \tag{4.89}$$

The backward Euler method is obtained when $\alpha = 1$.

$$\begin{aligned}\mathbf{s}_{n+1} &= \mathbf{s}_n + \Delta t\dot{\mathbf{s}}_{n+1} \\ \zeta_{n+1} &= \zeta_n + \Delta t\dot{\zeta}_{n+1}\end{aligned} \tag{4.90}$$

The backward Euler method is always stable. Both of these schemes are first order accurate

4.3.3 MD Model Implementation

Traditionally the creep models included in the material libraries of the quasi-static finite element codes at SNL have used forward Euler integration. Sub-stepping is often needed when the global time step, chosen based on accuracy conditions, is larger than the time step required for stability. Frequently it is necessary to start a simulation with a small time step in order to accurately represent the primary creep behavior. An added benefit of using a small step size is that it often reduces the number of iterations the nonlinear conjugate gradient solver needs to satisfy equilibrium of the system.

Once the transient creep phase has passed it often becomes more efficient to use integration algorithms which are unconditionally stable. The approach used in this work is that whenever the global time step is smaller than the time step required for stability (Cormeau 1975) the forward Euler method is used, otherwise the backward Euler method is used. When the backward Euler method is used a system of two nonlinear equations must be solved. The reduction from 7 equations (6 stress components plus the evolution equation) is based on the ideas presented by Schreyer (2002).

Using the stress state at the beginning of the step we evaluate the critical time step Δt_{cr}. If the specified time step interval Δt is less than $A_{\Delta t} \cdot \Delta t_{cr}$ ($A_{\Delta t}$ is a user specified value $0 \le A_{\Delta t} \le 1$) the integration is performed explicitly; otherwise, the backward Euler integration method is used.

As stated earlier we know the stress tensor $\boldsymbol{\sigma}_n$ and state variable ζ_n at the beginning of the time step $t = t_n$. The strain rate tensor $\dot{\boldsymbol{\varepsilon}}$ and the time step Δt are given and the objective is to determine the stress tensor $\boldsymbol{\sigma}_{n+1}$ and state variable ζ_{n+1} at the end of the step.

In order to determine which flow potential is active we compute the Lode angle ψ corresponding to the stress state at the beginning of time step using Eqn. (4.64).

$$\psi = \frac{1}{3}\sin^{-1}\left[\frac{-3\sqrt{3}J_3}{2J_2^{3/2}}\right] \qquad -\frac{\pi}{6} \le \psi \le \frac{\pi}{6}$$

The closeness of the stress state $\boldsymbol{\sigma}_n$ to the corner region $\psi = \frac{\pi}{6}$ or $-\frac{\pi}{6}$ is then used to determine which flow potential will be used. If the stress state is within a user specified tolerance (e.g., θ = 0.1 degree) to the corner region the von Mises flow potential is used; otherwise, the Tresca flow potential will be used. Converting the Lode angle in radians ψ to Lode angle in degrees ψ^* this is represented by

$$\begin{aligned} &\left|\psi^*\right| < 30^0 - \theta \quad \text{use Tresca} \\ &\left|\psi^*\right| \ge 30^0 - \theta \quad \text{use von Mises} \end{aligned} \tag{4.91}$$

When the Tresca flow potential is active the integration takes place in deviatoric principal stress space. The principal directions of the gradient $\mathbf{g}^T$ are taken to be the same as the principal directions of the trial deviatoric stress (Borja et al. 2003). The advantage of performing the integration in principal stress space is the simplicity of computing the gradient and the necessary partial derivatives needed by the Newton Raphson algorithm. The draw back of operating in principal stress space is that the spectral decomposition (principal values and directions) of a 3x3 symmetric matrix needs to be computed.The principal directions $\mathbf{n}_A$ and principal deviatoric trial stresses $s^{tr}_{A\,n+1}$ are computed using a Jacobi iteration algorithm (Press et al. 1992). The Jacobi method has also been used in an implicit implementation of a three-invariant, isotropic-kinematic hardening cap plasticity model (Foster et al. 2005). There are other options for performing the spectral decomposition that may prove more efficient (e.g., Scherzinger and Dorhmann 2008) than the current method and they should be considered.

Whenever the backward Euler algorithm is used it possible that the Newton Raphson iteration will not converge. To avoid having the entire simulation abort it is highly recommended that the Adaptive Time Stepping with METHOD = MATERIAL be used with GROWTH FACTOR and CUTBACK FACTOR specified. Setting CUTBACK FACTOR to a number less than 1 allows Adagio to reduce the time step if the MD model fails to converge or the nonlinear conjugate gradient algorithm fails to meet the user specified tolerances for the equilibrium solution.

Another advantage of using the Adagio Adaptive Time Stepping option with the METHOD = MATERIAL is the MD model will evaluate the relative change in equivalent stress and equivalent creep strain over the current time step Δt and calculate what the next time step Δt_{n+1} should be. These two time steps are denoted Δt_σ and Δt_ε. The minimum of these two estimates is used to determine the value for the next time step Δt_{n+1}. Smaller values of ε_{tol} will result in smaller time steps. Setting ε_{tol} = 0.005-0.01 is generally sufficient.

$$\Delta t_\sigma = \varepsilon_{tol} \frac{\sigma_{eq\ n+1}}{\left|\sigma_{eq\ n+1} - \sigma_{eq\ n}\right|} \Delta t \qquad \Delta t_\varepsilon = \varepsilon_{tol} \frac{\varepsilon^c_{eq\ n+1}}{\left|\varepsilon^c_{eq\ n+1} - \varepsilon^c_{eq\ n}\right|} \Delta t$$
$$\Delta t_{n+1} = \min\left(\Delta t_{\sigma,} \Delta t_\varepsilon\right) \tag{4.92}$$

Introducing α_s and α_g as reduction and growth factors the time step computed based on relative changes in variables may be restricted according to

$$\begin{aligned} &\text{If } \Delta t_{n+1} < \alpha_s \Delta t \quad \text{then } \Delta t_{n+1} = \alpha_s \Delta t \\ &\text{If } \Delta t_{n+1} > \alpha_g \Delta t \quad \text{then } \Delta \mathrm{t}_{n+1} = \alpha_g \Delta t \end{aligned} \tag{4.93}$$

Experience with the MD model generally suggests using a small time step at the start of the run and letting the MD model compute the time step for the code rather than having the user specify the time step sizes. Both the MD model and the Adaptive time stepping option have input that controls the maximum growth and reduction of the time step from one step to the next.

The more stringent of two sets, Adagio's GROWTH FACTOR and CUTBACK FACTOR and the MD model's α_s, α_g, will be used if they are specified differently. In some cases the relative change in variables keeps driving the time step computed by the MD model lower and lower. Setting $\alpha_s = 1$ in the MD model input prevents this from happening but setting CUTBACK FACTOR < 1 allows Adagio to handle failure to converge issues.

In this implementation we have also added the option of using the von Mises flow potential exclusively. This is invoked by setting the MD model input parameter ITYPE = 1. The default is to use the Tresca flow potential or ITYPE = 0.

Table 4.3-1 lists the input required by the MD model. In addition two elastic constants are required. Generally for the MD model these are the shear modulus and the bulk modulus but other combinations are allowed.

Table 4.3-1. Inputs required by MD model.

Model Variable	Input Variable Name	Model Equation Reference
A_1	A1	(4.68)
Q_1/R	Q1/R	(4.68)and (4.70) R is the universal gas constant
n_1	N1	(4.68)
B_1	B1	(4.70)
A_2	A2	(4.69)
Q_2/R	Q2/R	(4.69)and (4.70)
n_2	N2	(4.69)
B_2	B2	(4.70)
σ_o	SIG0	(4.71)
q	QLC	(4.70)
m	M	(4.74)
k_o	K0	(4.74)
c	C	(4.74)
α	ALPHA	(4.76)
β	BETA	(4.76)
δ	DELTALC	(4.77)
$A_{\Delta t}$	AMULT	Multiplier on computed critical time step to determine when to switch from explicit to implicit integration
ε_{tol}	EPSTOL	(4.92)
α_g	GRWFAC	(4.93)
α_s	SHKFAC	(4.93)
θ	ANGLE	(4.91) input in degrees
-	ITYPE	ITYPE = 0 use Tresca ITYPE = 1 use von Mises

4.3.4 MD Model Application

One example illustrating the use of the new MD Creep model implementation has been described in Stone et al. (2010). This work examined the behavior of storage rooms in a generic salt repository for two different constitutive representations of the salt. A staggered-in-time scheme with the thermal analysis leading the geomechanical analysis was used. In this method, the thermal analysis moves forward a thermal time step, without any update from the geomechanics code. Once the thermal time step has been completed, temperatures are passed back to the geomechanics code and a quasistatic solution is obtained for the same time interval. Updated

nodal displacements are then passed back to the thermal analysis code for use in updating the geometry for the next time step. Ninety-six processors were used in all simulations.

Figure 4-3.1 illustrates the region represented in the model. The region labeled canister represents the heat generating source, the green region is a simulated backfill and the remainder is salt. Points A and B are used to record the convergence of the alcove and access tunnel as the salt creeps inward.

The MD Creep model and the standard power law creep (PLC) model were both used to compare the rate of storage room closure. Through appropriate selection of input it is possible to reduce the MD Creep equations to those of the standard power law creep model. This allows for a comparison of the two different numerical implementations since the MD Creep model uses combined explicit/implicit integration and the standard power law creep model uses explicit integration exclusively.

The storage room closure is driven by the elevated temperatures generated by the heat producing waste. Figure 4-3.2 shows the temperature history computed at the center of the canister and the mid-wall location. The calculations showed that the use of the MD Creep model results in a faster rate of room closure compared to the PLC model (Figure 4-3.3). This is due to the inclusion of primary creep in the formulation in the MD Creep model while the PLC model only represents secondary or steady-state creep.

In general, the full MD Creep model requires significantly more computational effort than the MD model with parameters adjusted to simulate the PLC model. A surprising result was the increase in simulation time associated with the standard PLC model when compared to the simulation time using the MD with PLC-only parameters. This result (96 hours for PLC compared to 32 hours for MD reduced to PLC) suggests that the adaptive integration scheme used in the MD model should also be applied to the standard PLC model. The analysis effort is also dominated by the cost associated with the contact algorithm for the deforming alcove and access tunnel surfaces (Figures 4-3.4 and 4-3.5). It should be noted that the deformation of the repository is quite complex and the use of a robust, large deformation, contact algorithm is necessary. If the determination of repository response to complete drift closure is required then the increased cost of the analysis requiring the contact algorithm should be expected.

Additional information regarding the simulations can be found in the paper by Stone et al. (2010).

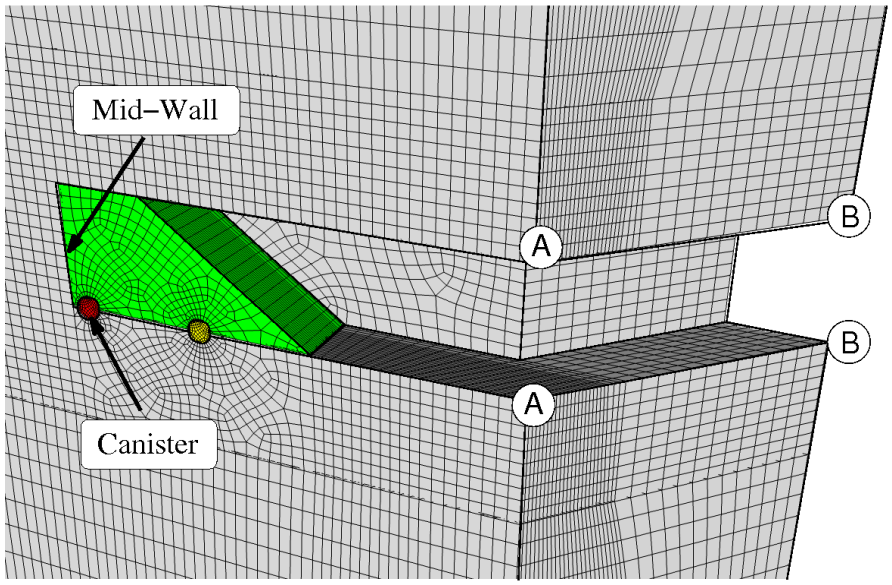

Figure 4.3-1. Schematic showing the location of points at the alcove and access tunnel corners where closure and temperature is being reported.

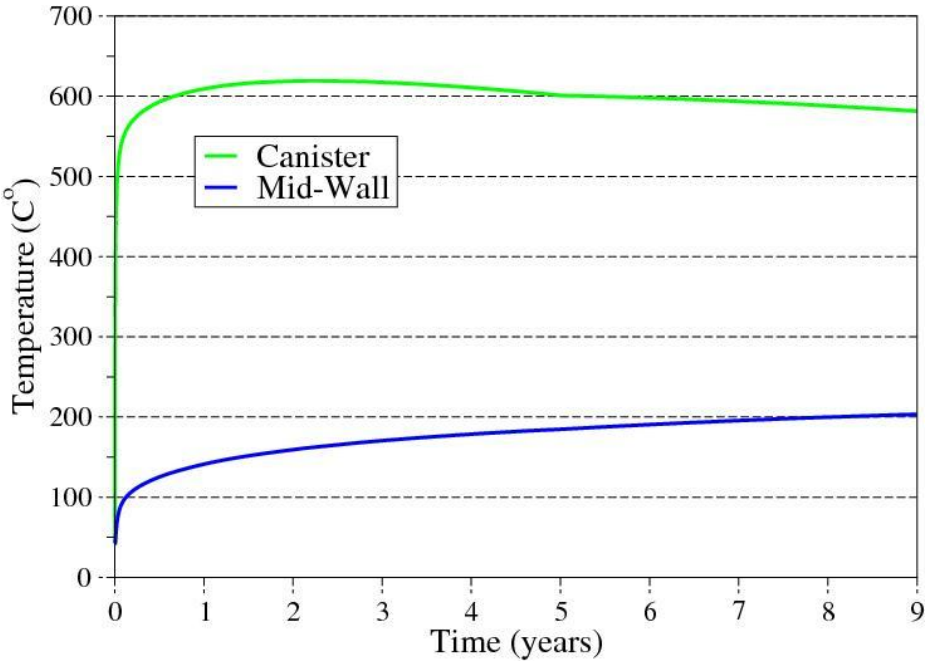

Figure 4.3-2. Temperature histories at the canister centerline and at the mid-wall location.

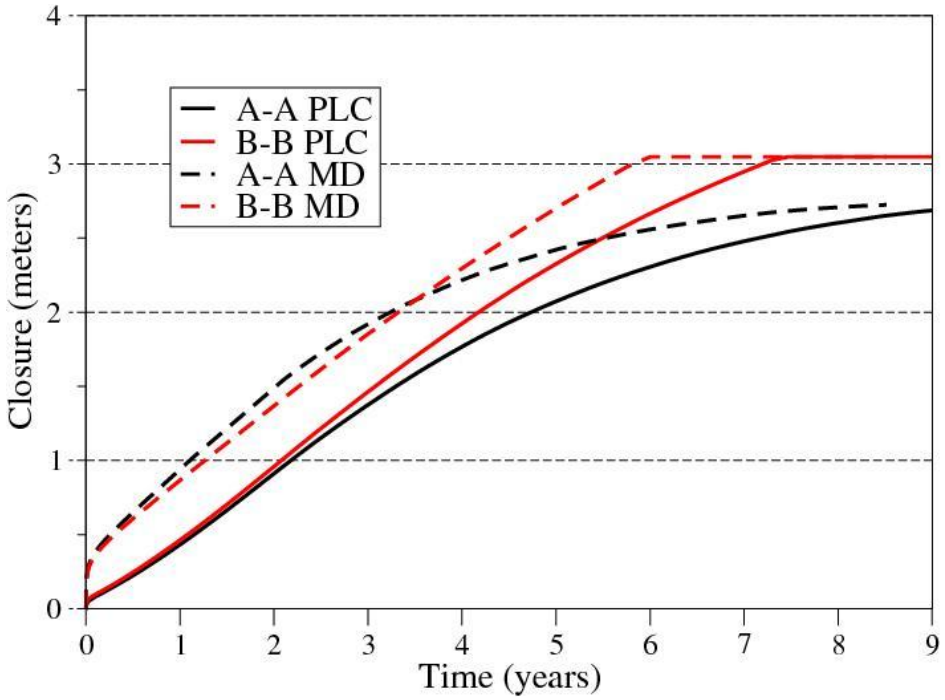

Figure 4.3-3. Closure histories for the analysis comparing the MD and PLC models

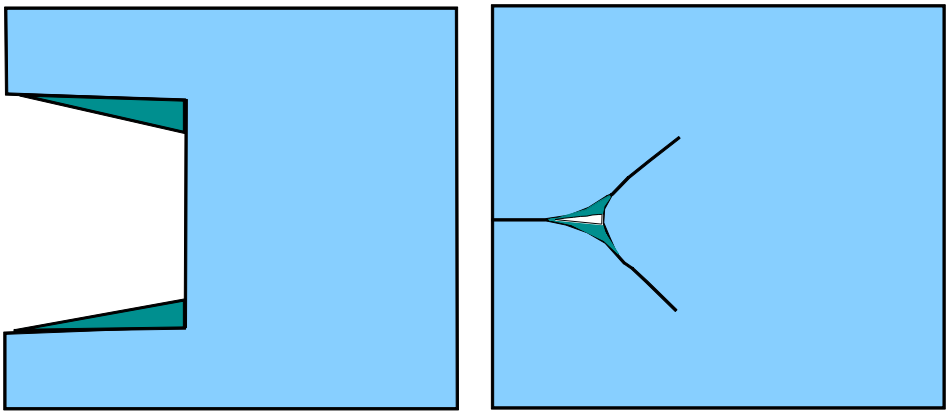

Figure 4.3-4. Undeformed and deformed views of the access tunnel looking from the back of the model toward the alcove–access tunnel intersection.

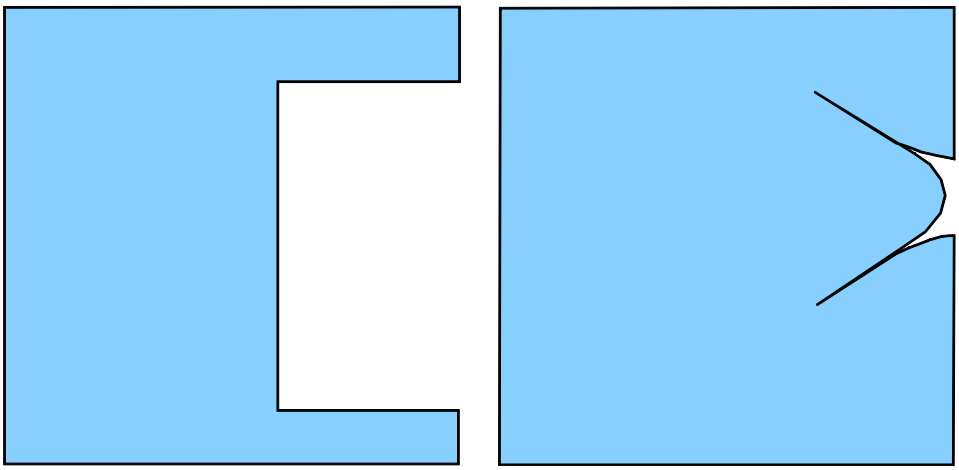

Figure 4.3-5. Undeformed and deformed views of the access tunnel–alcove intersection looking down the access tunnel toward the back of the model.

Another example of the use of this model has been described in Sobolik et al. (2010). This study involved predictions of the geomechanical behavior at the West Hackberry Strategic Petroleum Reserve site. They also compared an early implementation of the MD Creep and PLC models in JAS3D (Blanford et al. 2001) and concluded that the calculations using the MD Creep model produced predictions of geomechanical behavior that more closely matched field measurements than those that used the PLC model; however, in their application the MD model was approximately four times slower than the PLC model. Perhaps future Stategic Petroleum Reserve simulations will be performed using the Sierra codes and we will be able to further improve the performance of the MD Creep model for those types of problems.

5. Multiphysics Coupling

5.1 Introduction

Early in its development, the Sierra software system was designed to facilitate multiphysics coupling between member physics modules. In this chapter we will focus on coupling of fluid flow physics, energy transport, reactive species transport, and geomechanics. Developments under this project for each of these individual physics modules were discussed in the foregoing chapters. Multiphysics coupling of these modules was a focus for this project, enabling the goal of developing a so-called THMC (Thermal-Hydrologic-Mechanical-Chemical) numerical simulation platform. Some applications of current interest to SNL include geologic sequestration of anthropogenic CO_2, gas generation in rapid thermal decomposition of porous high explosive, encapsulant foams and ablative materials, and modeling electrochemistry-induced swelling of fluid-filled porous electrodes for the design of thermal batteries. In the following we will discuss the techniques developed to enable THMC for geosystems, and chapter 8 includes examples of the application of multiphysics coupling.

5.2 Solving Multiphysics Problems

5.2.1 Considerations for Coupling Multiphysics Problems

There are various strategies and trade-offs for solving multiphysics problems. One may consider a spectrum of strategies from fully coupled to very loosely coupled methods. Each has advantages and disadvantages.

For the fully coupled method, wherein the full system of discrete equations is solved simultaneously in one large matrix problem, one may include the following trade-offs:

- Provides a consistent solution
- Known convergence properties
- Expensive to solve
- Requires compatible algorithms among physics

Another technique is the use of segregated methods, in which various subsets of the full system of equations are solved in sequence. This method can be implemented with various levels of "tight" to "loose" coupling. Some properties of segregated methods include:

- Can be efficient to solve (smaller, well-conditioned matrices)
- Allows separate meshes, time steps, discretizations
- Best de-coupling strategy may be unknown
- May be more expensive in the long run

Since the Sierra platform includes very diverse physics modules, using a diverse set of numerical methods particular to the type of physics being modeled, the segregated method has been developed for coupling multiphysics problems. This technique is flexible as it allows loose to tight coupling methods to be applied. For time-dependent problems, a loosely coupled approach could mean solving, for example, fluid flow and geomechanics with coupling fields "frozen" within the time steps, and only updating these fields between physics modules at the end of the

timestep. A more tightly coupled approach would iterate the two systems of equations to a user-specified tolerance within the time step. With proper control of error norms, this technique can be made to produce the same solution as the fully coupled approach, albeit perhaps requiring a significant amount of subcycling. However, the degree of coupling can be controlled by the user via user-defined logic which can be specified entirely through the input command file.

5.2.2 Building Blocks for Coupled Equations

In Sierra, a region (`REGION`) is abstractly defined as a mesh (grid) and a set of fields (e.g., pressure, temperature, concentration), and perhaps constraints. For concreteness, we will continue the discussion in terms of the porous flow physics in Sierra/Aria and the geomechanics in Sierra/Adagio. Each of these Sierra modules is a stand-alone code that solves its partial differential equations (PDEs) in a single matrix. Sierra/Aria for example generally accomplishes this using Newton iteration with either analytical, or numerical (via finite difference approximation) Jacobian, or using the NOX solver in the Trilinos package (Heroux et al. 2005).

Multiple regions can be coupled in one simulation via transfers (`TRANSFER`). A transfer copies or interpolates data between regions, either the entire mesh or between selected element blocks, or sidesets/nodesets. Each region can specify its own discretization, both in terms of its mesh and the order of interpolants for the solution variables in the PDEs being solved in the region. Fields may be copied when the two regions are using the same mesh and when the field has the same interpolation representation in the two regions, e.g., node variable in both region or element variable in both regions. Otherwise, fields can be interpolated between different meshes and converted between interpolant types (e.g., fluid pressure can be a node variable in Sierra/Aria and an element variable in Sierra/Adagio).

5.2.3 Various Levels of Coupling

The sequencing of the transfers described above is user-defined and can include user-defined logical conditionals. These two capabilities allow a variety of levels of coupling between the regions. The input file specification in Sierra codes includes a `PROCEDURE` block in which the user defines the solution control instructions. These include the sequence of solves and transfers of multiphysics modules being coupled.

The schematic in Figure 5.2-1 illustrates some options for levels of iteration and convergence within the segregated strategy in a fluid flow and mechanics multiphysics problem. To facilitate coupling with disparate flow and mechanics time scales, the coupling strategy allows for different time steps in the flow solve compared to the mechanics solve. This is illustrated by a conditional on whether to perform the mechanics solve within this time step. If time steps are synchronized, the controller allows intra-time-step iterations. The coupling may be dynamically controlled by monitoring a norm measuring the degree of variation in the deformed porosity, thereby controlling the frequency of mechanics solves compared to flow solves. These various levels of coupling can be defined by user input.

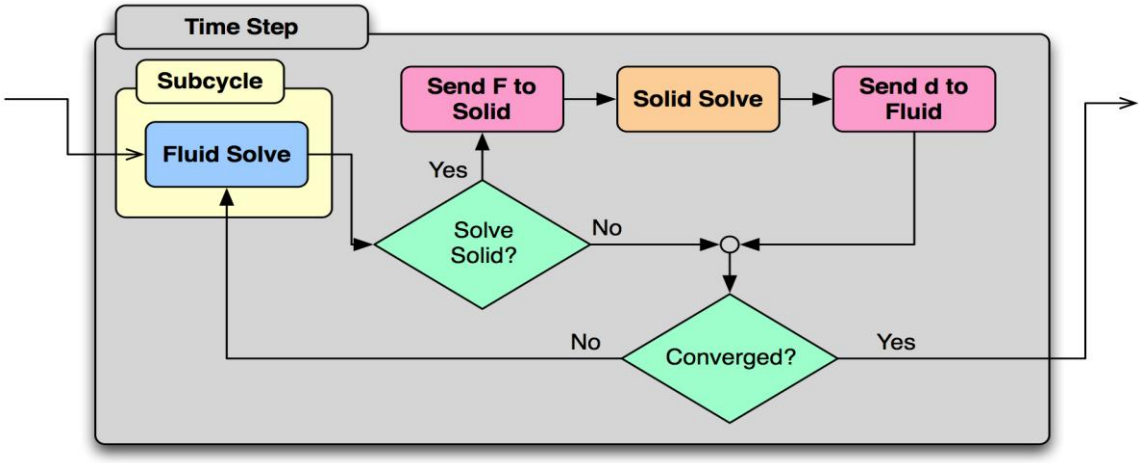

Figure 5.2-1. Options for solution control.

The schematic also illustrates "subcycling" within the fluid solve itself. For example, if the fluid solve involves multiphase porous flow and reactive transport, these two sets of equations could be segregated and solved to convergence within Sierra/Aria itself. This control logic will be used to implement operator splitting in chemically reactive flow and transport problems solved with Sierra/Aria. Here the algorithm involves splitting the advective/diffusive processes from chemical reactions, to deal with disparate time scales.

5.3 Multiphysics Coupling for THMC

Flow through deformable porous materials is coupled to solid mechanics by virtue of Terzaghi's principle of effective stress, wherein stresses in porous materials are borne by both pore pressure and the stress field in the solid skeleton. Here we discuss our Sierra implementation for coupling of nonisothermal multiphase, multicomponent porous flow capability in Sierra/Aria with the geomechanics capability in Sierra/Adagio. The geomechanics is coupled to the flow via the variation in the fluid pore pressures, whereas the flow problem is coupled to mechanics by the concomitant material strains which alter the pore volume (porosity field) and hence the permeability field.

5.3.1 Coupling Geomechanics and Flow in Porous Media

Treatments of coupled deformation and flow in porous materials begin with the works of von Terzaghi (1943) and Biot (1941) on consolidation. These papers introduce the important concept of effective stress in saturated porous media for describing the "settlements of soils under load." In a more recent paper, Schrefler and Scotta (2001) define the mixture fluid pressure for an air and water system as $p = S_w p_w + S_a p_a$, which is used in the effective stress principle, augmented by the volumetric deformation of solid particles (Biot and Willis 1957),

$$\boldsymbol{\sigma}^{eff} = \boldsymbol{\sigma} + \alpha \mathbf{I}\, p \tag{5.1}$$

to couple the fluid pressures with the deformation mechanics; α is a material parameter, usually referred to as the Biot effective stress parameter. All constitutive models in Sierra/Adagio are based on the effective stress. Chapter 4 presents more details on the treatment of the effective stress model for multiphase systems.

Owing to the dynamic deformation of the porous skeleton, our formulation is naturally in terms of a moving (accelerating) coordinate system. Much existing work in coupling flow and geomechanics resorts to small deformation theory, such that material deformation can be assumed negligible. For example, see the review by Rutqvist et al. (2001). In contrast, in this work both flow and mechanics implementations allow for large deformation and both compute solutions on dynamically deforming grid. The coupling of porosity and mechanical deformation can be generally defined from kinematics in terms of the mechanical deformation gradient ($\mathbf{F}$),

$$\frac{1-\phi_0}{1-\phi} = \det \mathbf{F} \tag{5.2}$$

where ϕ_0 refers to the porosity in the reference configuration. This formula attributes deformation of the porous body to change in porosity, assuming the solid material is much more rigid than the pores. The deformation gradient is computed in Sierra/Aria, using the transferred displacement field computed in Sierra/Adagio. In addition to the displacement field, other measures of deformation and/or damage can also be transferred for use in Aria. For example, variations in permeability based on a model of damage, which could itself be based on say critical shear, can be modeled in this way.

To facilitate coupling with disparate flow and mechanics time scales, the coupling strategy implemented in Sierra/Arpeggio allows for different time steps in the flow solve compared to the mechanics solve. If time steps are synchronized, the controller allows intra-time-step iterations. In cases where the time scale for deformation is long compared to the flow time scale, the coupling is dynamically controlled by monitoring a norm measuring the degree of variation in the deformed porosity approximated in Sierra/Aria, thereby controlling the frequency of mechanics solves compared to flow solves, or vice versa. To measure the degree of deformation from a prior synchronization time, a model for the porosity variation during the intervening time for the flow simulation is defined by the `Rock_Deformable` porosity model defined in chapter 2, repeated here in the form,

$$\phi = \phi_n \left[1 + C_r \left(p - p_n \right) \right].$$

The subscript *n* denotes the porosity and pressure fields corresponding at the last synchronization time. The user may define a tolerance $\left\| \phi - \phi_n \right\| > \varepsilon_\phi$ to trigger a synchronization procedure wherein the modules transfer fields in order to reset the reference fields in the porosity model. This introduces a jump in porosity in Sierra/Aria and a jump in pore pressure in Sierra/Adagio, the magnitude of which is controlled by the tolerance on estimated porosity variation.

This is but one error measure that can be conceived. Other error norms can be defined as appropriate for the problem at hand. For example, if the mechanics time scale is fast compared to flow, then a different error norm, measuring pore pressure variations would be more appropriate.

5.4 Verification: Dynamically Coupled Flow and Mechanics

In this verification problem we consider the subsidence of a reservoir resulting from extraction of fluid via a centrally located well. Geomechanics is coupled to flow via the variation in the fluid pore pressures, whereas the flow problem is coupled to mechanics by the concomitant material strains which alter the pore volume (porosity field) and hence the permeability field. The implementation for multiphysics coupling was verified by comparing the solution to subsidence "problem 1" discussed by Dean et al. (SPE-79709, 2003), as depicted in Figure 5.4-1 below. The figure shows the effects of the level of coupling the porosity to the flow problem. In the solution marked "uncoupled" porosity, the porosity variation in the flow problem is not transferred from the mechanics solution; it is approximated with a constant value of matrix compressibility (see Eqn. (2.7)) in the flow simulation (however, the displacements are transferred and the flow mesh allowed to deform.). In the solution marked "coupled" porosity, the displacements are transferred to the flow problem and the change in porosity is mapped from the deformation gradient as described in the previous section. The comparison shows the uncoupled porosity to ultimately lead to significant error in the subsidence over the well, whereas the fully coupled solution agrees with Dean et al.

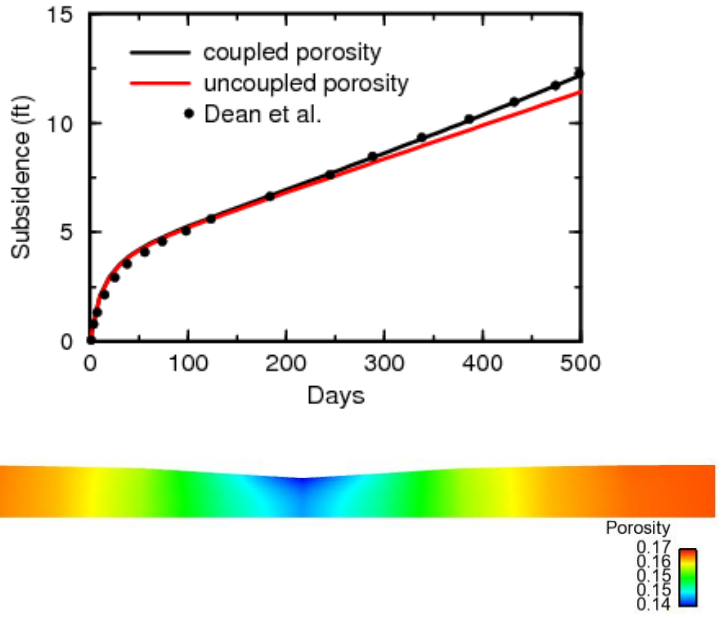

Figure 5.4-1. Comparison of the time history of subsidence due to production in a porous layer, under two levels of geomechanics/flow coupling, with the solution of Dean et al. (2003). Also shown is the final porosity distribution and (exaggerated) subsidence on a cross section through the layer.

6. Thermodynamics

6.1 Introduction and Summary

The thermodynamic behavior of CO_2-H_2O fluids and their mixtures is of fundamental importance to the quantitative description of fluid/rock interactions in geologic environments. For example, it is known that aqueous fluids in porous rock can have significant concentrations of CO_2 and NaCl and their interactions with co-existing host minerals are important to reactive transport scenarios assessing the fate of greenhouse gases in geologic storage/disposal, mineral stability in diagenetic and hydrothermal systems, and the formation of economic ore deposits.

In this study, we are focused on the non-ideal behavior of CO_2-H_2O-NaCl fluid mixtures primarily at temperatures below 100°C and at pressures ranging from ambient to 600 bars. These pressure-temperature (P-T*)* conditions are relevant to CO_2 sequestration where this phase is injected into aquifers within porous geologic formations reaching supercritical conditions at depth (Spycher, Pruess et al. 2003). In order to quantitatively characterize and predict the fate of CO_2 and its interaction with aqueous and solid phases in geologic media, it is crucial to accurately calculate the pressure-temperature-composition (P-T-X*)* properties of CO_2-H_2O-NaCl co-existing mixtures. This is achieved in this study using equations of state (EoS) formulations and the thermodynamic formulations implemented in the computational tool Cantera (Moffat and Goodwin 2011). The main problem with the thermodynamic and volumetric properties of CO_2-H_2O mixtures is to obtain an accurate description of these across their multiphase and compositional domains for the pressure and temperature range of interest (Spycher, Pruess et al. 2003; Duan, Hu et al. 2008; Mao and Duan 2008). This problem becomes exacerbated when additional components such as NaCl, among others, are also part of the fluid mixture. EoS expressions have been developed for a number of years to accurately capture the thermodynamic and volumetric properties of pure fluid phases and to a fair extent their mixtures (Spycher, Pruess et al. 2003; Duan, Hu et al. 2008; Mao and Duan 2008; Akinfiev and Diamond 2010). Given the strong reliance of bounding EoS parameters to existing data, sometimes there are extrapolation issues within the P-T-X domain and in some cases discrepancies between different EoS formulations could give rise to consistency problems.

In this work, we will limit our fluid solubility calculations to temperatures below 100°C but pressures up to 600 bars following the approach of Spycher et al. (2003). The following sections will provide descriptions on the calculation of thermodynamic and volumetric properties of CO_2-H_2O-NaCl fluids and their EoS implementation and usage in Cantera to calculate solubility relations in this system. Some of the EoS used in this work is already implemented in Cantera but is combined with others to obtain the necessary parameter values demonstrating the flexibility of Cantera for model implementation and development. A detailed description of the Spycher et al. (2003) implementation in the form of a thermodynamic class object into Cantera is given to make this approach more general within the object-oriented platform of the Cantera code suite.

Although Cantera is linked into the Sierra software suite as a third-party library, the preferred method of utilizing thermodynamics functions in the flow module is through the use of (adaptive) tables, which is discussed in section 6.6. The direct linking of Cantera to dynamically

compute thermodynamics data would be computationally expensive. However, this linked approach will be investigated in future work for certain coupled flow and chemistry problems.

6.2 Cantera Computational Tool

Cantera is a general purpose, object-oriented, constitutive modeling package distributed as an open source application developed by Professor David G. Goodwin from the applied physics department at Caltech. The code suite is hosted on sourcefource.net and Google Code. The multicomponent real fluid modules described here have been copyrighted by SNL/DOE for open source distribution and have been added to the Google Code Cantera distribution site. Cantera has been developed with interfaces to C++, FORTRAN, Python, and Matlab. Its origins lie in modeling combustion systems and chemical vapor deposition processes [(Goodwin and Aivazis 1999; Goodwin 2003; Moffat and Goodwin 2011). However, its use and application has been extended to solid oxide fuel cell (SOFC) modeling (Hao and Goodwin 2007), battery modeling (Colclasure and Kee 2010), and the modeling of soot formation (Moffat 2007). Of direct benefit to this project, Cantera has been extended to model the liquid thermodynamic properties of brines by the addition of a Pitzer molality-based approach (Moffat and Colon 2009). Essentially, the basic thermodynamic principles to compute fluid-solid equilibria from the EQ3/6 code (Wolery and Jarek 2003) developed by Dr. Thomas J. Wolery of Lawrence Livermore National Laboratory, has been incorporated into Cantera. Cantera also has the capability to compute multiphase chemical equilibrium between solids, aqueous species, and gases. Incorporating the thermodynamic databases developed for EQ3/6 as part of the Yucca Mountain Project including the Pitzer database (2007), Cantera has inherited an extensive and validated capability to model the thermodynamics of brine systems, including dissolved gases within the brines (i.e., CO_2) and their geochemical interactions with mineral systems. It should be noted that Cantera has the flexibility of accepting inputs from various comprehensive thermodynamic database sources for solids and fluids. This allows Cantera to be a powerful testing tool for models and data given the continuous expansion and refinements typical of thermodynamic database development.

We have extended Cantera to include a multicomponent real EoS capability. Previously, Cantera had several models for pure real fluids. That is, a fluid that could be a gas or a liquid and has a critical point. Models of this sort are based on the Helmholtz free energy formulation. However, previously these models have been limited to single species gases and liquids. The CO_2-H_2O is a binary system and, therefore, Cantera needed to be expanded to include the possibility of H_2O being present in the $CO_{2(g)}$ and $CO_{2(liq)}$ phases. We chose our initial implementation to be the multicomponent Redlich-Kwong (R-K) equation system; Prausnitz et al. has an extensive discussion of this system of equations (Prausnitz, Lichtenthaler et al. 1986). This system also has been applied to the CO_2-H_2O system by Spycher et al. (2003) and essentially implemented within Cantera to calculate CO_2 solubility.

6.3 Thermodynamic Properties

6.3.1 Equation of State

There is a myriad of EoS formulations to calculate the pressure-volume-temperature (P-V-T) properties of fluids and a good discussion of these and their uses is given by Prausnitz et al. (1998). The thermodynamic properties of CO_2, H_2O, and NaCl as pure single phase fluids are implemented in Cantera in the form of EoS and their associated parameters. For example, the

thermodynamic properties computed for CO_2 are implemented in Cantera through the EoS given by Reynolds (1979). As a test, the fugacity coefficient of pure CO_2 is computed as a function of pressure and temperature. The results are presented in Figure 6-3.1 in the form isotherms as a function of pressure. The obtained values are in excellent agreement to those given by the tabulations of Angus et al. (1976) and those reported in Spycher et al. (Spycher, Pruess et al. 2003).

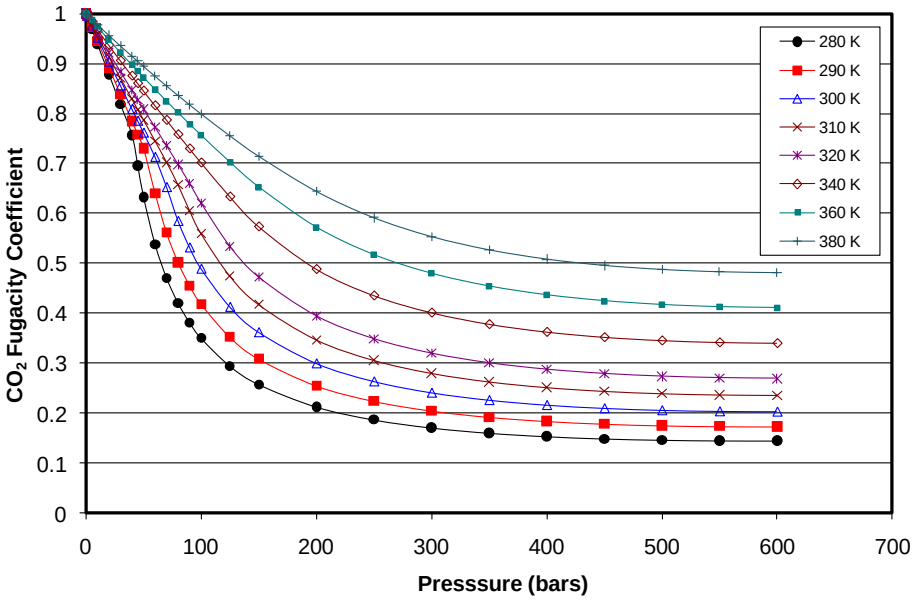

Figure 6.3-1. Plot of pure phase CO_2 fugacity coefficients using the EoS by Reynolds (1979) implemented in Cantera.

Accurate representation of fugacity coefficients is important in this case to capture their behavior as a function of pressure and temperature when use in combination with other thermodynamic approaches to calculate CO_2 solubilities in the solution phase.

Volumetric properties of the pure CO_2, H_2O, and NaCl phases are also important for the calculation of mixed fluid properties at the conditions of interest in this study. The EoS for pure CO_2 and H_2O implemented in Cantera are used in this study. For NaCl solutions, there are a couple of options in Cantera: the HKFT EoS for ions and the Pitzer approach. The HKFT (Helgeson-Kirkham-Flowers-Tanger; see (Moffat and Jove Colon 2009)) EoS is implemented through the `HMWSoln` thermodynamics object and works well with dilute solutions up to molalities of ~1 molal. The Pitzer formulation relates the excess Gibbs energy of the electrolyte to volume through its derivative with respect to pressure:

$$V^{EX} = \left(\frac{\partial G^{EX}}{\partial P} \right)_T \tag{6.1}$$

where G^{EX} is the excess Gibbs molal free energy computed from the Pitzer equations, V^{EX} corresponds to the excess volume, and P stands for the pressure (Rogers and Pitzer 1982; Krumgalz et al. 2000; Peiper et al. 1984). The desired volumetric properties of the NaCl

electrolyte mixture (i.e., NaCl and H_2O) can be obtained such as the density of the solution mixture:

$$\rho_{NaCl} = \frac{1000 + mM_{w_{NaCl}}}{(1000/\rho_{H_2O}) + mV^{\phi}_{NaCl}} \tag{6.2}$$

where m is the NaCl(aq) or electrolyte concentration in molality units, $M_{w_{NaCl}}$ refers to the molecular weight of the solute or NaCl (58.4428 g/mol), ρ_{H_2O} represents the H_2O density, and V^{ϕ}_{NaCl} denotes the apparent molal volume of the NaCl solute. The latter is obtained from the Pitzer formulations by:

$$mV^{\phi}_{NaCl} = m\bar{V}^{\circ}_{NaCl} + \left(\frac{\partial G^{EX}}{\partial P}\right)_T = m\bar{V}^{\circ}_{NaCl} + V^{EX} \tag{6.3}$$

where $\bar{V}^{\circ}_{NaCl}$ delineates the standard partial molar volume of NaCl(aq) at infinite dilution, and V^{EX} corresponds to the excess volume computed from the Pitzer equations. Unfortunately, the Pitzer parameterization in Cantera is solely expressed as a function of temperature and the pressure effects are mainly captured by $\bar{V}^{\circ}_{NaCl}$ which can be readily obtained from the Cantera EoS implementation for standard thermodynamic properties of ions. To implement the Pitzer relations by the derivative given by Eqn. (6.1), a required set of volumetric Pitzer parameters for a given electrolyte need to be specified. Such implementation is feasible given the flexibility in Cantera thermodynamic class objects to incorporate these changes (see Moffat and Colon (2009)) for a description of such implementation).

It should be noted, however, that the effects of pressure on the thermodynamic properties of electrolyte mixtures are known to be much less pronounced than those of temperature. Moreover, the amount of experimental volumetric data needed with sufficient level of accuracy for the parameterization in the Pitzer formulation at a given range of pressures and temperatures is scarce and limited to relatively few electrolytes. Figure 6-3.2 shows the prediction of solution densities as a function of molality concentration and pressure. Notice the good agreement at 1 molal NaCl concentration between the Cantera predictions and the comprehensive data tabulations of Pitzer et al. (1984). However, there is a clear discrepancy, although small, at 5 molal NaCl concentration. This discrepancy is expected for the aforementioned reasons and the calculation results are just shown for comparison. Even when the density predictions at 5 molal follow the proper trend given by the data tabulation, the slight shift in the curve toward larger values (approximately 2-3%) demonstrates the need to account for ion interactions close to the salt solubility. Nevertheless, as already noted, the discrepancies are small and these are even lower NaCl concentrations (~0.5 – ~3 molal) common to deep-seated aquifers.

A more recent EoS considered in the calculation of volumetric properties of H_2O-CO_2-NaCl fluid mixtures are those advanced by Duan et al. (2008), and Mao and Duan (2008). This approach is also based on the use Pitzer formulations for the computation of volumetric properties of electrolytes (as explained above) where the EoS fitting parameters were obtained using a comprehensive set of data for this system. The EoS formulations advanced by these authors were implemented in Cantera but not as part of the Pitzer implementation within a thermodynamic class object as will be described later. The implementation was coded in

separately and is specific to H_2O-CO_2-NaCl fluids as advanced by the authors. Such implementation makes use of the Cantera native EoS and the thermodynamic class objects to retrieve the standard thermodynamic properties of these phases and related parameter data. This EoS implementation provides for a better description of the volumetric properties of fluid mixtures for this system and also allows for great flexibility to implement and combine complex models to accurately describe fluid properties. The implementation and reported parameter data were tested at various pressures, temperatures, and phase composition producing results in good agreement with the reported data. Figure 6-3.2 shows the excellent agreement between the NaCl(aq) solution densities computed using the EoS by Mao and Duan (2008) and those reported by Pitzer et al. (1984). It should be noted that Akinfiev and Diamond (2010) use a similar approach where NaCl(aq) apparent molar volumes are corrected using the Pitzer approach. Density calculations using this EoS for 1 molal NaCl(aq) essentially overlap with those given by Pitzer et al. (1984) and are omitted from the figure for clarity.

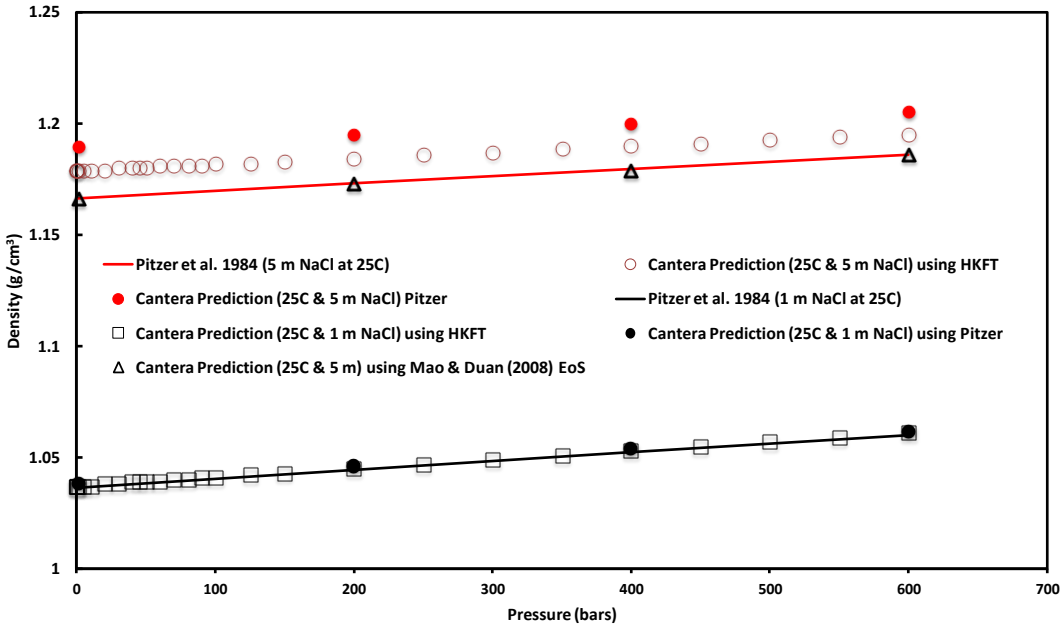

Figure 6.3-2. Plot of NaCl(aq) densities at 25°C as a function of pressure and salt concentration. Notice the excellent agreement between the Cantera predictions using the EoS by Mao and Duan (2008) and the comprehensive tabulations of Pitzer et al. (1984). Cantera Pitzer calculations are shown for comparison (see text).

The solubility relations of the H_2O-CO_2-NaCl system are implemented using the approach of Spycher et al. (2003). One form of the implementation is done through the use of the appropriate equations given by the authors using some of the EoS native to Cantera. The other form is implemented within the `ThermoPhase` class object in Cantera and will be described in a later section. The implementation described here is more specific (as the one for the fluid volumetric properties) but it is straightforward and takes advantage of other EoS and class objects within Cantera.

6.3.2 Model Description

Spycher et al. (2003) describes the solubility of CO_2 in fluids by using thermodynamic formulations in the form of mutual solubilities between liquids and gases. That is, the equilibrium solubility of CO_2 and H_2O between the gas and the liquid phase can be expressed by mass action laws as follows:

$$CO_{2(aq)} = CO_{2(g)} \tag{6.4}$$

$$H_2O_{(liq)} = H_2O_{(g)} \tag{6.5}$$

The equilibria given by these two reactions can be described through the following thermodynamic relations:

$$\begin{aligned} \Delta G^{\circ}_{rxn,CO_{2(aq)}} &= -RT\ \ln K_{CO_2} = -RT\ \mathrm{Ln}(f_{CO_{2(g)}} / a_{CO_{2(aq)}}) \\ K_{CO_2} &= f_{CO_{2(g)}} / a_{CO_{2(aq)}} \end{aligned} \tag{6.6}$$

$$\begin{aligned} \Delta G^{\circ}_{rxn,H_2O} &= -RT\ \ln K_{H_2O} = -RT\ Ln(f_{H_2O_{(g)}} / a_{H_2O_{(liq)}}) \\ K_{H_2O} &= f_{H_2O_{(g)}} / a_{H_2O_{(liq)}} \end{aligned} \tag{6.7}$$

The equilibrium constant K_i changes with pressure and temperature. The expression for K_i that accounts for pressure corrections is given by Prausnitz et al. (1998):

$$\exp\left(\frac{(P - \mathrm{P}^{\circ}_{ref})\bar{V}_i}{RT}\right) \tag{6.8}$$

where K°_i is the equilibrium constant at the absolute temperature T at the reference pressure of P°_{ref} (1 bar). $\bar{V}_i$ is the standard partial molal volume at T and R is the gas constant. The exponential term corresponds to the "Poynting" correction for pressure on the Gibbs energies of the reaction as described by Prausnitz et al. (1998). Equation (6.8) can be related to the expression for fugacities (f_i) by Prausnitz et al. (1998):

$$f_i = \phi_i y_i P \tag{6.9}$$

where ϕ_i stands for the fugacity coefficient, y_i refers to the mole fraction of the phase, and P is the total pressure of the system. Combination of Eqns. (6.4), (6.5), and (6.7) result in the needed expression that relates fugacities with thermodynamic constants and these can be recasted as follows—after Spycher et al. (2003):

$$f_{H_2O} = \phi_{H_2O(g)} y_{H_2O(g)} P_T = K_{H_2O} a_{H_2O} \tag{6.10}$$

$$f_{CO_2} = \phi_{CO_2(g)} y_{CO_2(g)} P_T = K_{CO_2(g)} a_{CO_2(aq)} \tag{6.11}$$

The equation for $y_{H_2O(g)}$, for example, can be obtained by combining Eqns. (6.6) and (6.8) and some term rearrangement to yield:

$$y_{H_2O} = \frac{K^{\circ}_{H_2O(T,P^{\circ}_{ref})}}{\phi_{H_2O(g)} P_T} a_{H_2O} \exp\left(\frac{(P - P^{\circ}_{ref}) \bar{V}_{H_2O(l)}}{RT} \right) \tag{6.12}$$

The value for a_{H_2O} is taken as unity given the relatively low solubility at the considered pressure and temperature conditions. In cases where NaCl(aq) or dissolved $CO_{2(aq)}$ are present in large amounts, activity coefficient models such as Pitzer need to be considered to account for H_2O activities deviating from unity. This will be discussed later for the computation of $CO_{2(aq)}$ in the liquid phase. The values for $K^{\circ}_{H_2O(T,P^{\circ}_{ref})}$ as a function of temperature (and 1 bar) are computed from the native EoS for pure gases and aqueous species in Cantera from their Gibbs energies of reaction of the mass action law expression. Similarly, values for $\bar{V}_{H_2O(l)}$ as a function of temperature were also obtained from the EoS implementation in Cantera. Values for $\phi_{H_2O(g)}$ are derived from the R-K EoS expression given by Spycher et al. (2003), which is described in a later section but is also given here for completeness:

$$\begin{aligned} \ln \phi_i = & -\ln \frac{PV}{RT} + \ln\left(\frac{V}{V - b_{mix}} \right) + \frac{b_i}{V - b_{mix}} \\ & - \frac{2\sum a_{ij} y_i}{RT b_{mix} \sqrt{T}} \ln\left[\frac{V + b_{mix}}{V} \right] + \frac{a_{mix} b_i}{RT b_{mix}^2 \sqrt{T}} \ln\left[\frac{V + b_{mix}}{V} \right] - \frac{a_{mix}}{RT b_{mix} \sqrt{T}} \left(\frac{b_i}{V + b_{mix}} \right) \end{aligned}$$

where a_{mix}, b_{mix}, and b_i are interaction parameters specific to a given mixture, in this case a CO_2-H_2O fluid. The implementation of Spycher et al. (2003) reduces the expansion form of these terms for this binary system through the adoption of key assumptions on the solubility of H_2O in the CO_2-rich phase which is rather low. Therefore, it is assumed then that the properties of CO_2 in the mixture can be represented with a sufficient level of accuracy by treating this species as a

pure phase instead of a mixture. Such an assumption is very important in simplifying the representation of these mixing parameters and thus the implementation of this expression in the Cantera code. Notice that this expression requires the phase volume V_i which can be computed from the resulting R-K cubic equation as done by Spycher et al. (2003). These authors use the analytical approach by Nickalls (1993) based on the Cardan's solution for solving cubic equations and it is discussed in section 6.4.4. In the current Cantera implementation, it is assumed that the volume in the mixed fluid CO_2-rich phase can be described by treating it as a pure phase on the basis of low H_2O solubility into the CO_2-rich phase for the pressure and temperature conditions considered in this study. Such treatment allows for the direct retrieval of the pure phase thermodynamic properties from the native EoS in Cantera. The results of this approach were checked by comparing values for volumes obtained from solving the R-K cubic equation (using Mathematica®) along with the parameters given by Spycher et al. (2003) and those obtained from the native EoS for pure CO_2 in Cantera. The resulting volumes from this comparison are in very good agreement for the pressure and temperature range of interest.
The mass fraction of $H_2O_{(g)}$ in the CO_2-rich phase (i.e., $y_{H_2O(g)}$) was computed as function of pressure for a temperature of 50°C and the result is given in Figure 6.3-3. The resulting curve was compared to the one given by Spycher et al. (2003) and the agreement is excellent. For this EoS implementation, the parameter b_{CO_2} which relates to the mixing terms in Eqn. (6.11) is slightly different – 28.2 cm^3/mol instead of 27.8 cm^3/mol as given by Spycher et al. (2003). This parameter needed to be modified to obtain better consistency with the $y_{H_2O(g)}$ values at the high pressure range. The reason for this slight discrepancy was not determined in this work but plausible reasons are the use of a different EoS to obtain CO_2 volumes instead of R-K expression and associated parameters in Spycher et al. (2003) or slight discrepancies in the Gibbs energies resulting small differences in $K^{\circ}_{H_2O(T,P^{\circ}_{ref})}$ as a function of temperature. In any case, the resulting curve is nearly identical to that reported by Spycher et al. (2003) along with the data therein.

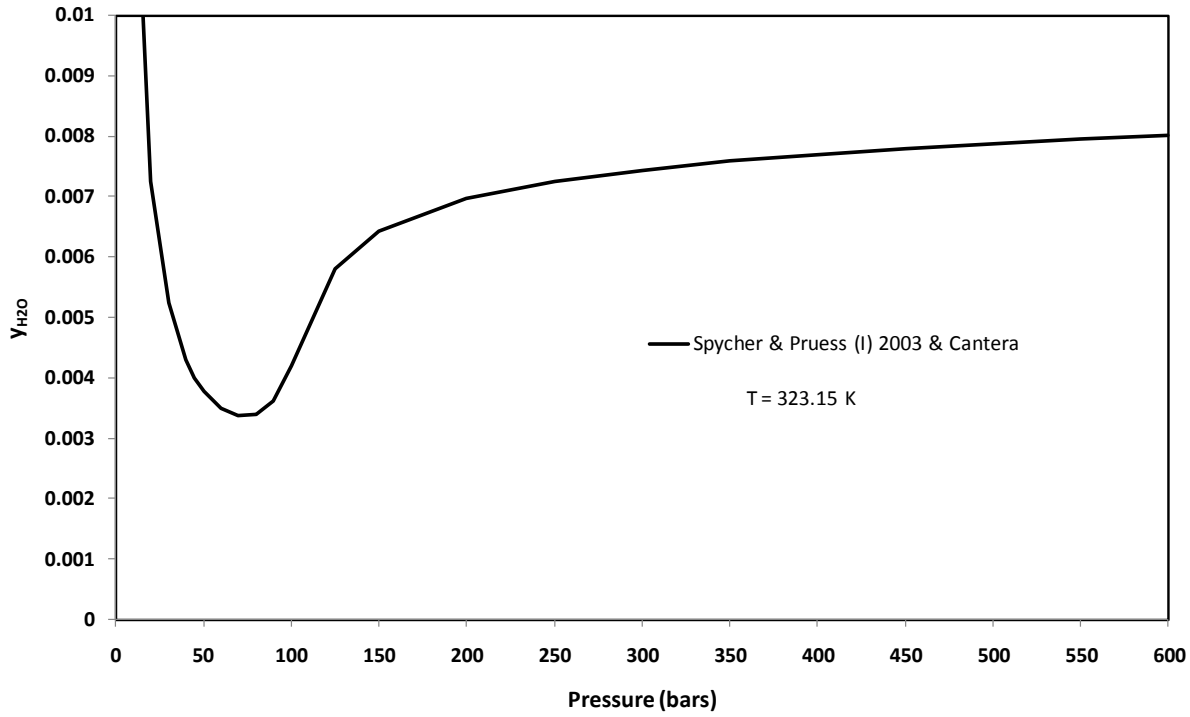

Figure 6.3-3. Plot of the predicted mole fraction of H_2O $\left(y_{H_2O(g)}\right)$ in the CO_2-rich phase at 50°C as function of pressure using Cantera and the model implementation of Spycher et al. (2003).

The solubility of CO_2 in the aqueous phase was computed using the EoS native to Cantera for pure phase CO_2 and H_2O, and the Pitzer model parameters for $CO_{2(aq)}$ neutral species from Corti et al. (1990) and Mariner (2007). The Pitzer model parameters for activity coefficients of $CO_{2(aq)}$ neutral species have been tested for natural brine cases (Mariner 2007) and problems involving carbonate equilibria for a wide range of pressures of temperatures(Corti, Depablo et al. 1990; Mariner 2007; Moffat and Jove Colon 2009). The model as implemented also makes use of the Cantera solver (VCS) to compute chemical equilibrium speciation in the aqueous phase (Moffat and Jove Colon 2009). The results of this model implementation are given in Figure 6.3-4 for CO_2 solubility in 0.5 molal NaCl solution.

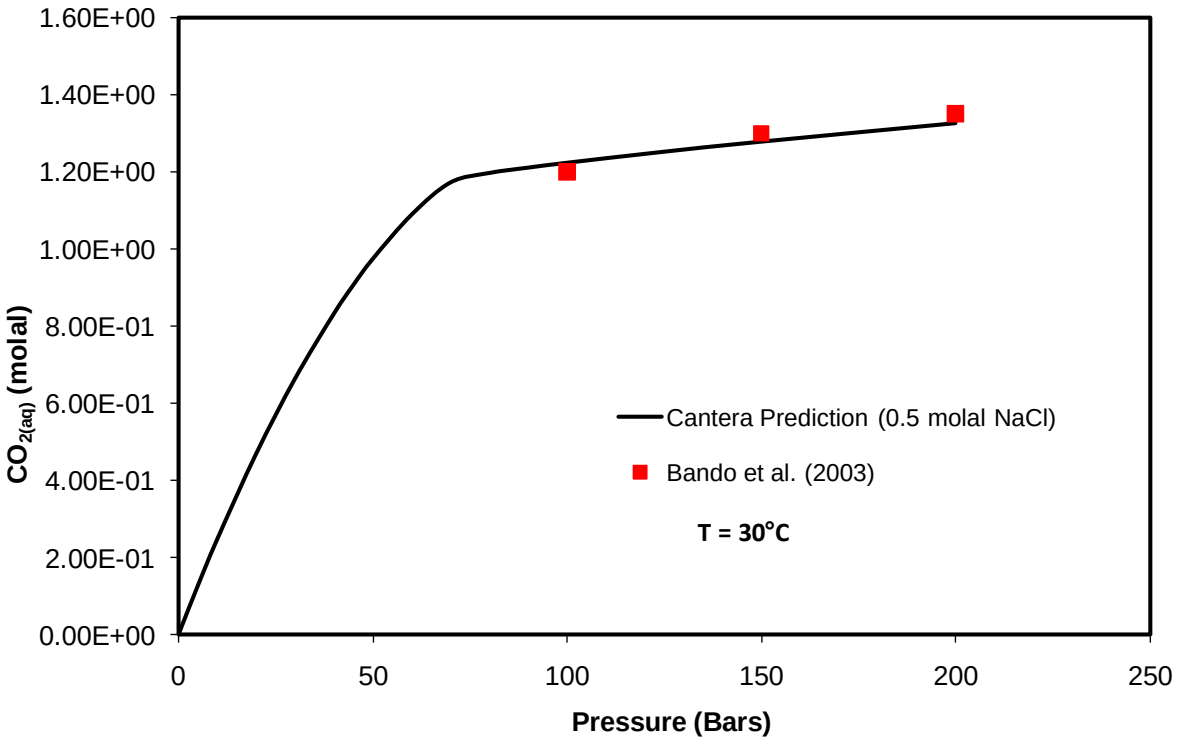

Figure 6.3-4. Plot of predicted CO_2 solubility at 30°C in 0.5 molal NaCl solution as a function of pressure using Cantera and the Pitzer model. Notice the close correspondence with the data by Bando et al. (2003).

The results indicate a close correspondence with the model and the solubility curves reported in Spycher and Pruess (2005). Code runs for salt-free systems also produces solubility curves that are in excellent correspondence with those presented in Spycher et al. (2003) and the solubility data given by Bando et al. (2003) in NaCl(aq) solutions, particularly at elevated pressures. It should be noted that $CO_{2(aq)}$ volumetric and solubility data for salt-bearing systems is relatively scarce; even more so at the elevated pressures of interest for CO_2 sequestration. Still, there is some data available comprising a wide temperature range up to 250°C (Spycher and Pruess 2010). It is envisioned that applications of this thermodynamic implementation in Cantera will be expanded and tested at temperatures typical of hydrothermal systems.

The thermodynamic description and chemical equilibria for the CO_2-H_2O-NaCl system has been implemented in Cantera with encouraging results. Such implementation demonstrates the capabilities of Cantera to model complex multiphase cases of chemical equilibria and thermodynamic properties of mixed fluid systems over a wide temperature and pressure range.

6.4 Implementation of Multicomponent Redlich-Kwong EoS within Cantera's ThermoPhase Objects

6.4.1 Introduction

This section describes another implementation of the Spycher et al. (2003) approach to describe multiphase equilibria in the CO_2-H_2O system. This implementation is native to the Cantera thermodynamic class objects and therefore more general with the goal of introducing a rigorous capability base for modeling non-ideal multiphase systems. The native base class thermodynamics object within Cantera is called `ThermoPhase`. `ThermoPhase` consists of a large set of queries about the values of thermodynamics functions, and the values/ properties of the mechanical EoS. Under `ThermoPhase` are objects that implement mole fractions and species elemental compositions. The `HMWSoln` thermodynamics object, which implements the Pitzer equations, is a derived object of the `ThermoPhase` class.

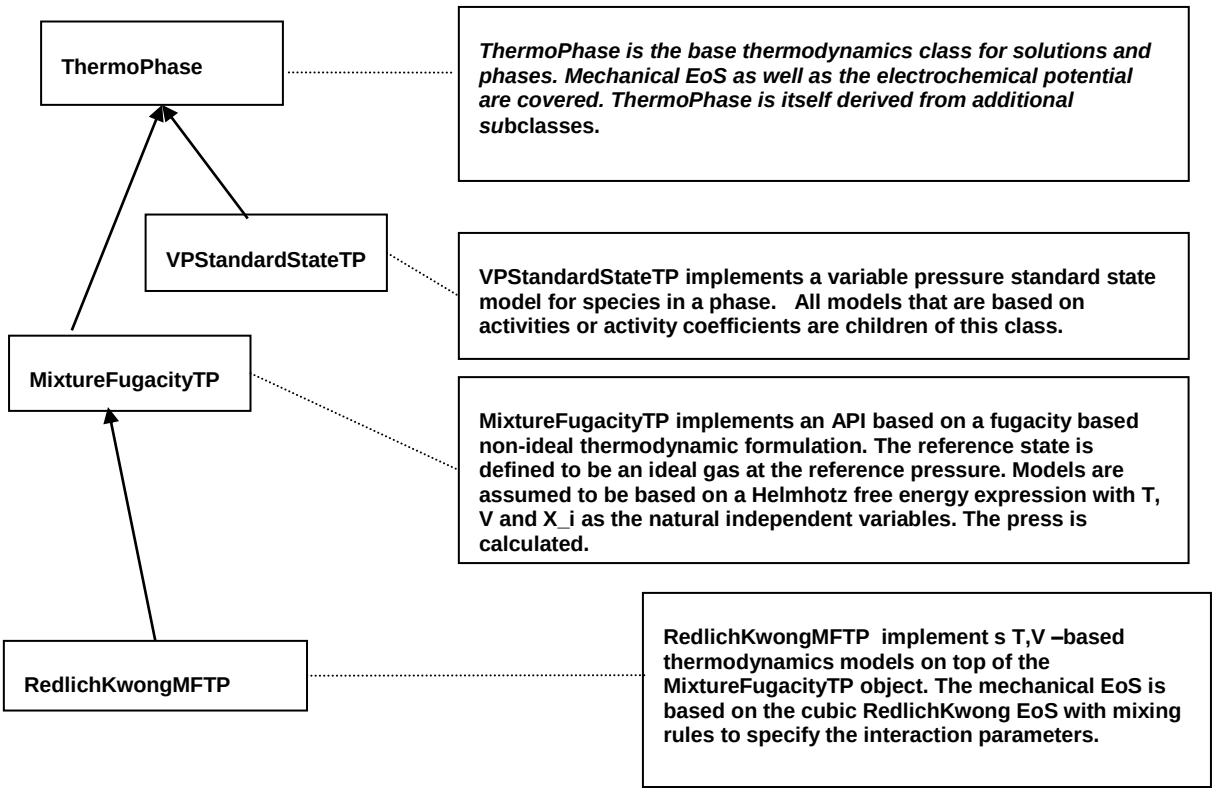

Figure 6.4-1. Layout of thermodynamic objects associated to the `ThermoPhase` class in Cantera.

Figure 6-4.1 describes the inheritance of objects within this architecture. The `HMWSoln` object is derived from several hierarchical class components. However, to describe the multicomponent real-gas EoS, a fugacity representation is needed. This involves applying a representation of a reference state model for each species in the mixture, which is based on the ideal gas EoS applied at a given pressure. Fugacities are then calculated integrated over the pressure (P) range

of interest at constant temperature (T). This approach is actually applicable even if the system turns out to be in the liquid state. This is fundamentally different from an activity model based system such as the Pitzer equation set, which is based on setting a standard state that is a function of temperature and pressure. Therefore, we have spawned a new intermediate class called `MixtureFugacityTP` to reflect this split in the thermodynamics representations. Models based on the `MixtureFugacityTP` class are assumed to be based on a Helmholtz free energy representation of the phase with independent variables being the temperature, density (or molar volume), and the mole fractions of the species. Then, a class called `RedlichKwongMFTP` implements the temperature-volume based R-K EoS model representation as a child of the `MixtureFugacityTP` class. Figure 6-4.1 displays this inheritance relationship with the R-K EoS.

6.4.2 Calculation of the Total Helmholtz Free Energy Equation

We define the molar volume of the mixture as *v*, which is related to the total volume of the mixture by $V = nv$. Then,

$$P = \frac{RT}{v - b_{mix}} - \frac{a_{mix}}{\left(\sqrt{T}\right)v\left(v + b_{mix}\right)} = \frac{n_T RT}{V - n_T b_{mix}} - \frac{n_T^2 a_{mix}}{\left(\sqrt{T}\right)V\left(V + n_T b_{mix}\right)} \tag{6.13}$$

Following Spycher et al. (2003), we calculate the following mixture formulas for the coefficients in Eqn.(6.14).

$$a_{mix} = \sum_{i=1}^{N}\sum_{j=1}^{N} X_i^T X_j^T a_{ij} \qquad\qquad b_{mix} = \sum_{i=1}^{N} X_i^T b_i \tag{6.14}$$

Here, X_i^T refers to the mole fraction of species *i* in the combined liquid and gas phase system represented by the R-K EoS. Note, a_{ij} and b_i may be functions of the temperature as well. The first task it to generate the Helmholtz free energy representation of the EoS. We do this by recognizing that

$$\left.\frac{d\left(nA\right)}{d\left(nv\right)}\right|_{T,n_i} = -P \tag{6.15}$$

So we can take the integral of $P(V)$

Using

$$\int \frac{dV}{V\left(V + b\right)} = \frac{-1}{b}\ln\left[\frac{V + b}{V}\right],$$

we obtain

$$nA = -RTn_T \ln\left(v - b_{mix}\right) - \frac{a_{mix} n_T}{b_{mix}\sqrt{T}}\ln\left[\frac{V + n_T b_{mix}}{V}\right] + c\left(T, n_i\right).$$

$c\left(T, n_i\right)$ is the integration constant that we can then identify with

$$c\left(T,n_i\right)=RTn_T\ln\left(v_{RS}^o\right)+\sum_i n_i\,a_{RS,i}^o\left(T\right)+\sum_i RTn_i\ \ln X_i\,.$$

In the last expression, V_{RS}^o is the reference state volume approximation, which is the ideal gas approximation at the adopted reference state pressure of 1 bar.

$$v_{RS}^o=\frac{RT}{1bar}=\frac{RT}{p^o} \tag{6.16}$$

$a_{RS,i}^o\left(T\right)$ is Helmholtz free energy of the i^{th} species in its reference state, which is defined as an ideal gas at a temperature T and at the reference pressure, p^o, one bar.

$$a_{RS,i}^o\left(T\right)=u_{RS,i}^o-Ts_{RS,i}^o \tag{6.17}$$

Therefore, the final result is Eqn. (6.18).

$$na=\sum_i n_i\,a_{RS,i}^o\left(T\right)+\sum_i RTn_i\ \ln X_i\ -RTn_T\ln\left(\frac{p^o\left(V-n_Tb_{mix}\right)}{n_TRT}\right)-\frac{a_{mix}n_T}{b_{mix}\sqrt{T}}\ln\left[\frac{V+n_Tb_{mix}}{V}\right] \tag{6.18}$$

Eqn. (6.18) may be rearranged to yield Eqn. (6.19).

$$na=\sum_i n_i\,a_{RS,i}^o\left(T\right)-\sum_i RTn_i\ \ln\frac{p^oV}{n_iRT}+RTn_T\ln\left(\frac{V}{V-n_Tb_{mix}}\right)-\frac{a_{mix}n_T}{b_{mix}\sqrt{T}}\ln\left[\frac{V+n_Tb_{mix}}{V}\right] \tag{6.19}$$

This formula can be compared to the Prausnitz formula (3.4-11) (Prausnitz et al. 1986, p. 38), to verify our formulation.

$$na=\int_V^\infty\left(P-\frac{n_TRT}{V}\right)dV-\sum_i RTn_i\ \ln\frac{p^oV}{n_iRT}+\sum_i n_i\,a_{RS,i}^o\left(T\right)\qquad a_{RS,i}^o=u_{RS,i}^o-Ts_{RS,i}^o \tag{6.20}$$

In this formula, we have modified Prausnitz's formula by adding a p^o to the ln term to ensure that this term is unitless, as is obviously required (note: there is an existing error in the Prausnitz' book).

Having arrived at the general expression for Helmholtz free energy, the remaining thermodynamic potentials required for computing thermodynamic properties for equilibrium calculations can be derived. For completeness, these are given in Appendix B.

6.4.3 Solution Methods within the Objects

We have implemented a traditional approach to solving the vapor dome problem for the multicomponent R-K equation set. In this approach, which is strictly a constant mole number approach, we solve for the equilibration of the gas and liquid molar Gibbs free energies at a particular temperature and pressure.

$$f\left(P\right)=G_l\left(T,P\right)-G_v\left(T,P\right) \tag{6.21}$$

The update to $f\left(P\right)$ is generated from the following differential formula,

$$dG_l = -VdP$$

so that the update to the pressure may be determined from the following Eqn. (6.22).

$$\nabla P=-\left(\frac{1}{V_l}-\frac{1}{V_g}\right)\left(G_l-G_g\right) \tag{6.22}$$

This formula is extremely efficient when a good starting guess can be generated for V_l , V_g , and *P*. However, there is problem with generating good initial guesses especially around the critical point. The key to the method involves finding a pressure where there are three solutions to the P-V-T equation. Once the algorithm had been adjusted to account for this issue, the method is robust as long as a starting pressure with multiple solutions can be found.

However, the traditional approach to the vapor dome problem is not actually correct for the multicomponent R-K problem and moreover is not sufficient either; a key point that is not sufficiently addressed in the current iteration and especially within the papers by Spycher et al. (2003) and Spycher and Pruess (2010). The reason why the traditional vapor dome problem is not correct is because the mole fractions of species on the vapor side and on the liquid side may not be the same. Therefore, the equations that are actually applicable in this case are represented by Eqn. (6.23).

$$\mu_l^i\left(T,P\right)=\mu_g^i\left(T,P\right) \quad \text{for all species } i \tag{6.23}$$

What this means in practice is that for a particular temperature the saturation pressure changes because the mole fractions on each side of the interface may be different. For the CO_2/H_2O problem we have seen 15% changes in the predicted saturation pressure due to this effect. Moreover, solution of the vapor dome problem is not sufficient. This means that while the vapor dome represents one form of a miscibility gap, the multicomponent R-K EoS actually have multiple miscibility gaps, the other ones being associated with coordinates representing mole fractions. For an N species multicomponent R-K equation system, the Gibbs phase rule reduces to the following equation for the number of degrees of freedom, $2+N-\pi$, where π is the number of stable phases present. Therefore, when there are two species in the system, there can be at most two phases present in a region according to this rule. Three stable phases may only be present along a line in *T, P* space. The fact that there are two phases that are stable at any point means that there is a miscibility gap along a mole fraction direction. This can and does happen within the multicomponent R-K equation set, depending upon the values of the interaction parameters (e.g., $a_{i,j}$) that are the off-diagonal entries. Therefore, the proper treatment of the R-K phase space is to assign labels associated with the gas phase and with multiple liquid phases that may develop. We have associated each of these liquid phases with a primary component within the liquid. The following labels are used that address this complexity.

```
FLUID_SUPERCRIT

FLUID_GAS

FLUID_LIQUID_0

FLUID_LIQUID_1

FLUID_LIQUID_2
```

We have added a supercritical fluid label in this equation system, because it is still useful to flag compositions which are above their critical temperature and or pressure at a given composition. There are multiple liquid labels that may be assigned; they are assigned based on the maximum species in that phase. Therefore, the CO_2 rich liquid phase is labeled `FLUID_LIQUID_0`, while the H_2O rich liquid phase is labeled `FLUID_LIQUID_1`, if the multiple R-K EoS is used for both the H_2O and CO_2 liquid phases.

In general, equilibrium in miscibility gap systems can be simply handled by the equilibrium solver, even if there are multiple phases represented by the same EoS treatment, as long as there is a separate `ThermoPhase` object for each local minimum in the Gibbs energy function. Note, if multiple `ThermoPhase` objects are bumped into the same local minimum then the system will become degenerate at the end of the calculation as it approaches an equilibrium state. Therefore, the equilibrium solver is actually used to solve the multiple species vapor dome problem. This works as long as the equilibrium solver has separate `ThermoPhase` objects for both sides of the vapor dome that it can test for relative stability.

This discussion also points out the necessity of forcing individual `ThermoPhase` objects to stay or remain in their respective local Gibbs energy minimums within which they were originally

assigned. This is again accomplished using a field within each object that forces the labels defined above not to change, if at all possible. Therefore, an R-K gas object defined as a forced `FLUID_GAS` label stays as an R-K gas object even if the liquid phase is more stable, and a `FLUID_LIQUID_0` object stays as a liquid object dominated by species 0 even if the gas phase is more stable. The phases can theoretically exist in a metastable manner even though they are not the stable phase up until the point at which they cease to become a local Gibbs energy minimum. This point or the locus of points in *PV* space is called the spinodal decomposition curves for the phase system. The spinodal decomposition curves are calculated within the multicomponent R-K system as well. Internally, it is a significant help in some algorithms to understand where these curves exist. In a numerical context, their values are more significant than the saturation pressure curve itself, and they are calculated using the following equation for both the liquid side and the gas side of the vapor dome.

$$\left.\frac{dP}{dV}\right|_T = 0 \tag{6.24}$$

Forcing the `ThermoPhase` objects to be in one state or another turns out to be essential for the CO_2-H_2O problem. We have found that the water phase is adequately modeled by the previously developed `HMWSoln` object that represents concentrated brines (Moffat and Colon 2009). Thus, the water liquid phase is handled. However, the CO_2 rich liquid phase and the non-ideal gas phase are then handled by multicomponent R-K `ThermoPhase` objects that have been developed within this project. These multicomponent R-K `ThermoPhase` objects are restricted to range only within their assigned roles.

6.4.4 Solution of the Cubic Equation of State

At the heart of these calculations is the solution of the R-K cubic EoS.

$$av^3 + bv^2 + cv + d = 0 \tag{6.25}$$

We choose to solve Eqn. (6.25) using the Nickalls method (Nickalls 1993). Essentially, what this does is give a fairly full proof method of finding all of the real roots of Eqn. (6.25) using analytical formulae related to the arc cosine function. However, there are several complications in using the Nickalls method. The first is that, while the method is analytical, the actual formulas suffer from ill-conditioning in some regions. In particular, as the region trends towards the ideal gas limit, the formulas become singular, and calculation of the discriminants in many of the expressions requires the subtraction of two large numbers. Because we are using finite arithmetic, these singularities must be guarded against by the inclusion of additional logic. For example, in the limit of the ideal gas solution, the original formulae in the Nickalls method are discarded in favor of simpler ones. Additionally, at the very end of the solution procedure, each of the solutions found by Eqn. (6.25) is refined using a standard Newton's method approach in order to obtain better accuracy, which is lost due to the ill-conditioning. Typically we are seeking 13 or 14 digits of accuracy from the solution of Eqn. (6.25), so that inaccuracies in the solution of the cubic EoS do not affect property calculations elsewhere in the routine.

It should be noted also that Nickall's method provides for the solution of the turning points to Eqn. (6.25). However, these turning points are not related to the spinodal curve representing the limits of the stability of each phase. Therefore, their calculation is of no importance.

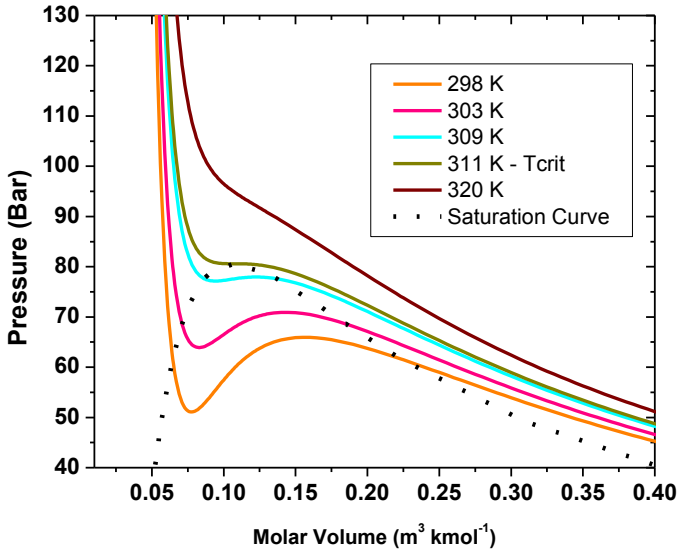

Figure 6.4-2. Illustration of P-V-T relationships calculated with the Redlich-Kwong (R-K) EoS. The calculated curves are for the pure CO_2 phase.

6.4.5 General Issues with Equilibrium

In general the equilibrium issues between phases are much more complex due to the multispecies aspect. Let us take the case of two species in a R-K fluid. In general we can have three phases present, L1, L2, and G. L1 would be a liquid dominated by component 1, while L2 would be a liquid dominated by component 2. The phase rule states that the number of degrees of freedom in this case is 2 + 2 – P. So, if all three phases are present, then this must occur only along a line in T,P space. This is in fact what occurs within the CO_2-H_2O system. L1 in this case would be H_2O. The CO_2 turns from gas to liquid along a line in T,P space. However, what is significantly different and complicating is that the concentration of water in the liquid CO_2 and gaseous CO_2 is different. This type of complication can only be handled via the equilibrium solver. Therefore, the R-K multispecies `ThermoPhase` object must be constructed so as to permit only gas or liquid phases below the critical point. Then, for the case of two species, there may be three R-K phases present, one representing L1, one representing L2, and one representing G. One of the three R-K phases will be unstable with respect to the other phases, and therefore, have a zero mole number assigned to it. This is permissible. Generalizations to more than two species are straightforward when paying attention to the phase rule (Smith and Van Ness 1975): 2 + N – P. In general, there can be N + 1 phases to be considered, with only N phases present within an area of T, P space, and with N+1 phases present along one dimensional lines in T,P space.

What does this mean for the R-K multispecies object? It means that a lot of the equilibrium issues should be relegated to the equilibrium solver to adjudicate. However, the R-K object should handle all equilibrium issues assuming that the R-K fluid stays at a constant composition. As long as the R-K fluid is at a constant composition, the critical point, the saturation pressure, and the spinodal curves may be calculated. The equilibrium with respect to the gas to liquid phase transition may be also calculated. However, this equilibrium will be only a minimum condition. The extra degrees of freedom associated with the change in composition will cause phase transitions to occur sooner. Additionally, a gas and liquid R-K phase in equilibrium with one another will have different compositions in the different phases and occupy a region in T,P space rather than a line. This complex equilibrium situation may be handled by the equilibrium solver only. Calculation of the spinodal curve is important because that limits the viability of the local phase condition.

6.5 Verification Problems

6.5.1 First Problem – Verification of CO_2 Pure Fluid Behavior

Spycher uses the following pure species CO_2 parameters for the R-K parameterization:

$$a_{CO2} = 7.54\times10^{7} - 4.13\times10^{4} T \text{ bar cm}^{6} \text{ K}^{0.5} \text{ gmol}^{-2} \tag{6.26}$$
$$b_{CO2} = 27.80 \text{ cm}^{3} \text{ gmol}^{-1}$$

These values produced the following critical properties:

$T_c = 311.022$ K (critical temperature)
$P_c = 8.06\times10^{6}$ Pa (critical pressure)
$V_c = 107.$ cm^3 gmol^{-1} (critical volume)

The critical properties of CO_2 were compared to an existing `PureFluid` implementation of CO_2 within Cantera. The comparison was close in terms of the predicted critical properties, but not as close in terms of predicting the saturation curves. This property of the R-K EoS is well known.

6.5.2 Second Problem – Calculation of H_2O Parameters

The H_2O critical properties are:

$T_c = 647.286$ K (critical temperature)
$P_c = 22.089\times10^{6}$ Pa (critical pressure)
$V_c = 56.8$ cm^3 gmol^{-1} (critical volume)

Because the b_{H2O} value is specified by Spycher et al. (2003) in order to specify the partial molar volume of H_2O in the CO_2-rich phase, we have left the value unchanged. Then, we have to fit a_{H2O} to the T_c value. Then, we noticed that the 100°C vapor pressure for water was grossly

overpredicted. This necessitated adding a temperature term to the a_{H2O} value, just as in the CO_2 case. The procedure yields the values given below.

$$a_{H2O} = 1.745\times10^{8} - 8.0\times10^{4}T \text{ bar cm}^{6} \text{ K}^{0.5} \text{ gmol}^{-2} \qquad (6.27)$$

$$b_{H2O} = 18.18 \text{ cm}^{3} \text{ gmol}^{-1}$$

6.5.3 Third Problem – Prediction of Water Solubility in the CO_2–rich Phase

In order to test the multicomponent R-K capability within Cantera, we duplicated calculations presented in Spycher et al. (2003). Sample results are presented in Figure 6.5-1 for one temperature.

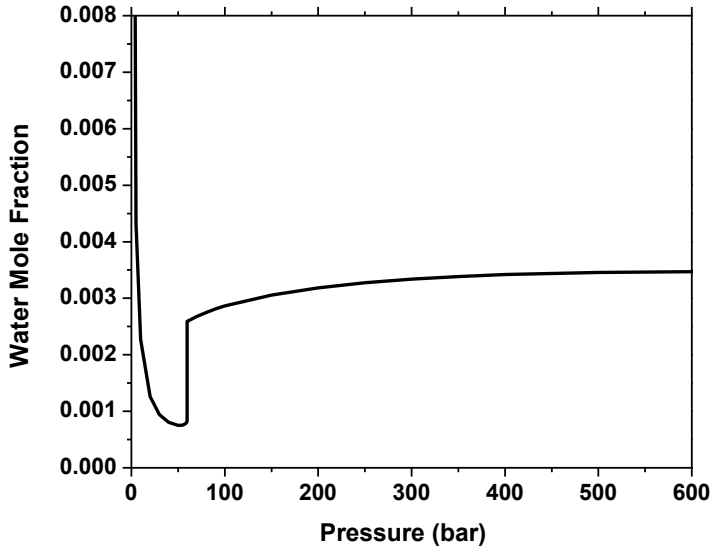

Figure 6.5-1. Prediction of the mole fraction of water in the CO_2 phase at 18ºC as a function of the pressure.

Calculations were carried out within Cantera using the equilibrium solver to calculate the equilibrium mole fraction of water in the CO_2 rich phase. Equilibrium was achieved against three different `ThermoPhase` objects representing the real behavior of water with virtually identical results: a real `PureFluid ThermoPhase` object for water, a brine phase with CO_2 solubility enabled using the `HMWSoln ThermoPhase` object, and another R-K phase with an almost pure H_2O mole fraction used as an initial guess.

The jump in the solubility of water in the CO_2 phase is due to the abrupt phase transition between the gas CO_2 phase at low pressures and the liquid CO_2 phase at high pressures. The liquid CO_2 phase had a higher solubility for water than the gas CO_2 phase. Note, also that this phase transition occurred at 56 bars, and not at a pressure that would have been predicted by a constant

mole fraction approximation of the system (i.e., 62 bars), a point that has been previously discussed above. The results of Figure 6.5-1 agree quite well with Spycher et al. (2003).
An additional point should be discussed. The equilibrium solver demonstrated some hysteresis in its calculation of the CO_2 gas to liquid phase transition in this calculation. This hysteresis was created because the equilibrium solver must have an a priori instantiation of an alternative phase to test against in order to find a global minimum in the Gibbs free energy. Without this, it may get stuck in local minimums. This is a well-known issue with Gibbs free energy minimization techniques. In order to get around this problem, we supplied both a CO_2 gas and liquid phase R-K object to the equilibrium solver. It could then choose between the two (once it knew that there was a choice!) in order to find the global minimum for the equilibrium problem.

6.5.4 Fourth Problem - Prediction of the CO_2 Solubility in the Liquid Water Phase

To complete the calculation, we report the results for the prediction of the CO_2 solubility in the brine phase as a function of the pressure. The results for 18ºC are presented in Figure 6.5-2. The calculations were carried out by equilibrating a R-K multicomponent ThermoPhase object representing the gas phase and liquid CO_2 phases. The liquid H_2O phase was represented by an `HMWSoln` object, with multiple species, using the usual carbonate anions and H+, representing the CO_2 within the brine phase. These parameters were taken from the Yucca Mountain Project database. The carbonate anions were all in low concentrations relative to the total concentration of the aqueous CO_2 species.

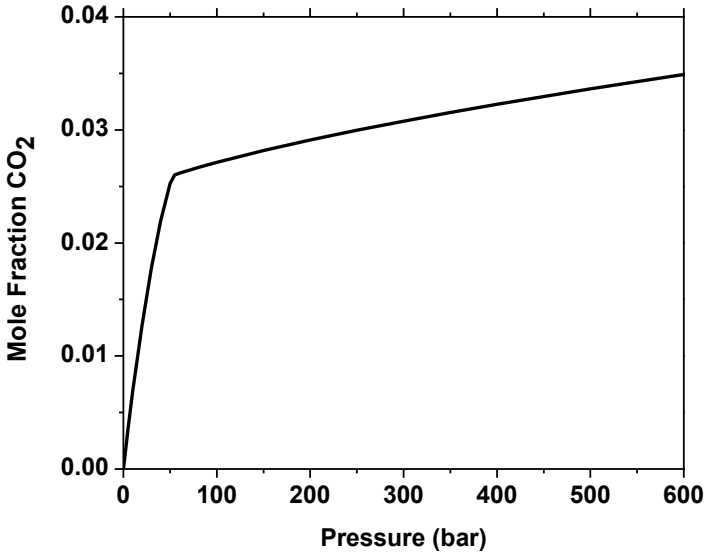

Figure 6.5-2. Prediction of the mole fraction of CO_2 in the brine phase at 18ºC as a function of the pressure.

The model mostly duplicates the results of Spycher et al. (2003). However, it shows more clearly that there is an inflection point in the CO_2 mole fraction solubility due to the gas to liquid CO_2 phase change. This was not brought out in the Spycher et al. (2003) paper, because their solution method was not coupled enough to capture this effect.

Note that we attempted to use the R-K multicomponent model to represent the H_2O rich phase. However, it turned out that the solubility of CO_2 in water was underpredicted by this model by two orders of magnitude. This serves as a reminder that thermodynamic data should be verified before being used, especially when the data is used in a parameter region for which it was not originally fitted.

6.6 Adaptive Grid Scheme for Table Look-up

As described in the foregoing sections, evaluation of general EoS for fluid mixtures can be computationally costly and challenging to implement. Determination of equilibrium compositions, which must be performed at each grid point, for each time step, only adds to the computational expense. This section describes three different approaches we used to speed up EoS calculations—improved solvers, look-up tables, and adaptive tables.

For the Span and Wagner (1996) and Modified Redlich-Kwong (McPherson et al. 2008) EoS with pressure and temperature as primary variables, the most time consuming step is the solve to find density. Using the ideal gas density as an initial guess, we found that Newton's method converged slowly, often failing to converge at all. The modified Newton iteration used by Han and McPherson's code was more robust, but it was only marginally faster than Newton's method. A hybrid bisection-secant method performed much better than either the Newton or modified Newton approaches. This hybrid method uses the bisection method to get within the radius of convergence, then the secant method to converge on the solution. The method achieved a 6x speedup over the Newton and modified Newton methods, and converged in all regimes in which it was tested.

It is likely one could achieve additional speedup by using more specialized solvers tailored to the specific EoS, better initial guesses motivated by the physics, and series acceleration such as Anderson acceleration (Walker and Ni 2010). However, instead of pursuing these techniques, we investigated replacing the run-time solver with pre-computed lookup tables.

For standard lookup tables on a regular rectangular grid using both nearest neighbor and bilinear interpolation, the computation was approximately 1000 times faster than the standard Newton’s method. However, the tables took up approximately 100 MB per thermodynamic variable for single phase calculations that only depended on pressure and temperature (not mole fraction). As expected, high refinement levels were needed to resolve the thermodynamic surface near the critical point, but were superfluous in most of the rest of the domain.

To reduce the memory requirement, we implemented 2D and 3D adaptive lookup tables as plugins to be used with the Aria finite element code. In this method, thermodynamic state space (e.g., *P*-*T* space) is recursively subdivided into smaller and smaller boxes, on which nearest neighbor or multi-linear interpolation is done. In regions where a coarse grid is good enough, the subdivision stops, whereas in regions where more detail is needed (such as near the critical point), the grid is refined.

The adaptive lookup tables achieved a 600x speedup over Newton’s method, while reducing the memory footprint to approximately 200 KB per thermodynamic variable for single phase

calculations that only depended on pressure and temperature. Furthermore, adaptive tables provide a general method for connecting EoS codes to compositional simulators. Adaptive tables can be pre-computed using only the EoS code. The table is then available to any simulator capable of reading the adaptive table format.

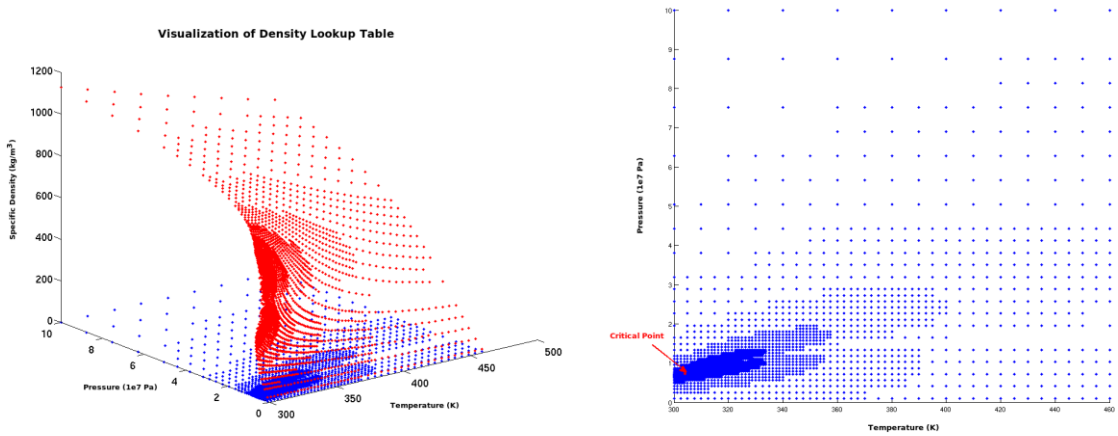

Figure 6.6-1. Adaptive table visualization for density as a function of pressure and temperature using the Span & Wagner EoS.

Since adaptive tables with non-uniform refinement contain hanging nodes, adaptive multi-linear interpolation of the thermodynamic surface may have (small) discontinuities. Such discontinuities have the potential to create instabilities when used with numerical methods that expect the thermodynamic surface to be weakly differentiable. Nevertheless, the adaptive tables have worked fine in practice.

Two potential future research directions to remedy the hanging node discontinuity are as follows. First, one could adjust the values in the table at the hanging nodes so that the surfaces match up, though this would incur a slight decrease in accuracy in the more refined region. Second, one could implement more advanced interpolation methods such as Coons patches (Forrest 1972) in 2D, or Gordon surfaces (Gordon 1971) in higher dimensions, though this would incur an increase in computational time.

7. Random Fields Using Fourier Expansions for Modeling Heterogeneity

Random fields (RFs), often also referred to as stochastic processes (SPs), can be thought of as extensions to random variables (RVs). While RVs only apply as a constant over a give time interval or space region for a given sample, RFs are an entity that can be thought of as a different random variable *at each point in space or time*. Thus, in general RFs can be thought of as a non-countable collection of random variables and this property allows one to handle situations that require more analytical flexibility than random variables can accommodate. In Figure 7.0-1 we provide an illustration of the difference between RV and RF realizations. Note that RVs are uniform over the domain D while RFs can have spatial (or time) variation.

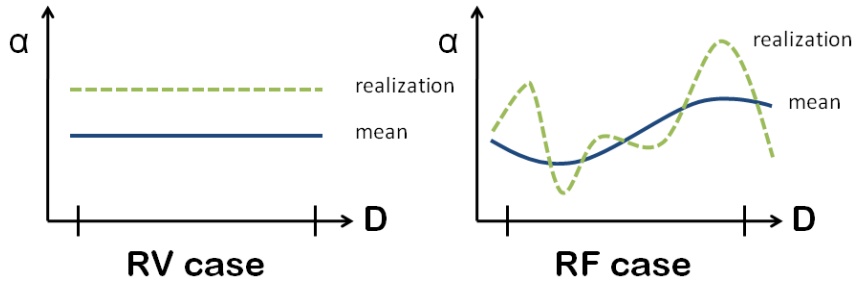

Figure 7.0-1. Illustration of the difference between realizations of RVs and RFs.

In geomechanics, where various constitutive properties of soil have been observed to vary spatially and where data are often quite sparse, researchers and analysts have employed RFs for many years. However, specific computational forms of RFs that we commonly encounter involve large numbers of random variables, one for each grid, say, in a computational discretization of a continuum.

In this chapter, we describe an approach that takes a different view of building such a computational form—we approximate our random fields based on canonical global properties of the field and construct expansions that depend on a minimal number of random variables.

While reducing the number of random variables in the model is itself sufficient motivation for our approach, there is a second, equally important aspect. These canonical expansion methods, and expansions that derive from them, have been the subject of much research over recent years; much of this research has been focused specifically on the development of computationally efficient numerical quadrature algorithms for performing so-called uncertainty propagation as compared with more common Monte Carlo sampling techniques. This research has yielded reductions in computational burdens on the orders of magnitude scale.

Here we describe the foundational aspects of these expansion methods, and provide an example where we compute an expansion for an important output flow response in a heterogeneous porous medium.

We then use this construction as the basis for developing a generalization to conditional simulations, an approach that constrains a random field to match limited, sparse data acquired via experiments on the physical domain of the field being modeled computationally. While we are early in the development phase of this approach, we provide a simple example of such a simulation using realizations from an analytical random field, and we describe our anticipated future work in some detail in the text.

7.1 An Introduction to Random Fields

The foundation of random fields are *random variables*, which are widely used in science and engineering to represent uncertainty in quantities. In the context of modeling and simulation, these quantities can be input parameters or output responses.

Mathematically speaking, RVs are (measurable) functional mappings with a domain consisting of a sample space, Ω, of elementary events that is well-defined in the context of a probability space. A probability space consists of a triple, $(\Omega, \mathcal{S}, P)$, which includes, in addition to the sample space, a σ-algebra $\mathcal{S}$ of subsets of Ω called events, and a probability measure P. Each of these entities has well-established and precise mathematical properties (Rosenthal 2000). A real random variable X is a real-valued function mapping the sample space to the real line: $X: \Omega \to \mathbf{R}$.

A *random field* is a function, α, on a product space $\mathbf{D} \times \Omega$ where the index set, $\mathbf{D}$, is the domain of a non-probability space. Often, in engineering applications $\mathbf{D}$ is the domain of the original deterministic problem. Note that for any $x \in \mathbf{D}$, the function $\alpha(x, \cdot)$ is a random variable. In fact, one way to view a RF is to think of it as a collection of RVs indexed over $\mathbf{D}$; this includes the case where $\mathbf{D}$ is an uncountable continuum as would be the case, for example, if it were the real line, $\mathbf{D} = \mathbb{R}$, or some continuum subset of it.

RFs have similarities with finite vectors of RVs (VRVs), since the value of the RF at two points $x, y \in \mathbf{D}$ is correlated. In fact, an RF can be determined completely by the family of all joint cumulative distribution functions (CDFs) (Papoulis 1991) over all sets of finite points $\{x_i\}_{i=1}^{N} \subset \mathbf{D}$. However, RFs are different from vectors of RVs in that they are typically described by an infinite number of RVs, as we discuss below. There are also technical mathematical requirements such as measurability and separability that apply to random fields we will consider, and we direct the interested reader to Rosenthal (2000) for more detail on these.

Under suitable assumptions, a zero-mean RF α can be decomposed using a so-called Karhunen-Loève (KL) expansion (Schwab and Tudor 2006)

$$\alpha(x, \omega) = \sum_{i=0}^{\infty} \sqrt{\lambda_i} \phi_i(x) \eta_i(\omega) \tag{7.1}$$

where the $\{\lambda_i\}$ and $\phi_i(x)$ come from the KL eigenproblem, which is given by

$$\int_{\mathbf{D}_\alpha} r(x, y) \phi_i(y) dy = \lambda_i \phi_i(x). \tag{7.2}$$

and the $\eta_i(\omega)$ are zero-mean, uncorrelated RVs. In Eqn. (7.2), $\mathbf{D}_\alpha (\subset \mathbf{D})$ is deterministic problem subdomain that the RF occupies, α, which we state here for the only time throughout this

document to make the point that the RF need not occupy the entire physical problem domain; this is commonly the case. Also in Eqn. (7.2) $r(x,y) = E[\alpha(x,\cdot)\alpha(y,\cdot)]$ is the *correlation function* of the RF and $E[\ \cdot\ ]$ is the operator of mathematical expectation

$$E[f] = \int_{\Omega} f(\omega)\, dP(\omega). \tag{7.3}$$

where Ω and P are constituents from the baseline probability triple in the RF as described herein. We note that Eqns. (7.1) and (7.2) provide information about the deterministic properties of the RF based on its correlation function. The RV coefficients, η_i, are computed by projection onto the eigenfunctions as follows:

$$\eta_i(\omega) \equiv \frac{1}{\sqrt{\lambda_i}} \int_{\Omega} \alpha(x,\omega)\, \phi_i(x)\, dx \tag{7.4}$$

which, due to the spectral nature of the KL eigenproblem, can be shown to be zero mean and uncorrelated (orthogonal). Thus, the only information we get on $\eta_i(\omega)$, which derives from the canonical nature of the KL relationships, is that

$$\begin{aligned} E[\eta_i] &= 0 \\ E[\eta_i\, \eta_j] &= \delta_{ij}\ . \end{aligned} \tag{7.5}$$

We emphasize that there is still work to do to acquire the necessary probabilistic information to specify fully the RF model; in particular, one should not take this to mean that they have any particular independence characteristics whatsoever. Regardless, this relates to the non-trivial process of building the actual models for RFs from experimental information, and is the subject of a later section in this document, and we will not comment on it further here.

The variance can be computed at each point $x \in D$ as

$$E[\alpha^2(x,\cdot)] \equiv \sum_{i=1}^{\infty} \lambda_i\, \phi_i^2(x)$$

with global average variance

$$\frac{1}{|D|} \int_{\mathbf{D}} E[\alpha^2(x,\cdot)]\, dx \equiv \frac{1}{|D|} \sum_{i=1}^{\infty} \lambda_i$$

where we use the fact that the eigenfunctions are normalized to have unit $L^2(D)$ norm.

Finally, we mention that while the above definitions apply to the case of a zero-mean RF, it is trivial to generalize them to the non-zero mean case by defining the mean field, $m(x) \equiv E[\alpha(x,\omega)]$, and substituting $\alpha - m(x)$ for α in the above relationships. In this case, the correlation function is replaced by the *covariance function*, $C(\ \cdot\ ,\ \cdot\ )$, where

$$C(x,y) = E[(\alpha(x,\omega) - m(x))(\alpha(y,\omega) - m(y))]. \tag{7.6}$$

7.2 Computational Considerations of RFs: Discretization

7.2.1 Stochastic Discretization

Because the set **D** in all of the above is usually uncountable, as it is for the case of a time interval defined on the real line, then, as we mentioned previously, the RF can be thought of as an uncountable collection of RVs. The assumption of topological separability allows us to reduce our considerations to a countably infinite number of RVs as in Eqn. (7.1), From this countable set our discretization process will involve developing criteria to restrict this set finite number. The way we will do this is to truncate the sum in Eqn. (7.1) based on a variance criterion, which will leave us with a finite number of η_i. Whatever criteria this process entails, IT is a modeling decision, and we will refer to the finite number of RV coefficients retained as the *stochastic dimension* of the approximation to the RF.

Once we have established the stochastic dimension, for various technical reasons we will need to get the approximate RF into a form that is amenable to simulation and evaluation. For the time being we will assume that the available experimental data give sufficient probabilistic information to perform a change of variables to a new set of RVs for which the probability measures are well known and accessible. Polynomial Chaos Expansions (PCEs) are generalized Fourier expansions (Kolmogorov and Fomin 1975) in a vector of uncorrelated, and thus independent, standard normal RVs (Papoulis 1991), $\boldsymbol{\xi} = (\xi_1, \ldots, \xi_N)$, where N is the stochastic dimension. The set of orthogonal basis functions for these RVs is the well-known multi-dimensional Hermite polynomials (Abramowitz and Stegun 1970). Thus, again omitting the technical details, in our work we assume that a PCE approximation to our RF is given, which has the following form

$$\alpha^{(n)}(x, \boldsymbol{\xi}) = \sum_{i=0}^{n} a_i(x)\Gamma_i(\boldsymbol{\xi}), \tag{7.7}$$

where $\Gamma_i(\cdot)$ are the aforementioned Hermite polynomials, and the generalized Fourier coefficients, $a_i(x)$, are given by

$$a_i(x) = \frac{E[\alpha(x,\cdot)\Gamma_i(\cdot)]}{E[\Gamma_i^2(\cdot)]}. \tag{7.8}$$

Here the expectation E is taken with respect to the joint probability density function (PDF) (Papoulis 1991) of the m-dimensional independent, standard normal RVs.

We note that the PCE pairing of standard normal RVs with Hermite polynomials is not arbitrary: The weighting function for the inner product that arises from its underlying Sturm-Liouville system equation can be identified simply by inspection as coinciding with the probability density function of the standard normal RV. Of course this means that other pairings can be considered that originate similarly. For example, an exponentially distributed RV defined on the interval $[0, \infty]$ is affiliated with the Laguerre polynomials (Abramowitz and Stegun 1970). Note that for the case of finite dimensional collections, none of the underlying theory, nor the operations necessary for constructing a generalized Fourier expansion, rely on a particular RV/orthogonal polynomial pairing. Thus, theoretically, it is possible that PCEs can be generalized to any appropriate pairing. These generalizations, often termed Askey Expansions (Xiu and Karniadakis 2002,2003; Schwab and Alexandru 2006) in the literature, are the subject of active research.

7.2.2 Deterministic Discretization

At this point, we have discussed an approximation process that has yielded a discretization of the stochastic sub-problem. That is, on our now finite stochastic dimension we have finite-order expansions of the vector of RVs in the domain of the PCE. We have yet to discuss the Fourier coefficients, which are still defined on the continuum domain **D**. To accomplish our overall computation, we must discretize these as well.

The strategy that we assumed in this project, which is based on a finite element approach, is to discretize and approximate the functions $r(x, y)$ and $\phi_i(x)$, the domain **D**, and the operator represented by the equality in Eqn. (7.2) using a finite element strategy on the grid and shape function set of the original deterministic problem. The residual equations comprise a discrete generalized matrix eigenvalue problem on the same degrees of freedom. At this point, both the $\phi_i(x)$, and concomitantly, the $a_i(x)$, in Eqns. (7.1) and (7.7) will have been discretized on the finite element mesh and interpolated either to the node locations or the elements depending on the natural modeling context for the RF.

Computational realizations of the approximate RF for α are now specified on the finite element mesh given for $\mathbf{D}_\alpha$.

7.3 Putting Things Together: Non-Intrusive UQ

At this point, we have given a fairly concise overview of what a RF is, and how we get to a discretized version of Eqn. (7.7) suitable for using in a computational setting. The question now is: How do we assess the effects, say, of a RF representing an input parametric uncertainty on the system response?

Consider the input-output Model Problem depicted in Figure 7.3-1, which can be represented as

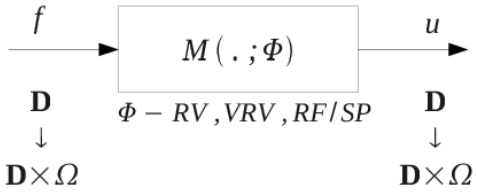

Figure 7.3-1. Model Problem.

$$u = \mathbf{M}(f; \Phi). \tag{7.9}$$

In Eqn. (7.9), **M** is the operator, f the system external input, u the output or system response, and Φ is representing, generally, a vector containing any parameters that may be present in the transformation from input to response. Examples could include parameters in material constitutive models, or even boundary or initial conditions. Here, we will consider the case of a parameters in material models as RFs, and we will set $\Phi = \alpha$, a scalar, real-valued RF.

When we have an input or parameter in our system that is a RF (or even a RV), we have implicitly migrated the deterministic output function to one requiring a probability space as a constituent. We will expand this similarly to α to arrive at a PCE for the output

$$\tilde{u} = \sum_{i=0}^{n_u} u_i(x)\Gamma_i(\boldsymbol{\xi}), \tag{7.10}$$

where we comment that n_u here is generally different than n in the sum of Eqn. (7.7).

To compute the approximate output, $\tilde{u}$, we must compute the (discretized) Fourier coefficients, $u_i(x)$, in Eqn. (7.10). We do this by substituting the expansions for u and α into Eqn. (7.9), subtracting the right hand side from both sides of this equation, then, as with any Galerkin scheme, projecting the result onto the Hermite polynomials. When we do this, we arrive at the following expression for the u_i

$$u_i = \frac{E[\mathbf{M}(f;\tilde{u})\,\Gamma_i]}{E[\Gamma_i^2]} \tag{7.11}$$

where we have exploited the orthogonality of the Γ_i relative to the multidimensional standard normal measure. This explains why the PCE and more generally the Askey pairings use special functions from Sturm-Liouville eigensystems, and also demonstrates that the basis function/RV pairings are made by comparisons with the Sturm-Liouville weighting function and the PDFs of RVs in them.

In our simplified RF analysis framework, depicted graphically in Figure 7.3-2, we used the SNL software package Dakota (Eldred et al. 2007a, 2007b, 2007c) as a driver and other user tools developed at SNL for constructing the discretized $\tilde{u}$ (`ComputeKL`), for taking the input RV realizations passed from Dakota via plain-text files and using them to generate realizations for $\tilde{u}$ (`RealizeRF`), and for passing this information to the given Sierra analysis codes. The mechanism we used was via entity identifiers, such as material blocks or element side sets, with the realization values embedded as variables into ExodusII databases. We identified that data entity and variable name to the analysis code using Sierra user input in appropriate sections. Previously, we also coordinated with Sierra code developers to define how this data is to be accessed by the analysis code, and to ensure that the heterogeneous data is processed by the code correctly. Finally, we provided a means to post-process the analysis code output to the actual realization of $\tilde{u}$, and put them all together using a user-defined function shell script interface per Dakota requirements.

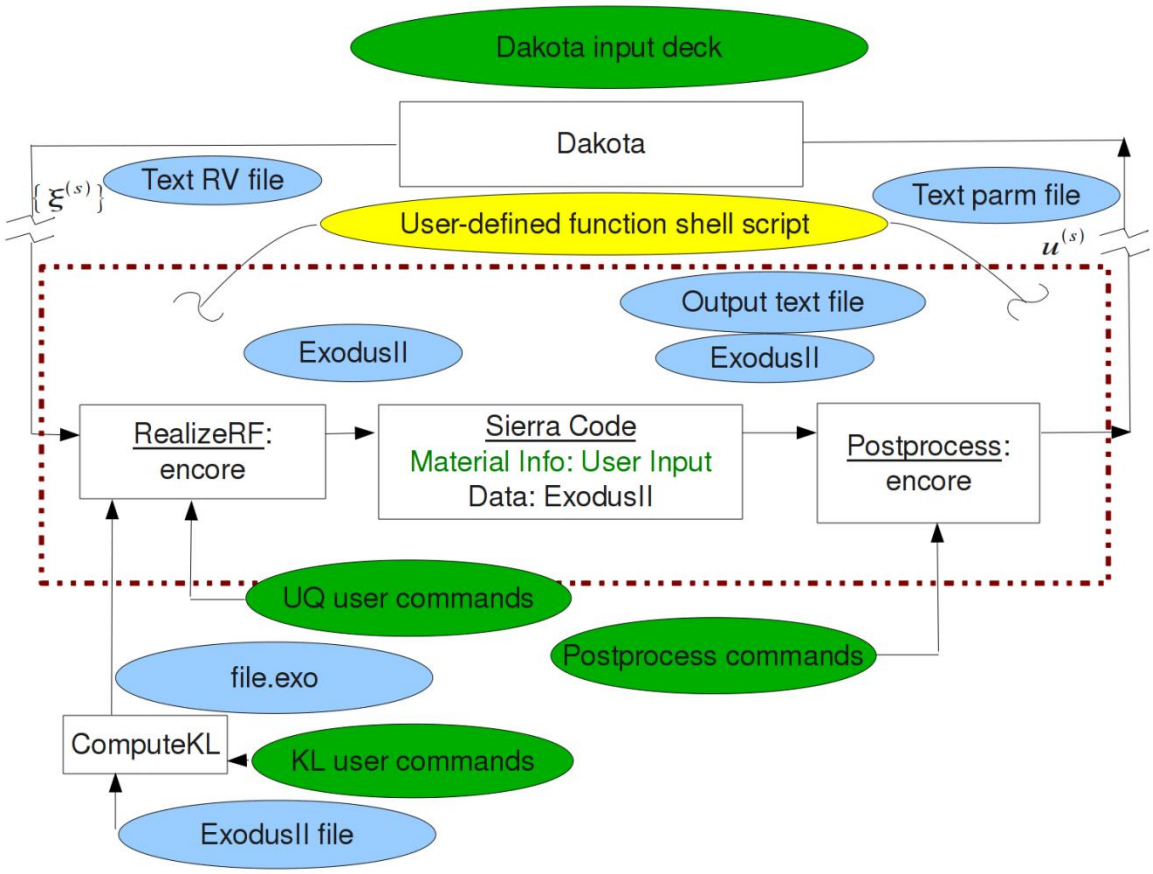

Figure 7.3-2. Graphical depiction of Sierra/Dakota RF framework.

In the next section, we illustrate this newly developed capability via our example application.

7.4 Example Application: Porous Flow

An important application of random fields is modeling uncertain material properties of subsurface zones, for use in reservoir modeling of transport of water, hydrocarbons, chemicals, and more recently, in carbon sequestration. We illustrate in this section the use of a scalar random field that models the intrinsic permeability in a subsurface zone.

Our test problem is a three-dimensional reservoir simulation for carbon sequestration. The domain D is a rectangular volume of dimension $600 \times 30 \times 500$ meters with the vertical direction along the y-coordinate. An abandoned well is located near one corner of the domain, extending upwards for an additional 130 meters. The simulation code models the two-phase transport of brine and CO_2 within the reservoir as a flux of CO_2 enters the reservoir from another well at one corner of the domain. The main response quantity of interest is the time history of the CO_2 leakage out of the top of the well.

The stochastic nature of the simulation arises from the unknown intrinsic permeability of the reservoir, which we model as a spatial random field K. In order to generate realizations of K and

thus of the CO_2 leakage, we build a truncated KL series representation of K. Using a mesh of approximately 90,000 hex elements, we solve the approximate KL eigenvalue problem

$$\int_D r(x,y)\,\phi(y)\,dy = \lambda\,\phi(x), \quad x \in D \tag{7.12}$$

using a Galerkin finite element based on piecewise constant basis functions. The covariance kernel was anistropic, using length scales $L = (50,5,25)$ and parametric form

$$r(x,y) = \prod_{d=1}^{3} \exp\left(-\frac{|x_d - y_d|}{L_d}\right). \tag{7.13}$$

The matrix associated with the discrete problem is an $N \times N$ dense matrix with $N \approx 90{,}000$, which cannot be stored in memory. Our solver for the KL eigenproblem is based on a matrix free operator (implemented in the Sierra/Encore code) and a Krylov-based iterative Davidson solver (implemented in the Trilinos/Anasazi code). The KL solver was run on 24 processors requiring about 15 hours of wall clock time in order to compute the first ten pairs of eigenvalues and eigenfunctions. We plot four of the ten eigenfunctions in Figure 7-4.1. The ten eigenvalues ranged from 41870 down to 28325.

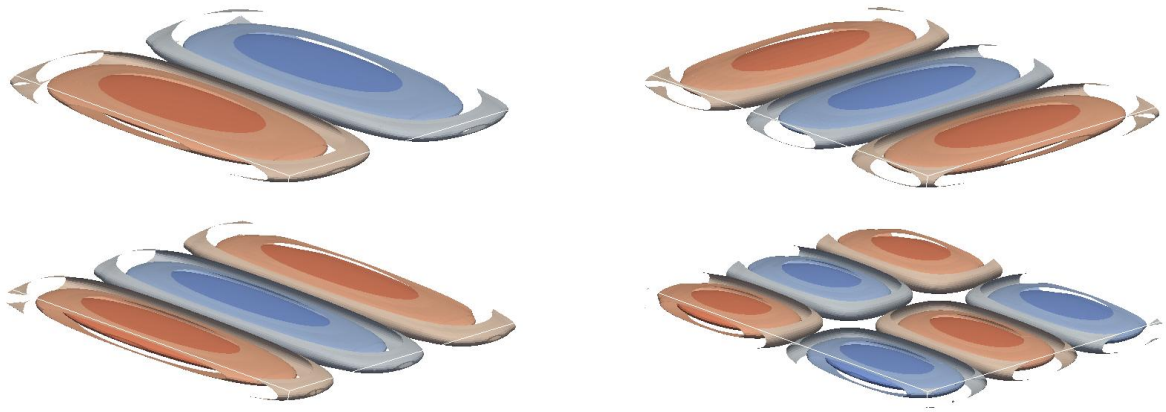

Figure 7.4-1. KL eigenfunctions 3, 4, 8 and 10 for the log intrinsic permeability $\alpha = \log K$

The representation of K then took the form

$$K \approx K_0\,10^{\alpha}, \quad \alpha \equiv \sum_{i=1}^{N} \sqrt{\lambda_i}\,\phi_i\,\eta_i \tag{7.14}$$

where K_0=1e-14 is the mean value of K and $\{(\lambda_i, \phi_i)\}_{i=1}^{N}$ are the (approximate) solutions to Eqn. (7.12). In this case the zero-mean random field α is actually the logarithm of the random field K.

The coefficients $\{\eta_i\}_{i=1}^{N}$ are uncorrelated random variables with no spatial dependence, the "coordinates" of the random field in stochastic space. They also have mean zero and unit variance. For this calculation, we made the additional assumption that they were distributed as Gaussian RVs. Due to the constraints imposed by the KL eigenproblem, this implies that they were independent identically distributed (iid) standard normal random variables.

For the nondeterministic simulation, we chose $N = 4$ and computed a polynomial response function over this four-dimensional space for the maximum CO_2 leakage flux over a specified time (150 days). This was done using the DAKOTA software tool using a non-intrusive sparse grid integration of level three. The total number of model runs required was 201, each requiring 4-10 hours of wall clock time using 32 processors. A sample plot of a realization of K and the resulting CO_2 saturation field is shown in Figure 7-4.2. The effect of the non-uniform permeability can be seen in the increased mobility of CO_2 along the right hand boundary. The resulting surrogate model was sampled until a distribution function was obtained for the maximum CO_2 leakage flux (see Figure 7.4-3). We can also plot the time history of the CO_2 leakage flux for a number of realizations to see the spread in the data. At any point in time, a distribution could be calculated by the same integration method used for the maximum CO_2 leakage flux. In Figure 7.4-4 a representative sample of time histories are shown for the CO_2 leakage flux (as a percentage of the input CO_2 flux from the well). We see agreement for about the first 50 days, but then significant divergence occurs by about 100 days.

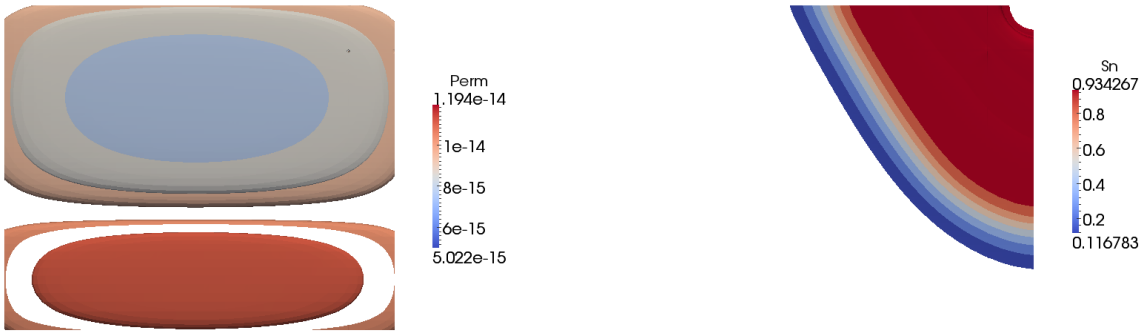

Figure 7.4-2. Sample realization of K using sparse grid integration from DAKOTA. (left) contours of K. (right) contours of CO_2 saturation at 150 days.

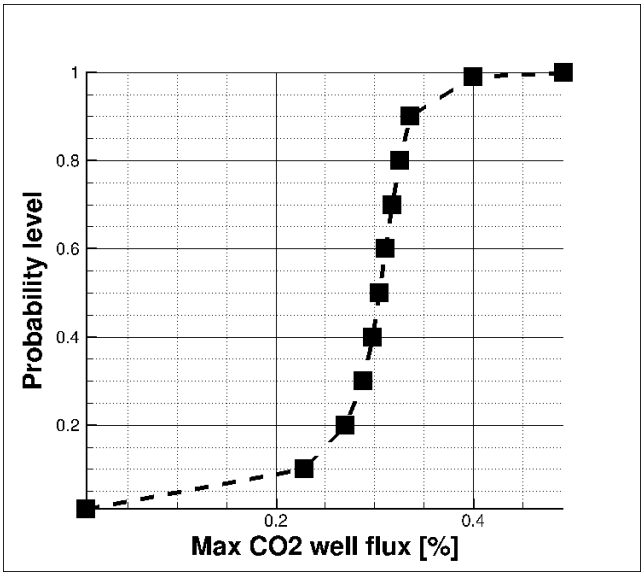

Figure 7.4-3. Cumulative distribution function for maximum CO_2 leakage flux.

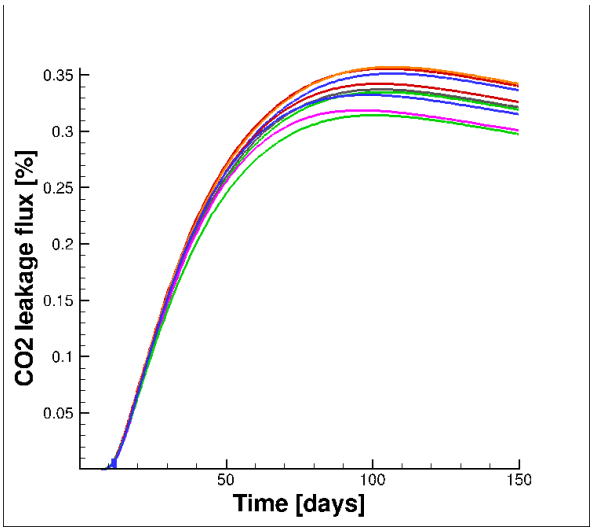

Figure 7.4-4. Sample time histories of CO_2 leakage flux for some realizations of K.

7.5 Example Application: Soil Properties

In this section, we extend the methods of the previous section to develop a generalization to conditional simulations, which, for example, constrain a random field to match limited, sparse data acquired via experimental measurement.

Let $K(\mathbf{x}) > 0$, $\mathbf{x} \in D$, represent a soil property of interest (e.g., permeability, porosity, density, etc.) in region $D \subset \mathbb{R}^3$. In this section, we propose a non-Gaussian random field model for K, and provide algorithms to generate statistical samples of this model.

Typical information on K includes one or more of the following: (i) the mean function; (ii) the covariance function; (iii) the marginal distribution, that is, $\Pr(K(\mathbf{x}) \leq a)$, for all $a \in \mathbb{R}$; and (iv) a collection of n measurements, denoted by $\kappa_1, \ldots, \kappa_n$, taken at sites $\mathbf{u}_1, \ldots, \mathbf{u}_n \in D$. Note that one or more of the measurements $\{\kappa_j\}$ may be subject to measurement uncertainty. In section 7.5.1, we propose a model that is consistent with each piece of information listed above; algorithms to generate independent realizations of the model are discussed in section 7.5.2. Several examples are provided in section 7.5.3, including models for soil properties over one- and two-dimensional spatial domains.

7.5.1 Model Definition

Let K be a random field expressed as

$$K(\mathbf{x}) = \mu(\mathbf{x}) + \sigma(\mathbf{x})\,\overline{K}(\mathbf{x}),\ \mathbf{x} \in D, \tag{7.15}$$

where $\mu(\mathbf{x}) = \mathrm{E}[K(\mathbf{x})]$ and $\sigma^2(\mathbf{x}) = \mathrm{Var}[K(\mathbf{x})]$ are deterministic functions that denote the mean and variance of K, respectively, and $\overline{K}(\mathbf{x})$ is a random field with zero mean and unit variance. Herein we model $\overline{K}$ as

$$\overline{K}(\mathbf{x}) = h(G(\mathbf{x}); \mathbf{x}) = F^{-1} \circ \Phi(G(\mathbf{x})), \tag{7.16}$$

where G is a Gaussian random field with zero mean, unit variance, and covariance function $\rho(\mathbf{x},\mathbf{y}) = \mathrm{E}[G(\mathbf{x})\,G(\mathbf{y})]$, Φ is the CDF of a standard Gaussian random variable, that is, $\Phi(u) = (2\pi)^{-1/2}\int_{-\infty}^{u} e^{-v^2/2}\,\mathrm{d}v$, and F is an arbitrary CDF with zero mean and unit variance. It is common to refer to G as the Gaussian image of $\overline{K}$.

We note that $\overline{K}$ and K are Gaussian fields if, and only if, $F = \Phi$; otherwise $\overline{K}$ and K are non-Gaussian. Further, $\overline{K}$ is a homogeneous random field if, and only if, G is homogeneous and the mapping h is independent of $\mathbf{x} \in D$; otherwise $\overline{K}$ is inhomogeneous. K defined by Eqn. (7.15) is homogeneous if, and only if, $\overline{K}$ is homogeneous and $\mu(\mathbf{x}) = \mu$ and $\sigma(\mathbf{x}) = \sigma$ are independent of $\mathbf{x}$.

The marginal distribution and covariance functions of random field K can be expressed in terms of F and ρ defined above. The marginal CDF of K is

$$\begin{aligned}\Pr(K(\mathbf{x}) \le a) &= \Pr\left(\overline{K}(\mathbf{x}) \le \tfrac{a-\mu(\mathbf{x})}{\sigma(\mathbf{x})}\right)\\ &= \Pr\left(G(\mathbf{x}) \le \Phi^{-1} \circ F\left(\tfrac{a-\mu(\mathbf{x})}{\sigma(\mathbf{x})}\right)\right)\\ &= F\left(\tfrac{a-\mu(\mathbf{x})}{\sigma(\mathbf{x})}\right)\end{aligned} \tag{7.17}$$

where F is defined by Eqn. (7.16). The covariance function of K is

$$c(\mathbf{x},\mathbf{y}) = \mathrm{Cov}[K(\mathbf{x})\,K(\mathbf{y})] = \sigma(\mathbf{x})\,\sigma(\mathbf{y})\,\xi(\mathbf{x},\mathbf{y}) \tag{7.18}$$

where

$$\xi(\mathbf{x},\mathbf{y}) = \mathrm{E}[\overline{K}(\mathbf{x})\,\overline{K}(\mathbf{y})] = \int_{\mathbb{R}^2} h(u;\mathbf{x})\,h(v;\mathbf{y})\,\phi_2(u,v;\rho(\mathbf{x},\mathbf{y}))\,\mathrm{d}u\,\mathrm{d}v, \tag{7.19}$$

is the covariance function of $\overline{K}$, $h(u;\mathbf{x})$ is defined by Eqn. (7.16), $\phi_2(u,v;\rho)$ denotes the joint PDF of a zero mean Gaussian random vector with two coordinates and covariance matrix $\begin{bmatrix}1 & \rho\\ \rho & 1\end{bmatrix}$, and $\sigma(\mathbf{x}) = \sqrt{c(\mathbf{x},\mathbf{x})}$. In general, there is no closed-form solution to Eqn. (7.19) so that solutions for ξ must be obtained numerically.

We propose the model for K defined by Eqns. (7.15) and (7.16) for several reasons. First, by careful selection of quantities μ, σ, F, and ρ, the random field K can be calibrated to match specified second-moment properties and marginal distributions. Second, the calibration of K to the measured data is also straightforward by requiring G to be a conditional Gaussian random field. Third, the non-Gaussian random field K is simply a mapping of a suitable Gaussian random field G. Hence, generating samples of K is straightforward and involves two steps: (i) generate samples of Gaussian field G using, for example, its Karhunen-Loéve expansion; and (ii)

map each sample by Eqns. (7.15) and (7.16) to produce samples of K. Alternatively, step (ii) can be achieved via the polynomial chaos approximation.

7.5.2 Sample Generation

As mentioned, suppose that the following information on K, the random field representing a particular soil property of interest over D, is known and available:

- $\mu(\mathbf{x}) = \mathrm{E}[K(\mathbf{x})]$, the mean function;
- $c(\mathbf{x},\mathbf{y}) = \mathrm{E}[(K(\mathbf{x}) - \mu(\mathbf{x}))\,(K(\mathbf{y}) - \mu(\mathbf{y}))]$, the covariance function, for any two points $\mathbf{x}$ and $\mathbf{y}$ in D;
- The marginal distribution of $\overline{K}$, $F(a;\mathbf{x}) = \Pr(\overline{K}(\mathbf{x}) \le a)$, for all $a > 0$; and
- A collection of n permeability measurements, denoted by $\kappa_1, \ldots, \kappa_n > 0$, taken at sites $\mathbf{u}_1, \ldots, \mathbf{u}_n \in D$. The measurements may or may not be taken error free.

Our approach can be generalized to the case where some of the items above are unknown. For example, we can use the measurement data to estimate the mean and/or covariance functions of K.

The following four steps can be used to calibrate K, the random field model for permeability, and to generate independent samples of K over D:

1. Map the measured data on K to G via
$$g_j = \Phi^{-1} \circ F\left(\frac{\kappa_j - \mu(\mathbf{u}_j)}{\sigma(\mathbf{u}_j)}\right) \tag{7.20}$$
2. Solve for ξ as a function of $\rho \in [-1,1]$ using Eqn. (7.19). Invert this relationship to solve for $\rho(\mathbf{x},\mathbf{y})$ as a function of $\xi(\mathbf{x},\mathbf{y}) = c(\mathbf{x},\mathbf{y})/\sqrt{c(\mathbf{x},\mathbf{x})\,c(\mathbf{y},\mathbf{y})}$.
3. Generate samples of Gaussian field G, a Gaussian random field with zero mean and covariance function ρ using, for example, its Karhunen-Loéve expansion. Enforce G to interpolate through $\{g_j,\ j = 1, \ldots, n\}$ by making it a conditional Gaussian random field (see Appendix C).
4. Map each sample of G to a sample of K using Eqns. (7.15) and (7.16). Alternatively, the polynomial chaos approximation can be used for this step.

7.5.3 Examples

We next present two examples to illustrate the calibration and sample generation of the random field K. The first is limited to one spatial dimension and is completely academic so as to illustrate various features of the approach. We then consider a more realistic example over a 2D spatial domain.

1D random field

Here we construct $K(\mathbf{x}) = K(x)$, a non-Gaussian random field over a 1D spatial domain, $x \in D = (0,1)$. The following information on K is assumed known:

$$\mu(x) = \frac{1}{2}\sin(\pi x),$$

$$c(x,y) = \frac{1}{10}e^{-|x-y|/5}, \text{and}$$

$$F(a) = \Phi(\ln a),\ a > 0. \tag{7.21}$$

By Eqn. (7.21), K is a lognormal random field with mean $\mu(x)$, covariance function $c(x-y)$, and constant variance $\sigma^2 = 1/10$. Suppose further that $n = 3$ measurements $\kappa_1 = 1.35$, $\kappa_2 = 1.57$, and $\kappa_3 = 1.28$, are taken at sites $u_1 = 1/4$, $u_2 = 1/3$, and $u_3 = 3/4$, without error.

Shown in Figure 7.5-1(a) are 100 samples of $K(x)$ calibrated to the available information using the approach presented in section 1.5.2; the measurements (u_j, κ_j), $j = 1,2,3$, are denoted by blue dots in the figure. We note that, because all measurements are assumed error free, each sample of K passes through the points (u_j, κ_j), $j = 1,2,3$. Further, the variance of the field is greatest at points x far from any measurement site.

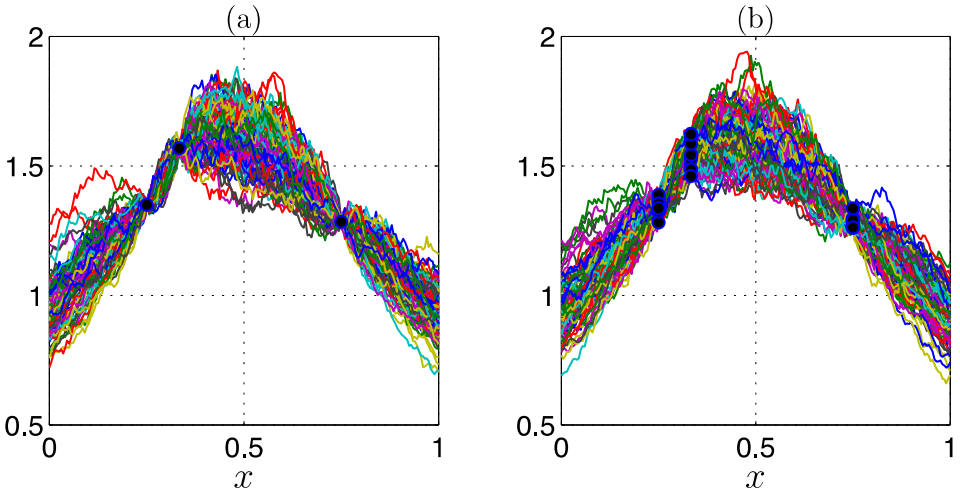

Figure 7.5-1. 100 samples of random field $K(x)$ assuming: (a) perfect measurements, and (b) measurement errors.

Suppose now that each site measurement is subject to experimental error, and the statistics of these errors are known. For illustrative purposes we assume the κ_i, $i = 1,2,3$, to be iid lognormal random variables each with variance $1/10$; the mean values of κ_1, κ_2, and κ_3 in this case coincide with the measurements without error listed above. Figure 7.5-1(b) illustrates 100 samples of $K(x)$ for this case. In general, the inclusion of measurement error leads to increased variance in the process for all $x \in (0,1)$.

2D random field

In this section, we illustrate the use of the proposed model over a 2D spatial domain by considering a particular data set of interest to the geostatistical community. Data on coal ash for the Robena Mine Property in Greene County, PA, is listed in Table 7.5-1; this data is taken directly from (Cressie 1993). The values for u_1 and u_2 define the site locations and correspond to east-west and north-south coordinates, respectively, and the values for the measurements κ are in units of per cent coal ash. For this example, we assume all measurements are taken without error; the extension of the method to include measurement error is straightforward as demonstrated in section 7.5.3.

Table 7.5-1. Available coal ash measurements (taken from [Cressie 1993, 34]).

u_1	u_2	κ (% coal ash)	u_1	u_2	κ (% coal ash)
4	7	11.11	7	10	9.16
4	8	11.04	7	11	10.7
4	9	11.75	7	12	8.45
4	10	10.17	8	7	8.69
4	11	9.37	8	8	11.58
4	12	10.11	8	9	10.19
5	7	10.96	8	10	10.04
5	8	10.28	8	11	9.27
5	9	9.78	8	12	8.9
5	10	10.55	9	7	11.17
5	11	11.21	9	8	9.46
5	12	11.46	9	9	9.15
6	7	10.83	9	10	11.19
6	8	13.07	9	11	9.28
6	9	11	9	12	8.07
6	10	11.61	10	7	9.39
6	11	9.93	10	8	8.54
6	12	10.41	10	9	8.15
7	7	10.09	10	10	8.1
7	8	10.47	10	11	10.13
7	9	9.79	10	12	7.96

Cressie and other authors have studied this data set extensively, and applied various kriging interpolation methods. Herein, we apply the proposed random field $K(x_1, x_2)$ to model per cent coal ash over domain $D = [4,7] \times [10,12]$. The mean of the field is assumed to take the form

$$\mu(\mathbf{x}) = \mu(x_1, x_2) = a_0 + a_1\, x_1 + a_2\, x_2 + a_3\, x_1\, x_2, \tag{7.22}$$

where a_j, $j = 0,1,2,3$, are coefficients determined using linear regression analysis on the available date from Table 7.5-1. Further, the covariance function of K is given by

$$c(\mathbf{x},\mathbf{y}) = \sqrt{c(\mathbf{x},\mathbf{x})\, c(\mathbf{y},\mathbf{y})}\, \xi(\mathbf{x},\mathbf{y}) \tag{7.23}$$

where ξ, defined by Eqn. (7.19), has been estimated by Cressie (see [Cressie 1993, 157]).

One sample of $K(x_1, x_2)$, the random field modeling per cent coal ash over D is illustrated by Figure 7.5-2 assuming the marginal distribution of K is Gaussian, i.e., assuming F defined by Eqn. (7.16) is given by Φ, the CDF of the standard Gaussian random variable. The measurements listed in Table 7.5-1 are also shown and denoted by black dots in the figure.

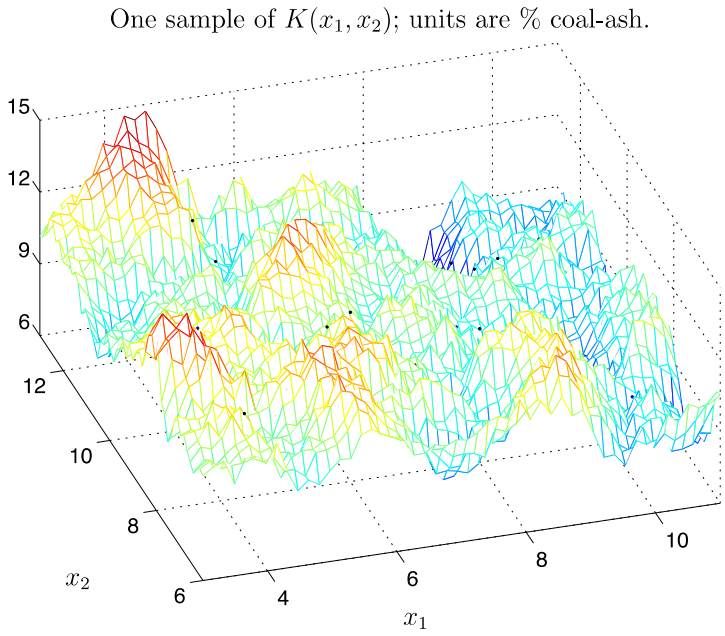

Figure 7.5-2. One sample of Gaussian random field modeling coal-ash.

Of coarse, a Gaussian distribution may be inappropriate when modeling percent coal ash since it permits small but negative values for K. Therefore, consider Figure 7.5-3, which is identical to Figure 7.5-2 except that we have assumed the marginal distribution of the field K to be uniform rather than Gaussian. Note that in both cases, because it is assumed all measurements are taken without error, the samples of K pass through each measurement point.

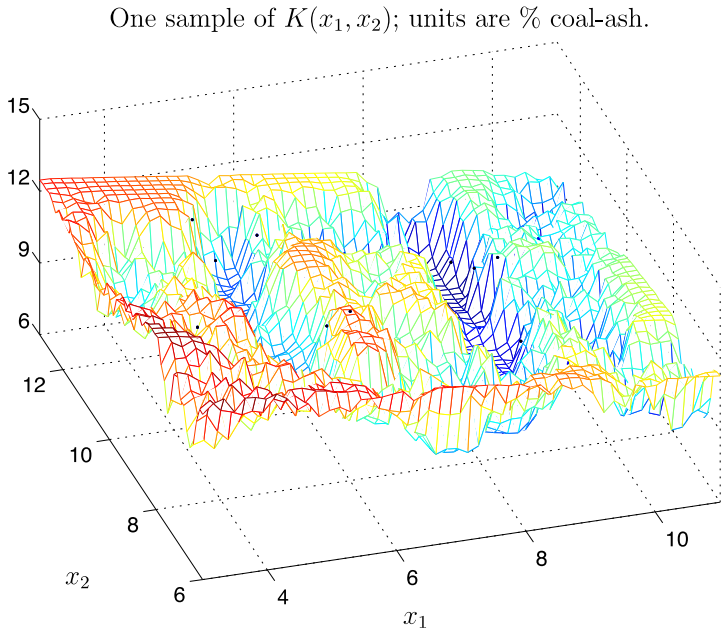

Figure 7.5-3. One sample of uniform random field modeling coal-ash.

7.6 Conditional Simulation by Kriging

Here we discuss another method to model soil properties based on a kriging conditional simulation combined with the PCE/KL approach. We start with the brief introduction to kriging and then augment it with a probabilistic description based on PCE.

7.6.1 Brief Introduction to Kriging

Consider an RF, $Z_0(x, \omega)$, where Z could be, for example, permeability of the soil, and x an element of the spatial domain, **D**. We assume that $Z_0(x, \omega)$ has a covariance function C as defined in Eqn. (7.6), but with the additional property that it depends functionally only on the difference in the spatial locations. I.e. $C(x, y) = C(h)$ with $h = (x - y)$. We all assume mean, $\mu(x)$, which is possibly spatial dependent. To account for non-zero mean of the underlying process regression terms are included in the functional form of predictor. We will closely follow Sasena (2002) and Lophaven et al. (2002) to describe kriging predictor with regression, also known as *universal kriging* in the geological applications. Our unknown random field is represented by following model:

$$Z(\mathbf{x}, \omega) = \mathbf{f}^T \boldsymbol{\beta} + \mathbf{Y}(\mathbf{x}, \omega) \tag{7.24}$$

where **f** is a vector of the regression functions:

$$\mathbf{f} = [f_1(x), f_2(x), \cdots, f_k(x)]^T \tag{7.25}$$

β vector of unknown constants

$$\boldsymbol{\beta} = [\beta_1, \beta_2, \cdots, \beta_k]^T$$

and **Y** is zero mean random process.

We also introduce an $n \times k$ matrix $\mathbf{F}$

$$\mathbf{F} = \begin{bmatrix} f_1(x_1) & f_2(x_1) & \cdots & f_k(x_1) \\ \vdots & & & \vdots \\ f_1(x_n) & f_2(x_n) & \cdots & f_k(x_n) \end{bmatrix}$$

where the f_i are described in Eqn. (7.25). A vector of sampled values that represents a realization of the stochastic process at x_i is given by

$$\mathbf{z^{(s)}} = \left[Z^{(s)}(x_1), Z^{(s)}(x_2), \cdots, Z^{(s)}(x_n)\right]^T$$

and, for the sampled data, Eqn. (7.24) can be rewritten as:

$$\mathbf{z^{(s)}} = \mathbf{F\beta} + \mathbf{y} \tag{7.26}$$

where

$$\mathbf{y} = [Y(x_1), Y(x_2), \cdots, Y(x_n)]^T$$

We would like to construct predictor

$$\hat{\mathbf{z}} = \mathbf{c_x^T z}$$

which is linear with respect to sampled data, unbiased and has minimum variance property. This type of predictor is usually referred to as Best Linear Unbiased Predictor (BLUP). The condition of the predictor being unbiased is expressed as follows, after multiplying Eqn. (7.26) by $\mathbf{c}_x^T$ and taking the expectation of the result,

$$E[\hat{\mathbf{z}}] = E[\mathbf{c_x}^T \mathbf{z}] = E[\mathbf{c_x}^T \mathbf{F\beta}] + E[\mathbf{c_x}^T \mathbf{y}] \, .$$

It can be shown after some linear algebra manipulations that solution for predictor takes form Eqn. (7.19):

$$\hat{\mathbf{z}}(x) = \mathbf{c_x z} = \mathbf{f}_x^T \widehat{\boldsymbol{\beta}} + \mathbf{r_x}^T \mathbf{R}^{-1}(z - \mathbf{F}\widehat{\boldsymbol{\beta}}) \tag{7.27}$$

where

$$\widehat{\boldsymbol{\beta}} = (\mathbf{F}^T \mathbf{R}^{-1} \mathbf{F}) \mathbf{F}^T \mathbf{R}^{-1} \mathbf{z} \tag{7.28}$$

7.7 Conditional Simulation

Given data sampled from the random field at points x_α, realizations of that random field conditioned on data can be constructed. One of the methods to achieve that is so-called *conditioning by kriging* (Journel 1981). The method requires constructing a kriging predictor for

sampled data, $Z_{0K}(x, Z_0(x_\alpha))$, as well as an additional zero-mean independent random field $Z_s(x)$ with the same covariance $C(h)$ and then a second kriging predictor, $Z_{sK}(x)$, built using realizations of the $Z_s(x_\alpha)$. The new conditioned random field takes form

$$Z_{sc}(x) = Z_{0K}(x, Z_0(x_\alpha)) + [Z_s(x) - Z_{sK}(x, Z_s(x_\alpha))] \,. \tag{7.29}$$

It is possible to show that a RF defined by Eqn. (7.29) has covariance $C(h)$ and, since kriging is an interpolator, realizations of this RF match the data at the sample points. We show a typical example of this method of conditional simulation in Figure 7.7-1, where we show a full-field RF conditional simulation, and in Figure 7.7-2 we zoom into the plot to observe the typical behavior at the data sample points where the reader can see that the simulated RF is constrained to pass through the data at those points.

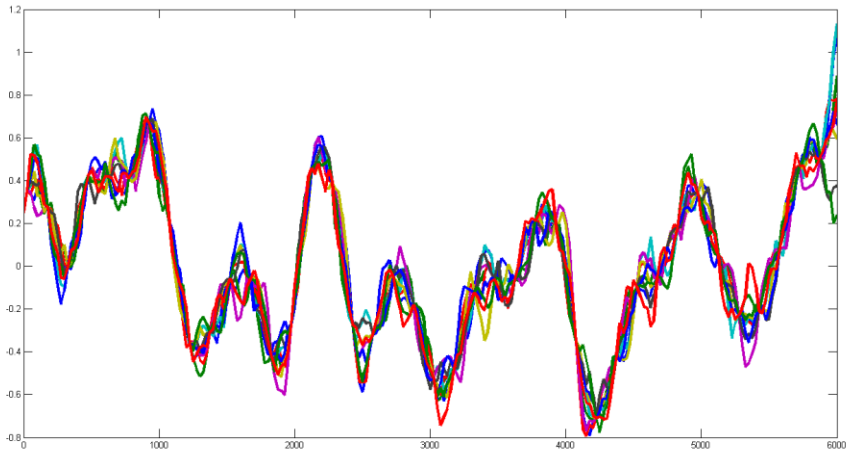

Figure 7.7-1. Typical example of kriging conditional simulation

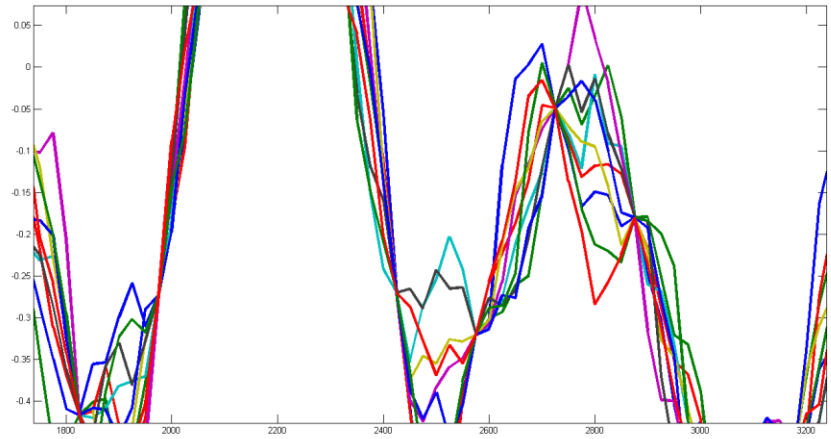

Figure 7.7-2. Zoom of kriging conditional simulation at a sampled data points

The ability to perform this conditional simulation depends on the generation of unconditioned random field $Z_s(x)$ with prescribed covariance. One possible method is based on the KL expansion, similar to Eqn. (7.1):

$$Z_s(x) = \sum_{i=0}^{N} \sqrt{\lambda_i}\phi_i(x)\eta_i \tag{7.30}$$

where, as before, λ_i and ϕ_i are eigenvalues and eigenvectors of the KL eigenproblem, Eqn. (7.2).

While this equation can be solved using a standard spatial discretization approach, as was described in the Section 2.2, a new, potentially very efficient method is being explored based on approximation of the kernel, $R(x, y)$, in the KL eigenproblem, and reducing it to degenerate form Eqn. (7.20). A detailed description of this method will be the subject of a separate report.

Non-gaussian conditional simulation can be achieved by proper selection of the $Z_s(x)$. Non-gaussian properties can be modeled by selection of non-normal η_i in the Eqn. (7.30), method described in section 7.5, or by the procedure presented in Sakamoto and Ghanem (2002). A comparison of these procedures and the selection of the most efficient is the subject of future research.

7.7.1 The Nexus to RF Expansion

Our conditional simulation, while generally based on an KL expansion, needs to be put into a form that: (1) adheres to the original assumptions on the covariance; (2) is amenable to fitting to data; and (3) is amenable to its use in generating samples of the target RF. To satisfy all three, we are proposing to convert the KL random variables, η_i from Eqn. (7.1), which after truncation can be assembled into a zero-mean unit-correlation vector of RVs, into an expression in terms of a vector standard normal RVs. Ultimately, we will express the KL RVs as a dependent PCE.

Conceptually, in the scenario where full probabilistic information is available, this step is always possible using the so-called *Rosenblatt transformation* (Rosenblatt 1952) along with an intermediate vector of uniform RVs with components U_i. Assuming a stochastic dimension of n, the n-dimensional transformation for the case where the η_i are all absolutely continuous (Rosenthal 2000) is based on the following identity:

$$\begin{aligned} u_1 \quad & P\{\eta_1 \le h_1\} = F_1(h_1) \\ u_2 \quad & P\{\eta_2 \le h_2 | \eta_1 = h_1\} = F_2(h_2|h_1) \\ \vdots & \\ u_n \quad & P\{\eta_n \le h_n | \eta_{n-1} = h_{n-1}, \dots, \eta_1 = h_1\} = F_n(h_k|h_{n-1}, \dots, h_1) \end{aligned} \tag{7.31}$$

where the $F_i(\,\cdot\,|\,\cdot\,)$ are Conditional Cumulative Distribution Functions (CCDFs) (Rosenthal 2000). Interested readers should refer to Rosenblatt (1952) to convince themselves that the transformation, $\mathbf{u} = T_1(\mathbf{h})$, of the real vector, $\mathbf{h}$, into the real vector, $\mathbf{u}$, will take the vector of RVs, η_i, into a vector of uniform RVs, $\mathbf{U}$, the latter of which can be shown to have components, U_j, that are independent, uniform RVs on the interval $[0,1]$ of $\mathbb{R}$. That is,

$$\mathbf{U} = T_1(\boldsymbol{\eta}) \tag{7.32}$$

where the vectors are defined in the natural way relative to the component RVs. We note that this is the vector RV extension to the transformation described in Eqn. (7.16) . We also note that for the case where the η_j have discontinuous CCDFs, a similar transformation process is still possible although beyond the scope of our brief discussion here.

To complete our full transformation, we perform the same process, only now from a vector of independent standard normal RVs, $\boldsymbol{\xi}$, to uniform using T_2. Now using the common vector of uniform RVs as the nexus one can readily see that the transformation from KL RVs to standard normal RVs is given by

$$\boldsymbol{\eta} = T_1^{-1} T_2(\boldsymbol{\xi}) = T(\boldsymbol{\xi}) \ . \tag{7.33}$$

The equality is, by definition, in distribution.

Once we have the transformation in Eqn. (7.33), it is a simple matter to build a polynomial chaos expansion for the $\boldsymbol{\eta}$ by making the appropriate symbol transcriptions in Eqn. (7.7) and replacing the RF, α, in Eqn. (7.8) with the vector $T(\boldsymbol{\xi})$, and truncating based on an mean-square error criterion.

In constructing the above transformation, we re-emphasize that we assumed that we had full probability information available to us. Unfortunately, this is rarely if ever the case. We now turn to the problem of building a finite-order PCE expansion for $\boldsymbol{\xi}$ in the face of limited data, which has only recently gained attention in the research community, and thus is left as a subject for future work.

We start with an explicit statement of our expansion

$$\hat{\boldsymbol{\eta}}(\boldsymbol{\xi}) = \sum_{i=0}^{m} \mathbf{g}_i \Gamma_i(\boldsymbol{\xi}), \tag{7.34}$$

where each of the PCE coefficients, $\mathbf{g}_i$, is an n-vector, as is $\boldsymbol{\eta}$ and $\boldsymbol{\xi}$, and the $\Gamma_i(\boldsymbol{\xi})$ are the Hermite polynomials now accommodating a vector argument. We will need to estimate the coefficients with the proviso that $\hat{\boldsymbol{\eta}}$ satisfies the KL RV criteria of zero mean and delta correlation as given in Eqn. (7.5). Note that in the conceptual case described above, the Rosenblatt transformation, these constraints are satisfied by definition through the canonical nature of the KL expansion.

We derive our $\hat{\boldsymbol{\eta}}$ samples, $\hat{\boldsymbol{\eta}}^{(s)}, s = 1, \dots, M$ from M samples of the original data using the identity given by Eqn. (7.4) using our now discretized eigenfunctions from the KL eigenproblem, Eqn. (7.2), for our sample covariance.

In Ghanem et al. (2008), the authors assumed that the components of $\hat{\boldsymbol{\eta}}$ were statistically independent and estimated the PCE coefficients of the uncoupled expansions one at a time using a maximum likelihood estimation (MLE) approach constrained by the KL RV criteria. Thus, they maximized the likelihood function

$$L(g_{kj}; j = 1, \dots, p) = \prod_{i=1}^{M} p_{\hat{\eta}_{(k)}}(\hat{\eta}_k^{(i)} | g_{kj}; j = 1, \dots, p) \tag{7.35}$$

where the g_{kj} are the p PCE coefficients in the expansion for $\hat{\eta}_k$, $p(\cdot \mid \cdot)$ is the Conditional PDF of the data given a set of coefficients. Finally, the maximization constraint is

$$\sum_{j=1}^{p} g_{kj}^2 = 1 \ . \tag{7.36}$$

Desceliers et al. (2007) followed a similar path by again assuming independence of the KL RVs η_i in an MLE approach, although the authors assembled a full likelihood for all the expansion coefficients simultaneously before executing the constrained optimization process.

Arnst et al. (2010) take this a step further by adding a Bayes estimation process to estimate posterior probabilities for the $\boldsymbol{\eta}_i$. In their approach, they use a Markov-Chain Monte Carlo (MCMC) sampling scheme to estimate the likelihoods in conjunction with Maximum Entropy-based priors. This approach allows one to consider the PCE coefficients as themselves random variables whose uncertainty domain models the epistemic uncertainty due to data limitations.

While none of the above related techniques were implemented during the course of our work, we emphasize that the attractive feature is that the correlation function that we assume in the construction of our conditional simulation is not modified due to the constraint represented by Eqn. (7.5).

7.8 Concluding Remarks on RF Expansions

In this section, we have motivated the use of Karhunen-Loève based random field expansions both as a means to minimize the stochastic dimension in the representations of random fields, as well as their computational efficiency vs. sampling-based methods for uncertainty propagation. We then described two methods for generating conditional simulations of these random fields based on these expansions.

8. Applications

8.1 Introduction

This chapter includes several applications and studies performed during this project. They are included to illustrate the scope of analyses that have been performed and to demonstrate numerical analysis capabilities that are available in the Sierra software. The applications also serve to demonstrate completion of milestone goals set at the beginning of the project.

8.2 Leaky Well—Benchmark and Effect of Heterogeneity

Injection of CO_2 into formations containing brine has been proposed as a long-term sequestration solution. A significant obstacle to sequestration performance is the presence of existing wells providing a transport pathway out of the sequestration formation. The leaky well benchmark study by Class et al. (2009) was designed to test a wide range of mathematical and numerical models applied to specific aspects of CO_2 sequestration. The models tested include: COORES (developed at IFP Energies), DuMu^x (developed at University of Stuttgart), ECLIPSE (developed at Schlumberger), ELSA (developed at Princeton University), FEHM (developed at Los Alamos National Laboratory), GEM (developed by the Computer Modeling Group), GPRS (developed at Stanford University), IPARS-CO_2 (developed at UT/Austin), MoReS (developed by Shell), MUFTE (developed at University of Stuttgart), ROCKFLOW (developed jointly by the German Federal Institute for Geosciences and Natural Resources and the University of Hannover), RTADD2 (developed by The French Geological Survey), TOUGH2 (developed at Lawrence Berkeley National Laboratory), and VESA (developed at Princeton University). Three benchmark problems were tested in the study. The first problem explores the leakage rate of CO_2 into overlying formations through a leaky well. This problem was used as a starting point in the current research as a way to verify that the multiphase fluid dynamics models used here replicate the results from the benchmark study and to explore the effect of heterogeneity on the leak rate.

A cross section of the leaky well scenario taken from Class et al. (2009) is shown in Figure 8.2-1. The model domain is 1,000 by 1,000 m with an injection well at the center and a single leaky well 100 m away. The geologic formation consists of two 30 m aquifers separated by a 100 m aquitard. CO_2 is injected at a constant rate into the lower aquifer for the duration of the simulation. The leak rate is measured as a fraction of the total CO_2 injected, monitored at the midpoint in the aquitard along the leaky well. Table 8.2-1 presents the pertinent fluid and material properties, along with details of the domain and applied initial/boundary conditions, used in the benchmark study.

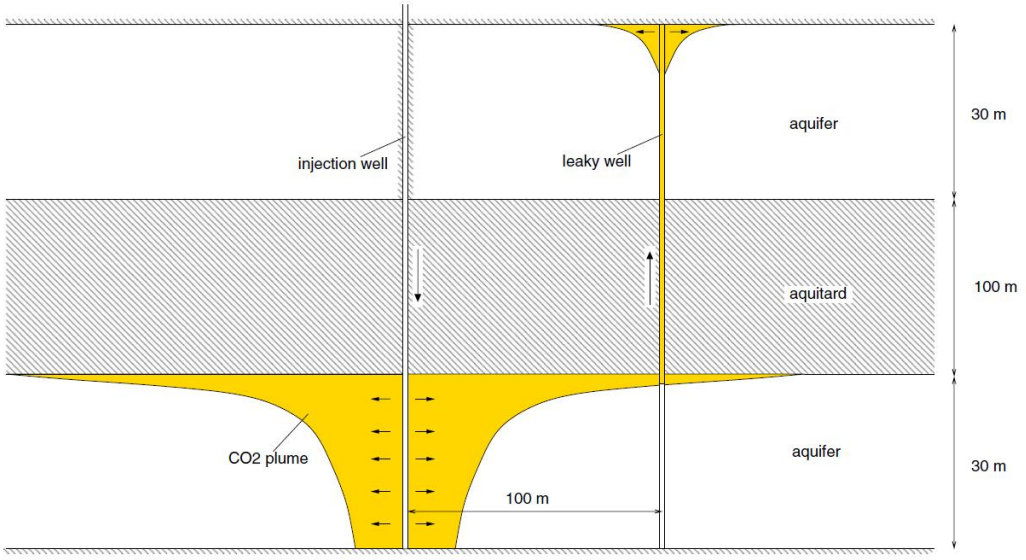

Figure 8.2-1. Cross-section of the 3D leaky well benchmark study (taken from Class et al.).

Table 8.2-1. Geometry, fluid and material properties, and initial/boundary conditions for the leaky well benchmark study.

Parameter		Value	Units
Domain geometry	Aquifer depth	2,840-3,000	m
	Aquifer thickness	30	m
	Aquitard thickness	100	m
	Dimensions of the model domain	1,000 x 1,000 x 160	m
	Distance between wells	100	m
	Leaky and injection well radius	0.15	m
Fluid properties	CO_2 density	479	kg/m^3
	Brine density	1,045	kg/m^3
	CO_2 viscosity	3.950E-05	Pa-s
	Brine viscosity	2.535E-04	Pa-s
Porous media properties	Aquifer permeability	2E-14	m^2
	Leaky well permeability	1E-12	m^2
	Porosity	0.15	-
	Residual brine saturation	0	-
	Residual CO_2 saturation	0	-
	Relative permeability	Linear (kra = Sa)	
	Capillary pressure	-	
Initial conditions, boundary conditions and simulation time	Initial conditions	Hydrostatic pressure distribution	Pa
	Initial saturation	Brine	-
	Initial pressure	3.086E07	Pa
	Lateral boundary conditions	Dirichlet equal to initial conditions	Pa
	Top and bottom boundary conditions	No Flow	
	Injection rate	8.87	kg/s
	Simulation time	1000	days

8.2.1 The Leaky Well Benchmark Problem

To reduce computations and facilitate visualization, one half of the full three-dimensional model described above was taken by cutting with a vertical plane of symmetry along the x-axis through the midpoints of the injection and leaky wells. A structured mesh composed of just over 431,000 finite elements (hexahedral) was used. The height of each of the aquifers was discretized into 10 equal intervals of 3 m. Smaller elements were used in the vicinity of the wells and between the wells increasing in size toward the outer boundaries.

The boundary and initial conditions are as given in Table 8.2-1 except that the boundary of symmetry created by the cutting plane is treated as no flow. Additionally, the CO_2 saturation was held at zero over the outside lateral boundaries of the lower aquifer. This simulation was carried out to 1200 days using 2809 adaptive time steps. Calculations were run on 480 processors for 3.5 days.

Figure 8.2-2 shows the CO_2 saturation at 200 days. The CO_2 is injected along the entire depth of the injection well but rises to the top of the aquifer as it spreads outward. Recall that the top of the lower aquifer is adjacent to the impermeable aquitard and is represented with a no-flow condition. The CO_2 has risen through the leaky well and into the upper aquifer. There the spreading is again predominately at the top surface.

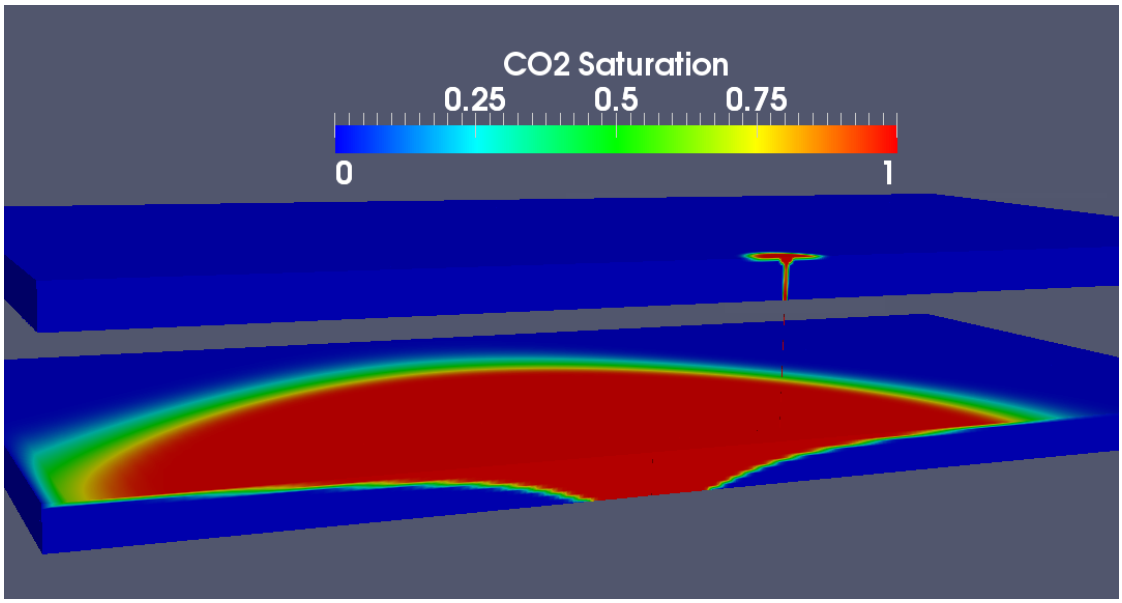

Figure 8.2-2. CO_2 saturation at 200 days.

Class uses a semi-analytical solution to define values of specific measures of simulation results. One measure is the approximate time it takes for the injected CO_2 to reach the leaky well (arrival time). The CO_2 is declared to have arrived at the leaky well when the leakage value exceeds $5x10^{-3}$%. The leakage value is defined as the calculated leakage rate taken at the midpoint of the aquitard in the leaky well divided by the injection rate and expressed as a percentage. The other measures are the maximum leakage value, and the leakage value at 1000 days. Table 8.2-2 compares the values of the three measures for the semi-analytical solution, the simulation

presented by Class et al., and the Sierra/Aria results. The Sierra/Aria values fall between the values for those of the semi-analytical solution and Class et al., except for the maximum leakage value which is 3.6% lower than that reported by Class et al.

Table 8.2-2. Measures of comparison between solutions.

Measure	Semi-analytical	Class et al. results	Sierra/Aria results	Units
Approximate arrival time of CO_2	14	8	11	days
Maximum leakage value	0.231	0.222	0.214	%
Leakage value at t=1,000 days	0.109	0.126	0.116	%

In addition to Sierra/Aria, STOMP, developed at Pacific Northwest National Laboratory (White and Oostrom 2006), was also used to model this problem and add insight into differences in results. STOMP uses finite difference methods to solve the PDEs that describe multiphase fluid dynamics. Sierra/Aria and STOMP differ in their inclusion of capillary pressure. STOMP simulations must include a capillary pressure vs. saturation curve. While this function can specify low values of capillary pressure, the amount cannot be set to zero as the Class et al. benchmark problem defines. The leaky well scenario setup in STOMP uses a quarter section of the model domain and assumes symmetry (no flow) along the internal axis. The problem specifications used by STOMP are given in Table 8.2-1. A minimal amount of capillary pressure is defined using a Van Genutchen function.

The range in leakage rates (max and min), as calculated by the 14 numerical models included in the benchmark study, are shown as dotted gray lines in Figure 8.2-3. The Sierra/Aria result is within the range of results reported in Class et al. The discrepancy in the peak leak rate, as calculated by STOMP, is believed to be a result of capillary pressure. STOMP requires some degree of capillary pressure in the model setup, and while this was set very low, the capillary pressure at the leaky well must be overcome to push CO_2 into the upper aquifer.

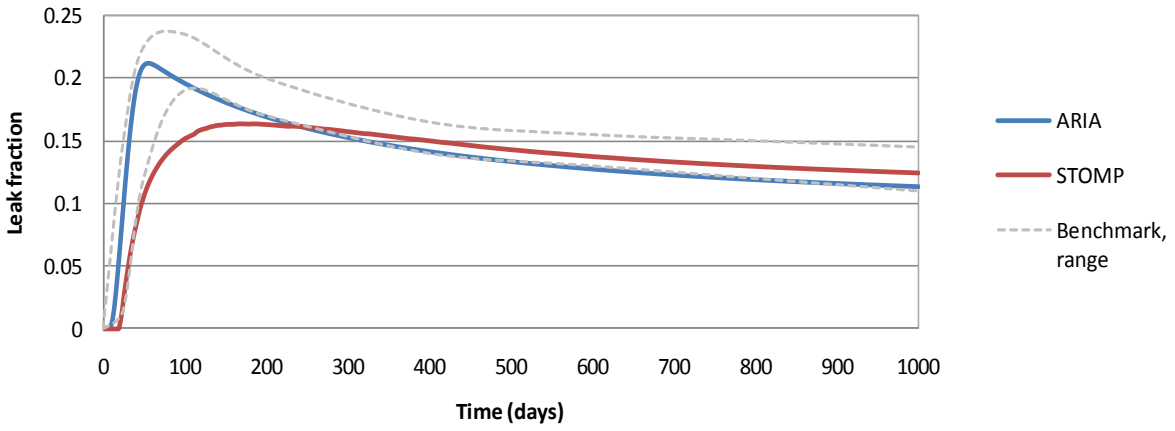

Figure 8.2-3. Time history of leakage value calculated by study participants.

8.2.2 Effect of Heterogeneity on Leakage Rates

The problem described in section 8.2.1 was used to explore the effect of material heterogeneity on the calculated leakage value. To facilitate computing multiple solutions using Aria, the computational demand of a simulation was reduced by using a quarter section of the domain as described in the model used by STOMP, and the upper aquifer is removed. The leaky well extends to the mid-point between the upper and low aquifers, where the pressure is held at the initial hydrostatic value. This will affect the leakage rates computed in this study compared to the benchmark. Also, to account for the heterogeneity in all directions, the leaky well was moved 45 degrees into the domain along a radial distance of 100 m from the injection well reducing the impact of the no-flow symmetry boundary. Ten different spatially correlated heterogeneous permeability and porosity fields were generated over the domain of interest using Sequential Gaussian Simulation (SGSIM). These heterogeneous fields are read from a file and stored as "field" vectors in Aria. Porosity values were selected from a Normal distribution over the range 0.1 to 0.2. The permeability values were selected from a lognormal distribution with direction-dependent correlation lengths as given in Table 8.2-3.

Table 8.2-3. Correlation lengths of heterogeneous permeability fields.

Direction	Correlation Length	Units
x-axis	50	m
y-axis	25	m
z-axis	5	m

Figure 8.2-4 shows the distribution of the permeability values generated over a regular grid and then interpolated to the nearest nodal location of the finite element mesh used in the simulation. The permeability field used in one of the simulations is shown in Figure 8.2-5.

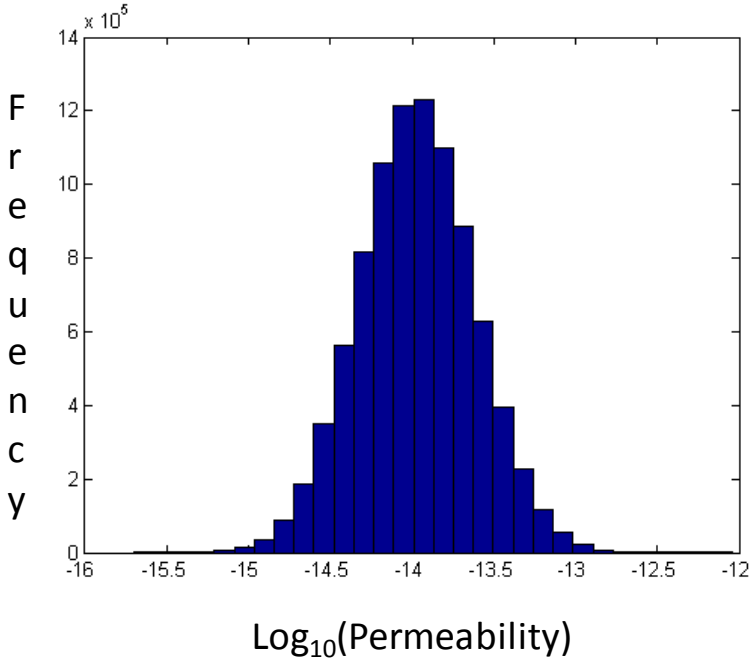

Figure 8.2-4. Assumed distribution of permeability.

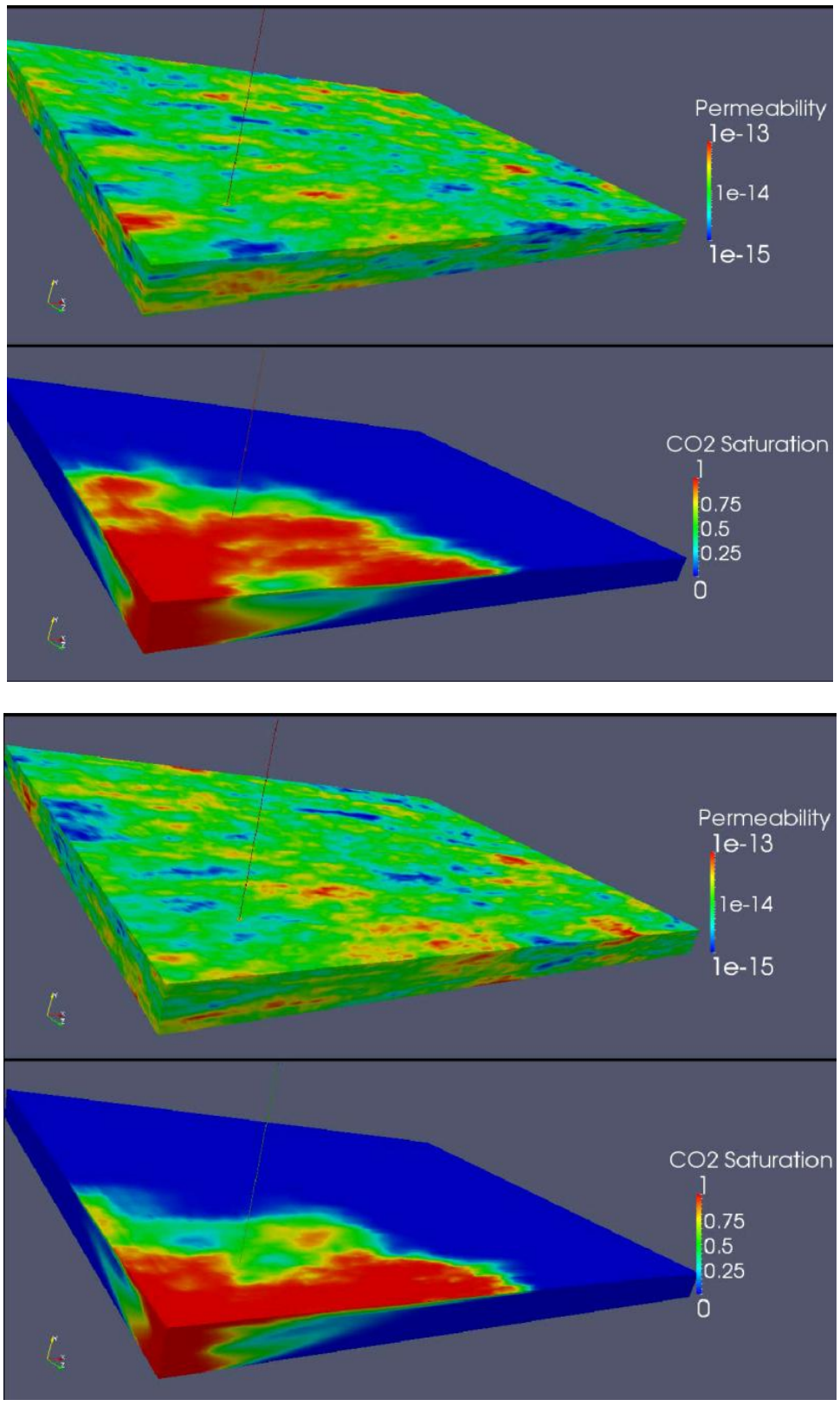

Figure 8.2-5. Two realizations of a spatially-correlated heterogeneous permeability field (top) and the corresponding CO_2 saturation at 80 days (bottom).

The simulation described in section 8.2.1, with geometry modifications described here, was run using each of the ten permeability fields. In this quarter section model, the injection well is at the left and front corner; the leaky well is visible along a diagonal in the interior of the domain. Two of the permeability fields generated by SGSIM are shown in Figure 8.2-5 with the corresponding calculated CO_2 saturation at 80 days. The location of low permeability zones can clearly be seen in the saturation distribution. Also, in the second realization example, the appearance of CO_2 at a high permeability zone on the surface suggests a faster subsurface path.

In two dimensions, the flow is more likely to be forced through a zone of low permeability and will eventually meet the leaky well. However in three dimensions, the flow may circumvent low permeability zones resulting in a faster travel time or a high permeability zone may divert the flow from ever reaching the leaky well. Therefore, one would expect the computed leakage value from a three-dimensional heterogeneous permeability field to exhibit greater variation.

The time history of the computed leakage value for each of the ten realizations is shown in Figure 8.2-6 and can be compared to the leakage value produced using the original constant permeability (Figure 8.2-3). As expected, the amount of CO_2 reaching the leaky well and its time-dependence shows significant variation. The leakage value average and standard deviation of the ten realizations are presented in Figure 8.2-7. The average in this problem is not directly comparable to the benchmark owing to geometry changes and the approximated outflow boundary conditions applied to the truncated well. To get a sense of the adequacy of ten realizations, a running average leakage value time history was computed as each realization was included. Figure 8.2-8 shows the average when including 1, 3, 6, 9, and all 10 realizations. There is only a small change in the average after the eighth realization is included.

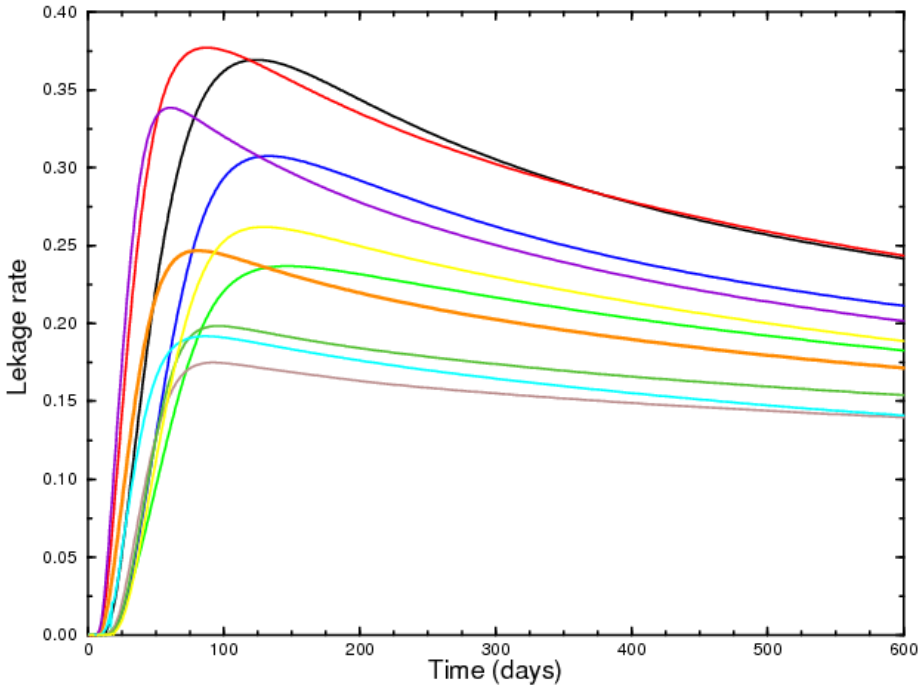

Figure 8.2-6. Comparison of leakage time histories for ten realizations.

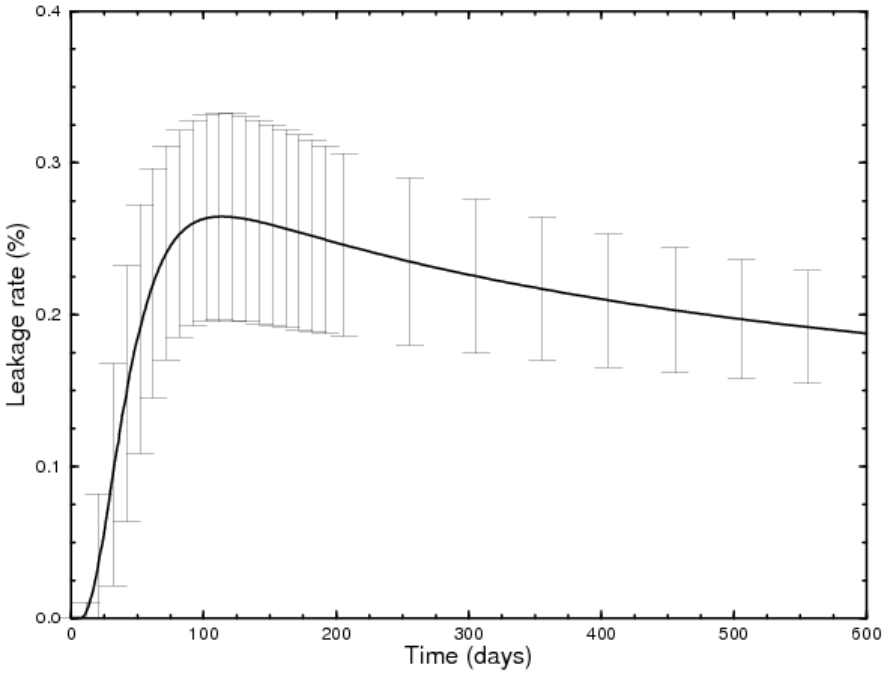

Figure 8.2-7. Average (curve) and standard deviation (bars) of leakage time histories for ten realizations.

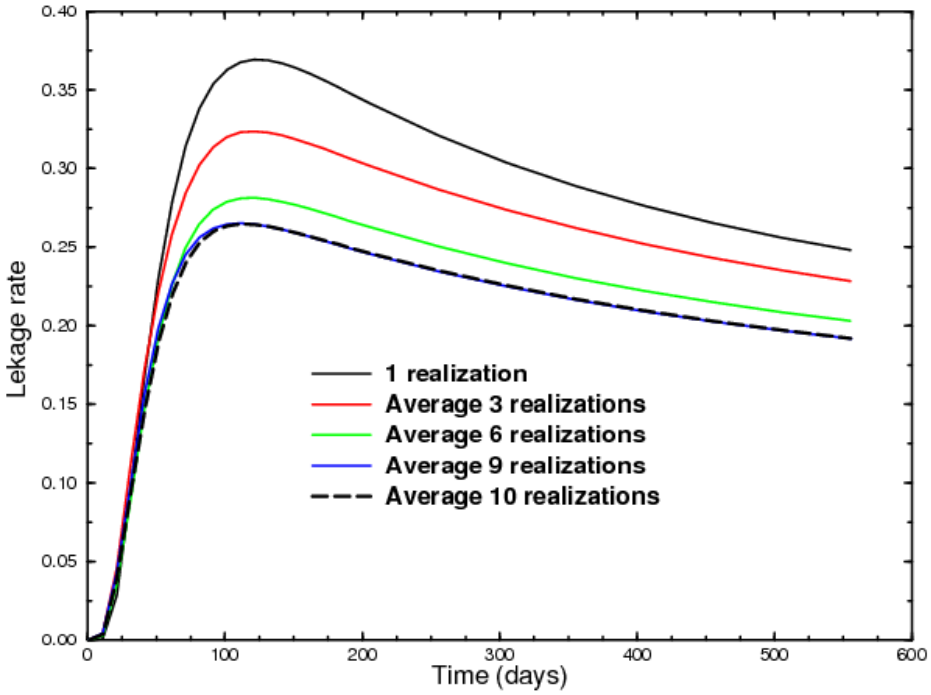

Figure 8.2-8. Running average of leakage time histories.

8.2.3 Geologic Controls in CO_2 Loss from a Leaky Well

To better understand how specific geologic controls impact the leakage rate, we employ three dimensional models of the CO_2 injection process into a sandstone aquifer with shale inclusions. The leaky well scenario used in this analysis replicates the benchmark study described in Class et al. (2009) with the addition of aquifer heterogeneity and capillary pressure. Simulations are carried out using STOMP (White and Oostrom 2006). The original intent was to perform a similar calculation with Aria, but this part of the study was never completed due to time constraints. Here, we examine the impact of heterogeneity on the amount of CO_2 released through a leaky well. A "design of experiments" approach is used to identify the most important parameters and combinations of parameters to control CO_2 migration while making efficient use of a limited number of computations. Additionally, two-dimensional and three-dimensional simulations are compared to quantify the influence that surrounding geologic media has on the CO_2 leakage rate.

Design of experiments is commonly used to analyze physical experiments to determine the relative importance of individual factors and combinations of factors on experimental results (Montgomery 2000). The design of experiments approach also determines the best set of experiments to run to avoid bias. With numerical experiments, randomization is not an issue, however, this approach is useful when considering numerical simulations that have a large number of factors or take a long time to run. Individual simulations in this study take approximately 3.5 days to run on a workstation with total available RAM memory of 11.3 GB. Given the long runtime, identifying key simulations to explore the parameter space is an important first step to the research.

The design of experiments analysis considers three factors related to heterogeneity that might influence the leak rate of CO_2 from a well. These factors are stratigraphic dip angle, shale inclusion size and shale fraction. For each factor, three levels are considered. These levels are segmented into low (-1), medium (0) and high (1) values for each factor. The three levels for stratigraphic dip are -15 degrees (dipping away from the leaky well), no dip, and 15 degrees (dipping towards the leaky well). The shale inclusion size is set to 25 m, 50 m, and 75 m. The size defines the diameter of a circular shale inclusion. The shale fraction is set to 10%, 20% and 30% of the total aquifer volume. The full factorial design, therefore, requires 3^3, or 27, simulations. Additionally, 4 realizations are run for each simulation.

Stratigraphic dip is added to the model by changing the hydrostatic boundary conditions. In this way, the aquifer heterogeneity and well configuration does not change between simulations using -15, 0, or +15 degree dip. While this facilitates not having to change the model grid for each instance of dip, the assumption does imply that the wells are always perpendicular to the stratigraphy. Based on the dip direction, the hydrostatic boundary conditions are symmetric across the line bisecting the injection and leaky well. The model domain is one half the model domain specified by Class et al. as described in section 8.2.1.

Heterogeneous fields are generated using ELLIPSIM. The ELLIPSIM program is included in the publicly available Geostatistical Software LIBrary (GSLIB) (Deutsch and Journel 1998). ELLIPSIM creates shale inclusions of a specified length, width and thickness over the model domain given a specified total area (or percent) for the inclusions. In this case, we define circular

lenses using the shale inclusion size. Each inclusion is 1 m thick. The shale fraction defines the total volume for the shale inclusions in the aquifer. An example ELLIPSIM field is shown in Figure 8.2-9, this field defines the heterogeneity in the lower aquifer. Simulation results include CO_2 saturation (i.e., Figure 8.2-10) and cumulative CO_2 leaked out of the lower aquifer after 1000 days (Figure 8.2-11).

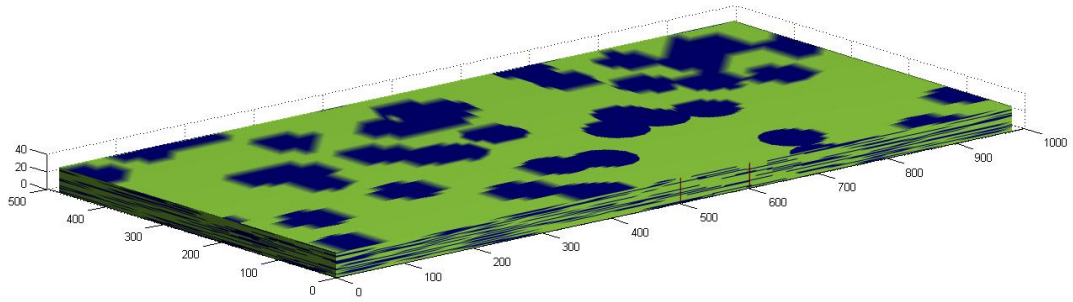

Figure 8.2-9. 3D view of heterogeneity in the lower aquifer. Example shows shale inclusions (blue) with 75 m diameter covering 30% of the domain surrounded by sand (green). The blocky nature of the shale inclusions on the outer regions of the model is due to grid discretization. The two vertical red lines indicate the position of the injection and leaky well.

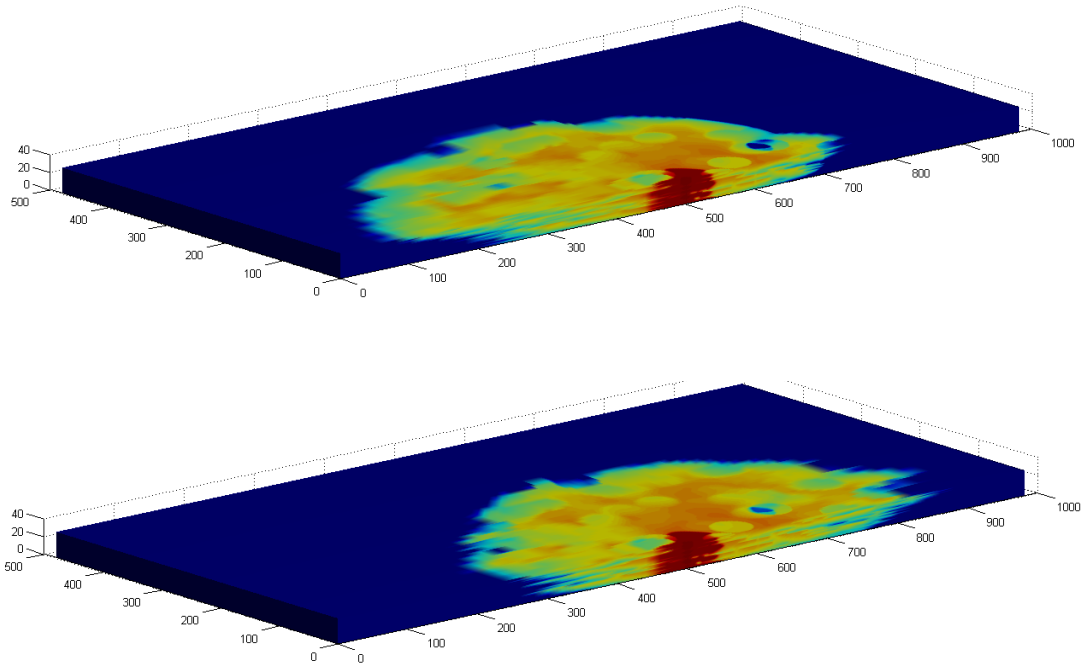

Figure 8.2-10. 3D view of CO_2 saturation in the lower aquifer after 500 days using the heterogeneity shown in Figure 8.2-9. The top figure has a negative dip, the bottom figure has a positive dip.

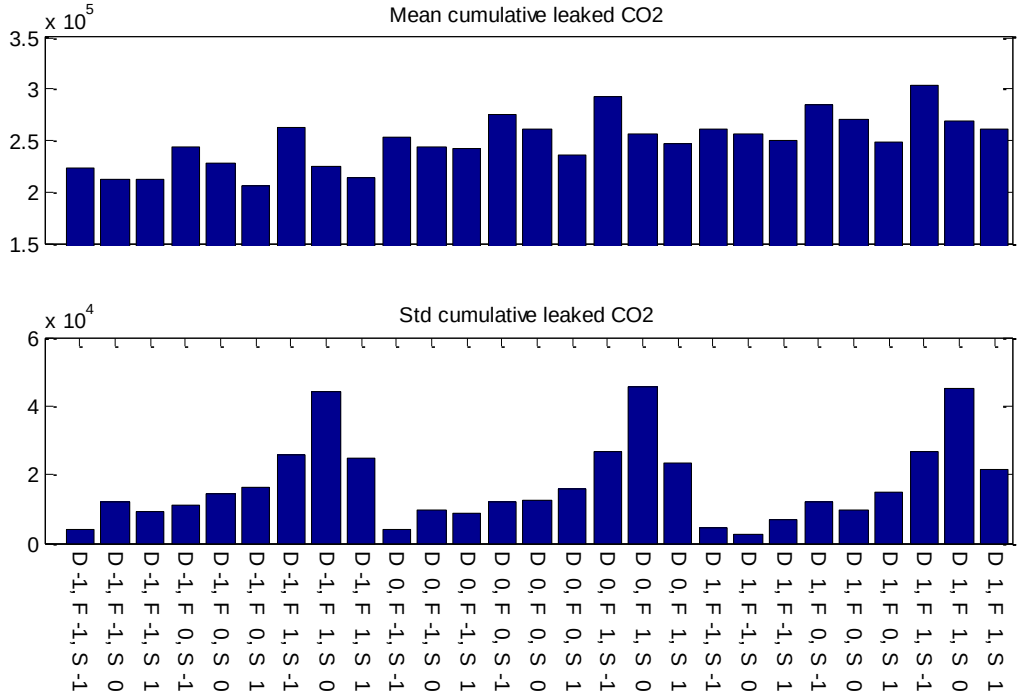

Figure 8.2-11. Mean and standard deviation of the cumulative leaked CO_2 for the 27 simulations and 4 realizations used in the design of experiments. D = stratigraphic dip, F = shale fraction, and S = shale inclusion size. Each factor has one of three levels, -1 = low, 0 = medium, 1 = high.

The mean cumulative leaked CO_2, based on the 27 simulations and 4 realizations from the design of experiments, shows a gradual increase in the leaked CO_2 with increasing dip. In the case where stratigraphic dip is positive (in the direction of the leaky well), the leak rate is increased. Dip, in conjunction with the buoyant force, plays a large role in CO_2 migration as seen in Figure 8.2-9. Additionally, cumulative leaked CO_2 increases slightly as the size of the shale inclusion decreases. The standard deviation of the leaked CO_2 shows that the variation in simulation results increases significantly as shale fraction increases.

The design of experiments analysis uses the mean cumulative leaked CO_2 to rank main and interaction effects using regression coefficients. The polynomial model includes the intercept, linear and quadratic interaction terms (Eqn. (8.1)). Main effects are defined by a single factor, while interaction effects are defined by two of the three factors.

$$y(x) = a_0 + \sum_{i=0}^{N} a_i x_i + \sum_{i<j}^{N} a_{ij} x_i x_j \tag{8.1}$$

Table 8.2-4 ranks the regression coefficient for each main and interaction effect. Results show that dip has the highest influence on the leak rate of CO_2. The second and third most influential factors are the shale inclusion size and shale fraction, respectively. The interaction between shale fraction and shale inclusion size is nearly as influential as shale fraction alone. The other

interaction terms (related to stratigraphic dip) are far less influential. The regression coefficients are used to create a quadratic response surface model, shown in Figure 8.2-12. The response surface illustrates that the lowest leak rate is associated with a negative dip, low shale fraction and high shale inclusion size while a high leak rate is associated with just the opposite. Due to the high variability in results related to the shale fraction, more realizations are needed to explore the interaction effects between shale fraction and shale inclusion size. Stratigraphic dip is not commonly included in simulation studies for carbon sequestration. While a limited number of simulations were used for this analysis, the results demonstrate the importance of dip on long term storage of CO_2.

Table 8.2-4. Design of experiments main and interaction effects, ranked according to influence on the leakage rate.

Main and interaction effect	Regression Coefficient	Rank
Stratigraphic dip	20924.3	1
Shale fraction	9993.2	3
Shale inclusion size	15567.0	2
Stratigraphic dip and shale fraction	928.9	5
Stratigraphic dip and shale inclusion size	764.0	6
Shale fraction and shale inclusion size	8731.9	4

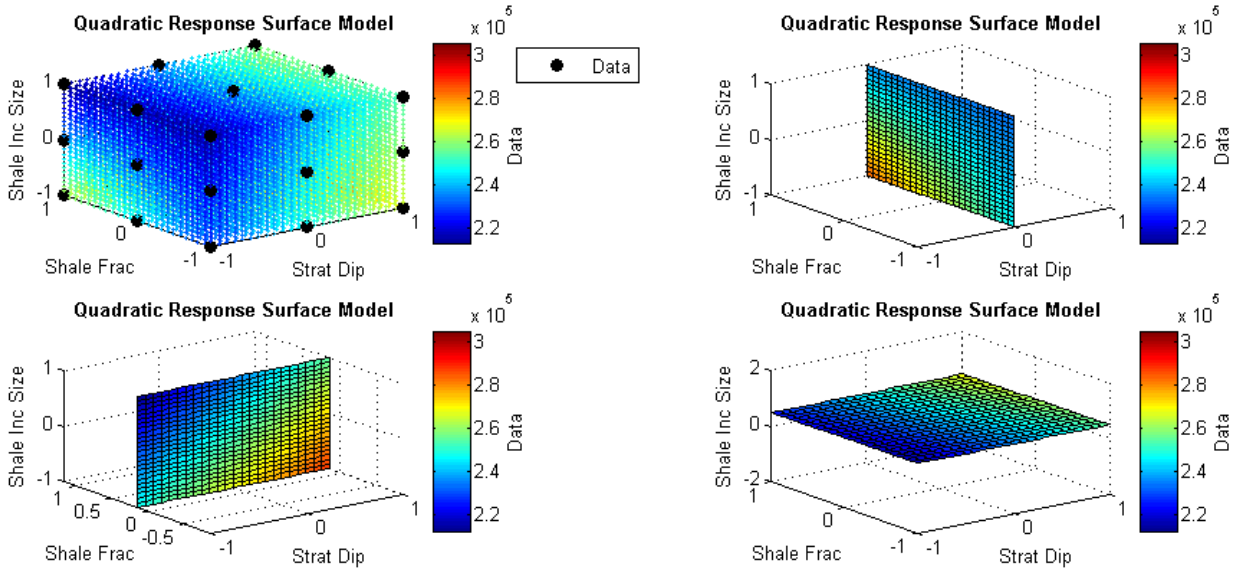

Figure 8.2-12. Response surface model from the design of experiments. The experimental data points are marked in the upper left plot. The data associated with the color bar is the average leak rate. -1, 0, and1 refer to the low, medium, and high levels for each of the factors.

Given the long run time for the 3D multiphase leaky well scenario, a 2D approximation would help to analyze a large number of simulations. When reducing a 3D model to a 2D section, several challenges arise. First, it is important to maintain the injection pressure. In the absence of

stratigraphic dip, this can be done by using a narrow radial section of the model, aligned with the injection and leaky well. The width of the radial section is equal to the diameter of the leaky well 100 m away from the injection point. Second, the 2D radial model assumes that the surrounding media has no impact on the leak rate. Using the benchmark case (no stratigraphic dip and homogeneous aquifer properties), the leak rate from the 2D and 3D models are compared in Figure 8.2-13. This analysis shows that the surrounding media plays a large role in the leakage rate that 2D models do not adequately capture. The presence of a leaky well induces pressure changes that influence CO_2 migration in the surrounding media.

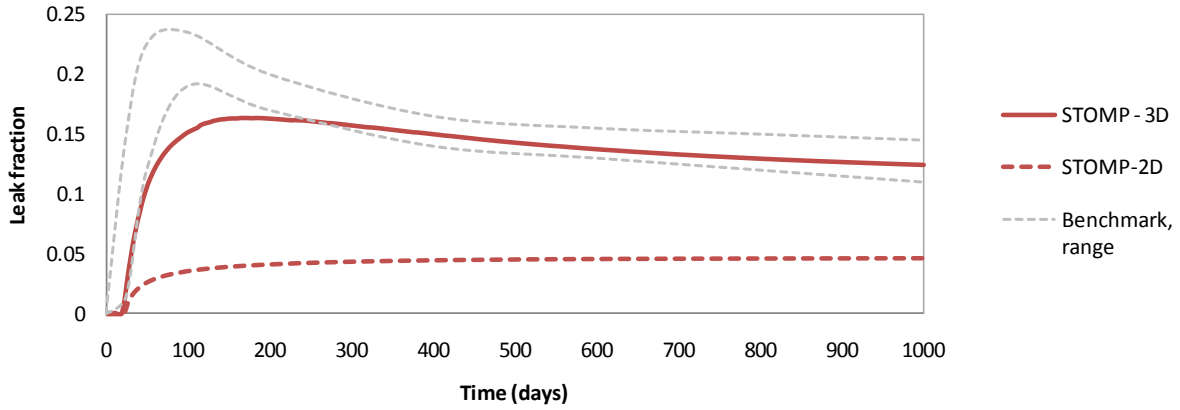

Figure 8.2-13. Leak fraction for the benchmark leaky well problem using a 3D and 2D model.

8.3 Clay/Shale Repository Example

This problem represents the first application of the THMC capability resulting from this project. The following is an excerpt of the complete problem, which has been discussed fully elsewhere (Hansen et al. 2010; Stone and Martinez 2010; Stone et al. 2011). The analyses utilized the capabilities of the Sierra codes Adagio for mechanical calculations and Aria for thermal/hydrological calculations.

This problem describes the simulation of a nuclear waste repository sited in a clay/shale stratigraphy. The model geometry can be defined via a “unit cell” model of a hypothetical waste repository sited in a 600-m thick clay/shale layer overlain by 100 m of sandstone and 200 m of other sediments (Figure 8.3-1). The entire domain is 900 m deep, 63.5 m wide, and 10 m in the horizontal direction perpendicular to the page. The repository is situated within the clay layer. Repository workings are represented by a horizontal, 5 m diameter access tunnel, with a perpendicular, 0.7 m diameter, 40 m long horizontal emplacement borehole. The waste packages occupy a distance of 30 m from the blind-end of the borehole, followed by a 3 m concrete plug, and finally a 7 m bentonite seal flush with the wall of the access tunnel.

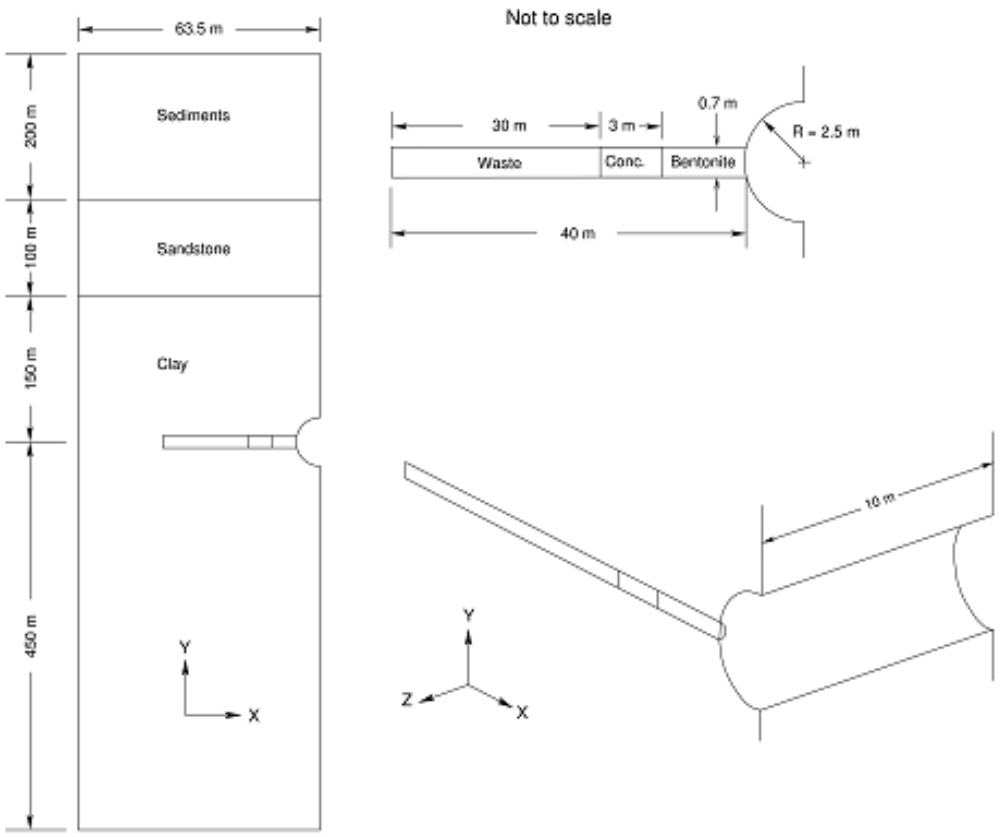

Figure 8.3-1. Schematic of the clay/shale repository model geometry.

A detail of the mesh at the repository horizon is shown in Figure 8.3-2. The finite element grid consists of 404,076 nodes and 383,214 eight-node hex elements. The analysis was run on a multiprocessor computer using 32 processors requiring approximately five hours of computer time for 10,000 years of simulation time.

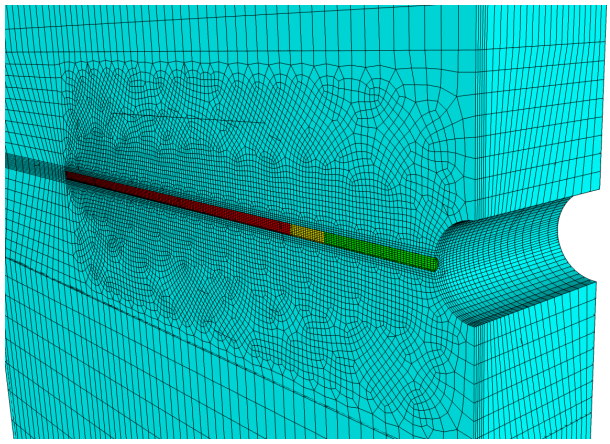

Figure 8.3-2. Closeup of finite element mesh at the waste horizon showing the access tunnel and horizontal waste borehole. The stored waste (red), concrete plug (yellow), and bentonite (green) materials are shown in the borehole.

The geometry shown in Figures 8.3-1 and 8.3-2 represents a "3D slice" taken from the repository. The vertical planes in the model are symmetry boundaries with normal displacements fixed against horizontal movement. The base of the model is fixed against vertical movement. The geologic materials—clay, sandstone, and sediments—are set to an initial hydrostatic stress condition (the horizontal normal stresses are equal to the vertical overburden stress). The applied external forces are body forces associated with weight of the overburden. Excavation of the access drift and emplacement boreholes is simulated by releasing the initial normal stresses at the free surfaces, over a construction period of one day. After excavation, the thermal loads and water vapor pressures are transferred from Aria and the coupled calculation is run out to 10,000 years.

8.3.1 Mechanical Model

With the exception of the clay layer, the stratigraphic materials were modeled as linear elastic; their properties are listed in Table 8.3-1. The clay and bentonite backfill were modeled with a crushable soil model; a more complete discussion of these material models can be found in Stone et al. 2011.

Table 8.3-1. Physical and elastic material properties.

Property	Waste Canister	Concrete Plug	Typical Sandstone	Surficial Sediments	Units
Density	1256.7	2247.3	2100	1800	kg/m^3
Young's Modulus	4.32	23.87	23.0	0.145	GPa
Poisson Ratio	0.3	0.2	0.3	0.2	—
Coefficient of Thermal Expansion	11.7E-06	12.0E-06	11.6E-06	11.6E-08	$C°^{-1}$

The thermal-hydrologic boundary and initial conditions are summarized in Figure 8.3-3. Initially, the entire domain is assumed to be at 20°C and initial saturation corresponding roughly to a (hydrologic) steady state with the upper surface set to 25% liquid saturation. The steady hydrostatic solution was computed separately, and results in nearly uniform saturations in each material, away from material interfaces. These steady saturations were applied as initial saturations in each material for the heat-driven simulation, with values as depicted in Figure 8.3-3.

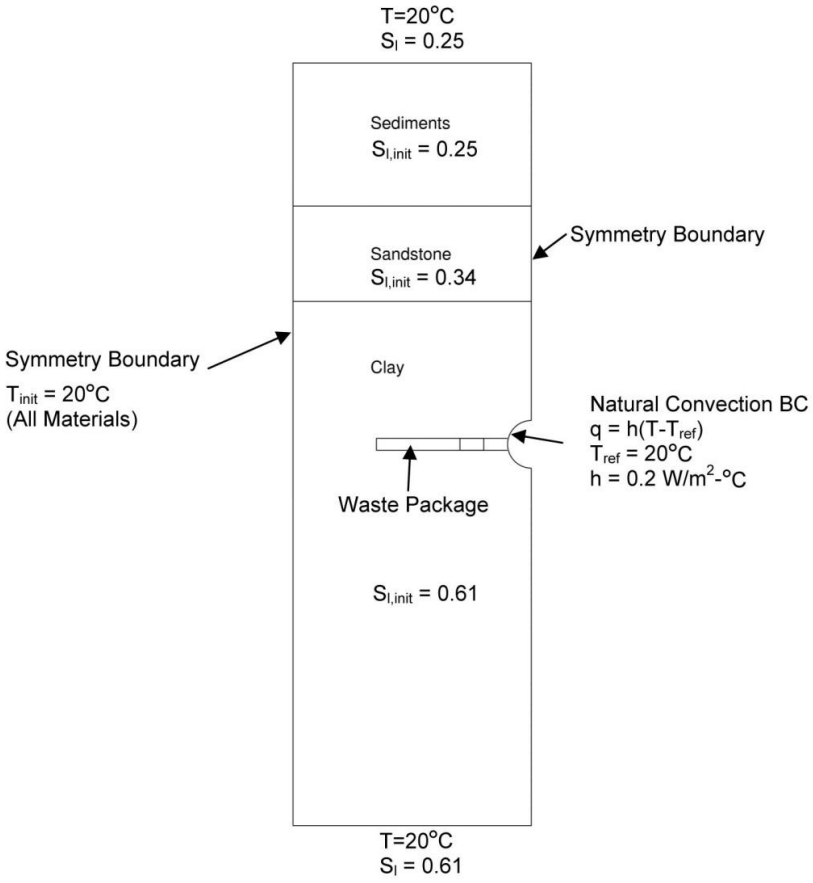

Figure 8.3-3. Schematic of hydrologic stratigraphy with initial and boundary conditions.

The top of the domain represents the ground surface and was set to a temperature of 20°C and a liquid saturation of 25%. The bottom boundary temperature was also set to 20°C. The access tunnel was assumed impermeable to flow and was subject to a natural convection boundary condition with 20°C reference temperature (Figure 8.3-3). All other surfaces were specified as symmetry surfaces, impermeable to mass flow and insulated from heat flow. For the high-level waste glass (HLWG) case, the initial saturation of the host rock was 61%, and this saturation condition was also maintained at the bottom boundary. For the pressurized water reactor (PWR) used nuclear fuel (UNF) cases (discussed below), the initial saturation was increased to 91% to evaluate the potential for pore pressure excursions and the associated mechanical responses. The thermal-hydrologic model assumes an unsaturated system occupied by water and its vapor. Air is not considered in the present model.

The waste package region is assumed to be composed of the clay material, but with uniform volume generation of decay heat. Three different thermal loads, depicted in Figure 8.3-4, were used in the analyses, to represent: (1) fresh HLWG; (2) the hottest PWR UNF considered for the Yucca Mountain license application; and (3) a bounding case for PWR UNF:

- The HLWG thermal power decays with a half-life of about 30 years (representing ^{137}Cs and ^{90}Sr) and rapidly decays to insignificance. For this case the power density for Hanford HLWG was scaled up to represent fresh HLW, such that peak emplacement

temperatures approach but do not exceed boiling. This condition was chosen to maximize evaporation and condensation behavior in the near field, without exceeding 100°C.

- The hottest PWR UNF case is based on the average base case PWR UNF thermal output used in performance assessment analyses to support the Yucca Mountain license application, which was then scaled up to envelop the estimated limiting waste stream (ELWS) PWR UNF developed for that application (see Hansen et al. 2010, sec. 1.3.1.2.5). It thus represents commercial UNF with the greatest thermal decay energy density that was considered for the license application.

The bounding case was developed by scaling up the Yucca Mountain ELWS by approximately 180%, to represent possible hotter, future waste forms. When decay storage is implemented for 50 years prior to emplacement, this bounding case resembles the HLWG case (Figure 8.3-4), hence the THMC analyses were conducted only for the three cases.

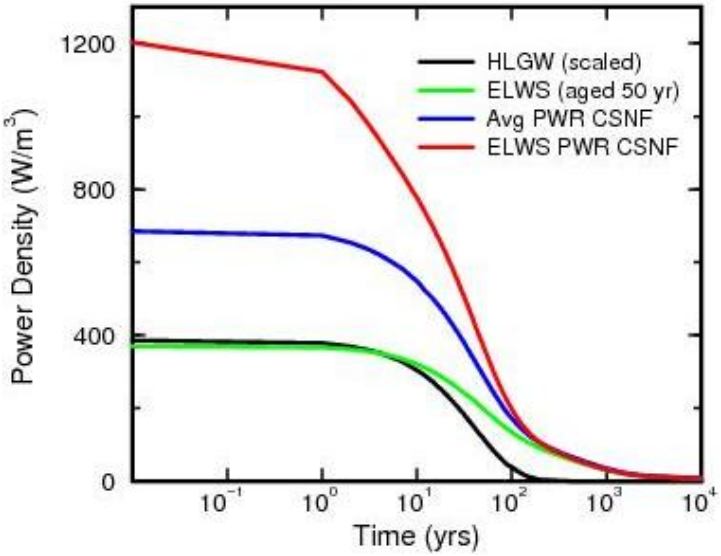

Figure 8.3-4. Normalized power curves for modeled waste.

8.3.2 Thermal-Hydrologic-Chemical Model

Material properties and parameters applied in the model are given in Table 8.3-2. Again, these values are within a realistic range of values for the type of porous material. Note that the porosity of the clay/shale formation is assigned a large value (30%) to investigate the potential for pore water and vapor mobilization. The permeability of the clay/shale formation is assigned a value of 10^{-16} m^2 for the HLWG case, and 10^{-19} m^2 for the hottest PWR UNF and bounding cases, reflecting a progression of cases intended to explore the maximum range of pore pressure and mechanical responses.

Curve fits to thermodynamic properties for water (liquid and vapor) are used in the model. The parameters "VG P_{c0}" and "VG β" refer to the van Genuchten model. The Udell cubic model of relative permeability was used. These models are discussed in chapter 2.

Table 8.3-2. Thermal-hydrologic material properties.

Property	Clay Formation	Sandstone	Sediments	Concrete Plug	Bentonite (Backfill/buffer)	Units
Porosity	0.3	0.2	0.4	0.1	0.276	-
Permeability	10^{-16} to 10^{-19}	10^{-15}	7×10^{-14}	10^{-18}	2.6×10^{-19}	(m^2)
Thermal Diffusivity	1.04×10^{-6}	1.40×10^{-6}	1.05×10^{-6}	4.55×10^{-7}	1.00×10^{-6}	(m^2/sec)
VG P_{c0}	10	10	8.63	10	10	(kPa)
VG β	1.69	1.69	1.88	1.69	1.69	-
S_r	0.11	0.11	0.2	0.11[a]	0.11	-

[a] Residual liquid saturation = 0.005 in relative permeability model.

The transport of radionuclides is also modeled. Initially, the entire domain is chosen to have zero concentration, except for the waste package region, which is taken to be equal to unity. The waste package region experiences a radiologic decay rate consistent with first order decay and a half-life of 30.1 years (^{137}Cs), which is also consistent with the thermal loading rate discussed in the previous section.

8.3.3 Thermal-Hydrologic-Mechanical-Chemical Model Results

The tunnel excavation occurs over several solution steps prior to the start of waste heating. Figure 8.3-5 shows color contour plots of maximum principal stress at the end of the excavation period. The plots show an area of tensile stress that exists in the access tunnel roof and floor at the location of the emplacement borehole. This location is unique due to the intersection of two symmetry planes (x- and z-directions). No tensile stresses were observed in the tunnel roof and floor for the linear elastic clay model. This illustrates the need for appropriate, site-specific material models for the clay/shale to get accurate stress results for tunnel integrity assessment. This result also shows the value of three-dimensional calculations and clearly identifies an area for further evaluation.

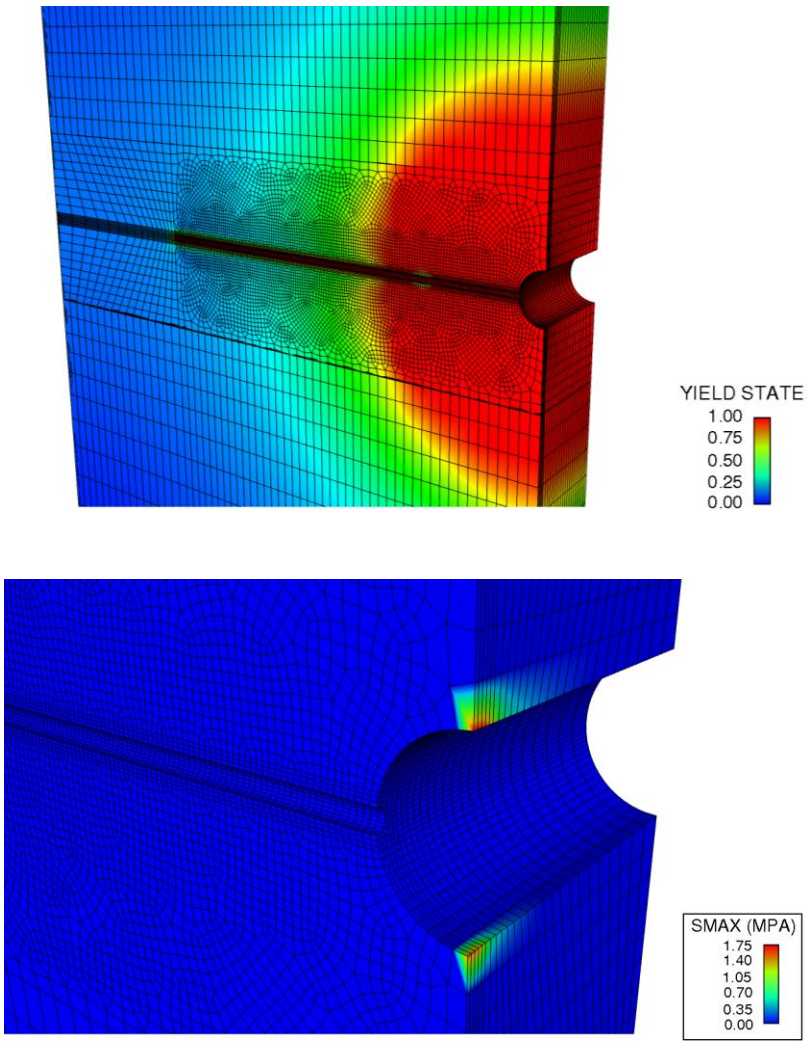

Figure 8.3-5. Contour plots of post-processed yield state variable and maximum principal stress (SMAX) after access tunnel excavation.

Figure 8.3-5 also shows the volume of clay material that is exhibiting nonlinear material response. The plotted yield state quantity is the non-dimensional ratio of the computed von Mises stress divided by the a_0 constant in the constitutive model. This figure indicates that the zone of inelastic response extends to a distance of several diameters surrounding the access tunnel, but not the emplacement borehole.

The peak emplacement borehole temperatures range from 83.5°C for the HLWG case, to greater than 200°C for the bounding case (Figures 8.3-6 and 8.3-7). For the HLWG case with relatively small temperature changes, thermal expansion of the solid matrix has a very small effect on the stress state. Also, displacements near the access tunnel are small. From these calculations, the largest structural response of the clay surrounding the access tunnel and emplacement borehole apparently occurs during excavation.

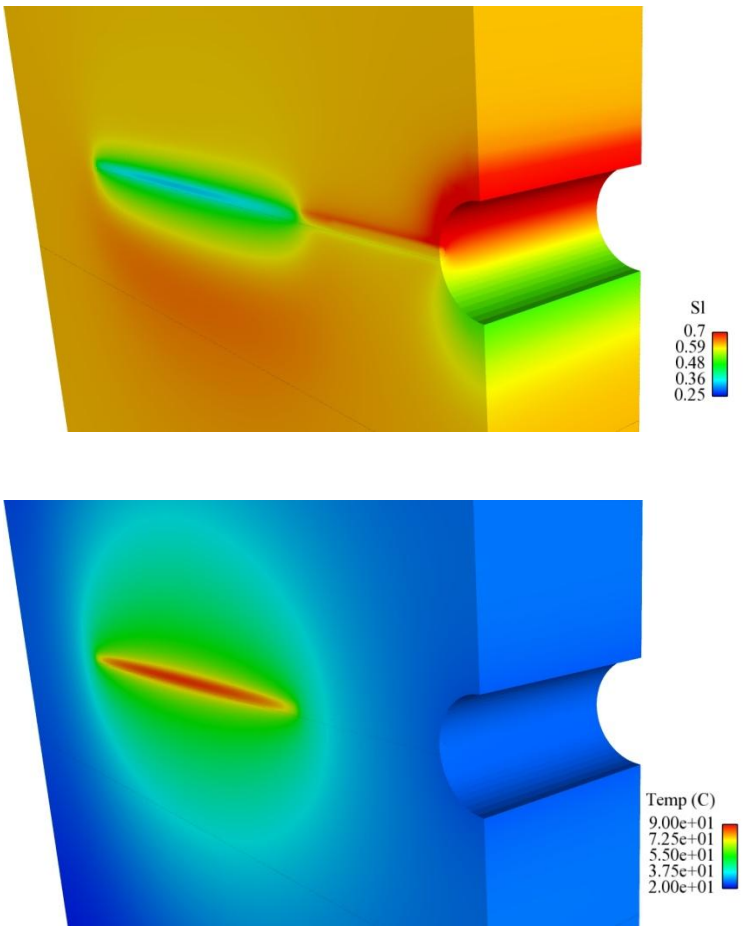

Figure 8.3-6. Liquid saturation (Sl) and temperature distributions near the waste packages at 16 years for the fresh HLWG thermal case.

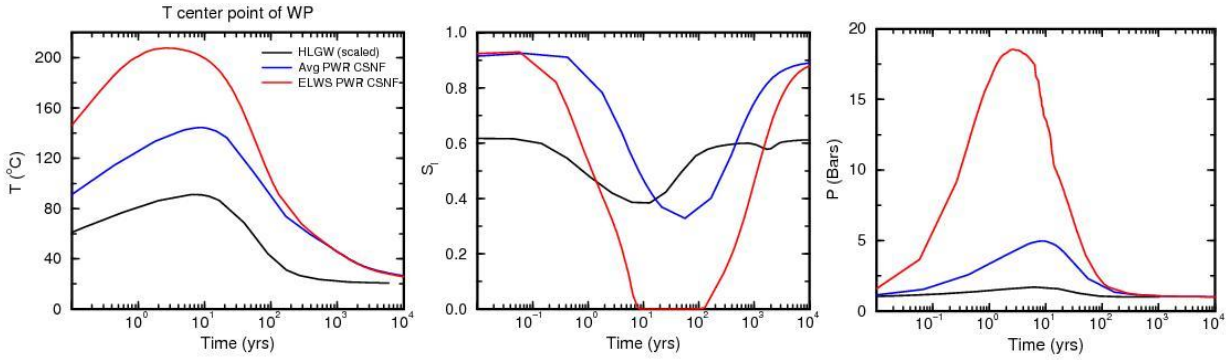

Figure 8.3-7. Time history in the emplacement borehole of temperature (left), liquid saturation (middle), and pore pressure (right).

All of the thermal power decay histories are defined such that the repository dries out noticeably within a few years and then re-wets as the repository cools down. For the HLWG case with greater rock permeability (10^{-16} m^2**;** Table 8.3-2), water is evaporated near the emplacement borehole, driven away by vapor pressure gradients, and condenses further out, forming a zone of increased saturation. Capillary gradients support liquid flow back toward the borehole. A zone of increased saturation forms below the borehole, subsequently seeping downward by gravity and dissipating by capillary action, see Figure 8.3-8. Note that the initial saturation of the host rock was set to 61% for this simulation.

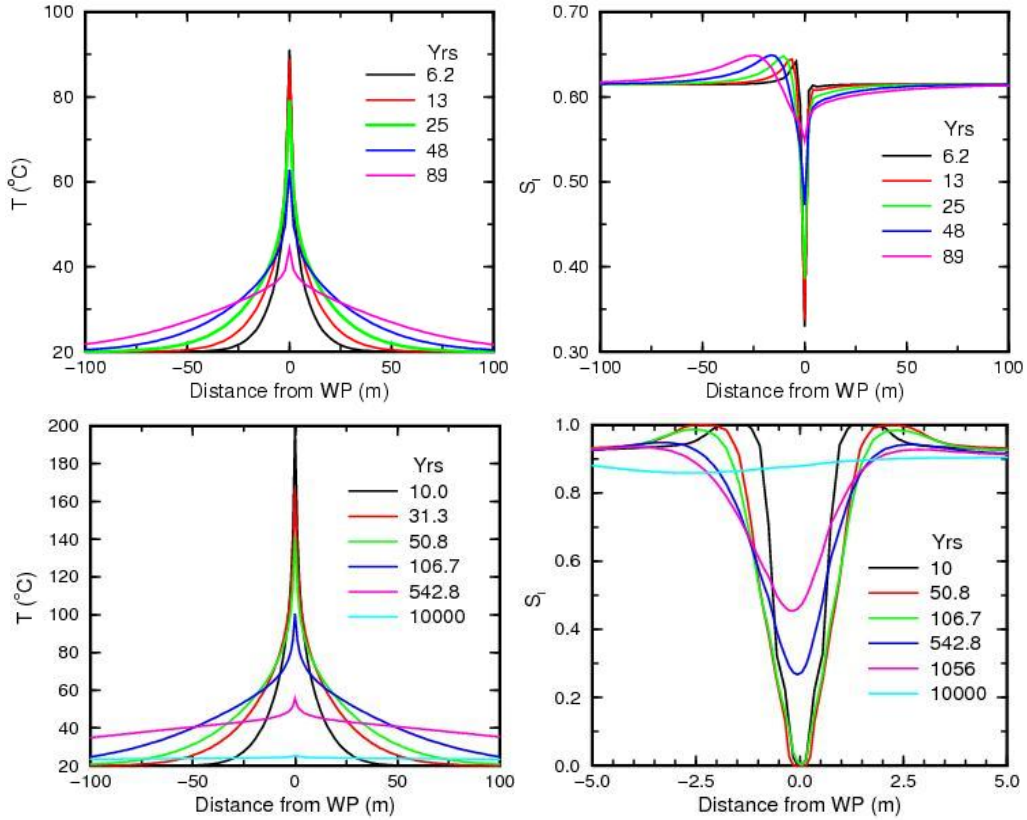

Figure 8.3-8. Temperature (T) and liquid saturation (Sl) distribution as a function of vertical distance from the waste package (WP), for the fresh HLWG thermal case (upper) and the bounding PWR UNF case (lower).

For the PWR UNF cases with lower permeability (10^{-19} m^2), the dewatering response occurs but the subsequent gravity-driven flow is much weaker, as indicated by the vertical symmetry of saturation profiles (Figure 8.3-8). Notice that the condensate fully saturates the pores, forming a saturated halo about the waste package. Pore pressure response closely follows the vapor pressure of water (Figure 8.3-7), with some dissipation especially for the HLWG case with greater permeability. Note that the initial saturation of the host rock was set to 91% for this simulation.

The spatial extent of elevated pore pressure and the time scale for dissipation are demonstrated for the bounding PWR UNF case, in Figure 8.3-9. Noting that this is a bounding case for which peak temperature greatly exceeds the 100°C limit, this result shows that the duration of elevated

temperatures is limited and the thermal gradients in the rock are small beyond a few meters distance. Thermo-diffusion (Soret effect) can therefore be excluded as a significant radionuclide transport process.

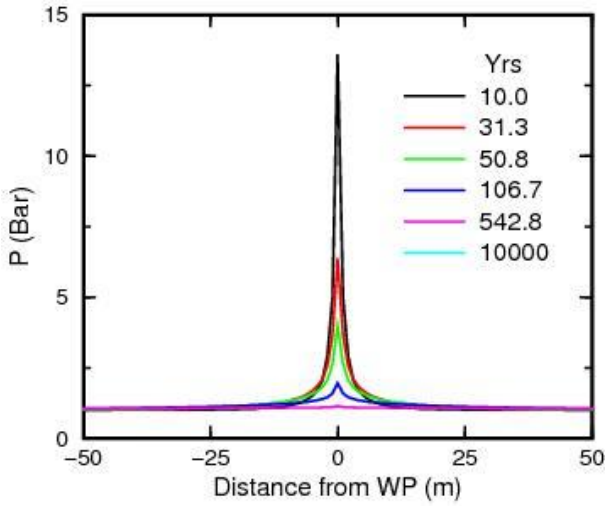

Figure 8.3-9. Pore pressure response as a function of vertical distance from the waste package for the bounding PWR UNF case.

Because of the short half-life and relatively large retardation factor used in this calculation, transport distances from the waste package are short relative to decay times. By approximately 30 years, sufficient radioactive decay has led to the near disappearance of solute in the vicinity of the repository, and by 60 years, the solute has nearly disappeared from the solution (see Stone et al. 2011). This shows that fission products comprising the constituents of HLW that have the greatest specific activities and shortest half-lives are completely isolated from the geosphere overlying the simulated clay/shale repository.

8.3.4 Summary

Results presented in the foregoing sections are generally consistent with calculations performed by international programs. The duration of elevated host rock temperatures can be limited to a few hundred years, during which substantial dewatering of the near-field host rock could occur, given sufficient permeability. The region of plastic deformation and stress conditions modified by excavation could be dominated by the larger diameter access drift. The behavior of ^{137}Cs in radionuclide transport simulations represents the isolation, and attenuation by radioactive decay, that is expected for disposal in clay/shale formations. Based on these results, and excavation disturbed zone (EDZ) investigations by international programs (Hansen et al. 2010, sec. 2.3.1), the extent of the EDZ is limited to a few meters and can be ignored as a transport path segment in the performance analysis of a generic clay/shale repository.

8.4 Coupled Porous Flow and Geomechanics for CO_2 Sequestration and Caprock Integrity Analysis

8.4.1 Introduction

Global consumption of fossil fuels has significantly increased levels of atmospheric CO_2, a greenhouse gas. Carbon capture and storage (CCS) is a promising mitigation strategy. CCS consists of capturing and sequestering CO_2 emissions from large "point sources" such as coal-fired power plants. A coal-fired power plant can produce several megatons of CO_2 per year and a typical design life is roughly 30 years. The storage of CO_2 in deep saline aquifers is one sequestration option under consideration. Depths of 1000 m or more are typically considered in order to assure injected CO_2 remains in a supercritical state, thereby minimizing pore volume requirements.

For long-term storage the saline aquifer, or reservoir, must be capped by at least one, possibly several, relatively impermeable layers, called caprocks. Both the choice of an adequate sequestration site and the control of the injection rate of supercritical CO_2 (sCO_2) into the reservoir are constrained by the requirement to maintain the integrity of the caprock. The integrity of a caprock layer may be quantified by the specification of an allowable average leakage rate. The leakage of a caprock layer can occur through porous flow within the caprock, flow within discrete fractures or joints, or flow within a fault. The injection of sCO_2 into the reservoir results in an increased pore pressure within the reservoir that varies with position and time as the sCO_2 flows throughout the reservoir. This change in pore pressure within the reservoir results in deformation of both the reservoir and the caprock layers. This deformation could reactivate impermeable fractures and faults as well as create new fractures, thus comprising the caprock integrity.

In this section, we model the injection sCO_2 into two idealized repositories (model problems) using a coupled flow (Aria) and geomechanics (Adagio) model. Model Problem 1 consists of a layered system with a single caprock. Model Problem 2 is identical to Model Problem 1 except for the presence of a fault. For each model problem we investigate the deformation of the caprock and assess the caprock integrity against potential shear failure.

8.4.2 Model Problem 1

For the first model problem, we consider the layered system shown in Figure 8.4-1, consisting of a single caprock layer (yellow) above the injection zone (red). The thickness of each layer is shown in the figure and Table 8.4-1 gives key parameters for each layer. The top of the caprock layer is 1350 m from the free surface. The injection rate schedule is shown in Figure 8.4-2. The injection schedule consists of a linear ramp up from an initial value of 1 MT/yr to a max rate of 3 MT/yr at year five, and a linearly ramp down to zero at the end of service life at year 30.

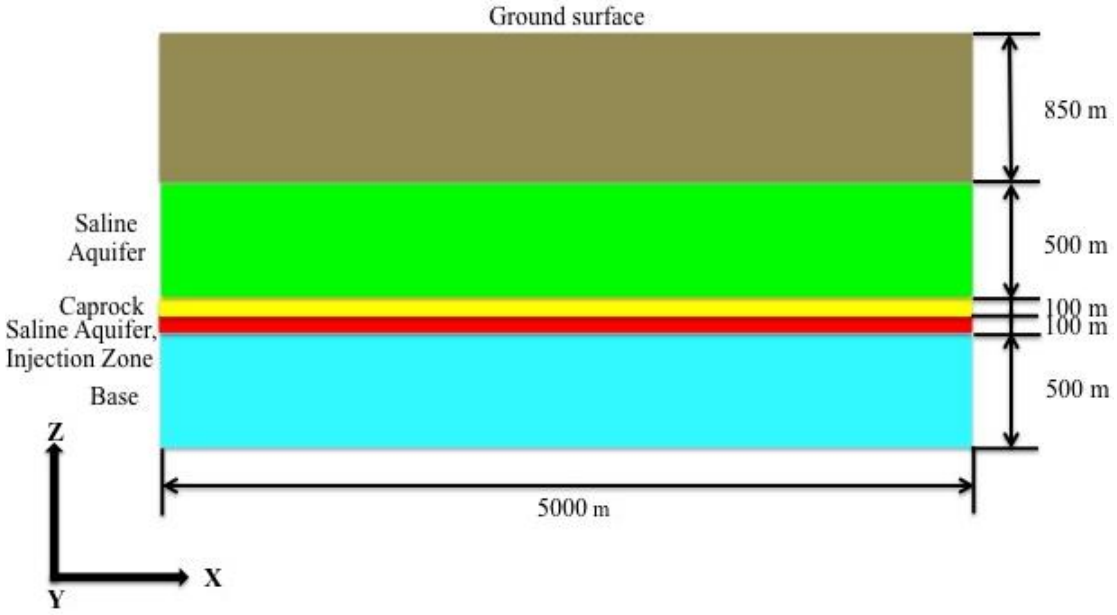

Figure 8.4-1. Schematic of Model Problem 1 consisting of a single caprock layer and injection reservoir. The thickness of each layer is given along with the horizontal length.

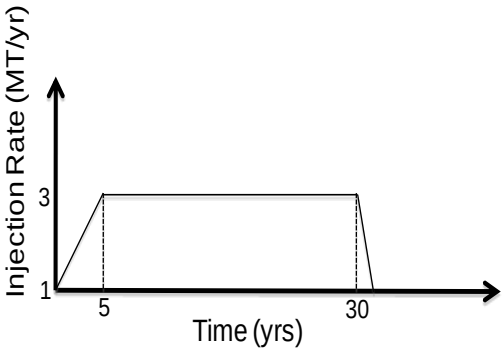

Figure 8.4-2. Injection rate schedule with a linear ramp up to max rate of 3 MT/yr at year five, and a linearly ramp down to zero at the end of service life at year 30.

The material properties of each layer are given in Table 8.4-1. Only two phases are considered: (1) brine, and (2) supercritical CO_2. The two phases are taken to be immiscible, with fluid properties as described in the leaky well benchmark problem discussed in section 8.2. The capillary pressure was modeled by the van Genuchten function with a low entry pressure (5 kPa). For simplicity, the mechanical response is taken to be linear elastic. Both the porous flow analysis and the mechanical analysis are taken to be isothermal.

Table 8.4-1. Material properties used in the porous flow and geomechanical analysis of Model Problem 1.

Property	Aquifer	Caprock	Injection zone	Base	Units
Density	2100	2100	2100	2100	Kg/m^3
Biot's coefficient	1	1	1	1	
Young modulus	20	50	20	50	GPa
Poisson's ratio	0.2	0.12	0.2	0.12	
Initial porosity	0.15	0.05	0.15	0.10	
Intrinsic permeability	2.0×10^{-14}	1.0×10^{-17}	2.0×10^{-14}	1.0×10^{-16}	m^2

Finite Element Model

The finite element mesh is shown in Figure 8.4-3. This mesh contains approximately 120,000 hexahedral elements. A detailed view of the mesh in the caprock and injection zones is also in Figure 8.4-3(b). Only one quadrant of the system is modeled. CO_2 is injected along the nearest edge in the figure uniformly over the depth of the injection zone. The two adjacent lateral sides are no-flow boundaries, the opposite lateral sides are constant pressure boundary boundaries corresponding to the initial hydrostatic state. The top and bottom surfaces are taken to be impermeable. For the mechanical model, all lateral sides and the bottom are fixed against normal motion. The region above the saline aquifer is not modeled, but instead a uniform pressure is applied representing the overburden.

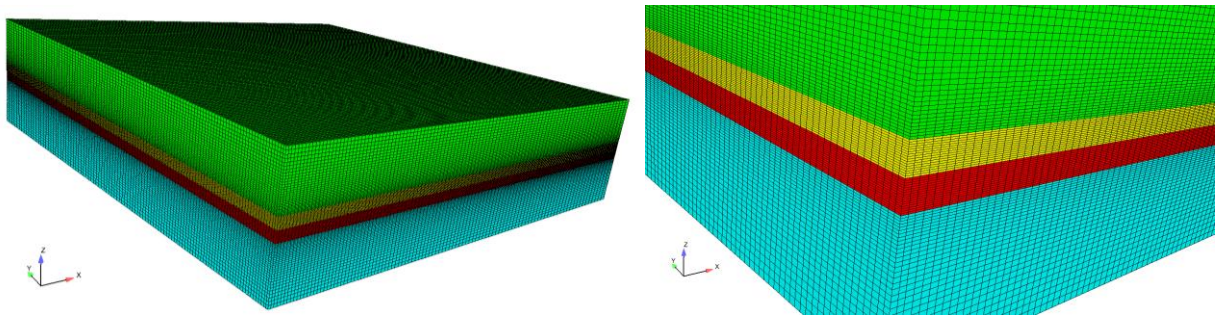

(a) (b)

Figure 8.4-3. Finite element mesh of Model Problem 1. The mesh contains approximately 120K elements. A detailed view of the caprock and injection zones is shown in (b).

Critical-Shear Failure Criterion

The stress sign convention for this example is positive in compression. The mechanical analysis uses the effective stress assumption in which the solid matrix of the porous medium effectively sees the total stress minus the pore pressure (Biot coefficient of 1.0). Thus, the deviatoric components of the stress tensor remain unchanged, but the hydrostatic stress in the solid matrix is reduced by the pore pressure. Following Rutqvist et al. (2007), we use a critical-shear failure criterion to assess the caprock integrity, as shown in Figure 8.4-4. This criterion is based on the Mohr-Coulomb failure criterion and provides a conservative estimate of the caprock integrity since it assumes that the caprock is composed of subscale fractures that have no cohesion, have a friction coefficient of 0.6, and are randomly oriented such that there is always a worst-case

oriented fracture with respect to shear slip. With these assumptions, shear slip is predicted to occur when the maximum principal effective stress is larger than three times the minimum principal effective stress. We define the *critical shear-stress* as $\sigma'_{p1} - 3\sigma'_{p3}$, so that a positive value represents a potential for shear slip. A secondary failure criterion is that the minimum principal effective stress should be compressive to avoid a tensile failure.

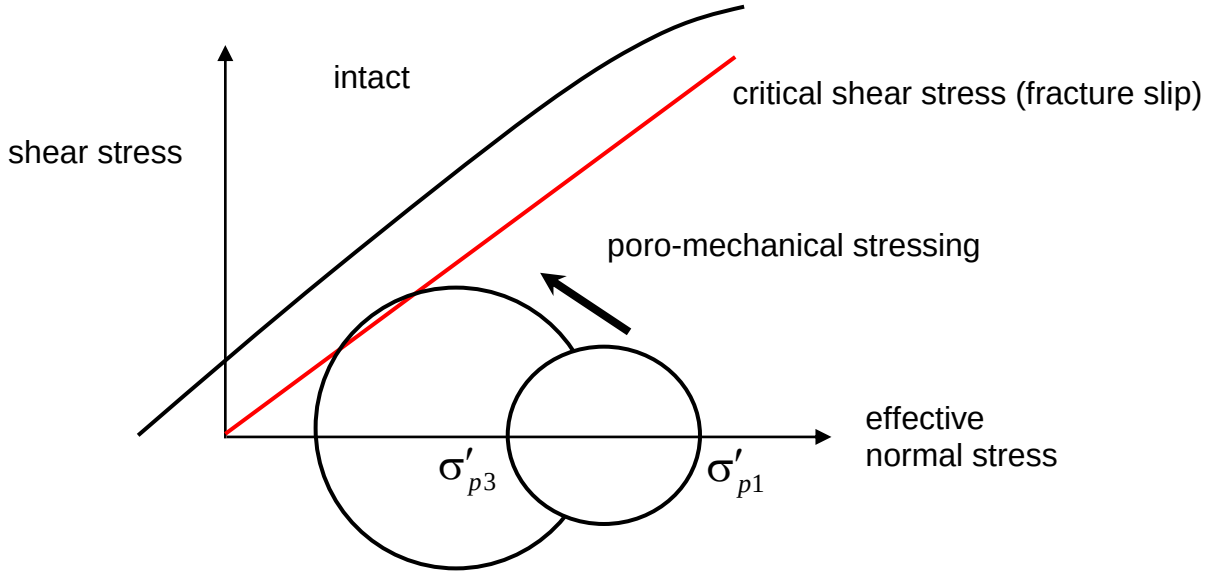

Figure 8.4-4. Mohr's circle representation of the stress state within a solid medium. All stresses are positive in compression. σ'_{p1} is the maximum effective principal stress. σ'_{p3} is the minimum effective principal stress. The red curve is the Mohr-Coulomb shear limit surface (critical shear failure criterion). Through the effective stress assumption, an increase in the pore pressure shifts the Mohr circle to the left. Stress redistribution can cause an increase or decrease in the diameter of the circle and thus the shear stress.

Regional Stress State

The initial stress state (before injection) strongly influences the allowable injection rates (Rutqvist et al. 2007). Any stress state that is not lithostatic has a nonzero shear stress and is thus "closer" to the critical-shear limit surface. Depending on the regional geological setting, the horizontal principle stresses can be less than (extensional) or greater than (compressional) the vertical stress. For this example, we assume that the vertical stress (σ_V) is a principal stress and we assume that the two horizontal principal stresses are equal (σ_H). For simplicity, we assume that the ratio of the horizontal stress value to the vertical stress value is a constant value throughout the reservoir. For the extensional stress state we take $\sigma_H = 0.7\sigma_V$ and for the compressional stress state we take $\sigma_H = 1.4\sigma_V$. These horizontal and vertical stresses are shown in Figure 8.4-5 as a function of depth. Since each layer has the same density, the both the vertical and horizontal stresses vary linearly in depth.

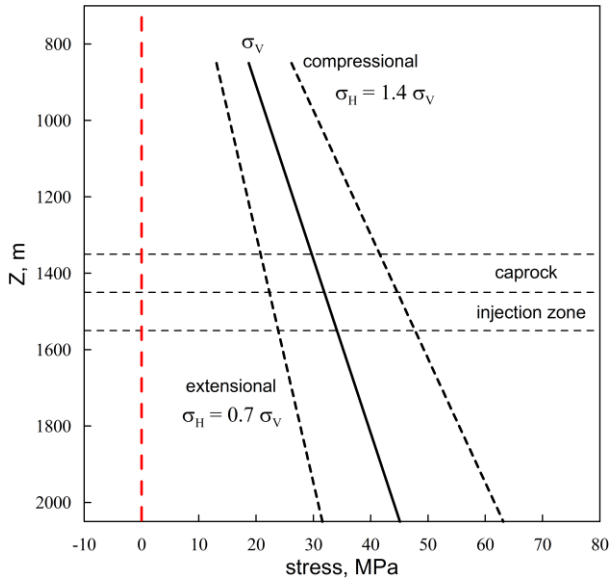

Figure 8.4-5. Variation of the horizontal and vertical stresses with depth for the extensional ($\sigma_H = 0.7\sigma_V$) and compressional ($\sigma_H = 1.4\sigma_V$) stress regimes.

Results and Discussion

The displacement vector field is shown in Figure 8.4-6 at year 5 for the extensional case. The maximum uplift at the top of the saline aquifer above the caprock is approximately 0.1 meters. The uplift increased monotonically to year 5 and then decreased monotonically thereafter. The displacement field for the compressional case was similar to the extensional case.

The variation in pore pressure with depth on the injection axis is shown in Figure 8.4-7, for the extensional case, at year 0, 5, and 30. Note that even though the permeability of the caprock is 2000 times less than the permeability of the injection aquifer, there is still significant change in pore pressure within the caprock in the vicinity of the injection zone. The caprock permeability in the present analysis is higher than have been used in similar analyses by others, e.g., Rutqvist et al. (2007). The peak pore pressure occurs at year 5.

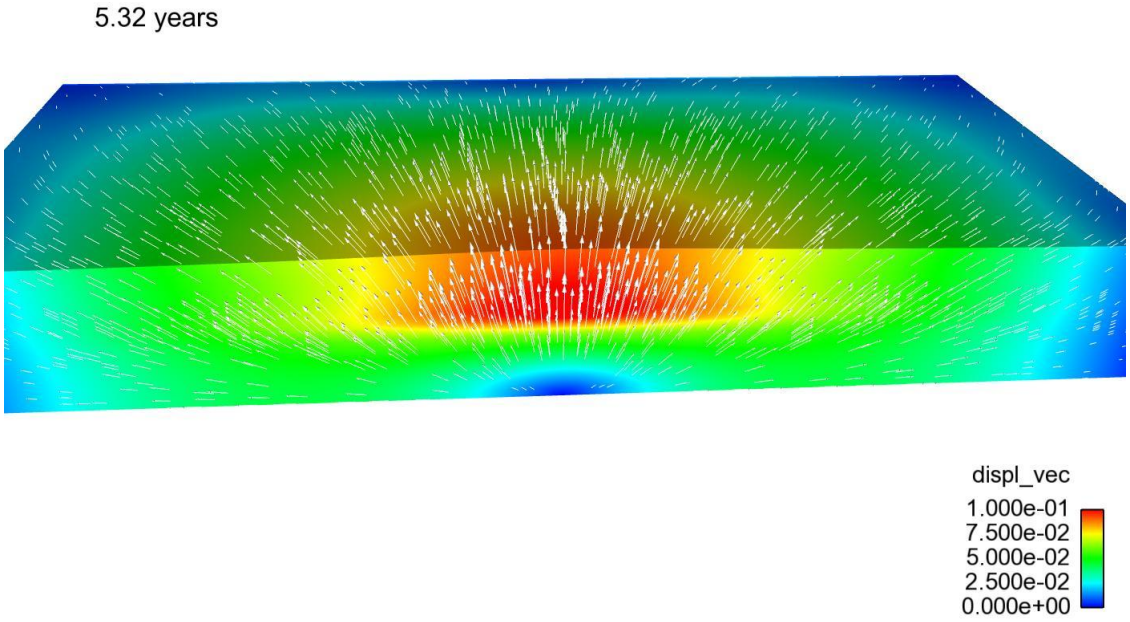

Figure 8.4-6. Displacement vector field at year 5 for the extensional case. The simulation results were reflected in the figure to obtain a full view. The color shading is the magnitude of the displacement vector in meters. The injection axis is on the front surface, middle axis.

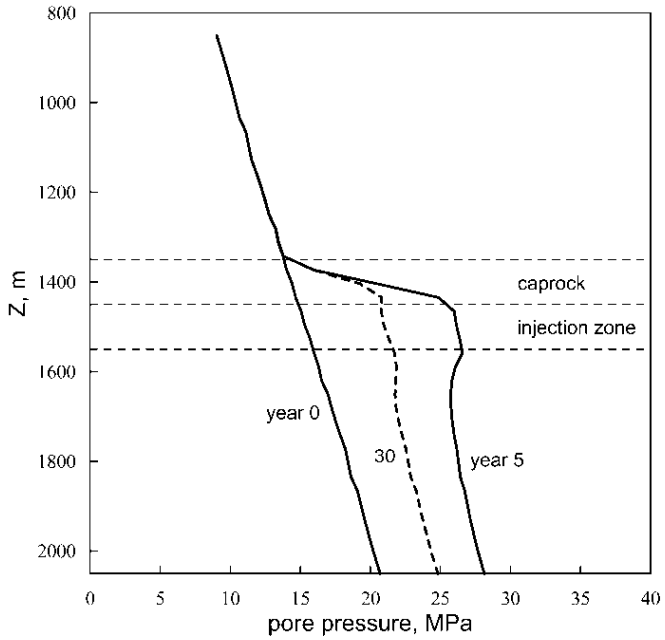

Figure 8.4-7. Variation of the pore pressure with depth on the injection axis, for the extensional case, at year 0, 5, and 30.

The critical-shear stress is shown in Figure 8.4-8 for both the extensional and compressional cases. As expected, the extensional case is the more severe case due to the lower mean stress. The critical shear stress is plotted as function of depth in Figure 8.4-9 on the injection axis. The critical shear stress is given at both the initial time and for year 5. A positive value represents a potential for shear slip on a worst-case oriented fracture.

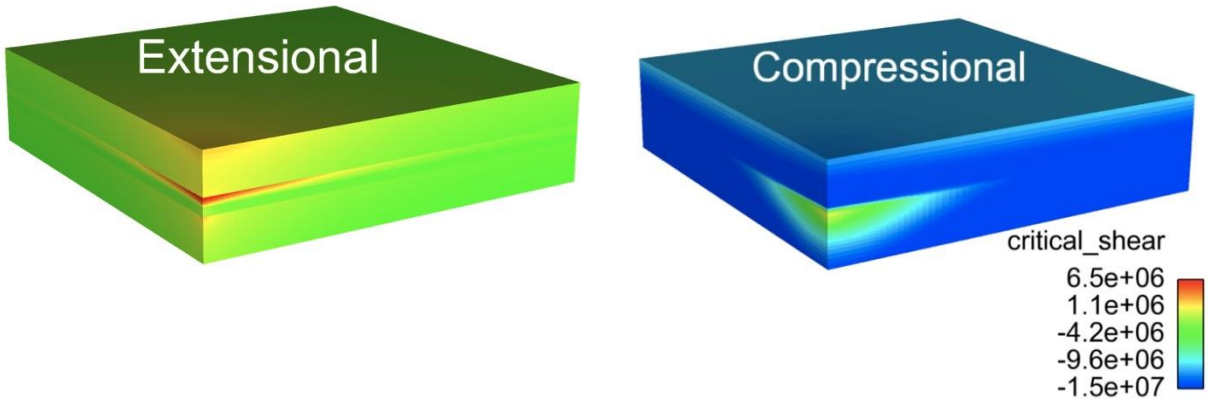

Figure 8.4-8. Comparison of critical shear stress for the (a) extensional and (b) compressional cases. A positive value indicates a potential for shear slip on a worst-case oriented fracture.

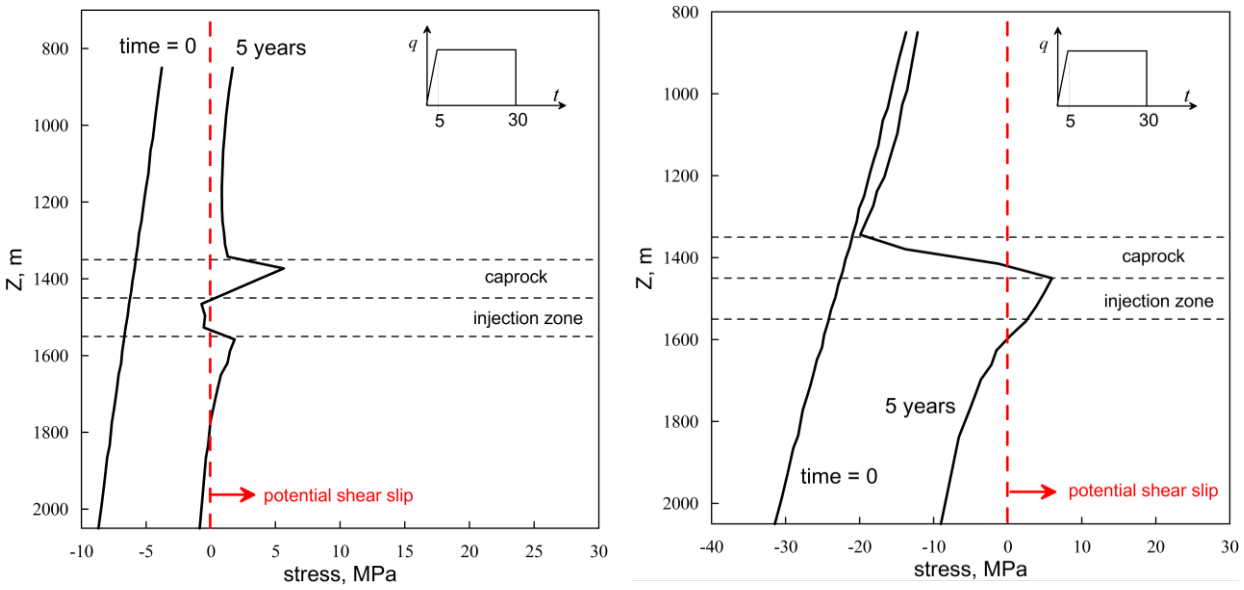

Figure 8.4-9. Critical shear stress variation as a function of depth on the injection axis at year 0 and year 5 in the (a) extensional and (b) compressional initial stress regimes. A positive value indicates a potential for shear slip on a worst-case oriented fracture.

8.4.3 Model Problem 2

Some faults can be difficult to detect. A fault in a sequestration site may pose a risk of leakage by reactivation during injection. For the second model problem, we consider the same layered system as in Model Problem 1, but with the addition of a fault as shown in Figure 8.4-10. The angle of the fault is 80 degrees from the horizontal axis (*x*-axis). The location of the fault is 1000 *m* from the injection axis in the injection zone. The thickness of the fault is 10 *m*. The fault extends through the model in the y-direction. The material properties of the fault are given in Table 8.4-2. Two cases are considered: (1) a low permeability fault, and (2) a high permeability fault.

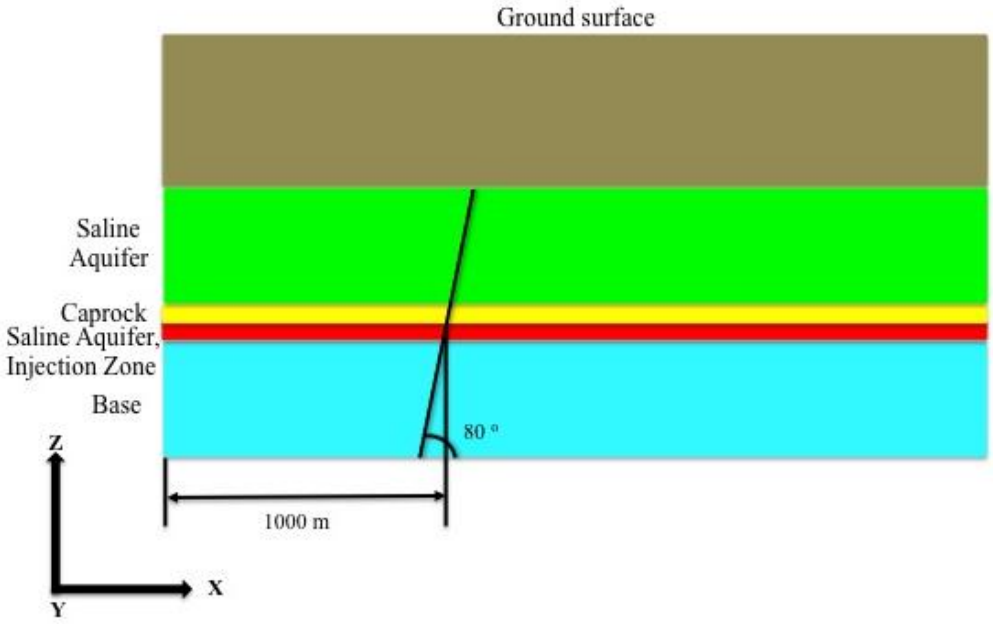

Figure 8.4-10. Schematic of Model Problem 2 consisting of a single caprock layer and injection reservoir along with the addition of a fault.

Table 8.4-2. Material properties used in the analysis of a fault in Model Problem 2.

Property	Low permeability fault	High permeability fault	Units
Density	2100	2100	Kg/m^3
Biot's coefficient	1.0	1.0	
Young modulus	5	5	GPa
Poisson's ratio	0.2	0.2	
Initial porosity	0.15	0.05	
Intrinsic permeability	1.0×10^{-17}	1.0×10^{-15}	m^2

Finite Element Model

The finite element mesh for the faulted system is shown in Figure 8.4-11. This mesh contains approximately 148K elements. A detailed view of the mesh is also in Figure 8.4-11(b). Only one quadrant of the system is modeled.

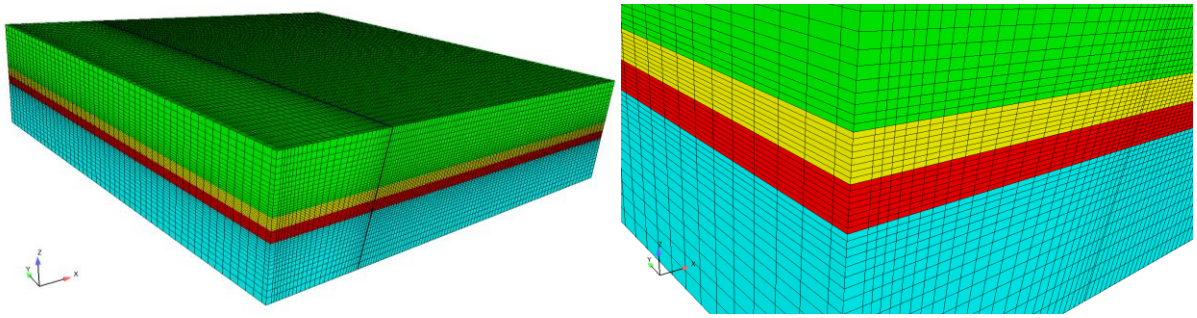

(a) (b)

Figure 8.4-11. Finite element mesh of Model Problem 2. The mesh contains approximately 148K elements. A detailed view of the fault zone is shown in (b).

Results and Discussion

Since the extensional initial stress case results in greater critical shear stress in the caprock compared to the compressional case, the simulations including the fault will only be presented for the extensional initial stress case. The low permeability fault acts as a barrier to migration of the CO_2 through the reservoir as shown in Figure 8.4-12. Figure 8.4-13 shows the resulting buildup of pore pressure behind the fault at year 17 which could reactivate the fault and cause leakage.

Figure 8.4-14 shows the critical shear stress and the deformed shape of the fault in the injection zone. Note the positive critical shear stress near the fault. Figure 8.4-15 shows the CO_2 saturation for the high permeability fault case. For this case, the fault provides a leak path for the CO_2 as illustrated in Figure 8.4-15(b). The leaked CO_2 pools at the upper surface, which was assumed impermeable, perhaps modeling an upper caprock layer. The distribution on the upper surface reflects the early arrival of CO_2 at the closest radial distance to the fault, followed by buoyancy-assisted upward migration through the high permeability fault. The critical consequence of the fault is breaching of the caprock. The solution illustrates buoyant migration through the fault *and* the upper (high permeability) aquifer once the caprock has been breached.

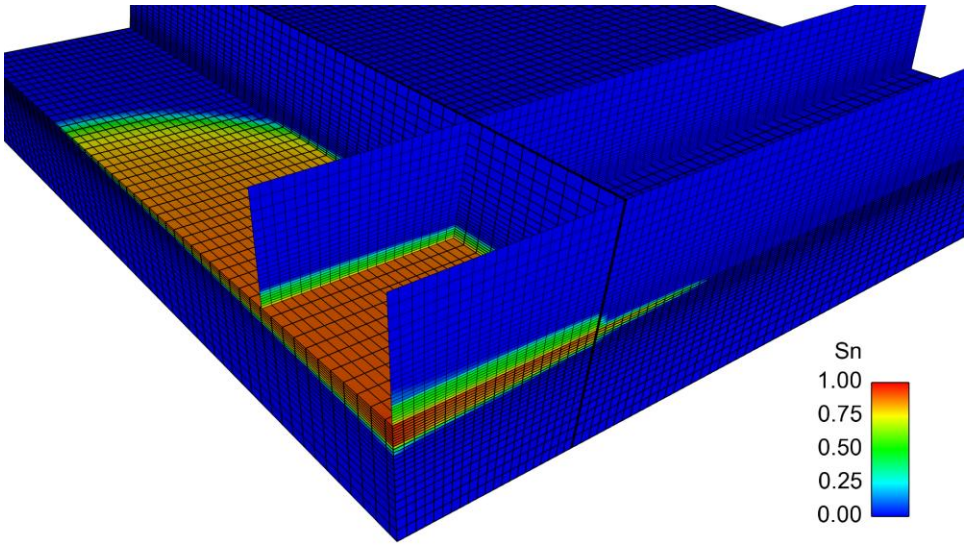

Figure 8.4-12. CO_2 saturation after 17 years of injection for the low permeability fault. The layers above the injection aquifer are not shown for clarity in viewing the extent of CO_2 migration. Two cutting planes of the caprock and upper layers are shown instead.

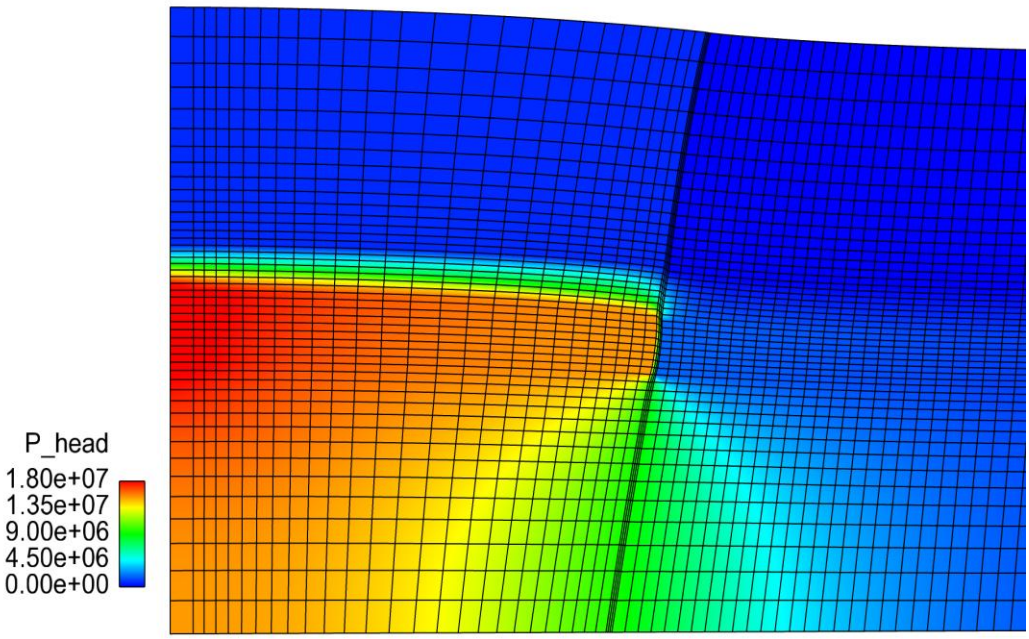

Figure 8.4-13. Pore pressure at year 17 for the low permeability fault. The displacement field is applied to the mesh with a scale of 750 to illustrate material deformation**.** Note the deformed shape of the fault within the injection zone.

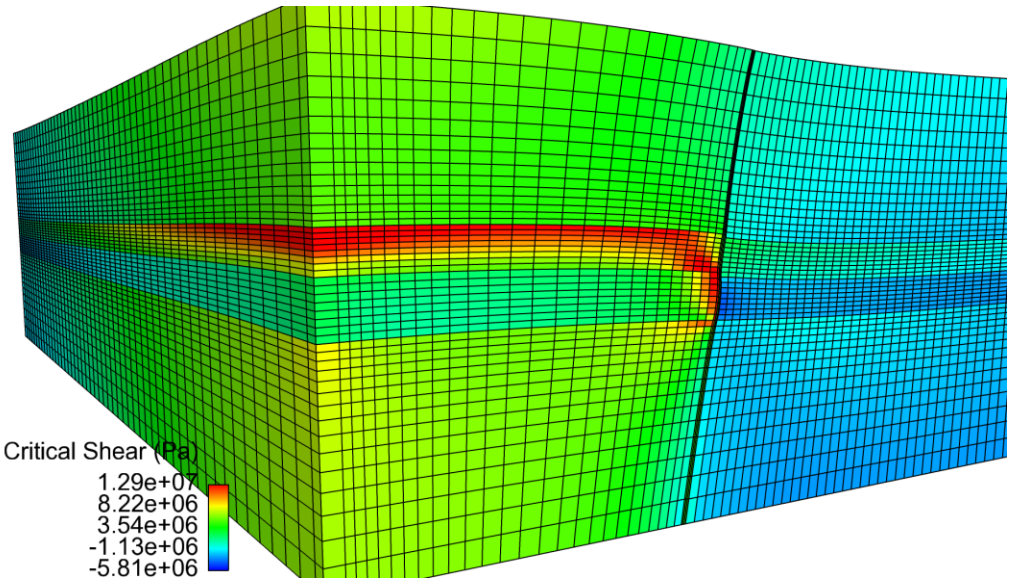

Figure 8.4-14. Critical shear stress at year 17 for the low permeability fault. The displacement field is applied to the mesh with a scale factor of 750. Note the deformed shape of the fault within the injection zone and the positive critical shear stress near the fault.

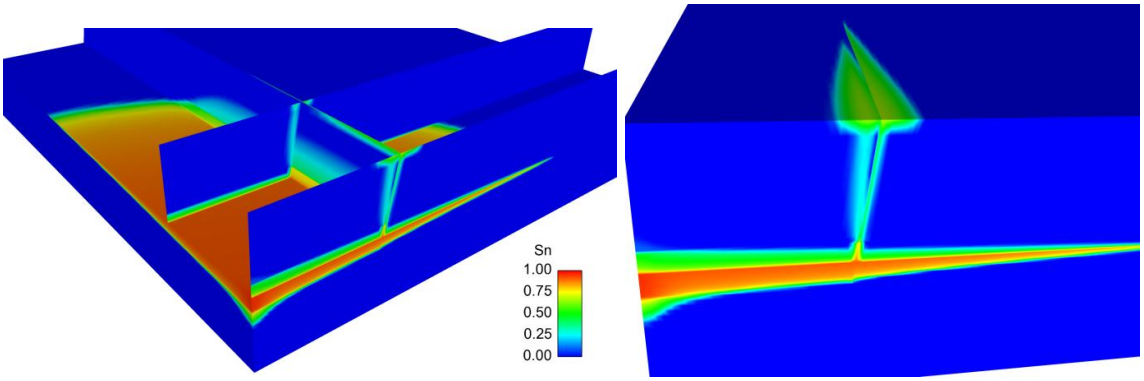

(a) (b)

Figure 8.4-15. High permeability fault in the extensional regional stress regime: (a) Interior view of CO_2 saturation after 27 years within the injection zone; (b) Exterior view of the CO_2 leakage through high permeable fault to the upper aquifer layer.

Future Work

The two model problems considered in this section are the first step in more detailed geomechanical analyses of CO_2 sequestration using Sierra. Future work will investigate the efficiency of the coupling scheme between Aria and Adagio, the effect of material heterogeneity in both the porous flow properties and mechanical properties, and the use of nonlinear elasto-plastic models in the geomechanical analysis (e.g., the SNL Geomodel).

8.5 Reactive Transport in Model Porous Media

A key aspect of this project was the development of reactive transport modeling capability. In this section we discuss the results of several benchmarking studies involving reactions of the type A+B → C**.** Though simple in appearance, this nonlinear reaction displays a rich variety of physical effects. In the following we consider the effects of reaction rates in transverse mixing of reactants in uniform flow (similar to porous flow) and slow, inertia-free flow in a model porous medium.

8.5.1 Instantaneous Reaction Flow Problem

For the case of an instantaneous reaction in a uniform flow field the steady state reaction product due to the transverse mixing of two parallel reactant streams can be solved analytically. A schematic of the physical system considered is shown in Figure 8.5-1.

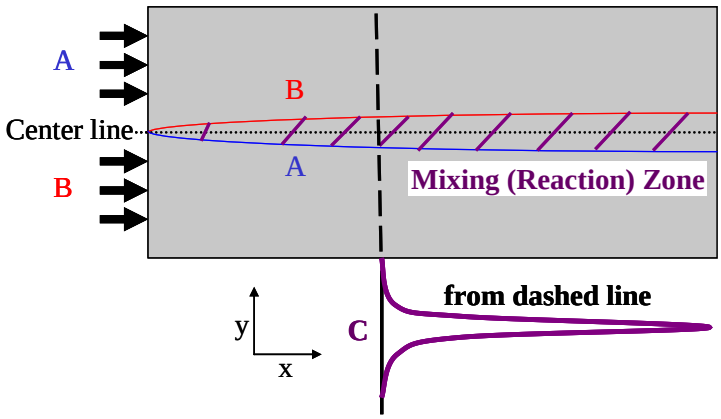

Figure 8.5-1. Schematic of instantaneous reaction in a uniform flow field profile. For instantaneous reaction A+B → C.

For the bimolecular reaction considered here the two solutes react and form the product (s_AA + s_BB → s_CC), where s_i is the stoichiometric coefficient of solute i. Symbols A, B, and C represent concentrations of reactants A, B, and the product C. For the simplified case where the stoichiometry is equimolar ($s_A = s_B = s_C = 1$), the rate of production of C at any point is equal to the rate of loss of each reactant:

$$r_C = -r_A = -r_B \tag{8.2}$$

The model describing steady state transport of these reactants and the product in porous media can be expressed by the advection-diffusion-reaction equations as follows:

$$\frac{\partial C_A}{\partial t} = 0 = -\mathbf{u} \bullet \nabla C_A + D_A \nabla^2 C_A - r_C \tag{8.3}$$

$$\frac{\partial C_B}{\partial t} = 0 = -\mathbf{u} \bullet \nabla C_B + D_B \nabla^2 C_B - r_C \tag{8.4}$$

$$\frac{\partial C_C}{\partial t} = 0 = -\mathbf{u} \bullet \nabla C_C + D_C \nabla^2 C_C + r_C \tag{8.5}$$

This is the system investigated in Acharya et al. (2007) where the following interpretation is described: "We also assume that the reaction rate is very large; that is, the reaction occurs instantaneously as soon as species A and B mix together. Under this assumption, solution of the coupled system of Eqns. (8.3) through (8.5) is greatly simplified. It can be seen that (assuming all the diffusion coefficients are equal) the quantity $C^* = \left(A - \frac{s_A}{s_B} B \right)$ is conserved. Under the assumption of instantaneous reaction, it is not possible for both to coexist at the same spatial location. Therefore instead of solving the coupled nonlinear system Eqns. (8.3) and (8.4), only the conservative transport equation for C* needs to be solved, and the values of A and B can be easily recovered from the positive and negative values of C*, respectively."

With the same strategy, the analytical solution for the product profile (Eqn. (8.5)) can be derived as follows:

$$\begin{aligned} &-\mathbf{u} \bullet \nabla C_{C^*} + D \nabla^2 C_{C^*} = 0 \\ &\frac{d C_{C^*}}{d t} = D \nabla^2 C_{C^*} \qquad \text{where } t = x / u_x \end{aligned} \tag{8.6}$$

Here, we use C*=B+C and $D_A = D_B = D_C$. For given initial condition (C*=0) and boundary condition (C* (y=0 at lower boundary) = 1), it transforms the advection and diffusion equation into a simple diffusion equation. The analytical solution at the distance x (=u*t) along the main flow direction is well known as

$$C^*(x, y) = C_0 erfc\left(\frac{y}{2\sqrt{Dt}} \right) \tag{8.7}$$

where C_0 is the concentration at the inlet. For the instantaneous reaction, the amount of product is determined by the concentration of the limiting reactant. As shown in Figure 8.5-1, the limiting reactant is A or B which diffuses into the other half domain. Once the limiting solute is completely consumed, the reaction will not occur any more. Thus, the concentration of product is given by

$$C(x, y) = \frac{C_0}{2} erfc\left(\frac{y - W/2}{2\sqrt{Dx / u_x}} \right) \tag{8.8}$$

Here, *y* is the distance from the bottom and *W/2* is the distance to the centerline. Since diffusion coefficients are the same, the product profile is symmetric along the centerline as shown in

Figure 8.5-1. Based on Eqns. (8.7) and (8.8), the product concentration is half of the inlet concentration and the reaction zone increases with the flow distance *x* as shown in Figure 8.5-1.

The chemically reactive flow problem was solved using the Aria reactive flow module described in chapter 3. The chemical reactions are solved along with the Navier-Stokes and continuity equations for the fluid flow in the model porous medium described below. The problem is solved in two dimensions representing a horizontal slice out of the flow field away from the vertical surfaces. The properties of the fluid are assumed not to vary as the chemical reaction proceeds. This assumption allows for a decoupling of the problem, where the steady state fluid flow can be solved initially and the constant flow field applied to the transient chemical species reaction and transport problem.

The specific equations solved are simplified by the assumption of steady state, incompressible flow, constant properties, and no body forces. Over the range of cases of interest the Reynolds number is on the order of 10^{-1}, so the Navier-Stokes equations can be simplified to the Stokes equation by removing the inertial terms. The continuity and Stokes equations solved for the fluid flow portion of the problem are:

$$\begin{aligned} \nabla \bullet \mathbf{u} &= 0 \\ \nabla p &= \mu \nabla^2 \mathbf{u} \end{aligned} \tag{8.9}$$

The initial condition for the fluid problem is zero flow ($\boldsymbol{u} = 0$) throughout the domain with boundary conditions of a specified inlet velocity in the x-direction ($u_x = U_0$), a zero pressure outlet condition, and the no-slip condition on the boundaries.

The reactant and product species transport is modeled using the transient versions of Eqns. 8.3 through 8.5 with the addition of a reaction rate constant. The above instantaneous reaction means that reaction occurs very fast as soon as A and B mix together, which can be described with a large reaction rate constant. For this case, Eqn. (8.2) can be expressed as

$$r_C = -r_A = -r_B = kC_AC_B \tag{8.10}$$

where *k* is the reaction rate (1/*t*). The species transport equations solved are:

$$\frac{\partial C_A}{\partial t} = -\mathbf{u} \bullet \nabla C_A + D_A \nabla^2 C_A - kC_AC_B \tag{8.11}$$

$$\frac{\partial C_B}{\partial t} = -\mathbf{u} \bullet \nabla C_B + D_B \nabla^2 C_B - kC_AC_B \tag{8.12}$$

$$\frac{\partial C_C}{\partial t} = -\mathbf{u} \bullet \nabla C_C + D_C \nabla^2 C_C + kC_AC_B \tag{8.13}$$

The initial and boundary conditions are the following:

$$
\begin{aligned}
&C_A(t=0) = C_B(t=0) = C_C(t=0) = 0 \\
&C_A(x=0, t>0) = \begin{cases} 0 & for \quad 0 < y < W/2) \\ C_{A,0} = C_0 & for \quad W/2 < y < W) \end{cases} \\
&C_B(x=0, t>0) = \begin{cases} C_{A,0} = C_0 & for \quad 0 < y < W/2) \\ 0 & for \quad W/2 < y < W) \end{cases} \\
&C_C(x=0, t>0) = 0 \quad for \quad y \geq 0
\end{aligned}
\tag{8.14}
$$

where W is the width of the channel in the y-direction. This solution method was applied to a series of benchmark problems to validate its capabilities. The benchmark problems were chemical reaction and transport in plug fluid flow, fluid flow through an array of circular cylinders, and chemically reacting flow in a circular array.

8.5.2 Discussion of Benchmark Cases

The initial benchmark problem solved is the simple case described above and illustrated in Figure 8.5-1 where two reactant streams (in a uniform flow) are injected into the top and bottom halves of a channel and allowed to diffusively mix and react to form product along the channel length. An asymptotic ($k \to \infty$) analytic solution exists for this scenario allowing direct comparison of the results of the numerical scheme to the idealized case. In this specific case the channel is 1 cm wide (y-direction) and 2 cm long (x-direction). The fluid is injected at a uniform velocity of 0.02 cm/s. The fluid carries reactants A and B at equal initial concentrations of 0.5. Both reactants and the product are assumed to have equal and constant diffusivities of 10^{-5} cm^2/s. The fluid is assumed to be water at room temperature with constant properties: density, ρ=1.0 gm/cm^3, and viscosity, μ=0.01 gm/cm/s.

The benchmark asymptotic solution assumes an instantaneous reaction between the two reactants. In the numerical scheme a reaction constant, k, is used to model the reaction. The numerical model was run with values of k from 0.01 to 1000 to determine the effect of the rate constant on the calculated product value and the computational requirements. Increasing values of k require smaller mesh element sizes in order to converge to a solution. The value of k = 1000 was selected as the best balance between solution accuracy and computational time. A comparison of the product profiles in the channel between the analytic solution and the numerical result for k = 1000 is presented in Figure 8.5-2.

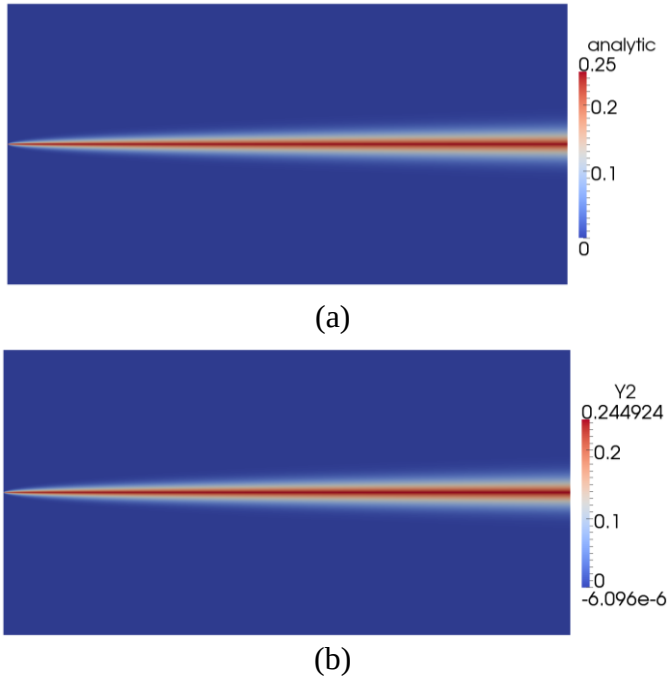

Figure 8.5-2. Comparison of the product concentration of the analytic solution and the numerical solution for k = 1000. (a) Analytic solution. (b) Numerical solution.

The comparison of the product profiles illustrates the similarity between the numerical solution and analytic solution. The analytic solution for the product profile is a concentration of 0.25 along the centerline of the channel. The numerical solution approaches this value to within 2%, a concentration of 0.244924 vs. 0.25. The effect of the selected value of k can be seen in the product concentration profiles in Figure 8.5-3.

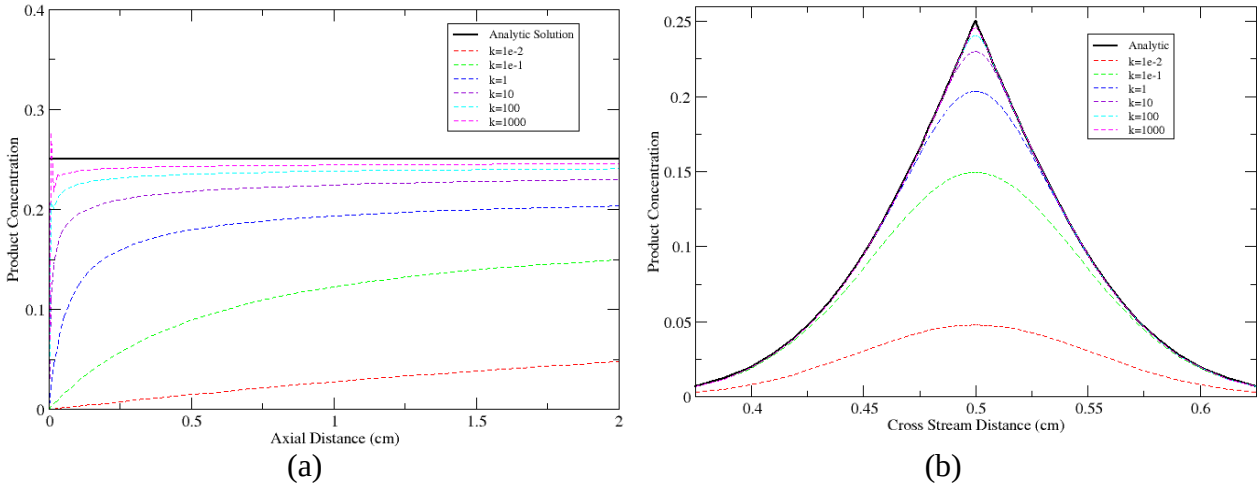

Figure 8.5-3. Comparison of the effect of the reaction rate constant, k, in the numerical solution to the asymptotic analytic solution. (a) Product concentration along the centerline of the channel in the flow direction. (b) Product concentration in the cross flow direction at the channel outflow.

The effect of the reaction rate constant is evident in either plot of the product concentration profile. In Figure 8.5-3(a), the increasing value of k brings the numerical solution closer to the instantaneous, analytic value of 0.25. The case of k = 1000 shows the best agreement to the analytic solution with a difference of 2%, but also indicates the limit on the current mesh size. The curve exhibits a spike in concentration over the first two mesh elements in the model which would be eliminated with a more refined mesh, at a greater computational expense. A similar result is seen in Figure 8.5-3(b), where the largest values of k demonstrate good agreement with the cross flow spread in the product concentration. Selection of a value of k = 1000 provides a numerical solution that closely correlates to the analytic solution while maintaining a low computational overhead.

The second benchmark case is a study of fluid flow through an array of circular cylinders. With the current two dimensional problem this results in a fluid flow around an array of circles. The spacing of the circles was taken from Sangini and Acrivos (1982) who developed an analytic expression for drag on a cylinder in a periodic array that demonstrated agreement to experimental results. The circles were spaced one non-dimensional unit apart in the x-direction and $\sqrt{3}$ non-dimensional units apart in the y-direction, on a center to center basis. The cylinder radius was varied to test different values of porosity in the array.

The numerical model used the same size mesh and property values specified in the previous benchmark problem. Figure 8.5-4 illustrates the three representative circles from the mesh where the drag was measured for comparison to Sangini and Acrivos.

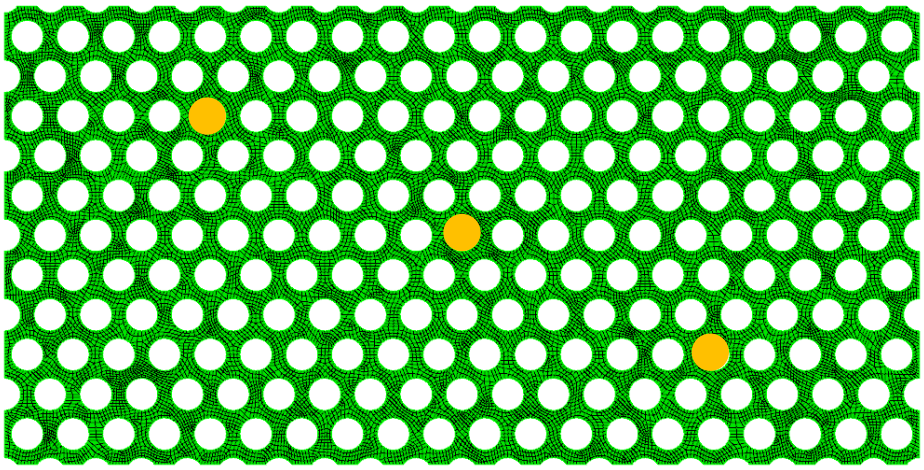

Figure 8.5-4. Array of circles used for comparing fluid drag to published results. The circles in gold are the circles where the drag is measured. The radius of the circles is 0.035 cm. The fluid flow is from left to right.

A series of five meshes was used with circle radii of 0.015 cm, 0.025 cm, 0.035 cm, 0.040 cm, and 0.045 cm. These radii corresponded to a range of cylinder volume fraction, c, from 0.078 to 0.73. The cylinder volume fraction is the ratio of volume occupied by the cylinders to the total volume of the geometry (assuming a unit depth for the 2D problem). For comparison to the published results the measured drag force, F, on a cylinder was non-dimensionalized by the fluid

viscosity, μ, and the mean flow velocity, U: $F^* = {}^{F}/_{\mu U}$. Table 8.5-1 contains the measured drag forces and non-dimensionalized quantities. Figure 8.5-5 compares the current numerical results to the published results.

Table 8.5-1. Measured drag quantities and non-dimensionalized values.

Cylinder radius	Drag Circle 1	Drag Circle 2	Drag Circle 3	*F*=drag avg	*U*	*c*	*F**
(cm)	(dyn)	(dyn)	(dyn)	(dyn)	(cm/s)		
0.015	0.00368	0.00370	0.00370	0.00370	0.0170	0.0778	21.7
0.025	0.00890	0.00893	0.00885	0.00889	0.0148	0.217	60.2
0.035	0.0299	0.0230	0.0299	0.0299	0.0124	0.435	242
0.040	0.0794	0.0796	0.0793	0.0794	0.0112	0.573	711
0.045	0.432	0.432	0.431	0.432	0.00998	0.729	4330

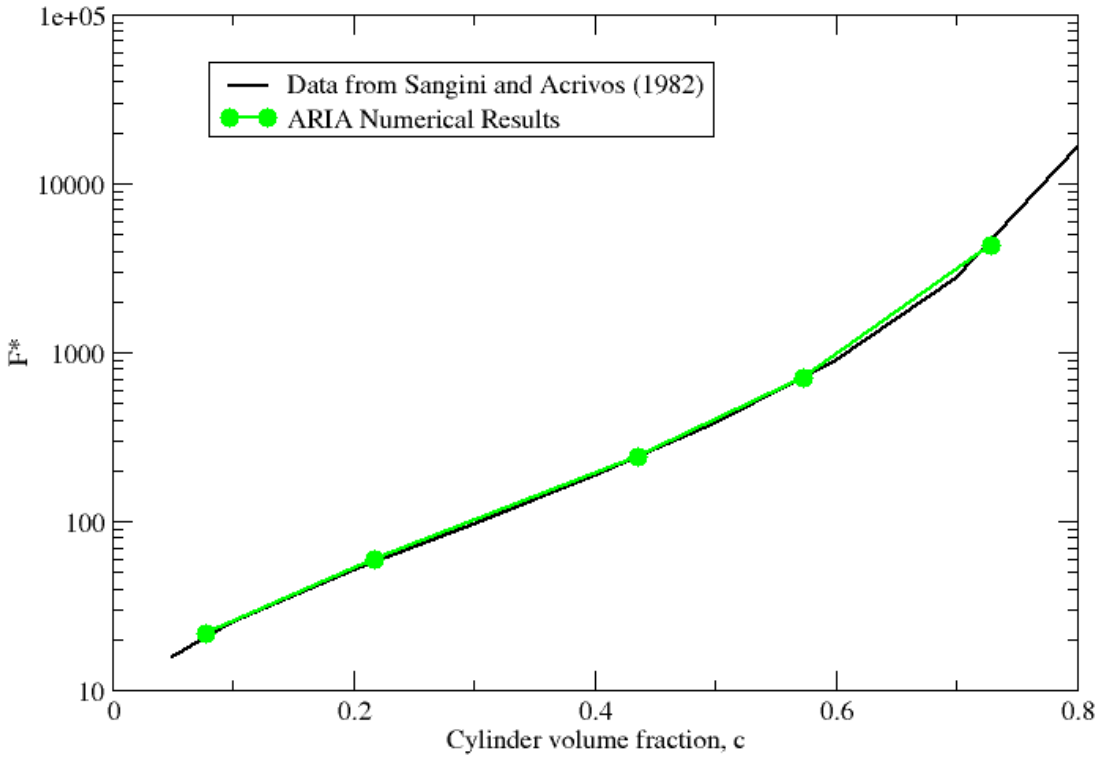

Figure 8.5-5. Comparison of the non-dimensional drag force computed by the numerical method to results published by Sangini and Acrivos (1982).

Figure 8.5-5 shows that the calculated drag forces match up well with accepted analytical and experimental results. The results of this benchmark problem demonstrate that the numerical method is correctly modeling the fluidic forces in an array of obstructions.

The third and final benchmark problem combines the fluid flow through an array of circles with the chemical reaction. The model parameters remain the same as in the previous two benchmarks. The mesh used contains circles with a radius of 0.035 cm, as in Figure 8.5-4. The results from the current finite element method are compared to results of the method of Yoon et al. (2011). The computational method in Yoon et al. (2011) consists of the lattice Boltzmann method for fluid flow and the finite volume method for reactive transport (LBFVM). The LBFVM numerical method was developed and validated in Willingham et al. (2008,2010). A comparison of the product profiles determined by each method is shown in Figure 8.5-6.

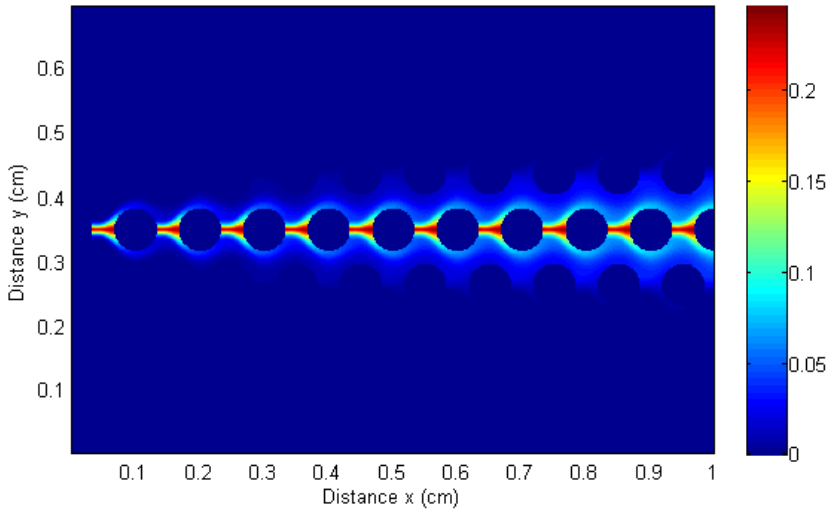

(a)

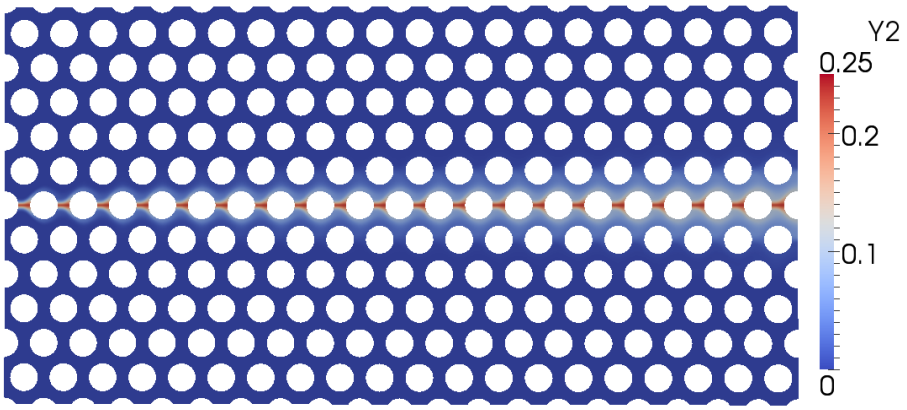

(b)

Figure 8.5-6. Comparison of the product profiles for reactive flow through an array of circles. (a) Result from the LBFVM of Yoon et al. (2011). (b) Result from the current finite element method.

Qualitatively the two methods predict similar concentration profiles. Quantitatively the models are not precisely the same. The LBFVM model uses a reaction rate constant, k, of 10^4 whereas the finite element model uses a value of $k = 100$. There is also a discrepancy in the fluid velocity between the two models due to different boundary conditions. The LBFVM has an average pore space velocity of 0.02 cm/s, while the average pore space velocity in the finite element model is

0.0182 cm/s. Despite these small differences the two numerical methods produce similar results. A direct comparison of the velocity and product profiles is shown in Figure 8.5-7.

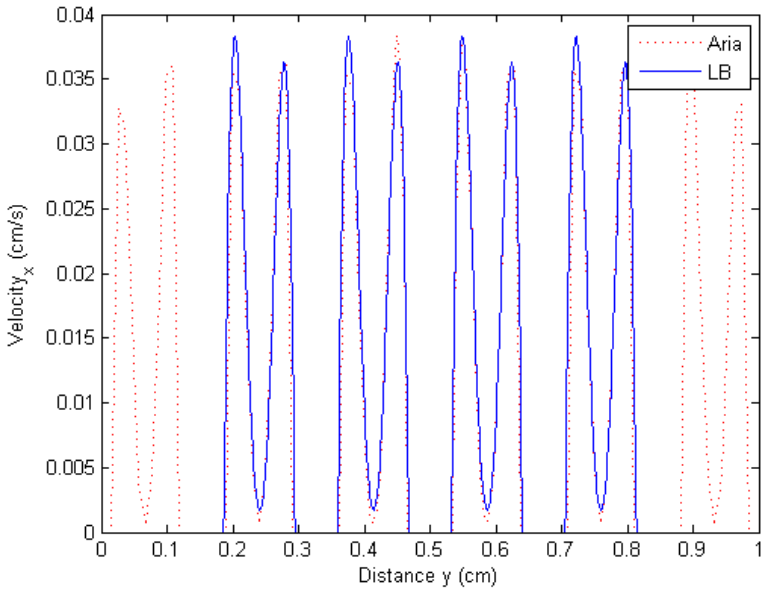

(a)

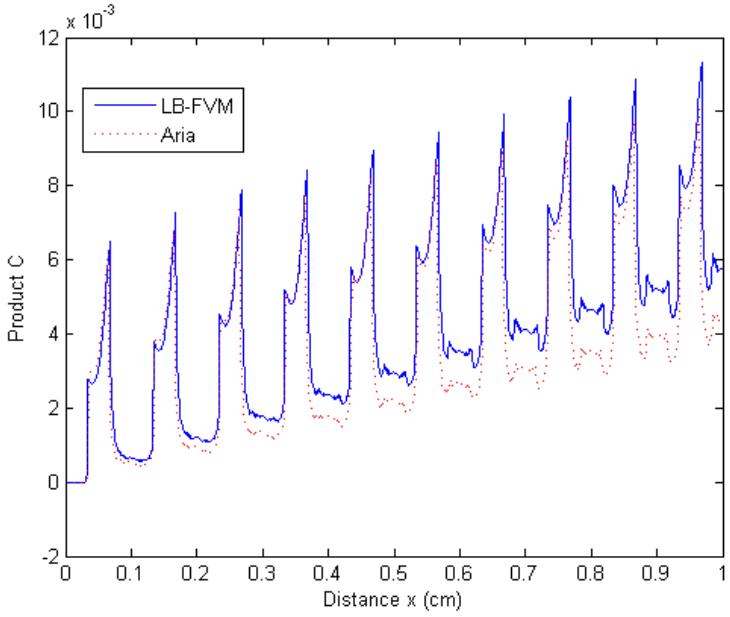

(b)

Figure 8.5-7. Comparison of the LBFVM and finite element (ARIA) methods for combined fluid and reactive transport. (a) Profile of velocity in the x-direction taken at the horizontal centerline of the computational mesh. (b) Profile of total product concentration, integrated in the cross flow direction, along the length of the mesh.

The velocity profile for flow between the pores, in Figure 8.5-7(a), is the same for the two methods except for the known velocity difference due to differing boundary conditions. The

cross flow integrated product profile in Figure 8.5-7(b) likewise demonstrates good agreement between the computational methods. The results from the finite element method grow smaller than the LBFVM results at large values of distance along the flow direction. The difference in product concentration can be attributed to the smaller value of reaction constant used in the finite element method. With a smaller rate constant, less product will be formed and leads to the difference seen between the codes. The favorable comparison of the finite element method to analytic and published results over the three benchmark problems lends confidence that the numerical method is properly solving for reactive transport within a representative porous media.

8.5.3 Future Applications

The finite element method described above and implemented using Aria has thus far been applied to simple benchmark cases to verify and validate the methodology. The results presented demonstrate that the implementation is correctly solving the fluid flow and reactive transport within porous media. In the future, the methodology could be applied to a wide range of problems. Immediate goals include inclusion of varying fluid viscosity caused by the chemical reaction. Fluids with changing viscosity are of interest in natural resource extraction and geological storage of materials. A key component of the finite element method is that it can readily scale, leading to plans to expand the models to model full three-dimensional problems and account for out of plane boundary interactions. Longer term goals include more complicated reaction pathways in order to model more realistic geologic chemistries. An initial system of interest is calcium carbonate ($CaCO_3$) precipitation and dissolution, a key reaction in the underground storage of captured carbon dioxide.

8.6 THMC model of a Repository Sited in Clay

As a final example, we consider another nuclear waste repository problem representative of scenarios being considered by the NEAMS project. The following problem is for demonstration purposes only, and does not represent any particular site or repository conditions, but does specify a realistic scenario.

8.6.1 Introduction and Problem Definition

This sample problem involves the effects of heat generating waste on the flow and transport of radioactive contaminants coupled with the geomechanical deformations of the surrounding subsurface region. Figure 8.6-1 is a schematic of the subsurface model. In the results presented below, the “basal unit” is also clay. The fault in the present model represents a material offset. The repository horizon is 1500 meters below the surface, sited in a clay/shale layer. The clay is overlain by a permeable sandstone layer, which is itself overlain by a sediment layer of similar permeability. The entire domain is assumed to be below the water table, much as many European repository systems (e.g., sited in granite). Tables 8.6-1 and 8.6-2 list key problem parameters.

Table 8.6-1. Parameters for elastic material model.

Property	Sediment	Sandstone	Clay	Units
Density	2100	2100	2100	kg/m^3
Young's Modulus	0.145	20	50	GPa
Poissons Ratio	0.2	0.2	0.12	---
Coefficient of Linear Thermal Expansion	1.16E-07	1.16E-05	1.4E-05	m/m-C°

Table 8.6-2. Flow and transport parameters.

Property	Sediment	Sandstone	Clay	Units
Initial Porosity	0.4	0.15	0.1	-
Permeability	5.0E-15	1.0E-14	1.0E-15	(m^2)
Thermal Diffusivity	6.95E-07	7.27E-07	7.27E-07	(m^2/sec)
Species Diffusivity	1.0E-08	1.0E-08	1.0E-08	(m^2/sec)
Retardation Factor	1.0	1.0	1.0	-

The repository is represented by a 5 m thick layer, 500 m by 250 m in plan view, backfilled with clay and packed to the same permeability as the surroundings, but with an elastic modulus of 5 GPa (compared to 50 GPa for the in-situ clay/shale). In the present simulation the repository radioactive decay power follows an exponential decay in time, with an initial power of 60 kW/acre, and a half-life of 50 years.

The initial regional stress state is assumed extensional with $\sigma_H = 0.7\sigma_V$, see section 8.4. The overburden pressure is specified at the top of the computational domain, and the bottom and lateral surfaces are fixed against normal displacement. There is also a regional (lateral) volumetric seepage rate of 5 cm/yr in the sediment, 10 cm/yr in the sandstone layer, and roughly 1 cm/yr in the clay layer.

A simple contaminant scenario is considered, for purposes of demonstration. The contaminants are composed of a two-member decay chain. The precursor species has a half-life of 100 years and the daughter species a much longer half-life, modeled here as a conserved species. The initial precursor inventory in the repository is modeled as unit concentration, with zero initial concentration elsewhere. The daughter species does not exist initially, and in the present demonstration neither species is adsorbed by the porous materials. The lateral seepage and buoyancy-induced flow are primary mechanisms for transport of contaminants from the repository to the biosphere.

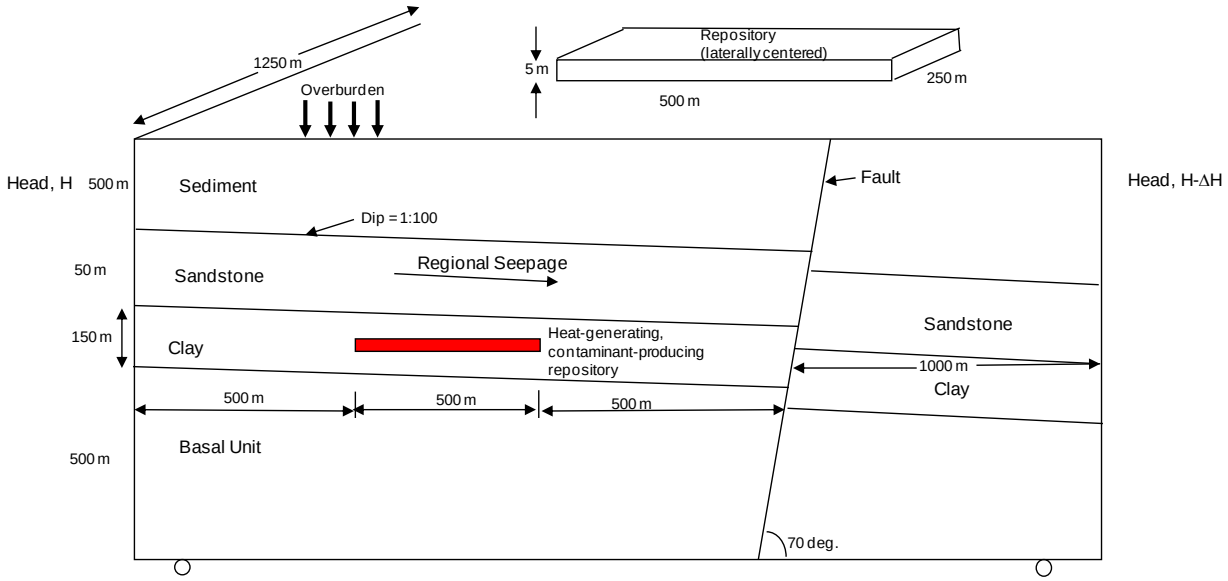

Figure 8.6-1. Schematic representation of the model geometry and geostratigraphy (not to scale).

8.6.2 Results

Figure 8.6-2 shows the temperature, vertical displacement and critical shear at 26 years in the sandstone and clay layers; the sediment layer has been removed to more clearly display the thermal expansion induced deformation. As noted, the actual vertical displacement is about 10 cm over the center of the repository. The repository attains a maximum temperature of about 135^{o} C at 26 years. The vertical component of effective stress displays a large gradient near the ends of the repository, and the repository horizon itself experiences a bow-shaped deformation. This is clearly displayed in the plot of critical shear (see section 8.4 for more discussion on the meaning and calculation of critical shear). Shear failure is indicated at the interfaces between the repository and the in-situ clay and at the interface with the sandstone. Together with the indicated warping of the repository horizon, the shear failure and mechanical deformations could damage the waste canisters and engineered barriers, indicating further investigations would be warranted.

Figure 8.6-3 shows a time sequence of the distribution of the daughter species; the precursor species disappears early owing to a short half-life and convective/diffusive processes. In this figure, the sandstone and clay near the repository have been removed to reveal the movement of the contaminant plume. The daughter species is formed from decay of its precursor near the repository, is convected upward by thermally induced buoyant upwelling through the repository into the fast-moving (10 cm/yr) horizontal flow in the sandstone. The plume is convected and diffused along the sandstone until it exits the domain, about 1.5 km from the repository, in roughly 2000 years. Not all of the contaminant exits the domain, some of it remains trapped in the adjoining sediment layer.

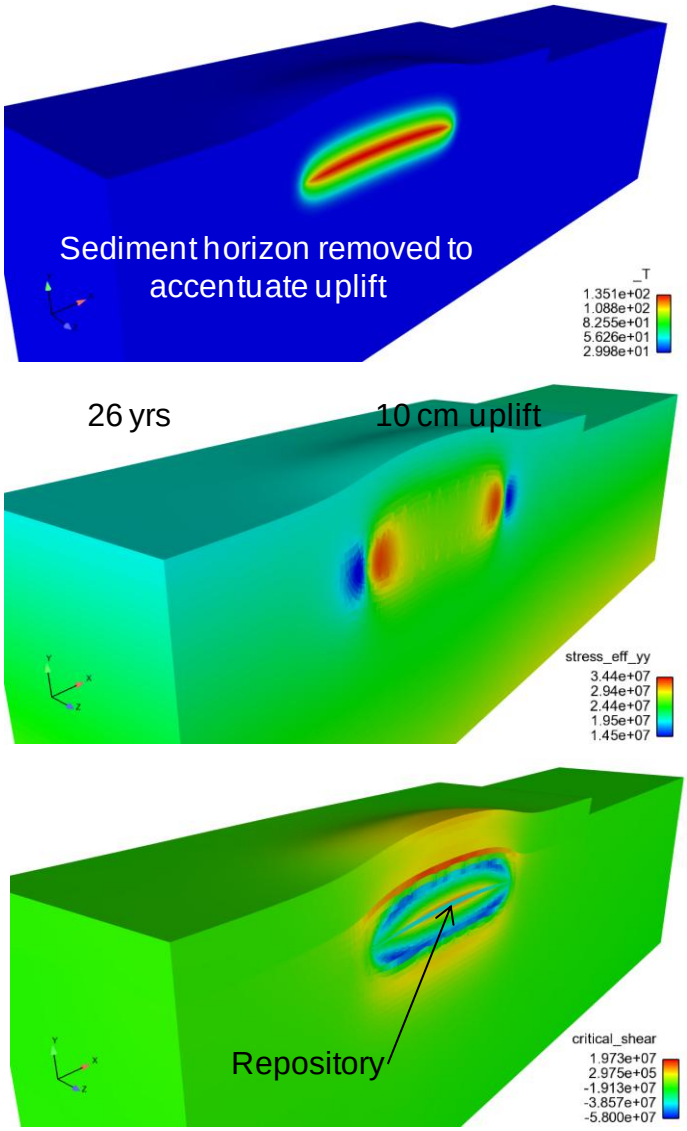

Figure 8.6-2. Distribution of temperature, vertical component of effective stress and critical shear at 26 years in the clay/shale and sandstone layers. The sediment layer has been removed to accentuate the thermal expansion induced deformation.

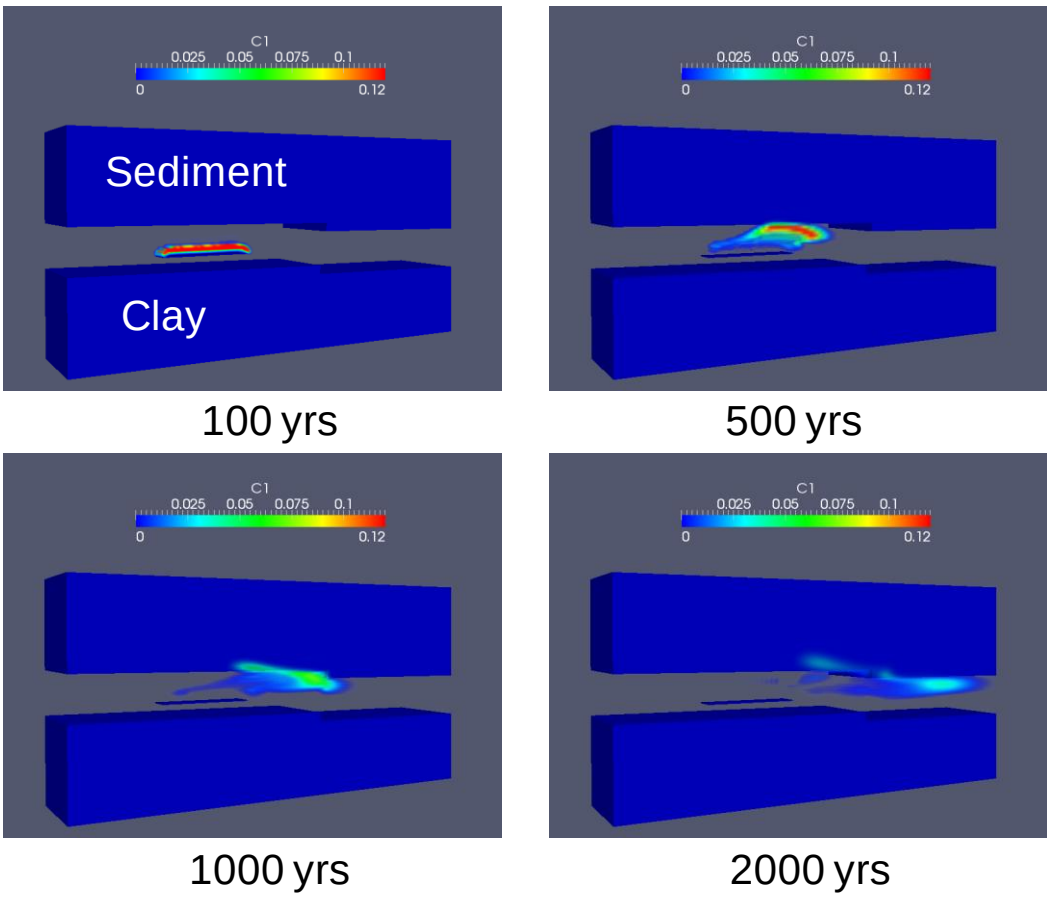

Figure 8.6-3. Time sequence of contaminant plume migration.

Though highly simplified, this demonstration problem suggests several features of this scenario that would warrant further study. There are a host of additional, important model features that could be considered, including permeability as a function of damage (e.g., critical shear), dissolution effects in the repository for better modeling of contaminant release, contaminant adsorption, either with a constant distribution coefficient or with nonlinear dependence on the local concentration (see Bear 1979), to name a few. The simulation displays and highlights some of the coupled multiphysics capabilities for geosystems modeling that are available in the Sierra system as a result of this research and development effort.

9. Conclusions

The foregoing chapters have summarized the research and development performed in this LDRD project. The main accomplishment was development of a foundational SNL capability for computational thermal, chemical, fluid and solid mechanics analysis of geosystems. The code was developed within the Sierra software system and was developed from the outset to run on massively parallel computers. Much auxiliary software is available for developing grids and viewing the results using parallel processing capabilities, enabling application of the software on massively parallel computers just as easily as on a single workstation.

Project milestone goals developed at the beginning of the project were ambitious and have been met, with the exception of the geochemical modeling, which was partially completed. First, multiphase flow physics models for porous media were developed, implemented and verified against solutions provided in the literature or in a few cases against analytical solutions. These models describe single- and two-phase flows in heterogeneous porous materials and can be coupled with heat and reactive species transport. The development and implementation of multiphase reactive species transport specific to porous media was also a major goal. This capability enables another goal, the development of computational geochemistry. Geochemistry models describing carbonate systems, crucial to subsurface sequestration of carbon dioxide, were formulated, implemented in Cantera and verified, as described in Chapter 3. Owing to time constraints, these models have not been applied in a reactive flow setting. However, the machinery is in place for fully coupled flow and geochemistry and its development will continue under the CFSES project mentioned in the introduction.

Multiphase models of the CO_2-brine system in particular and reactive species modeling in general require real fluid computational thermodynamics models. Thermodynamics models were developed in Cantera. Accurate equation of state (EoS)-based phase behavior of the CO_2-H_2O-NaCl system was developed and implemented. Additionally, phase behavior of general fluid mixtures can be modeled using a multicomponent Redlick-Kwong EoS. Cantera also provides thermodynamic functions such as activities and fugacities necessary for solving chemical reaction problems.

Several geomechanics constitutive models describing geomaterials have been developed and implemented into the Sierra software system. One model is specifically developed for describing creep, primarily for modeling of salt beds. A second model incorporates the influence of capillary pressure and phase saturation on the isothermal elasto-plastic response of porous materials whose pore space is saturated with liquid and gas phases. Finally, an elasto-plastic constitutive model for Castlegate Sandstone, was implemented in the SNL Geomodel using laboratory data provided by T. Dewers (6914). The Geomodel is a general constitutive model for describing a very large variety of geologic materials. Castlegate Sandstone is being utilized as representative of a saline reservoir for CO_2 sequestration simulations.

Geologic materials are highly spatially heterogeneous in their properties. Geostatistical methods are applied to model material variability. Aria and Adagio were enhanced to allow heterogeneous descriptions of properties as fields. Random field representation of material properties using the

Karhunen-Loeve (KL) expansion was developed. This construction was used as a basis for developing conditional simulations of properties constrained to sparsely known field data.

A general coupling strategy was developed for multiphysics simulations. Together with the physics models discussed above, this capability enables the ultimate goal of the project, coupled multiphase thermal, chemical, solid and fluid mechanics simulations in heterogeneous porous materials. This capability was demonstrated in Chapter 8.

The accomplishments of this project impact SNL's Energy, Climate and Infrastructure Security (ECIS) Strategic Management Unit's ability to respond to important national energy problems such as disposal of nuclear waste, CO_2 sequestration, bioremediation, and engineered geothermal systems. They also position SNL to more effectively compete for DOE, CRADA, and Work for Others projects in the area of energy security, a key to ensuring the nation's economic stability and national security. This work also impacts national security projects dealing with weapon safety and reliability, particularly in energetic materials, such as cook-off, smoldering, and multiphase material relocation, to name a few. Finally, this effort promoted close collaborations with the University of Texas at Austin Center for Subsurface Modeling and the Jackson School of Geosciences including the Bureau of Economic Geology on research issues related to reaction/transport modeling of deforming geomaterials. This effort expands the potential customer and application base for computational geosciences at SNL and addresses many technologically important applications of great national significance.

10. References

Abramowitz, M. and I. A. Stegun, eds. (1970) *Handbook of Mathematical Functions with Formulas, Graphs, and Mathematical Tables,* 9th printing. New York: Dover.

Acharya, R. C., A. J. Valocchi, C. J. Werth, and T. W. Willingham. (2007) Pore-scale simulation of dispersion and reaction along a transverse mixing zone in two-dimensional porous media. *Water Resources Research* 43:W10435.

Akinfiev, N. N. and L. W. Diamond. (2010) Thermodynamic model of aqueous CO_2-H_2O-NaCl solutions from -22 to 100 ^oC and from 0.1 to 100 MPa. *Fluid Phase Equilibria* 295(1):104–124.

Alonso, E. E., A. Gens, and A. Josa. (1990) A constitutive model for partially saturated soils. *Geotechnique* 40:405–430.

Angus, S., B. Armstrong, et al. (1976) *Carbon dioxide*. Oxford and New York: Pergamon Press.

Arnst, M., R. Ghanem, and C. Soize. (2010) Identification of Bayesian posteriors for coefficients of chaos expansions. *Journal of Computational Physics* 229(9):3134–3154.

Aziz K. and Settari A. (1979) Petroleum Reservoir Simulation. Applied Science Publishers Ltd., London.

Bachu, S., W. D. Gunter, et al. (1994) Aquifer Disposal of CO_2 Hydrodynamic and Mineral Trapping. *Energy Conversion and Management* 35(4):269–279.

Bachu, S. and J. J. Adams. (2003) Sequestration of CO_2 in geological media in response to climate change: Capacity of deep saline aquifers to sequester CO_2 in solution. *Energy Conversion and Management* 44(20):3151–3175.

Bando, S., F. Takemura, et al. (2003) Solubility of CO_2 in aqueous solutions of NaCl at (30 to 60) ^oC and (10 to 20) MPa. *Journal of Chemical and Engineering Data* 48(3):576–579.

Bear, J. (1972) *Dynamics of Fluids in Porous Media*. New York: Dover.

Bear, J. (1979) *Hydraulics of Groundwater*. New York: McGraw-Hill.

Benezeth, P., D. A. Palmer, et al. (2007) Dawsonite synthesis and re-evaluation of its thermodynamic properties from solubility measurements: Implications for mineral trapping of CO_2. *Geochimica et Cosmochimica Acta* 71(18):4438–4455.

Biot, M. A. (1941) General theory of three dimensional consolidation. *Journal of Applied Physics* 12:155–164.

Biot, M. A. and P. G. Willis. (1957) The elastic coefficients of the theory of consolidation. *Journal of Applied Mechanics* 24:594–601.

Bird R.B., W. E. Stewart, and E. N. Lightfoot. (1960) Transport Phenomena. John Wiley & Sons, New York.

Bishop, A. W. (1959) The principle of effective stress. *Teknisk Ukeblad* 106(39):859–863.

Blanford, M. L., M. W. Heinstein, and S. W. Key. (2001) *JAS3D-A Multi-Strategy Iterative Code for Solid Mechanics Analysis: User's Instructions,* Release 2.0, SAND Report (Draft). Albuquerque, NM: Sandia National Laboratories.

Borja, R. I. (2004) Cam-clay plasticity, Part V: A mathematical framework for three-phase deformation and strain localization analyses of partially saturated porous media. *Computer Methods in Applied Mechanics and Engineering* 193:5301–5338.

Borja, R. I., C. Tamagnini, and A. Amorosi. (1997) Coupling plasticity and energy-conserving elasticity models for clays. *Journal of Geotechnical and Geoenvironmental Engineering*. American Society of Civil Engineers 123(10):948–957.

Borja, R. I. and C. Tamagnini. (1998) Cam-Clay plasticity Part III: Extension of the infinitesimal model to include finite strains. *Computer Methods in Applied Mechanics and Engineering* 155:73–95.

Borja, R. I., K. M. Sama, and P. F. Sanz. (2003) On the numerical integration of three-invariant elastoplastic constitutive models. *Computer Methods in Applied Mechanics and Engineering* 192:1227–1258.

Carey, J. W., M. Wigand, et al. (2007) Analysis and performance of oil well cement with 30 years of CO_2 exposure from the SACROC Unit, West Texas, USA. *International Journal of Greenhouse Gas Control* 1(1):75–85.

Carey, J. W., R. Svec, et al. (2009) Wellbore integrity and CO_2-brine flow along the casing-cement microannulus. *Greenhouse Gas Control Technologies 9* 1(1):3609–3615.

———. (2010) Experimental investigation of wellbore integrity and CO_2-brine flow along the casing-cement microannulus. *International Journal of Greenhouse Gas Control* 4(2):272–282.

Chou, L., R. M. Garrels, et al. (1989. Comparative-study of the kinetics and mechanisms of dissolution of carbonate minerals. *Chemical Geology* 78(3–4):269–282.

Class H, A Ebigbo, et al. (2009) A benchmark study on problems related to CO2 storage in geologic formations, *Computational Geosciences*, **13**(4), 409-434.

Colclasure, A. M. and R. J. Kee. (2010) Thermodynamically consistent modeling of elementary electrochemistry in lithium-ion batteries. *Electrochimica Acta* 55:8960–8973.

Cormeau, I. (1975) Numerical stability in quasi-static elasto-visco-plasticity. *International Journal for Numerical Methods in Engineering* 9:109–127.

Corti, H. R., J. J. Depablo, et al. (1990) Phase-equilibria for aqueous systems containing salts and carbon-dioxide—Application of Pitzer theory for electrolyte-solutions. *Journal of Physical Chemistry* 94(20):7876–7880.

Cressie, N. A. C. (1993) *Statistics for Spatial Data.* (Probability and Mathematical Statistics series). New York: Wiley.

Dalen, V. (1979) Simplified finite-element models for reservoir flow problems. *SPE Journal.* 19(5):333–343.

Dean, R. H., X., Gai, C. M. Stone, and S. E. Minkoff. (2003) A comparison of techniques for coupling porous flow and geomechanics. Presented at SPE 79709, SPE Reservoir Simulation Symposium, 3–5 February, at Houston Texas.

Desceliers, C., C. Soize, and R. Ghanem. (2007) Identification of chaos representations of elastic properties of random media using experimental vibration tests. *Computational Mechanics* 39(6):831–838.

Deutsch, C. V. and A. G. Journel. (1998) *GSLIB Geostatistical Software Library and User's Guide*, 2d ed. Applied Geostatistics series. New York: Oxford University Press.

Duan, Z. H., J. W. Hu, et al. (2008) Densities of the CO_2-H_2O and CO_2-H_2O-NaCl systems up to 647 K and 100 MPa. *Energy & Fuels* 22(3):1666–1674.

Ebigbo, A., H. Class, and R. Helmig. (2007) CO_2 leakage through an abandoned well: Problem-oriented benchmarks. *Computational Geosciences* 11:103–115.

Elder, J. W. (1967) Steady free convection in a porous medium heated from below. *Journal of Fluid Mechanics* 27(part 1):29–48.

Eldred, M. S., S. L. Brown, et al. (2007a) *DAKOTA, A multilevel Parallel Object-Oriented Framework for Design Optimization, Parameter Estimation, Uncertainty Quantification, and Sensitivity Analysis: Version 4.1 Developers Manual* (Technical report) SAND2006-4056. Albuquerque, NM: Sandia National Laboratories.

———. (2007b) *DAKOTA, A multilevel Parallel Object-Oriented Framework for Design Optimization, Parameter Estimation, Uncertainty Quantification, and Sensitivity Analysis: Version 4.1 Reference Manual* (Technical report) SAND2006-4055. Albuquerque, NM: Sandia National Laboratories.

———. (2007c) *DAKOTA, A multilevel Parallel Object-Oriented Framework for Design Optimization, Parameter Estimation, Uncertainty Quantification, and Sensitivity Analysis: Version 4.1 Users Manual* (Technical report) SAND2006-6337. Albuquerque, NM: Sandia National Laboratories.

Fisher, R. A. (1926) On the capillary forces in an ideal soil; Correction of formulae given by W. B. Haines. *Journal of Agricultural Science* 16(3):492–505.

Forrest, A. (1972) On coons and other methods for the representation of curved surfaces. *Computer Graphics and Image Processing* 1(4):341–359.

Forsyth, P. A. (1991) A control volume finite element approach to NAPL groundwater contamination. *SIAM Journal of Scientific and Statistical Computing* 12:354–367.

Foster, C. D., R. A. Regueiro, A. F. Fossum, and R. I. Borja. (2005) Implicit numerical integration of a three-invariant isotropic/kinematic hardening cap plasticity model for geomaterials. *Computer Methods in Applied Mechanics and Engineering* 194:5109–5138.

Gallipoli, D., A. Gens, R. Sharma, and J. Vaunat. (2003) An elasto-plastic model for unsaturated soils incorporating the effects of suction and degree of saturation on mechanical behavior. *Geotechnique* 53(1):123–135.

Gautelier, M., J. Schott, et al. (2007) An experimental study of dolomite dissolution rates at 80^{o}C as a function of chemical affinity and solution composition. *Chemical Geology* 242(3–4):509–517.

Ghanem, R., A. Doostan, and J. Red-Horse. (2008) A probabilistic construction of model validation (Validation Challenge Workshop). *Computer Methods in Applied Mechanics and Engineering* 197(29–32):2585–2595.

Goodwin, D. G. (2003) An open-source, extensible software suite for CVD process simulation. Presented at EUROCVD-14 and CVD XVI, 27 April–2 May, at Paris, France.

Goodwin, D. G. and M. A. Aivazis. (1999) *A Modular, Object-Oriented Software Package for Chemical Kinetics and Chemical Thermodynamics.* Pasadena, CA: California Institute of Technology.

Gordon, W. (1971) Blending-function methods of bivariate and multivariate interpolation and approximation. *SIAM Journal on Numerical Analysis* 8(1)158–177.

Grigoriu, M. (2002) *Stochastic Calculus: Applications in Science and Engineering*. Boston: Birkhäuser.

Gunter, W. D. and E. H. Perkins. (1993) Aquifer disposal of CO_2-rich gases—Reaction design for added capacity. *Energy Conversion and Management* 34(9-11):941–948.

Gunter, W. D., E. H. Perkins, et al. (2000) Aquifer disposal of acid gases: Modelling of water-rock reactions for trapping of acid wastes. *Applied Geochemistry* 15(8):1085–1095.

Hangx, S. J. T. and C. J. Spiers. (2009) Reaction of plagioclase feldspars with CO_2 under hydrothermal conditions. *Chemical Geology* 265(1–2):88–98.

Hansen, F. D., E. L. Hardin, R. P. Rechard, G. A. Freeze, D. C. Sassani, P. V. Brady, C. M. Stone, M. J. Martinez, J. F. Holland, T. Dewers, K. N. Gaither, S. R. Sobolik, and R.T. Cygan. (2010) *Shale Disposal of US High-Level Radioactive Waste* (Technical report) SAND2010-2843. Albuquerque, NM: Sandia National Laboratories.

Hao, Y. and D. G. Goodwin. (2007) Numerical modeling of single-chamber SOFCs with hydrocarbon fuels. *Journal of The Electrochemical Society* 154:B207–B217.

Helmig, R. (1997) *Multiphase Flow and Transport Processes in the Subsurface*. Berlin: Springer-Verlag.

Hill, R. (1950) *The Mathematical Theory of Plasticity*. New York: Oxford University Press.

Huber, R. and R. Helmig. (2000) Node-centered finite volume discretizations for the numerical simulation of multiphase flow in heterogeneous porous media. *Computational Geosciences* 4:141–164.

Journel, A.G., C. J. Huijbregts. (1981) *Mining Geostatistics*. San Diego: Academic Press.

Kharaka, Y. K., D. R. Cole, et al. (2006) Gas-water-rock interactions in sedimentary basins: CO_2 sequestration in the Frio Formation, Texas, USA. *Journal of Geochemical Exploration* 89(1–3):183–186.

Karpov, I. K., K. V. Chudnenko, et al. (1997) Modeling chemical mass transfer in geochemical processes: Thermodynamic relations, conditions of equilibria, and numerical algorithms. *American Journal of Science* 297(8):767–806.

Kaszuba, J. P., D. R. Janecky, et al. (2003) Carbon dioxide reaction processes in a model brine aquifer at 200°C and 200 bars: Implications for geologic sequestration of carbon. *Applied Geochemistry* 18(7):1065–1080.

Kaszuba, J. P., D. R. Janecky, et al. (2005) Experimental evaluation of mixed fluid reactions between supercritical carbon dioxide and NaCl brine: Relevance to the integrity of a geologic carbon repository. *Chemical Geology* 217(3–4):277–293.

Kindred, J. S. and M. A. Celia. (1989) Contaminant transport and biodegradation—2. Conceptual model and test simulations. *Water Resources Research* 25(6):1149–1159.

Kolmogorov, A. N. and S. V. Fomin. (1975) *Introductory Real Analysis*. New York: Dover Publications.

Lasaga, A. C. (1998) *Kinetic Theory in Earth Sciences*. Princeton, NJ: Princeton University Press.

Lemieux, J. M. (2011) Review: The potential impact of underground geological storage of carbon dioxide in deep saline aquifers on shallow groundwater resources. *Hydrogeology Journal* 19(4):757–778.

Lophaven, S. N., H. Jacon, and B. Sondergaard. (2002) *DACE: A Matlab Kriging Toolbox Version 2.0* (Technical report) IMM-TR-2002-12, Informatics and Mathematical Modeling (IMM).—Copenhagen: Technical University of Denmark. http://www2.imm.dtu.dk/hbn/dace/dace.pdf.

Loret, B. and N. Khalili. (2002) An effective stress elastic-plastic model for unsaturated porous media. *Mechanics of Materials* 34:97–116.

Malvern, L. E. (1969) *Introduction to the Mechanics of a Continuous Medium*. Englewood Cliffs, NJ: Prentice-Hall.

Mao, S. and Z. H. Duan. (2008) The P,V,T,x properties of binary aqueous chloride solutions up to T=573 K and 100 MPa. *Journal of Chemical Thermodynamics* 40(7):1046–1063.

Mariner, P. E. (2007) *In-Drift Precipitates/Salts Model* (ANL-EBS-MD-000045 REV 03). Las Vegas, NV: Sandia National Laboratories.

Martinez, M. J., P. L. Hopkins, and P. C. Reeves. (2001) *PorSalsa User's Manual* (Technical report) SAND2001-1555. Albuquerque, NM: Sandia National Laboratories.

Martinez, M. J. and C. M. Stone. (2008) *Considerations for Developing Models of Multiphase Flow in Deformable Porous Media* (Technical report) SAND2008-5887. Albuquerque, NM: Sandia National Laboratories.

McGrail, B. P., H. T. Schaef, et al. (2006) Potential for carbon dioxide sequestration in flood basalts. *Journal of Geophysical Research-Solid Earth* 111(B12):B12201.

McPherson, B., W. Han, and B. Cole. (2008) Two equations of state assembled for basic analysis of multiphase CO_2 flow and in deep sedimentary basin conditions. *Computers & Geosciences* 34:427–444.

Moffat, H. K. (2007) *8. CADS: Cantera Aerosol Dynamics Simulator*, SAND2007-4216. Albuquerque, NM: Sandia National Laboratories.

Moffat, H. K. and C. F. Jove-Colon, (2009) *Implementation of Equilibrium Chemistry Speciation and Chemistry (EQ3 type) Calculations into Cantera or Electrolyte Solution* SAND2009-3115, Albuquerque, NM: Sandia National Laboratories.

Moffat, H. K. and D. G. Goodwin. (2011) Cantera: An object-oriented software toolkit for chemical kinetics, thermodynamics, and transport processes. http://code.google.com/p/cantera (accessed in July 2011). Retrieved July 2011 from http://code.google.com/p/cantera/.

Moller, N., J. P. Greenberg, et al. (1998) Computer modeling for geothermal systems: Predicting carbonate and silica scale formation, CO_2 breakout and H2S exchange. *Transport in Porous Media* 33(1-2):173–204.

Montgomery, D. (2000) *Design and Analysis of Experiments*, 7th ed. New York: Wiley.

Munson, D. E. (1979) *Preliminary Deformation-Mechanism Map for Salt (with Application to WIPP)* SAND70-0079. Albuquerque, NM: Sandia National Laboratories.

Munson, D. E. and P. R. Dawson. (1979) *Constitutive Model for the Low Temperature Creep of Salt (with Application to WIPP)* SAND79-1853. Albuquerque, NM: Sandia National Laboratories.

———. (1982) *A Transient Creep Model for Salt during Stress Loading and Unloading*, SAND82-0962. Albuquerque, NM: Sandia National Laboratories.

———. (1984) Salt constitutive modeling using mechanism maps. Presented 1st International Conference on the Mechanical Behavior of Salt, trans Tech Publications, Clausthal, Germany. 717–737.

Munson, D. E., A. F., Fossum, and P. E. Senseny. (1989) *Advances in Resolution of Discrepancies between Predicted and Measured in Situ WIPP Room Closures*, SAND88-2948. Albuquerque, NM: Sandia National Laboratories.

Newell, D. L., J. P. Kaszuba, et al. (2008) Significance of carbonate buffers in natural waters reacting with supercritical CO_2: Implications for monitoring, measuring and verification (MMV) of geologic carbon sequestration. *Geophysical Research Letters* 35(23).

Nickalls, R. W. D. (1993) A new approach to solving the cubic: Cardan's solution revealed. *The Mathematical Gazette* **77**(480):354–359.

Notz, P. K., S. R. Subia, M. M. Hopkins, H. K. Moffat, and D. Noble. (2007) *Aria 1.5: User Manual*, SAND2007-2734. Albuquerque, NM: Sandia National Laboratories,

Papoulis, A. (1991) *Probability, Random Variables, and Stochastic Processes*, 3rd ed. New York: McGraw-Hill.

Perkins, E. H. and W. D. Gunter. (1995) Aquifer disposal of CO_2-rich greenhouse gases: Modelling of water-rock reaction paths in a siliciclastic aquifer. *Water-Rock Interaction* 895–898.

Pitzer, K. S., J. C. Peiper, et al. (1984) Thermodynamic properties of aqueous sodium-chloride solutions. *Journal of Physical and Chemical Reference Data* 13(1):1–102.

Plummer, L. N., T. M. L. Wigley, et al. (1978) Kinetics of calcite dissolution in CO_2-water systems at 5 degrees C to 60 degrees C and 0.0 to 1.0 atm CO_2. *American Journal of Science* 278(2):179–216.

Pokrovsky, O. S. and J. Schott. (1999) Processes at the magnesium-bearing carbonates solution interface—II. Kinetics and mechanism of magnesite dissolution. *Geochimica Et Cosmochimica Acta* 63(6):881–897.

Prausnitz, J. M., R. N. Lichtenthaler, et al. (1986) *Molecular Thermodynamics of Fluid-Phase Equilibria*. Englewood Cliffs, NJ: Prentice-Hall.

Press, W. H., S. A. Teukolsky, W. T. Vetterling, and B. P. Flannery. (1992) *Numerical Recipes in FORTRAN, The Art of Scientific Computing*. New York: Cambridge University Press.

Pruess, K. (1987) *TOUGH User's Guide*, LBL-20700 (NUREG/CR-4645). Berkeley, CA: Lawrence Berkeley Laboratory.

Reynolds, W. C. (1979) *Thermodynamic Properties in SI: Graph, Tables, and Computational Equations for Forty Substances*. Stanford, CA: Stanford University**.**

Rosenblatt, M. (1952) Remarks on a multivariate transformation. *The Annals of Mathematical Statistics* 23(3):470–472.

Rosenthal, J. S. (2000) *A First Look at Rigorous Probability Theory*. River Edge, NJ: World Scientific Publishing.

Rutqvist, J., L. Borgesson, M. Chijimatsu, A. Kobayashi, L. Jing, T. S. Nguyen, J. Noorishad, and C-F. Tsang. (2001) Thermohydromechanics of partially saturated geologic media: Governing equations and formulation of four finite element models. *International Journal of Rock Mechanics & Mining Science* 38:105–127.

Rutqvist J, Birkholzer F, Cappa F, and Tsang C-F. (2007) Estimating sustainable injection pressure during geological sequestration of CO_2 using coupled fluid flow and geomechanical fault-slip analysis, *Energy Conversion and Management*, **48**, 1798-1807.

Sakamoto, S. and R. Ghanem. (2002) Simulation of multi-dimensional non-gaussian non-stationary random fields. *Probabilistic Engineering Mechanics* 17:167-176.

Sangini, A. S. and A. Acrivos. (1982) Slow flow past periodic arrays of cylinders with application to heat transfer. *International Journal of Multiphase Flow* 8(3):193–206.

Sasena, M. J. (2002) *Flexibility and Efficiency Enhancements for Constrained Global Design Optimization with Kriging Approximations*. PhD thesis, University of Michigan, Ann Arbor.

Scherzinger, W. M. and D. C. Hammerand. (2007) *Constitutive Models in LAME* (Technical report) SAND2007-5873. Albuquerque, NM: Sandia National Laboratories.

Scherzinger, W. M. and C. R. Dohrmann. (2008) A robust algorithm for finding the eigenvalues and eigenvectors of 3x3 symmetric matrices. *Computer Methods in Applied Mechanics and Engineering* 197:4007–4015.

Schofield, A. N. and C. P. Wroth. (1968) *Critical State Soil Mechanics.* London: McGraw-Hill.

Schott, J., O. S. Pokrovsky, et al. (2009) The link between mineral dissolution/precipitation kinetics and solution chemistry. *Reviews in Mineralogy and Geochemistry* 70:207–258.

Schrefler, B. A. and R. Scotta. (2001) A fully coupled dynamic model for two-phase fluid flow in deformable porous media. *Computational Methods in Applied Mechanics and Engineering* 190:3223–3246.

Schreyer H. L. (2002) On time integration of viscoplastic constitutive models suitable for creep, *International Journal for Numerical Methods in Engineering*, **53**: 637-652.

Schwab, C. and R. A. Todor. (2006) Karhunen-Loève approximation of random fields by generalized fast multipole methods. *Journal of Computational Physics* 217(1):100–122.

Shiraki, R. and S. L. Brantley. (1995) Kinetics of near-equilibrium calcite precipitation at 100°C—An evaluation of elementary reaction-based and affinity-based rate laws. *Geochimica Et Cosmochimica Acta* 59(8):1457–1471.

Shiraki, R., P. A. Rock, et al. (2000) Dissolution kinetics of calcite in 0.1 m NaCl solution at room temperature: An atomic force microscopic (AFM) study. *Aquatic Geochemistry* 6(1):87–108.

Sierra Solid Mechanics Team. (2009) *Adagio 4.14 User's Guide*, SAND2009-7410. Albuquerque, NM: Sandia National Laboratories.

Simo, J. C. and T. J. R. Hughes. (1998) *Computational Inelasticity*. New York: Springer-Verlag.

Smith, J. M. and H. C. Van Ness. (1975) *Introduction to Chemical Engineering Thermodynamics*, 3rd ed. New York: McGraw-Hill.

Smith, W. R. and R. W. Missen. (1982) *Chemical Reaction Equilibrium Analysis: Theory and Algorithms*. New York: Wiley.

Sobolik, S. R. , J. E. Bean, and B. L. Ehgartner (2010) Application of the Multi-Mechanism Deformation Model for Three-Dimensional Simulations of Salt Behavior for the Strategic Petroleum Reserve, ARMA 10-403. Presented at 44th U. S. Rock Mechanics Symposium and 5th U. S.-Canada Rock Mechanics Symposium, 27–30 June, at Salt Lake City, UT.

Span, R. and W. Wagner. (1996) A new equation of state for carbon dioxide covering the fluid region from the triple-point temperature to 1100 K at pressures up to 800 MPa. *Journal of Physical and Chemical Reference Data* 25:1509–1596.

Spencer, B. W. et al. (2011) *Adagio 4.20 User's Guide*, SAND2011-1825. Albuquerque, NM: Sandia National Laboratories.

Spycher, N., K. Pruess, et al. (2003) CO_2-H_2O mixtures in the geological sequestration of CO_2. I. Assessment and calculation of mutual solubilities from 12 to 100 °C and up to 600 bar. *Geochimica et Cosmochimica Acta* 67(16):3015–3031.

Spycher, N. and K. Pruess. (2005) CO_2-H_2O mixtures in the geological sequestration of CO_2. II. Partitioning in chloride brines at 12–100 °C and up to 600 bar. *Geochimica et Cosmochimica Acta* 69(13):3309–3320.

———. (2010) A Phase-Partitioning Model for CO_2-Brine Mixtures at Elevated Temperatures and Pressures: Application to CO_2-Enhanced Geothermal Systems. *Transport in Porous Media* 82(1):173–196.

Stone, C. M. (1997) *Final Disposal Room Structural Response Calculations*, SAND97-0795. Albuquerque, NM: Sandia National Laboratories.

———. (1997) *SANTOS—A Two-Dimensional Finite Element Program for the Quasistatic Large Deformation Inelastic Response of Solid*s, SAND90-0543. Albuquerque NM: Sandia National Laboratories.

Stone, C. M., J. F. Holland, J. E. Bean, and J. G. Argüello. (2010) Coupled thermal-mechanical analyses of a generic salt repository for high level waste, ARMA 10-180. Presented at 44th U. S. Rock Mechanics Symposium and 5th U. S.-Canada Rock Mechanics Symposium, 27–30 June, at Salt Lake City, UT.

Stone, C. M. and M. J. Martinez. (2010) Coupled multiphysics modeling to support energy R&D. Sandia National Laboratories, Science Matters website: www.sandia.gov/mission/ste/stories/2010/Science%20Matters%202010%20Fall/Individual%20articles/Stone9-2010.pdf

Stone, C. M., M. J. Martinez, T. Dewers, F. D. Hansen, E. L. Hardin, J. G. Argüello, and J. F. Holland. (2011) Coupled thermal-hydrological-mechanical-chemical analyses of a repository in clay/shale for high-level waste, ARMA-11-243. *Proceedings of the American Rock Mechanics Association (ARMA).* Presented at 45th U. S. Rock Mechanics/Geomechanics Symposium, 26–29 June, at San Francisco, CA.

Udell, K. S. and J. S. Fitch. (1985) Heat and mass transfer in capillary porous media considering evaporation, condensation, and non-condensible gas effects. Presented at the 23rd ASME/AICHE National Heat Transfer Conference, August 4-7, 1985, at Denver, CO.

van Genuchten, R. (1978) Calculating the unsaturated hydraulic conductivity with a new closed form analytical model. *Water Resources Bulletin*. Princeton, NJ: Princeton University Press.

van Genuchten, M. T. (1980) A closed-form equation for predicting the hydraulic conductivity of unsaturated soils. *Soil Science Society of America Journal* 44:892–898.

von Terzaghi, K. (1943) *Theoretical Soil Mechanics*. New York: Wiley.

Wagner, W. and A. Prub. (2002) The IAPWS formulation 1995 for the thermodynamic properties of ordinary water substance for general and scientific use. *Journal of Chemical Reference Data* 31(2):387–442.

Walker, H. and P. Ni. (2010) Anderson acceleration for fixed-point iterations. *SIAM Journal on Numerical Analysis*. In press.

White, M. D. and M. Oostrom. (2006) *STOMP subsurface transport over multiple phases, Version 4.0, User's guide,* PNNL 12034. Richland, WA: Pacific Northwest National Laboratory.

Willingham, T. W., C. J. Werth, and A. J. Valocchi. (2008) Evaluation of the effects of porous media structure on mixing-controlled reactions using pore-scale modeling and micromodel experiments. *Environmental Science & Technology* 42(9):3185–3193.

Willingham, T. W., C. Zhang, C. J. Werth, A. J Valocchi, M. Oostrom, and T. W. Wiestma. (2010) Using dispersivity values to quantify the effects of pore-scale flow focusing on enhanced reaction along transverse mixing zone. *Advances in Water Research* 33:525–535.

Wolery, T. J. and R. L. Jarek. (2003) *EQ3/6, Version 8.0: Software User's Manual*. Albuquerque, NM: Sandia National Laboratories.

Wolf, M., O. Breitkopf, et al. (1989) Solubility of calcite in different electrolytes at temperatures between 10-degrees and 60-degrees-C and at CO_2 partial pressures of about 1 Kpa. *Chemical Geology* 76(3–4):291–301.

Wood, D. M. (1990) *Soil Behaviour and Critical State Soil Mechanics*. Cambridge University Press.

Xiu, D. and G. E. Karniadakis. (2002) The Wiener-Askey polynomial chaos for stochastic differential equations. *SIAM Journal on Scientific Computing* 24(2):619–644.

———. (2003) A new stochastic approach to transient heat conduction modeling with uncertainty. *International Journal of Heat and Mass Transfer* 46(24):4681–4693,.

Yoon, H., A. J. Valocchi, C. J. Werth, and T. Dewers. (2011) Pore-scale simulation of mixing-induced calcium carbonate precipitation and dissolution in a microfluidic pore network, *Water Resources Research*. Submitted July 2011.

Zyvoloski, G. A., B. A. Robinson, and Z. V. Dash. (1995) *Models and Methods Summary for the FEHM Application* LA-UR-94-3787. Los Alamos, NM: Los Alamos National Laboratory Report.

11. Appendix A: Numerical Implementation of Fluid Flow

Unstructured Grid Finite Element-Based Discretization

The discretization is based on an unstructured grid finite element method (FEM), wherein variables are represented by a finite dimensional basis. Taking the nonisothermal air/water system as an example, the canonical form of the spatially discrete coupled system is:

$$\begin{bmatrix} R_{w,I} \\ R_{a,I} \\ R_{e,I} \end{bmatrix} = \int_{\Omega} N_I \sum_J N_J \begin{bmatrix} \dot{d}_{w,J} \\ \dot{d}_{a,J} \\ \dot{e}_J \end{bmatrix} d\Omega - \int_{\Omega} \nabla N_I \bullet \begin{bmatrix} \mathbf{F}_w \\ \mathbf{F}_a \\ \mathbf{q}_e \end{bmatrix} d\Omega - \int_{\Omega} N_I \begin{bmatrix} Q_w \\ Q_a \\ Q_e \end{bmatrix} d\Omega + \int_{\Gamma} N_I \begin{bmatrix} \mathbf{F}_w \bullet \mathbf{n} \\ \mathbf{F}_a \bullet \mathbf{n} \\ \mathbf{q}_e \bullet \mathbf{n} \end{bmatrix} d\Gamma \quad (11.1)$$

written as a system of residual equations, the right hand side of which represent the balance equations for water, air and energy. The indices *I* and *J* represent discrete nodal values of variables. Also, $d_\alpha = \phi\left(\rho_l Y_{\alpha l} S_l + \rho_g Y_{\alpha g}\left(1 - S_l\right)\right)$ represents the bulk density of component α, while *e* is the bulk energy density. This is the Galerkin finite element formulation (GFEM), which typically may be used for single phase systems, but usually needs modifications for multiphase systems, especially when involving phase transitions.

A lumped mass matrix promotes stability for temporal problems, which amounts to row-summing the mass matrix of an equation and placing the result on the diagonal,

$$\int_{\Omega} N_I \sum_J N_J \ \dot{d}_{w,J} d\Omega \rightarrow \dot{d}_{w,I} \int_{\Omega} N_I \ d\Omega \approx V_I \left(\frac{d_w^{n+1} - d_w^n}{t_{n+1} - t_n} \right) \quad (11.2)$$

where the last term includes a first-order discretization in time. The other modification needed is upwinding.

Edge-Based Upwind Flux

Experience has demonstrated that to solve multiphase flow problems with phase appearances or disappearances, an upwinded Darcy flux is necessary. A consistent method for applying upwinding on a finite element discretization is a method originally discussed by Dalen (1979) and later by Forsyth (1991). The method yields an edge-based mass conservative discretization.

Recall the Galerkin Darcy flux term (integrated by parts)

$$
\begin{aligned}
R_I^{flux} &= -\int_\Omega \nabla N_I \cdot \mathbf{F} d\Omega \\
&= -\int_\Omega \nabla N_I \cdot \left(-\lambda \mathbf{k} \cdot \left(\sum_J \nabla N_J P_J \right) \right) d\Omega \\
&= \sum_J \int_\Omega \lambda(\mathbf{x}) \nabla N_I \cdot \mathbf{k} \cdot \nabla N_J d\Omega P_J
\end{aligned}
\tag{11.3}
$$

in which we left off the gravitational term for clarity, and the spatial representation of the coefficient λ (=$Y\rho k_r / \mu$ for a multiphase flow problem) is not yet specified. The edge-based method derives from the following property of FEM,

$$
\sum_J \nabla N_J = 0; \quad \nabla N_I = -\sum_{J \neq I} \nabla N_J \tag{11.4}
$$

therefore,

$$
\nabla \sum_J N_J P_J = \sum_{J \neq I} \nabla N_J \left(P_J - P_I \right) \tag{11.5}
$$

If we apply this to the Galerkin flux residual above, we can get,

$$
\begin{aligned}
R_I^{flux} &= -\int_\Omega \nabla N_I \cdot \mathbf{F} d\Omega \\
&= -\int_\Omega \nabla N_I \cdot \left(-\lambda \mathbf{k} \cdot \left(\sum_{J \neq I} \nabla N_J \left(P_J - P_I \right) \right) \right) d\Omega \\
&= \sum_{J \neq I} \int_\Omega \lambda(\mathbf{x}) \nabla N_I \cdot \mathbf{k} \cdot \nabla N_J d\Omega \left(P_J - P_I \right)
\end{aligned}
\tag{11.6}
$$

To this point, this is still the Galerkin representation. Now we apply upwinding to the flow coefficient. Define,

$$
\lambda_{(I,J)}^u = \begin{cases} \lambda_J, & K_{IJ} \left(P_J - P_I \right) > 0 \\ \lambda_I, & K_{IJ} \left(P_J - P_I \right) < 0 \end{cases} \tag{11.7}
$$

where we have included the *assembled* transmissivity, as suggested by Forsyth,

$$
K_{IJ} = -\int_\Omega \nabla N_I \cdot \mathbf{k} \cdot \nabla N_J d\Omega \tag{11.8}
$$

so as to prevent “down-winding,” an unstable scheme. Applying these approximations and definitions yields

$$\begin{aligned} R_I^{flux} &= \sum_{J \neq I} \int_{\Omega} \lambda(\mathbf{x}) \nabla N_I \cdot \mathbf{k} \cdot \nabla N_J d\Omega \left(P_J - P_I \right) \\ &\approx \sum_{J \neq I} \lambda_{(I,J)}^{u} \int_{\Omega} \nabla N_I \cdot \mathbf{k} \cdot \nabla N_J d\Omega \left(P_J - P_I \right) \\ &= -\sum_{J \neq I} \lambda_{(I,J)}^{u} K_{IJ} \left(P_J - P_I \right) \end{aligned} \tag{11.9}$$

The minus sign comes from the definition of the transmissivity matrix. Notice that each term in the sum can be interpreted as the flux between nodes *I* and *J*, and that this flux has a conservative property,

$$F_{IJ} \equiv -\lambda_{(I,J)}^{u} K_{IJ} \left(P_J - P_I \right) = -F_{JI} \tag{11.10}$$

It is also noteworthy that the residual can be written in the form

$$R_I^{flux} = \int_{\Omega} \nabla N_I \cdot \mathbf{F}_I d\Omega \tag{11.11}$$

where the flux is defined by,

$$\mathbf{F}_I = -\mathbf{k} \cdot \sum_{J \neq I} \lambda_{(I,J)}^{u} \nabla N_J d\Omega \left(P_J - P_I \right) \tag{11.12}$$

The architectural difference between this form and the GFEM form is that here the discrete flux vector depends on the *I*-th node explicitly, as opposed to all the nodes, with no particular preference for any one particular node, as in the GFEM.

Including the transmissivity in the upwinding can be unwieldy in the usual processing of FEM; the assembled matrix would require a pre-processing loop over the elements, not to mention storing the transmissivity matrix. The alternative is to have meshes that produce no negative entries, but these are hard to come by. A solution that comes close is to use *vertex quadrature* for these upwinded flow terms.

Treatment of the gravity term

The formulation above rests on treating the flux in terms of the gradient of a flow potential. Here we define a pseudopotential that will allow us to use the foregoing forms of the upwinded flux. The gravitational potential can be written as,

$$\rho \mathbf{g} = \rho g \nabla \zeta \cong \rho(\mathbf{x}) g \sum_J \nabla N_J \zeta_J \tag{11.13}$$

where ζ is the elevation from a datum. The total potential can be written as

$$\nabla P + \rho \mathbf{g} = \sum_J \nabla N_J \left(P_J + \rho g \zeta_J \right) = \sum_J \nabla N_J \Psi_J \tag{11.14}$$

where the spatial representation of density is approximated by,

$$\rho_{IJ} = \frac{1}{2}\left(\rho_I + \rho_J \right) \tag{11.15}$$

The potential (pressure and gravity) gradient for the fluxes can then be defined by

$$\begin{aligned} &\nabla P + \rho \mathbf{g} \approx \sum_J \nabla N_J \Psi_J \\ &= \sum_{J \neq I} \nabla N_J \left((P_J - P_I) + \rho_{IJ} g (\zeta_J - \zeta_I) \right) \end{aligned} \tag{11.16}$$

12. Appendix B: Thermodynamic Functions for the Multicomponent R-K System

Calculation of the Expression for the Chemical Potential

We may take Eqn. (6.18), and find the formula for the chemical potential

$$\mu_i = \left.\frac{d\left(nA\right)}{d\left(n_i\right)}\right|_{T,V,n_j} = \int_V^\infty \left[\left(\frac{dP}{dn_i}\right)_{T,V} - \frac{RT}{V}\right] dV - RT\ln\left(\frac{p^o V}{n_i RT}\right) + RT + a_i^o$$

This can be expanded to

$$\begin{aligned}\mu_i = a_{RS,i}^o\left(T\right) + RT\ln X_i - RT\ln\frac{p^o V}{n_T RT} + RT + RT\ln\left(\frac{V}{V - n_T b_{mix}}\right) + \frac{RTn_T b_i}{V - n_T b_{mix}} \\ - \frac{2\sum_j a_{ij} n_j}{n_T b_{mix}\sqrt{T}}\ln\left[\frac{V + n_T b_{mix}}{V}\right] + \frac{a_{mix} b_i}{b_{mix}^2\sqrt{T}}\ln\left[\frac{V + n_T b_{mix}}{V}\right] - \frac{n_T a_{mix}}{b_{mix}\sqrt{T}}\left(\frac{b_i}{V + n_T b_{mix}}\right)\end{aligned} \tag{12.1}$$

And then rearranged to yield Eqn. (12.2):

$$\begin{aligned}\mu_i = \mu_{RS,i}^o\left(T\right) + RT\ln X_i + RT\ln\frac{P}{p^o} - RT\ln\frac{PV}{nRT} + RT\ln\left(\frac{V}{V - n_T b_{mix}}\right) + \frac{RTn_T b_i}{V - n_T b_{mix}} \\ - \frac{2\sum a_{ij} n_j}{n_T b_{mix}\sqrt{T}}\ln\left[\frac{V + n_T b_{mix}}{V}\right] + \frac{a_{mix} b_i}{b_{mix}^2\sqrt{T}}\ln\left[\frac{V + n_T b_{mix}}{V}\right] - \frac{n_T a_{mix}}{b_{mix}\sqrt{T}}\left(\frac{b_i}{V + n_T b_{mix}}\right)\end{aligned} \tag{12.2}$$

The first three terms of Eqn. (12.2) are recognized as the EoS for the ideal gas approximation. The remaining terms may be identified with an activity coefficient representation for the mixture, Eqn. (12.3).

$$\begin{aligned}RT\ln\gamma_i = -RT\ln\frac{PV}{n_T RT} + RT\ln\left(\frac{V}{V - n_T b_{mix}}\right) + \frac{RTn_T b_i}{V - n_T b_{mix}} \\ - \frac{2\sum a_{ij} n_i}{n_T b_{mix}\sqrt{T}}\ln\left[\frac{V + nb_{mix}}{V}\right] + \frac{a_{mix} b_i}{b_{mix}^2\sqrt{T}}\ln\left[\frac{V + n_T b_{mix}}{V}\right] - \frac{n_T a_{mix}}{b_{mix}\sqrt{T}}\left(\frac{b_i}{V + n_T b_{mix}}\right)\end{aligned} \tag{12.3}$$

where the standard state includes the ideal gas pressure term,

$$\mu_i^o\left(T,P\right) = \mu_{RS,i}^o\left(T\right) + RT\ln\frac{P}{p^o} \tag{12.4}$$

Derivation of the Fugacity Expressions

The fugacity expressions may be calculated from the following starting point

$$\mu_i\left(T,P\right)-\mu_i^o\left(T,P\right)=RT\ln\frac{f_i}{f_i^o} \tag{12.5}$$

Where the circled reference state is the ideal gas reference state where $f_i^o = X_i P$. Then

$$\begin{aligned}RT\ln\frac{f_i}{X_i P}&=\mu_i\left(T,P\right)-\mu_i^o\left(T,P\right)\\&=-RT\ln\frac{PV}{nRT}+RT\ln\left(\frac{V}{V-nb_{mix}}\right)+\frac{RTnb_i}{V-nb_{mix}}\\&\quad-\frac{2\sum a_{ij}n_i}{nb_{mix}\sqrt{T}}\ln\left[\frac{V+nb_{mix}}{V}\right]+\frac{a_{mix}b_i}{b_{mix}^2\sqrt{T}}\ln\left[\frac{V+nb_{mix}}{V}\right]-\frac{na_{mix}}{b_{mix}\sqrt{T}}\left(\frac{b_i}{V+nb_{mix}}\right)\end{aligned}$$

Therefore, the fugacity coefficient is equal to

$$\begin{aligned}\ln\phi_i&=-\ln\frac{PV}{n_T RT}+\ln\left(\frac{V}{V-n_T b_{mix}}\right)+\frac{n_T b_i}{V-n_T b_{mix}}\\&\quad-\frac{2\sum a_{ij}n_i}{RTn_T b_{mix}\sqrt{T}}\ln\left[\frac{V+n_T b_{mix}}{V}\right]+\frac{a_{mix}b_i}{RTb_{mix}^2\sqrt{T}}\ln\left[\frac{V+n_T b_{mix}}{V}\right]-\frac{na_{mix}}{RTb_{mix}\sqrt{T}}\left(\frac{b_i}{V+n_T b_{mix}}\right)\end{aligned} \tag{12.6}$$

This last equation agrees with that given by Spycher et al. (2003).

Derivation of the Entropy Expression

The entropy can be derived from the following expression:

$$nS=-\left.\frac{d\left(nA\right)}{d\left(T\right)}\right|_{V,n_i}$$

Taking the derivative of Eqn. (6.20) yields,

$$nS=-\left.\frac{d\left(nA\right)}{d\left(T\right)}\right|_{V,n_i}=\int_V^\infty\left[\frac{n_T R}{V}-\left(\frac{dP}{dT}\right)_{V,ni}\right]dV+R\sum_i n_i\ln\left(\frac{p^o V}{n_i RT}\right)+\sum_i n_i s_i^o-Rn_T$$

Note that this expression again differs from that in Prausnitz. However, this is resolved after considering that the standard states are actually at constant pressure, and we are taking a constant volume differentiation. Taking that into account gets rid of the $-Rn_T$ factor at the end of the expression leading to the one in Prausnitz's book. Note also that this agrees with the ideal gas entropy limit, or with taking the derivative of the Gibbs free energy with respect to temperature at constant pressure, which is consistent with the reference state.

$$nS = -\left.\frac{d\left(nA\right)}{d\left(T\right)}\right|_{V,n_i} = \int_V^\infty \left[\frac{n_T R}{V} - \left(\frac{dP}{dT}\right)_{V,ni}\right] dV + R\sum_i n_i \ln\left(\frac{p^o V}{n_i RT}\right) + \sum_i n_i s_i^o \tag{12.7}$$

Now, we will assume in the analysis below that only has a dependence on temperature. Then, we can calculate the derivative of the pressure with temperature.

$$\left(\frac{dP}{dT}\right)_{V,ni} = \frac{nR}{V - nb_{mix}} - \frac{n^2}{\left(\sqrt{T}\right)V\left(V + nb_{mix}\right)}\left[\frac{da_{mix}}{dT} - \frac{a_{mix}}{2T}\right] \tag{12.8}$$

Then, we can calculate the integral as we did before.

$$\begin{aligned} nS = -\left.\frac{d\left(nA\right)}{d\left(T\right)}\right|_{V,n_i} &= \int_V^\infty \left[\frac{n_T R}{V} - \frac{n_T R}{V - n_T b_{mix}} + \frac{n_T^2}{\left(\sqrt{T}\right)V\left(V + n_T b_{mix}\right)}\left[\frac{da_{mix}}{dT} - \frac{a_{mix}}{2T}\right]\right] dV \\ &+ R\sum_i n_i \ln\left(\frac{p^o V}{n_i RT}\right) + \sum_i n_i s_i^o \end{aligned} \tag{12.9}$$

$$\begin{aligned} nS = -\left.\frac{d\left(nA\right)}{d\left(T\right)}\right|_{V,n_i} &= n_T R \ln\left[\frac{V - b_{mix} n_T}{V}\right] + \frac{n}{b_{mix} T^{0.5}} \ln\left[\frac{V + b_{mix} n_T}{V}\right]\left(\frac{da_{mix}}{dT} - \frac{a_{mix}}{2T}\right) \\ &+ R\sum_i n_i \ln\left(\frac{p^o V}{n_i RT}\right) + \sum_i n_i s_i^o \end{aligned} \tag{12.10}$$

We can also separate out the parts of the last term,

$$\begin{aligned} nS = -\left.\frac{d\left(nA\right)}{d\left(T\right)}\right|_{V,n_i} &= n_T R \ln\left[\frac{V - b_{mix} n_T}{V}\right] + \frac{n_T}{b_{mix} T^{0.5}} \ln\left[\frac{V + b_{mix} n_T}{V}\right]\left(\frac{da_{mix}}{dT} - \frac{a_{mix}}{2T}\right) \\ &- R\sum_i n_i \ln X_i - Rn_T \ln\left(\frac{n_T RT}{p^o V}\right) + \sum_i n_i s_i^o \end{aligned} \tag{12.11}$$

Lastly, we can separate out the ideal gas contributions for the enthalpy from the correction to the ideal gas contribution.

$$\begin{aligned} nS = -\left.\frac{d\left(nA\right)}{d\left(T\right)}\right|_{V,n_i} &= n_T R \ln\left(\frac{PV}{n_T RT}\right) + n_T R \ln\left[\frac{V - b_{mix} n_T}{V}\right] + \\ &\frac{n_T}{b_{mix} T^{0.5}} \ln\left[\frac{V + b_{mix} n_T}{V}\right]\left(\frac{da_{mix}}{dT} - \frac{a_{mix}}{2T}\right) - R\sum_i n_i \ln X_i - Rn_T \ln\left(\frac{P}{p^o}\right) + \sum_i n_i s_i^o \end{aligned} \tag{12.12}$$

Most of the terms in the second line of Eqn. (12.12) are the ideal gas contributions, while all of the terms in the first line are corrections to the ideal gas EoS.

Derivation of the Internal Energy Expression

We can calculate the total internal energy from the expression,

$$nA = nU - nTS \tag{12.13}$$

Then,

$$nU = \sum_i n_i u_i^o + \frac{n_T}{b_{mix} T^{0.5}} \ln\left[\frac{V + b_{mix} n_T}{V}\right]\left(T\frac{da_{mix}}{dT} - \frac{a_{mix}}{2}\right) - \frac{a_{mix} n_T}{b_{mix}\sqrt{T}} \ln\left[\frac{V + n_T b_{mix}}{V}\right]$$

This can be simplified to,

$$nU = \sum_i n_i u_i^o + \frac{n_T}{b_{mix} T^{0.5}} \ln\left[\frac{V + b_{mix} n_T}{V}\right]\left(T\frac{da_{mix}}{dT} - \frac{3a_{mix}}{2}\right) \tag{12.14}$$

Derivation of the Total Enthalpy Expression

We can calculate the total enthalpy from the expression

$$nH = nU + PV \tag{12.15}$$

Then,

$$nH = \sum_i n_i u_i^o + PV + \frac{n_T}{b_{mix} T^{0.5}} \ln\left[\frac{V + b_{mix} n_T}{V}\right]\left(T\frac{da_{mix}}{dT} - \frac{3a_{mix}}{2}\right) \tag{12.16}$$

$$nH = \sum_i n_i H_i^o + PV - n_T RT + \frac{n_T}{b_{mix} T^{0.5}} \ln\left[\frac{V + b_{mix} n_T}{V}\right]\left(T\frac{da_{mix}}{dT} - \frac{3a_{mix}}{2}\right) \tag{12.17}$$

Derivation and Self-Consistency of the Total Gibbs Free Energy Expression

We can calculate the total internal energy from the expression

$$nG = nA + PV \tag{12.18}$$

Plugging in the expression for the Helmholtz free energy

$$nG = \sum_i n_i a_{RS,i}^o(T) + PV - \sum_i RTn_i \ln\frac{p^o V}{n_i RT} + RTn_T \ln\left(\frac{V}{V - n_T b_{mix}}\right) - \frac{a_{mix} n_T}{b_{mix}\sqrt{T}} \ln\left[\frac{V + n_T b_{mix}}{V}\right]$$

This can be simplified

$$nG = \sum_i n_i \mu_{RS,i}^o(T) + PV - n_T RT - \sum_i RTn_i \ln\frac{p^o V}{n_i RT} + RTn_T \ln\left(\frac{V}{V - n_T b_{mix}}\right) - \frac{a_{mix} n_T}{b_{mix}\sqrt{T}} \ln\left[\frac{V + n_T b_{mix}}{V}\right] \tag{12.19}$$

We can verify the last expression by calculating the additional equation, Eqn. (12.20).

$$nG = \sum_i n_i \mu_i \left(T, P, n_i\right) \tag{12.20}$$

Let us take Eqn. (12.2),

$$n_i \mu_i = n_i \mu^o_{RS,i}\left(T\right) + RTn_i \ln X_i + RTn_i \ln \frac{P}{p^o} - RTn_i \ln \frac{PV}{nRT} + RTn_i \ln\left(\frac{V}{V - n_T b_{mix}}\right) + \frac{n_i RTn_T b_i}{V - n_T b_{mix}}$$
$$- \frac{2\sum a_{ij} n_j n_i}{n_T b_{mix}\sqrt{T}} \ln\left[\frac{V + n_T b_{mix}}{V}\right] + \frac{a_{mix} b_i n_i}{b^2_{mix}\sqrt{T}} \ln\left[\frac{V + n_T b_{mix}}{V}\right] - \frac{n_T a_{mix}}{b_{mix}\sqrt{T}}\left(\frac{b_i n_i}{V + n_T b_{mix}}\right)$$

We obtain,

$$\sum n_i \mu_i = \sum_i n_i \mu^o_{RS,i}\left(T\right) + \sum_i RTn_i \ln X_i + RTn_T \ln \frac{P}{p^o} - RTn_T \ln \frac{PV}{nRT} + RTn_T \ln\left(\frac{V}{V - n_T b_{mix}}\right) +$$
$$\frac{RTn_T^2 b_{mix}}{V - n_T b_{mix}} - \frac{2n_T^2 a_{mix}}{n_T b_{mix}\sqrt{T}} \ln\left[\frac{V + n_T b_{mix}}{V}\right] + \frac{a_{mix} n_T b_{mix}}{b^2_{mix}\sqrt{T}} \ln\left[\frac{V + n_T b_{mix}}{V}\right] - \frac{n_T^2 a_{mix}}{b_{mix}\sqrt{T}}\left(\frac{b_{mix}}{V + n_T b_{mix}}\right),$$

which can be then simplified to,

$$\sum n_i \mu_i = \sum_i n_i \mu^o_{RS,i}\left(T\right) + \sum_i RTn_i \ln X_i - RTn_T \ln \frac{p^o V}{nRT} + RTn_T \ln\left(\frac{V}{V - n_T b_{mix}}\right) + \frac{RTn_T^2 b_{mix}}{V - n_T b_{mix}}$$
$$- \frac{n_T a_{mix}}{b_{mix}\sqrt{T}} \ln\left[\frac{V + n_T b_{mix}}{V}\right] - \frac{n_T^2 a_{mix}}{b_{mix}\sqrt{T}}\left(\frac{b_{mix}}{V + n_T b_{mix}}\right).$$

Further simplification leads to Eqn. (12.21).

$$\sum n_i \mu_i = \sum_i n_i \mu^o_{RS,i}\left(T\right) + \sum_i RTn_i \ln X_i - RTn_T \ln \frac{p^o V}{nRT} + RTn_T \ln\left(\frac{V}{V - n_T b_{mix}}\right)$$
$$- \frac{n_T a_{mix}}{b_{mix}\sqrt{T}} \ln\left[\frac{V + n_T b_{mix}}{V}\right] + PV - n_T RT \tag{12.21}$$

The two equations, Eqn. (12.19)and Eqn. (12.21), agree.

Derivation of First Derivatives of the Pressure

Let us calculate the derivative of pressure with respect to temperature, volume, and mole number.

$$PV = \frac{n_T RTV}{V - n_T b_{mix}} - \frac{n_T^2 a_{mix}}{\left(\sqrt{T}\right)\left(V + n_T b_{mix}\right)}$$

$$\left.\frac{dP}{dT}\right|_{V,ni} = \frac{n_T R}{V - n_T b_{mix}} - \frac{n_T^2}{\left(T^{1/2}\right)V\left(V + n_T b_{mix}\right)}\left(\frac{da_{mix}}{dT} - \frac{a_{mix}}{2T}\right) \tag{12.22}$$

$$\left.\frac{dP}{dV}\right|_{T,ni} = \frac{-n_T RT}{\left(V - n_T b_{mix}\right)^2} + \frac{n_T^2 a_{mix}}{\left(T^{1/2}\right)V^2\left(V + n_T b_{mix}\right)} + \frac{n_T^2 a_{mix}}{\left(T^{1/2}\right)V\left(V + n_T b_{mix}\right)^2} \tag{12.23}$$

$$\left.\frac{dP}{dn_k}\right|_{T,V,ni} = \frac{RT}{V - n_T b_{mix}} + \frac{n_T RTb_k}{\left(V - n_T b_{mix}\right)^2} - \frac{2\sum_j n_j a_{kj}}{\left(T^{1/2}\right)V\left(V + n_T b_{mix}\right)} + \frac{n_T^2 a_{mix} b_k}{\left(T^{1/2}\right)V\left(V + n_T b_{mix}\right)^2} \tag{12.24}$$

These expressions are then used in subsequent derivations.

Derivation of Partial Molar Volume Expressions

For given conditions one can calculate the total volume of a mixture by solving the cubic EoS. However, it is less obvious how the partial molar volumes of the mixture are calculated. We start by manipulating the EoS to the following form

$$PV = \frac{n_T RTV}{V - n_T b_{mix}} - \frac{n_T^2 a_{mix}}{\left(\sqrt{T}\right)\left(V + n_T b_{mix}\right)} \tag{12.25}$$

Then, we can rearrange the following expression,

$$PV = \frac{n_T RTV}{V - n_T b_{mix}} - \frac{n_T^2 a_{mix}}{\left(\sqrt{T}\right)\left(V + n_T b_{mix}\right)}_{mix} = \frac{n_T RTV}{V - nb_{mix}} - \frac{n_T^2 a_{mix}}{\left(\sqrt{T}\right)\left(V + n_T b_{mix}\right)} - nRT\left[\frac{V - n_T b_{mix}}{V - n_T b_{mix}}\right] + n_T RT \tag{12.26}$$

$$PV = \frac{n_T RT\left(n_T b_{mix}\right)}{V - n_T b_{mix}} - \frac{\left(n_T^2 a_{mix}\right)}{\left(\sqrt{T}\right)\left(V + n_T b_{mix}\right)} + n_T RT$$

Now, we can formulate the partial molar volume expression, Eqn. (12.27) as

$$\bar{V}_i = \left.\frac{dV}{dn_i}\right|_{T,P,nj} \tag{12.27}$$

Carrying this out on Eqn. (12.26),

$$P\frac{dV}{dn_i}=\frac{RTn_Tb_{mix}}{V-n_Tb_{mix}}+\frac{n_TRTb_i}{V-n_Tb_{mix}}-\frac{n_TRTn_Tb_{mix}}{\left(V-n_Tb_{mix}\right)^2}\left(\frac{dV}{dn_i}-b_i\right)+RT$$
$$-\frac{\sum 2n_ja_{ij}}{\left(\sqrt{T}\right)\left(V+n_Tb_{mix}\right)}+\frac{\left(n_T^2a_{mix}\right)}{\left(\sqrt{T}\right)\left(V+n_Tb_{mix}\right)^2}\left(\frac{dV}{dn_i}+b_i\right)$$

Collecting terms yields,

$$\frac{dV}{dn_i}\left(P+\frac{n_TRTn_Tb_{mix}}{\left(V-n_Tb_{mix}\right)^2}-\frac{\left(n_T^2a_{mix}\right)}{\left(\sqrt{T}\right)\left(V+n_Tb_{mix}\right)^2}\right)=$$
$$RT+\frac{RTn_Tb_{mix}}{V-n_Tb_{mix}}+\frac{n_TRTb_i}{V-n_Tb_{mix}}+\frac{n_TRTn_Tb_{mix}b_i}{\left(V-n_Tb_{mix}\right)^2}-\frac{\sum 2n_ja_{ij}}{\left(\sqrt{T}\right)\left(V+n_Tb_{mix}\right)}+\frac{\left(n_T^2a_{mix}\right)b_i}{\left(\sqrt{T}\right)\left(V+n_Tb_{mix}\right)^2}$$

And then,

$$\left.\frac{dV}{dn_i}\right|_{T,P,nj}=$$
$$\frac{RT+\frac{RTn_Tb_{mix}}{V-n_Tb_{mix}}+\frac{n_TRTb_i}{V-n_Tb_{mix}}+\frac{n_TRTn_Tb_{mix}b_i}{\left(V-n_Tb_{mix}\right)^2}-\frac{\sum 2n_ja_{ij}}{\left(\sqrt{T}\right)\left(V+n_Tb_{mix}\right)}+\frac{\left(n_T^2a_{mix}\right)b_i}{\left(\sqrt{T}\right)\left(V+n_Tb_{mix}\right)^2}}{\left(P+\frac{n_TRTn_Tb_{mix}}{\left(V-n_Tb_{mix}\right)^2}-\frac{\left(n_T^2a_{mix}\right)}{\left(\sqrt{T}\right)\left(V+n_Tb_{mix}\right)^2}\right)} \quad (12.28)$$

This is a closed form expression for the partial molar volume. It is correct for the ideal gas limit. When its multiple with n_i is summed up over all species, it should equal *V* again. This is true for all partial molar properties.

Heat Capacities

Taking derivatives at constant pressure is not possible with a volume based EoS. However, we can take our cues from Wagner and Prub (Wagner and Prub 2002) who develop thermodynamic functions from a Helmholtz formulation with T and ρ being independent variables.

First, let us derive a useful formula,

$$dS=\left.\frac{dS}{dT}\right|_p dT+\left.\frac{dS}{dP}\right|_T dp$$

$$\left.\frac{dS}{dT}\right|_V = \left.\frac{dS}{dT}\right|_p + \left.\frac{dS}{dP}\right|_T \left.\frac{dP}{dT}\right|_V$$

$$\frac{C_V}{T} = \frac{C_p}{T} - \left.\frac{dV}{dT}\right|_P \left.\frac{dP}{dT}\right|_V$$

Now, it is a trick to rearrange $\left.\frac{dV}{dT}\right|_P$ so that it is a function of P. The resulting expression is

$$\left.\frac{dV}{dT}\right|_P = -\frac{\left.\frac{dP}{dT}\right|_V}{\left.\frac{dP}{dV}\right|_T} \tag{12.29}$$

Note, the negative sign in Eqn. (12.29) is correct. Eqn. (12.29) can be verified on any simple system, and is a trick worth remembering. Plugging it in yields Eqn.(12.30).

$$\frac{C_V}{T} = \frac{C_p}{T} - \frac{\left.\frac{dP}{dT}\right|_V}{\left.\frac{dP}{dV}\right|_T} \left.\frac{dP}{dT}\right|_V \tag{12.30}$$

Then, it is just a matter of developing the formulas.

There is an alternative to the above treatment starting with a differential expression for the change in enthalpy with constant mole numbers assumed.

$$dH = \left.\frac{dH}{dP}\right|_T dP + \left.\frac{dH}{dT}\right|_P dT$$

We can make that specific via Eqn. (12.31) (note this equation can easily be verified for an ideal gas case).

$$\left.\frac{dH}{dT}\right|_V = \left.\frac{dH}{dP}\right|_T \left.\frac{dP}{dT}\right|_V + \left.\frac{dH}{dT}\right|_P \tag{12.31}$$

Therefore,

$$C_p = \left.\frac{dH}{dT}\right|_V - \left.\frac{dH}{dP}\right|_T \left.\frac{dP}{dT}\right|_V = \left.\frac{dH}{dT}\right|_V - \left(V - T\left.\frac{dV}{dT}\right|_P\right)\left.\frac{dP}{dT}\right|_V \tag{12.32}$$

As derived in the next section, Eqn. (12.32) may be simplified for a volume-based formulation

$$C_p = \left.\frac{dH}{dT}\right|_V - \left.\frac{dH}{dP}\right|_T \left.\frac{dP}{dT}\right|_V = \left.\frac{dH}{dT}\right|_{V,ni} - \left(V + T \frac{\left.\frac{dP}{dT}\right|_{ni,V}}{\left.\frac{dP}{dV}\right|_{ni,T}} \right) \left.\frac{dP}{dT}\right|_{V,ni} \tag{12.33}$$

All of these quantities are readily calculated. Starting with the equation below, we derive the derivative of the enthalpy with respect to temperature.

$$nH = \sum_i n_i H_i^o + PV - n_T RT + \frac{n_T^2}{n_T b_{mix} T^{0.5}} \ln\left[\frac{V + b_{mix} n_T}{V}\right]\left(T\frac{da_{mix}}{dT} - \frac{3a_{mix}}{2}\right)$$

$$\left.\frac{dnH}{dT}\right|_{V,ni} = \sum_i n_i C_{p,i}^o + V \left.\frac{dP}{dT}\right|_{V,ni} - n_T R - \frac{n_T^2}{2n_T b_{mix} T^{1.5}} \ln\left[\frac{V + b_{mix} n_T}{V}\right]\left(T\frac{da_{mix}}{dT} - \frac{3a_{mix}}{2}\right)$$

$$+ \frac{n_T^2}{n_T b_{mix} T^{0.5}} \ln\left[\frac{V + b_{mix} n_T}{V}\right]\left(-\frac{1}{2}\frac{da_{mix}}{dT}\right) \tag{12.34}$$

Partial Molar Quantities – Partial Molar Enthalpy

We need to develop an equation to describe the enthalpy approximation as a function of n_i, v, and T. Normally, we could just take the derivative of the expression with respect to n_i to determine the partial molar enthalpy. However, partial molar quantities have a property that the pressure is held constant and therefore, we cannot just do this simple treatment and instead we adopt the following approach. We will calculate the derivative of the enthalpy with respect to mole number at constant volume. Then, we will derive a "fixed-up" formula for translating that result to a constant pressure result. Let us begin with the differential of the enthalpy expression at constant pressure. Then, we will take the derivative of the differential with respect to the i^{th} species mole number at constant volume, thereby generating an expression that relates the constant molar volume derivative to the constant pressure derivative, Eqn. (12.35),

$$d\left(nH\right) = \left.\frac{d\left(nH\right)}{dn_i}\right|_p dn_i + \left.\frac{d\left(nH\right)}{dP}\right|_{ni} dP$$

$$\left.\frac{d\left(nH\right)}{dn_i}\right|_V = \left.\frac{d\left(nH\right)}{dn_i}\right|_p + \left.\frac{d\left(nH\right)}{dP}\right|_{ni} \left.\frac{dP}{dn_i}\right|_V \tag{12.35}$$

Note that a more sophisticated treatment beginning with a full differential results in the same expression as Eqn.(12.35). The above equation then appears to be correct and has been shown to be correct by using the partial molar summation property rule. Now,

$$\left.\frac{dnH}{dP}\right|_{ni} = T\left.\frac{dnS}{dP}\right|_{ni,T} + V = V - T\left.\frac{dV}{dT}\right|_{ni,P} = V + T\frac{\left.\frac{dP}{dT}\right|_{ni,V}}{\left.\frac{dP}{dV}\right|_{ni,T}}$$

Therefore,

$$\left.\frac{dnH}{dn_i}\right|_{V,T,nj} = \left.\frac{dnH}{dn_i}\right|_{p,T,nj} + \left[V + T\frac{\left.\frac{dP}{dT}\right|_{ni,V}}{\left.\frac{dP}{dV}\right|_{ni,T}}\right]\left.\frac{dP}{dn_i}\right|_{V,T,nj} \tag{12.36}$$

Note, this formula works for the ideal gas case. Most of the expressions have already been derived previously. Here, we derive the last expression.

$$nH = \sum_i n_i H_i^o + PV - n_T RT + \frac{n_T^2}{n_T b_{mix} T^{0.5}} \ln\left[\frac{V + b_{mix} n_T}{V}\right]\left(T\frac{da_{mix}}{dT} - \frac{3a_{mix}}{2}\right) \tag{12.37}$$

$$\begin{aligned}\left.\frac{dnH}{dn_i}\right|_{V,T,nj} &= H_i^o + V\left.\frac{dP}{dn_i}\right|_{V,T,nj} - RT - \frac{n_T^2 b_i}{n_T^2 b_{mix}^2 T^{0.5}} \ln\left[\frac{V + b_{mix} n_T}{V}\right]\left(T\frac{da_{mix}}{dT} - \frac{3a_{mix}}{2}\right) \\ &+ \frac{1}{n_T b_{mix} T^{0.5}} \ln\left[\frac{V + b_{mix} n_T}{V}\right]\left(2\sum_j n_j\left(T\frac{da_{ij}}{dT} - \frac{3a_{ij}}{2}\right)\right) \\ &+ \frac{n_T^2}{n_T b_{mix} T^{0.5}}\left(\frac{b_i}{V + b_{mix} n_T}\right)\left(T\frac{da_{mix}}{dT} - \frac{3a_{mix}}{2}\right)\end{aligned} \tag{12.38}$$

Note, for an ideal gas, the following expression holds,

$$\left.\frac{dnH}{dn_i}\right|_{V,T,nj} = \left.\frac{dnH}{dn_i}\right|_{P,T,nj} \tag{12.39}$$

Partial Molar Quantities – Partial Molar Entropy

For the partial molar entropy we may use the following expression (Smith and Ness 1975):

$$\overline{S}_i = -\left.\frac{d\mu_i}{dT}\right|_{p,nj} \tag{12.40}$$

However, we are still left with a problem in determining the constant pressure property and the following formula provides the solution,

$$\left.\frac{d\mu_i}{dT}\right|_{V,nj} = \left.\frac{d\mu_i}{dP}\right|_{T,nj} \left.\frac{dP}{dT}\right|_{ni,V} + \left.\frac{d\mu_i}{dT}\right|_{P,nj} \tag{12.41}$$

Then, this may be simplified to

$$\left.\frac{d\mu_i}{dT}\right|_{P,nj} = \left.\frac{d\mu_i}{dT}\right|_{V,nj} - \bar{V}_i \left.\frac{dP}{dT}\right|_{V,nj} \tag{12.42}$$

Thus, we are left with developing one expression for the derivative of the chemical potential in order to calculate the partial molar entropies. We start with Eqn. (12.2) to develop the expression

$$\begin{aligned}
\mu_i &= \mu^o_{RS,i}(T) + RT\ln X_i + RT\ln\frac{P}{p^o} - RT\ln\frac{PV}{nRT} + RT\ln\left(\frac{V}{V-n_T b_{mix}}\right) + \frac{RTn_T b_i}{V-n_T b_{mix}} \\
&\quad - \frac{2\sum a_{ij}n_j}{n_T b_{mix}\sqrt{T}}\ln\left[\frac{V+n_T b_{mix}}{V}\right] + \frac{a_{mix}b_i}{b^2_{mix}\sqrt{T}}\ln\left[\frac{V+n_T b_{mix}}{V}\right] - \frac{n_T a_{mix}}{b_{mix}\sqrt{T}}\left(\frac{b_i}{V+n_T b_{mix}}\right) \\
\left.\frac{d\mu_i}{dT}\right|_{V,nj} &= \frac{d\mu^o_{RS,i}(T)}{dT} + R\ln X_i + R\ln\frac{nRT}{p^o V} + R + R\ln\left(\frac{V}{V-n_T b_{mix}}\right) + \frac{Rn_T b_i}{V-n_T b_{mix}} \\
&\quad + \frac{\sum a_{ij}n_j}{n_T b_{mix}T^{3/2}}\ln\left[\frac{V+n_T b_{mix}}{V}\right] - \frac{2\sum \frac{da_{ij}}{dT}n_j}{n_T b_{mix}\sqrt{T}}\ln\left[\frac{V+n_T b_{mix}}{V}\right] \\
&\quad + \frac{b_i}{b^2_{mix}\sqrt{T}}\ln\left[\frac{V+n_T b_{mix}}{V}\right]\left(\frac{da_{mix}}{dT} - \frac{a_{mix}}{2T}\right) - \frac{n_T}{b_{mix}\sqrt{T}}\left(\frac{b_i}{V+n_T b_{mix}}\right)\left(\frac{da_{mix}}{dT} - \frac{a_{mix}}{2T}\right)
\end{aligned} \tag{12.43}$$

In the limit of an ideal gas,

$$\left.\frac{d\mu_i}{dT}\right|_{V,nj} = \frac{d\mu^o_{RS,i}(T)}{dT} + R\ln X_i + R\ln\frac{P}{p^o} + R$$

and

$$\left.\frac{d\mu_i}{dT}\right|_{P,nj} = \frac{d\mu^o_{RS,i}(T)}{dT} + R\ln X_i + R\ln\frac{P}{p^o} + R - R = \frac{d\mu^o_{RS,i}(T)}{dT} + R\ln X_i + R\ln\frac{P}{p^o}$$

13. Appendix C: Conditional Gaussian Fields

Let $G(\mathbf{x})$, $\mathbf{x} \in D \subset \mathbb{R}^d$, $d \geq 1$, be a real-valued Gaussian random field with mean $\mu(\mathbf{x}) = \mathrm{E}[G(\mathbf{x})]$ and covariance function $\rho(\mathbf{x}, \mathbf{y}) = \mathrm{E}[(G(\mathbf{x}) - \mu(\mathbf{x}))\,(G(\mathbf{y}) - \mu(\mathbf{y}))]$. Suppose G is measured without error at n points $\{\mathbf{u}_k \in D,\ k = 1, \ldots, n\}$ and that $G(\mathbf{u}_k) = g_k$, $k = 1, \ldots, n$.

Consider the $m + n$ dimensional Gaussian random vector with coordinates

$$[G(\mathbf{x}_1), \ldots, G(\mathbf{x}_m), G(\mathbf{u}_1), \ldots, G(\mathbf{u}_n)]',\ \mathbf{x}_1, \ldots, \mathbf{x}_m \in D \text{ arbitrary}, \tag{13.1}$$

mean vector

$$\boldsymbol{\mu} = \begin{bmatrix} \boldsymbol{\mu}_1 \\ \boldsymbol{\mu}_2 \end{bmatrix} = \begin{bmatrix} \mu(\mathbf{x}_1) \\ \vdots \\ \mu(\mathbf{x}_m) \\ \mu(\mathbf{u}_1) \\ \vdots \\ \mu(\mathbf{u}_n) \end{bmatrix} \tag{13.2}$$

and covariance matrix

$$\boldsymbol{\gamma} = \begin{bmatrix} \boldsymbol{\gamma}_{11} & \boldsymbol{\gamma}_{12} \\ \boldsymbol{\gamma}_{21} & \boldsymbol{\gamma}_{22} \end{bmatrix} = \begin{bmatrix} c(\mathbf{x}_1, \mathbf{x}_1) & \cdots & c(\mathbf{x}_1, \mathbf{x}_m) & c(\mathbf{x}_1, \mathbf{u}_1) & \cdots & c(\mathbf{x}_1, \mathbf{u}_n) \\ \vdots & \ddots & \vdots & \vdots & \ddots & \vdots \\ c(\mathbf{x}_m, \mathbf{x}_1) & \cdots & c(\mathbf{x}_m, \mathbf{x}_m) & c(\mathbf{x}_m, \mathbf{u}_1) & \cdots & c(\mathbf{x}_m, \mathbf{u}_n) \\ c(\mathbf{u}_1, \mathbf{x}_1) & \cdots & c(\mathbf{u}_1, \mathbf{x}_m) & c(\mathbf{u}_1, \mathbf{u}_1) & \cdots & c(\mathbf{u}_1, \mathbf{u}_n) \\ \vdots & \ddots & \vdots & \vdots & \ddots & \vdots \\ c(\mathbf{u}_n, \mathbf{x}_1) & \cdots & c(\mathbf{u}_n, \mathbf{x}_m) & c(\mathbf{u}_n, \mathbf{u}_1) & \cdots & c(\mathbf{u}_n, \mathbf{u}_n) \end{bmatrix} \tag{13.3}$$

The first m coordinates of the Gaussian random vector defined by Eqn. (13.1) correspond to values of the field at arbitrary locations in D, and the last n coordinates of this vector correspond to the field at the known measurement sites.

It can be shown (see, for example, [Grigoriu 2002, 66]) that the conditional vector

$$[G(\mathbf{x}_1), \ldots, G(\mathbf{x}_m)]' | ([G(\mathbf{u}_1), \ldots, G(\mathbf{u}_n)]' = \mathbf{g}), \tag{13.4}$$

is Gaussian with $m \times 1$ mean vector $\tilde{\boldsymbol{\mu}}$ and $m \times m$ covariance matrix $\tilde{\boldsymbol{\gamma}}$, where

$$\begin{aligned} \tilde{\boldsymbol{\mu}} &= \boldsymbol{\mu}_1 + \boldsymbol{\gamma}_{12}\boldsymbol{\gamma}_{22}^{-1}(\mathbf{g} - \boldsymbol{\mu}_2) \\ \tilde{\boldsymbol{\gamma}} &= \boldsymbol{\gamma}_{11} - \boldsymbol{\gamma}_{12}\boldsymbol{\gamma}_{22}^{-1}\boldsymbol{\gamma}_{21} \end{aligned} \tag{13.5}$$

We note that $\tilde{\boldsymbol{\mu}}$ defined above is consistent with the "simple Kriging" interpolation scheme (Cressie 1993, chap. 3).

Because $\mathbf{x}_1, \ldots, \mathbf{x}_m \in D$ are arbitrary, the second moment properties of this vector constitute the second moment properties of the random field $G(\mathbf{x})$, conditional on measurements $\{G(\mathbf{u}_1), \ldots, G(\mathbf{u}_n)\}$. Samples of the conditional Gaussian field on the grid $\{\mathbf{x}_k,\ k = 1, \ldots, m\}$ can be produced by generating samples of the conditional Gaussian vector defined by Eqn. (13.4) using, for example, its Karhunen-Loéve expansion.

Distribution

1 Prof. M. Delshad (electronic copy)
delshad@mail.utexas.edu
Petroleum and Geosystems Engineering Dept.
Cockrell School of Engineering
University of Texas at Austin
Austin, TX 78712

1 Prof. M. F. Wheeler (electronic copy)
mfw@ices.utexas.edu
ICES
University of Texas at Austin
Austin, TX 78712

1	MS1321	R. M. Summers	1444 (electronic copy)
1	MS0384	D. B. Dimos	1500 (electronic copy)
1	MS0825	J. S. Lash	1510 (electronic copy)
1	MS0828	M. Pilch	1514 (electronic copy)
10	MS0836	M. J. Martinez	1514
1	MS0836	P. L. Hopkins	1516 (electronic copy)
1	MS0836	H. K. Moffat	1516 (electronic copy)
1	MS0346	M. Mesh	1523 (electronic copy)
1	MS0824	J. E. Bean	1525 (electronic copy)
1	MS0824	J. E. Bishop	1525 (electronic copy)
1	MS0824	J. Pott	1525 (electronic copy)
1	MS0824	P. Newell	1525 (electronic copy)
1	MS0346	R. Field	1526 (electronic copy)
1	MS0380	D. E. Womble	1540 (electronic copy)
1	MS0836	P. K. Notz	1541 (electronic copy)
1	MS0836	D. Z. Turner	1541 (electronic copy)
1	MS0382	B. Carnes	1544 (electronic copy)
1	MS0828	J. Red-Horse	1544 (electronic copy)
1	MS1469	A. C. Ratzel	4800 (electronic copy)
1	MS0771	S. A. Orrell	6200 (electronic copy)
1	MS0779	Y. Wang	6222 (electronic copy)
1	MS0779	C. Jove-Colon	6222 (electronic copy)
1	MS0734	S. M. Davison	6632 (electronic copy)
1	MS0701	M. C. Walck	6900 (electronic copy)
1	MS0735	J. A. Merson	6910 (electronic copy)
1	MS0751	K. Klise	6911 (electronic copy)
1	MS0751	T. Dewers	6914 (electronic copy)
1	MS0751	T. Pfeifle	6914 (electronic copy)
1	MS0751	H. Yoon	6914 (electronic copy)
1	MS0899	Technical Library	9536 (electronic copy)
1	MS0359	D. Chavez, LDRD Office	1911 (electronic copy)

Sandia National Laboratories